

Interactive Visualization for Assistance of Needle-Based Interventions

by

Christian Rieder

A thesis submitted in partial fulfillment
of the requirements for the degree of

**Doctor of Philosophy
in Computer Science**

Dissertation Committee:

Prof. Dr.-Ing. Horst K. Hahn (Dissertation Advisor)
School of Engineering and Science, Jacobs University Bremen, Germany

Prof. Dr.-Ing. Lars Linsen
School of Engineering and Science, Jacobs University Bremen, Germany

Prof. Dr.-Ing. Bernhard Preim
Department of Computer Science, University of Magdeburg, Germany

Date of Defense: March 22nd, 2013

School of Engineering and Science

Abstract

NEEDLE-BASED interventions are an important part of tumor ablation therapies. Due to their common technical procedure, low complication rate, and low cost, needle-based ablation therapies have become alternatives to surgical resections in clinical practice. To date, the most well-studied and clinically relevant ablation therapy is radiofrequency ablation (RFA) in the liver. However, achieving successful outcomes is a challenging task which depends on a variety of partially unknown reasons. This uncertainty is mirrored by the high local recurrence rates reported in clinical studies. The aim of this PhD thesis is the investigation of interactive visualization methods to support the physician in planning and assessing needle-based interventions, in particular RFA.

This work proposes a software workflow designed to guide the physician in planning the intervention in clinical practice. To support the physician with spatial information about pathological structures as well as finding trajectories without harming vitally important tissue, 2D slice and volume visualization techniques for interactive planning of needle-based interventions are presented. A further contribution for planning RFA is the fast approximation of the ablation zone, incorporating the heat-sink effects of blood vessels which decrease thermal ablation. In this approach, weighted distance fields are utilized to calculate the ablation zone within interactive frame rates on the graphics processing unit (GPU).

To support the assessment of needle-based interventions such as RFA, an image-processing workflow for automatic alignment of CT images is proposed. Based on segmentation masks of tumor and coagulation, the workflow enables an automatic rigid registration algorithm to perform at least as accurately as experienced medical experts, but in significantly less time. A further contribution is a novel overview visualization as well as a navigation tool, the so-called *tumor map*. The goal of this method is the combined visualization of the tumor and its surface distance to the coagulation necrosis to support the physician in reliable therapy assessment. The tumor map additionally serves as an interactive tool for intuitive navigation within a 3D volume rendering of the tumor vicinity as well as within familiar 2D viewers.

To facilitate the development of highly interactive visualization techniques, a rapid prototyping framework for GPU-based volume rendering is developed as part of this PhD thesis. The framework supports flexible extension and dynamic alteration of the volume rendering configuration. Therefore, a dynamic shader pipeline based on the *SuperShader* concept allows the user to insert custom shaders at run-time of the prototyping framework.

Kurzfassung

NADELBASIERTE Interventionen stellen einen wichtigen Teil von Ablations-therapien zur Behandlung von Tumoren dar. Durch ihre einfache Handhabbarkeit, geringen Komplikationsraten und geringfügigen Kosten gelten sie in der klinischen Routine als alternative Therapien gegenüber der chirurgischen Resektion. Bis dato ist die Radiofrequenz Ablation (RFA) in der Leber die meist studierte und klinisch relevanteste Ablationstherapie. Allerdings ist das Erreichen von erfolgreichen Resultaten eine herausfordernde Aufgabe, welche von teilweise unbekannt Ursachen abhängig ist. Klinische Studien spiegeln diese Unsicherheit in hohen Rezidivraten wieder. Das Ziel dieser Dissertation ist die Erforschung von interaktiven Visualisierungsmethoden um Radiologen bei der Planung und Bewertung von nadelbasierten Interventionen, insbesondere der RFA, zu unterstützen.

In dieser Arbeit wird ein Software-Workflow präsentiert, welcher den Radiologen bei der Planung von Interventionen in der klinischen Routine assistiert. Um den Radiologen mit räumlichen Information von pathologischen Strukturen zu unterstützen, sowie das Finden von Zugangswegen unter Berücksichtigung von Risikostrukturen zu erleichtern, werden 2D Slice- und 3D Volumenrendering Techniken vorgestellt. Ein weiterer Beitrag dieser Arbeit ist die schnelle Berechnung der Ablationszone unter Berücksichtigung der Kühleffekte von nahegelegenen Blutgefäßen, welche die Größe der Ablationszone reduzieren können. In diesem Verfahren werden gewichtete Distanzfelder verwendet, welches es erlauben die Ablationszone in Echtzeit auf der Grafikkarte zu berechnen.

Um die Bewertung von nadelbasierten Interventionen wie die RFA zu unterstützen, wird in dieser Arbeit ein Workflow für die automatische Registrierung von CT-Bildern vorgestellt. Dieser erlaubt es eine rigide Registrierung, welche auf Segmentierungen von Tumor und Koagulation basiert, so genau wie erfahrene Mediziner, aber in kürzerer Zeit zu berechnen. Ein weiterer Beitrag ist eine neue Übersichtvisualisierung, welche auch als Interaktionswerkzeug zur Steuerung von 3D Volumenrendering bzw. von 2D Ansichten dient. Das Ziel dieser Methode ist die kombinierte Visualisierung der Tumoroberfläche sowie deren Distanz zur Koagulation, um den Radiologen bei der Bewertung des Therapieerfolgs zu unterstützen.

Als Teil dieser Dissertation wird außerdem ein Prototyping-Framework zur Erstellung von interaktiven Volumenvisualisierungen entwickelt. Das Framework erlaubt es die Konfiguration des Volumenrenderings flexibel zu erweitern und dynamisch anzupassen. Hierfür ermöglicht eine dynamische Shaderpipeline, welche auf dem *SuperShader* Konzept basiert, dem Benutzer eigens angepasste Shaderprogramme zur Laufzeit des Systems hinzuzufügen.

Acknowledgment

THIS work would not been possible without the help of many people. First of all, I would like to thank my PhD advisor Prof. Dr.-Ing. Horst K. Hahn for having the time to support this PhD thesis with lots of scientific discussions. Further, I would like to thank the additional dissertation committee members Prof. Dr.-Ing. Lars Linsen and Prof. Dr.-Ing. Bernhard Preim for fruitful discussions and their helpful comments.

I give special thanks to Prof. Dr. Heinz-Otto Peitgen for enabling me to be member of the Fraunhofer MEVIS staff. Further, I would like to thank the medical collaborators, in particular Prof. Dr. med. Andreas H. Mahnken, Dr. med. Philipp Bruners, Dr. med. Peter Isfort, and Hong-Sik Na for their helpful feedback and for their participation in clinical studies. I'm grateful to the co-authors of the scientific publications for the discussions which were a great source of inspiration. Moreover, I want to thank the Fraunhofer MEVIS staff for the enjoyable work environment and funny conversations at the coffee machine.

Last, I would like to thank my family, particularly my parents, who always supported my ideas. Further, I owe special thanks to my wife Nadine and my kids Lisa and Paul for their patience and thoughtfulness which allowed me to work on this PhD thesis.

Table of Contents

Abstract	iii
Kurzfassung	iv
Acknowledgment	v
Table of Contents	vii
1 Introduction	1
1.1 Medical Background	2
1.2 Challenges and Contributions	2
1.3 Structure of this Thesis	4
2 Fundamentals	7
2.1 Image-guided Intervention	8
2.1.1 Planning	8
2.1.2 Intervention	9
2.1.3 Assessment	10
2.2 Radiofrequency Ablation	10
2.2.1 Introduction	12
2.2.2 Principles	12
2.2.3 Biophysical Effects	12
2.2.4 RF Systems and Electrodes	14
2.2.5 RFA of Liver Tumors	16
2.3 The Graphics Processing Unit	18
2.3.1 The Graphics Pipeline	18
2.3.2 GPU Programming	19
2.4 Direct Volume Rendering	21

2.4.1	The Volume-Rendering Pipeline	21
2.4.2	GPU-Based Volume Rendering	22
3	Workflow for Interactive Planning of RFA	25
3.1	Introduction	26
3.2	Related Work	27
3.3	Workflow-Based Software Support	28
3.3.1	Tumor Segmentation	29
3.3.2	Probe Placement	30
3.3.3	Vessel Segmentation	31
3.3.4	Numerical Simulation	31
3.4	Interactive Slice Visualization	32
3.4.1	Contour Rendering of Segmentation Masks	32
3.4.2	Visualization of Ellipsoidal Ablation Zones	32
3.4.3	Contour Rendering of the Coagulation Necrosis	34
3.5	Interactive Volume Visualization	35
3.5.1	Anatomical Volume Rendering	35
3.5.2	Probe Target View	36
3.5.3	Visualization of Tumors and Ablation Zones	37
3.5.4	Iso-Hull Visualization of the Coagulation Necrosis	38
3.6	Results and Discussion	39
3.7	Conclusions	43
4	Interactive Approximation of the Ablation Zone	45
4.1	Introduction	46
4.2	Related Work	47
4.3	Mathematical Background	48
4.4	Lookup Table-Based Approximation of the Ablation Zone	51
4.4.1	A Simplified Geometric Model	51
4.4.2	Pre-Calculation of the Patient Independent Ablation Zone	52
4.4.3	Calculation of the Patient Dependent Ablation Zone	53
4.4.4	Results and Discussion	54
4.5	GPU-Based Approximation of the Ablation Zone	57
4.5.1	Approximation utilizing a Weighted Distance Field	57

4.5.2	Estimating the Thermal Diffusion of the Vasculature	58
4.5.3	Deformation of the Ablation Zone	60
4.5.4	Application	62
4.5.5	2D Slice Visualization	63
4.5.6	3D Volume Visualization	66
4.6	Results	69
4.6.1	Comparison with the Numerical Simulation	69
4.6.2	Expert Evaluation	70
4.7	Discussion and Conclusions	73
5	Workflow for Automatic Alignment of Interventional Images	77
5.1	Introduction	78
5.2	Related Work	79
5.3	Registration Workflow	80
5.3.1	Lesion Segmentation	80
5.3.2	Automatic Rigid Registration	82
5.3.3	Manual Rigid Registration	82
5.3.4	Result Visualization	86
5.4	Evaluation	86
5.4.1	Specification of Robust Landmarks	87
5.4.2	Estimation of the Ground Truth Transformation	88
5.4.3	Landmark Transformation	90
5.5	Results and Discussion	90
5.6	Conclusions	92
6	Visual Support for Interactive Assessment of RFA	95
6.1	Introduction	96
6.2	Related Work	97
6.3	Preprocessing	99
6.4	Ablation Color Scheme	100
6.4.1	Color Scheme of Coagulation Zones	100
6.4.2	Visualization in 2D	101
6.4.3	Visualization in 3D	103
6.5	Tumor Map	104

6.5.1	Map Projection of the Tumor Surface	105
6.5.2	Cylindrical Mapping of the Tumor Surface	105
6.5.3	Tumor Map Layout	108
6.5.4	Interaction with the Tumor Map	110
6.6	Results	113
6.6.1	Implementation	114
6.6.2	Performance	115
6.6.3	Evaluation	115
6.6.4	Clinical Study	118
6.6.5	Outlook: Tumor Map for Intervention Planning	123
6.7	Discussion and Conclusion	124
7	A Shader Framework for Rapid Prototyping	129
7.1	Introduction	130
7.2	Related Work	131
7.3	Rapid Prototyping	132
7.4	Dynamic Shader Pipeline	133
7.4.1	Design Decisions	133
7.4.2	Basic Approach	134
7.4.3	Application to Volume Rendering	137
7.4.4	Application to Slab Rendering	137
7.5	Prototyping Environment	138
7.5.1	Volume Rendering Scene Graph	139
7.5.2	Custom Shader Pipeline	139
7.6	Example Applications	143
7.6.1	Stochastic Jittering of the Sample Position	144
7.6.2	Fragment Clipping for Multi-Volume Rendering	144
7.6.3	Dynamic Visualization of RF Ablation Zones	148
7.7	Results and Discussion	149
7.8	Conclusions	152
8	Summary	155
	Appendix	161
	List of Abbreviations	163

List of Figures 165
List of Tables 167
List of Own Publications 169
Bibliography 171

*Progress is not an illusion, it happens,
but it is slow and invariably
disappointing.*

(George Orwell)

1

Introduction

COAGULATION of living tissue by means of heat was mentioned in about 3000 B.C. in the Edwin Smith papyrus. Nowadays, thermal tumor ablation therapies such as radiofrequency ablation (RFA) have become an important part of image-guided interventional oncology. The aim of this PhD thesis is to investigate and develop interactive methods to support the physician in planning and assessing the therapy in a fast and intuitive way. In this chapter, the medical background and the technical challenges as well as the scientific contributions are outlined.

1.1 Medical Background

Recent studies report more than 3 million cancer diseases per year in Europe [55]. More than 50 % of the patients tend to get metastasis in the liver [133]. The first choice therapy is the surgical resection of the liver tumors. However, only 10–25 % of the patients are eligible for such a treatment [54]. Typical reasons are the general health conditions of the patients or multiple scattered lesions, which make the surgical resection impossible. Thermal tumor ablation therapies such as radiofrequency ablation (RFA), cryoablation or microwave ablation (MWA) have become important alternatives as part of image-guided interventional oncology. Due to its common technical procedure, low complication rate, and low cost, in particular RFA has become an established therapy in the clinical routine.

RFA is clinically indicated as a minimally invasive therapy if the tumor is of less than 30 mm in diameter, multiple lesions are scattered in the liver (1-3 nodules), or a surgical resection is contraindicated, e.g., due to the general constitution of the patient [58, 62, 122]. A recent study [22] reports that the initial treatment of secondary liver tumors larger than 25 mm has shown a high local recurrence rate because of inaccurately placed applicators or the inability to produce a predictable, large coagulation volume. Another study states that the local recurrence rates after RFA for tumors with an intentional margin of 0 mm and 10 mm are 14.5% and 6.5%, respectively [121].

1.2 Challenges and Contributions

A great challenge for tumor treatment with RFA is the accurate pre-interventional planning of the therapy in order to achieve complete destruction of all tumor cells (see Figure 1.1). In clinical practice, planning is based on 2D slices of the planning scan. Because the therapy is performed in 3D space, the identification of an appropriate therapy can be demanding using 2D slice visualizations alone. Another aspect is to perform the planning within few minutes due to the limited available time in clinical practice. In this work, a **workflow allowing for interactive visualization and image-processing**, which is designed to **guide the physician in planning** the intervention for use in clinical practice, is presented. Appropriate visualization and image processing methods are combined to support the physician in interactive finding of safe and feasible access paths. In contrast to related systems, RF applicators and corresponding ablation zones are fully integrated into familiar 2D slice visualizations as well as 3D volume renderings that emphasize surrounding risk structures without the need to calculate time-consuming segmentations and 3D reconstructions.

Taking the patient individual anatomy into account is essential to successfully achieve thermal treatment of cancer cells. In the case of RFA, particularly the cooling blood vessels determine the maximum size of the ablation zone. In clinical practice, the physician mentally estimates the ablation zone incorporating the

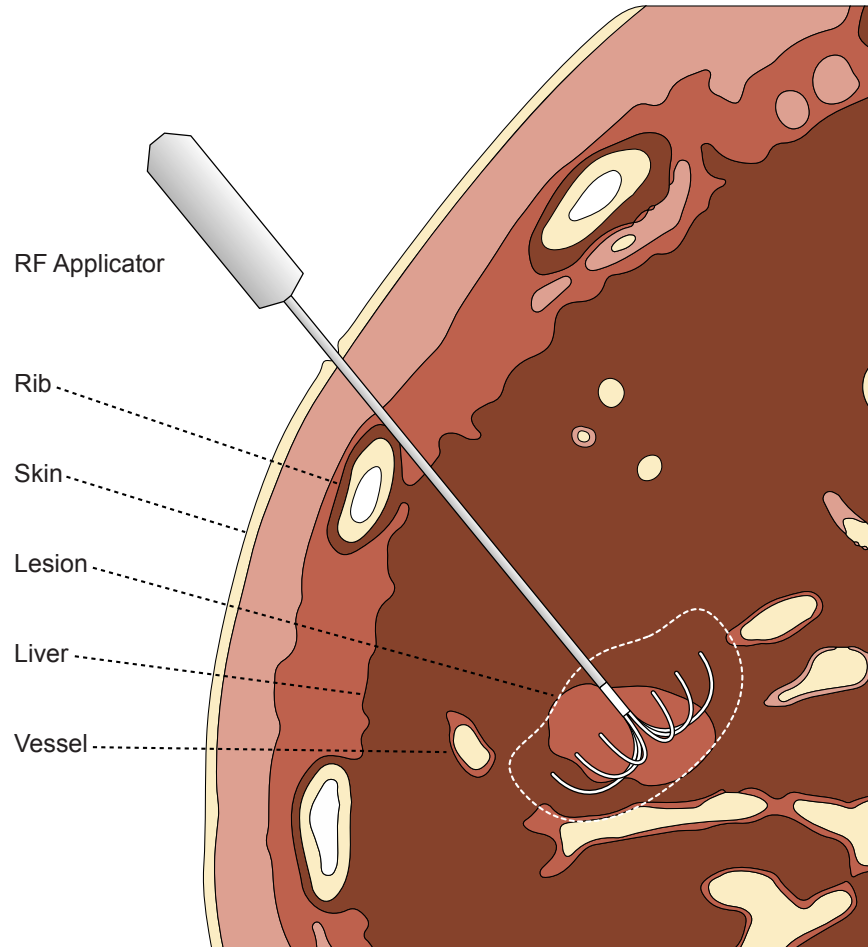


Figure 1.1: An umbrella-shaped monopolar applicator is percutaneously placed in the liver. The electrode is positioned in the tumor and the prongs are spread for ablation. The dotted line around the electrode prongs illustrates the expected ablation zone.

heat-sink effects. This method is prone to human error, which could lead to incomplete tumor ablation and resulting residual tumor growth. In this PhD thesis, two approaches to rapidly approximate the ablation zone in an interactive way are presented. The first method is based on a geometric **reconstruction of pre-computed numerical simulations**, which are stored in a **lookup table**. The second approach is an advancement that utilizes **weighted distance fields to approximate the ablation zone on the GPU**, accelerating the calculation to reach real-time frame rates. Performance and accuracy of both methods are higher than related approaches and allow the physician to interactively explore optimal probe positions taking the heat-sink effects into account. In contrast to related systems, the GPU-based approximation method is part of 2D as well as 3D volume renderings that visually emphasize the shape of the ablation zone.

To verify the treatment success of the RFA therapy, reliable post-interventional assessment of the ablation zone is required. Typically, pre- and post-interventional CT images have to be aligned to compare shape, size, and position of tumor and coagulation zone. Due to the different acquisition times and accordingly different coordinate systems of the pre- and post-interventional images, a registration is required to allow a fused visualization and a quantification of possible residual areas. In this work, a **workflow for automatic alignment of interventional CT images** is presented. Based on segmentation masks of tumor and coagulation, it is demonstrated that the workflow enables an automatic rigid registration algorithm to perform at least as accurately as experienced medical experts, but with significantly less time.

In clinical practice, both images are compared in a slice-by-slice manner in order to compare the geometrical properties of tumor and coagulation. The major challenge using this method is to correlate any spatial position in both images over all slices, which is in particular difficult if the soft-tissue is deformed or the shapes of tumor and coagulation significantly differ. A further challenge is the difficulty to evaluate the size of the ablative margin in the three-dimensional space as well as to quantify the ablation volume to prevent liver failure when planning RF ablation in patients with limited liver reserve [121]. In this PhD thesis, a novel **visualization as well as a navigation tool**, the so-called **tumor map**, is presented to ease the comparison. It is used for a combined visualization of the tumor and its surface distance to the coagulation necrosis in order to support physician in reliable therapy assessment. The proposed registration and visualization methods are integrated in a clinical software assistant. Using the software assistant, it is shown that interventional physicians are more sensitive in finding local tumor recurrences after RF ablation than using the conventional comparison method.

The creation of meaningful visualizations for medical diagnosis is challenging, due to the particular needs of the medical users. In the literature, effective visualization algorithms have been proposed, which often focus on specific scanning strategies or medical questions. A key problem within common direct volume rendering (DVR) frameworks is the high amount of effort required to develop appropriate visualizations and to customize the algorithms rapidly. In this PhD thesis, a novel **shader framework for rapid prototyping of DVR** is presented, which is integrated in the MeVisLab development environment. The key idea is a dynamic shader pipeline based on the *SuperShader* concept, which facilitates substituting pipeline steps during run-time while ensuring a valid final shader. Related systems do not allow for customization of shader code during run-time without the need to adjust the remaining shader or recompile the C++ source code.

1.3 Structure of this Thesis

After a report of the medical background and fundamentals (**Chapter 2**), novel techniques in the fields of pre-interventional planning, post-interventional assessment

and rapid prototyping of DVR are presented in the following chapters:

- **Chapter 3** presents a workflow allowing for interactive planning of RFA. In order to support the physician with spatial information of pathological structures as well as the finding of trajectories without harming vitally important tissue, 2D slice and volume visualization techniques are proposed.
- **Chapter 4** describes two novel approaches to interactively calculate the ablation zone considering the cooling blood flow. The first method is based on a geometric reconstruction of pre-computed numerical simulations, which are stored in a lookup table. The second approach utilizes weighted distance fields to approximate the ablation zone on the GPU in real-time.
- **Chapter 5** presents a workflow for automatic alignment of interventional CT images. Based on segmentation masks of tumor and coagulation, the workflow enables an automatic rigid registration algorithm to perform on average as accurately as four experienced medical experts, but with significantly less time.
- **Chapter 6** proposes a novel visualization as well as navigation tool, the so-called *tumor map*. It is used for a combined visualization of the tumor and its surface distance to the coagulation necrosis in order to support reliable therapy assessment.
- **Chapter 7** introduces a shader framework for rapid prototyping of DVR, which was integrated in the MeVisLab development environment. The key idea is a dynamic shader pipeline based on the *SuperShader* concept, which facilitates substituting pipeline steps during run-time while ensuring a valid final shader.
- **Chapter 8** provides the conclusion of this PhD thesis with respect to the above mentioned challenges. Finally, future research directions and further suggestions are outlined.

*Everybody talks about the weather, but
nobody does anything about it.*

(Mark Twain)

2

Fundamentals

THIS PhD thesis focuses on the software assistance of RFA of hepatic lesions, due to the abundance of publications, clinical studies, and hospitals supporting RFA in the liver. In this chapter the principles of image-guided interventions, in particular the RFA including the biophysical effects, are explained. Subsequently, common RF systems and applicator types used in clinical practice are presented. Because important contributions of this work are based on interactive visualization techniques, fundamentals of the graphics processing unit (GPU) and direct volume rendering (DVR) are also discussed.

2.1 Image-guided Intervention

Every image-guided intervention starts with visualizing the target lesion by means of imaging devices. The goal is to emphasize the target lesion as well as the surrounding anatomy such as potential risk structures. Various imaging modalities are available for image-guidance of needle-based interventions. In particular computed tomography (CT) and magnetic resonance imaging (MRI) are utilized to acquire anatomical data sets of the patient. CT is widely available at clinical sites and provides a good anatomical overview. Additionally, vascular structures may be enhanced by contrast agent. MRI provides similar imaging capabilities with better soft-tissue contrast. However, MR-guided interventions are only available in few specialized hospitals.

Based on the acquired anatomical images, lesion extents may be determined and an appropriate therapy determined by the physician [58]. Generally, image-guided interventions can be divided into three major steps [67]:

- Planning
- Intervention
- Assessment

which are discussed in the following sections (see Figure 2.1 (d)).

2.1.1 Planning

The success of an image-guided intervention depends on a well planned treatment strategy. To facilitate a sufficiently large ablation zone, which has to completely enclose the tumor, the expected ablation zone has to be estimated by the physician [142]. For that, appropriate ablation devices have to be determined and optimal positions considering the target region chosen [44]. To prevent incomplete destruction of the lesion, the patient individual anatomy has also to be taken into account. Effects which may limit the treatment of the tumor such as material properties of the target organ or neighboring blood vessels have to be considered [98]. Also, potential damage of important risk structures such as large vessels, ribs, and lungs, has to be minimized by choosing a safe needle path and placement of the applicator's active zone [184, 61].

In clinical practice, planning is typically performed on 2D slice images acquired from CT or MRI before the intervention [138] (see Figure 2.1 (a)). The pre-interventional images are used to plan the optimal trajectory to the target lesion and the optimal position of the applicator's active zone [19] (e.g., RF electrode, MW antenna). Particularly for difficult cases, the determination of an optimal trajectory under consideration of the above mentioned aspects may be demanding if only anatomical images are displayed. Another issue is the planning time available in the clinical routine. Typically, the planning has to be performed within few minutes.

Due to possible repositioning of the patient and resulting anatomical deformations, the planning may be performed immediately before the intervention in the operating room. Also, the anatomical situation changes due to the soft-tissue deformation caused by breathing motion. Thus, the actual path may differ from the prior planned optimal trajectory and the needle may be deformed during intervention. The physician has to cope with this uncertainty. As a consequence, the target volume includes a safety margin of approximately 10 mm around the tumor to handle those uncertainties and microscopic clusters of cancer cells around the visible tumor tissue [19].

The benefit of computer assistance for planning is the access path determination under consideration of important risk structures and the estimation of the expected ablation zone taking the patient individual anatomy into account. Due to the short planning time in clinical practice, a software assistant has to allow fast planning. Integrated image processing and visualization methods have to be embedded in an interactive workflow.

2.1.2 Intervention

During the intervention, the planned therapy strategy is applied in the operating room. The goal is to achieve complete destruction of all tumor cells without harming vitally important tissue. The intervention can be divided into three clinical workflow steps [67]:

- Targeting
- Monitoring
- Controlling

During targeting the needle is freehandedly introduced under image guidance in the patient to place it into the planned target region [130]. In the monitoring stage, the therapy process is monitored and the therapy parameters adjusted in order to obtain the intended coagulation necrosis. Finally, in the controlling step, the achieved coagulation necrosis is compared with the intended coagulation and a further ablation procedure performed if needed. Figure 2.1 (b) shows a peri-interventional control CT scan with two visible needles in the target region.

Due to a highly deformable organ situation such as the liver, the applicator is freehandedly placed by the physician under real-time image guidance. Typical imaging devices include CT fluoroscopy, X-Ray, Ultrasound and MRI [133]. However, MRI is less commonly used because of availability and cost. To give more control over the organ deformations during positioning of the applicator, breathing control is commonly used. For a procedure under local anesthesia, the patient has to perform breathing as commanded by the physician, i.e. hold breathing during targeting. Under general anesthesia, respiratory arrest may be performed by the anesthesiologist [107]. At the same time, the imaging device is enabled to track the insertion of the probe. Imaging and other monitoring devices, such as temperature

and impedance sensors, are used to control the therapy parameters in order to ensure optimal treatment. For instance induced energy or therapy duration may be adapted during monitoring [59]. MR thermometry is sometimes used to monitor the resulting heat distribution [45].

Computer assistance during the intervention may support the physician in the transfer of the planning data into the operation room. Registration methods allow to align the pre-interventional planning data with the peri-interventional data set of the patient's current anatomy. To reduce the radiation dose of CT imaging, optical infrared or electro magnetic tracking devices may allow for tracking of the probe position in relation to the pre-interventional planing data [123, 186].

2.1.3 Assessment

The goal of the assessment step is to verify the treatment success [67]. Typically, the spatial relations around the target volume are examined (see Figure 2.1 (c)). A successful therapy is assumed if the tumor is completely enclosed by the coagulation necrosis, which is identified by a lack of contrast enhancement. The therapy failed if residual tumor tissue is detected outside the coagulation necrosis [133]. Due to the above mentioned uncertainties, a safety margin has also to be considered [90].

In clinical practice, immediately after the intervention as well as 24 hours later, post-interventional data sets are acquired with CT or MRI to assess the therapy [68]. The pre- and post-interventional images are examined to evaluate the treatment success. Typically, shape, size, and position of pre-interventional lesion and post-interventional coagulation are visually compared [131] in parallel on two monitors. The major difficulty is the organ deformation due to the patient's movement and the different image acquisition times [89]. Thus, the physician has to mentally compensate the misalignment. Also, the volumetric image data sets are compared in a slice-by-slice manner. This manual procedure is time consuming and error-prone. Furthermore, to correlate the slices and to mentally fuse the three-dimensional shape of the lesions, considerable user experience is necessary.

The major benefit in computer assistance is related to image processing and visualization methods. Segmentation methods will ease the quantitative comparison of the lesions. For instance, volumetry and maximal diameters may be compared. Furthermore, image registration methods will support the physician in matching different time points and allow for compensation of organ deformations. Visualization methods may support the visual inspection of the lesions and emphasize the changes of their shapes.

2.2 Radiofrequency Ablation

As part of interventional oncology, thermal ablation therapy represents a local tumor treatment, where the tissue is coagulated by means of thermal energy. Applications of thermal tumor treatment include radiofrequency (RF) ablation, laser-induced

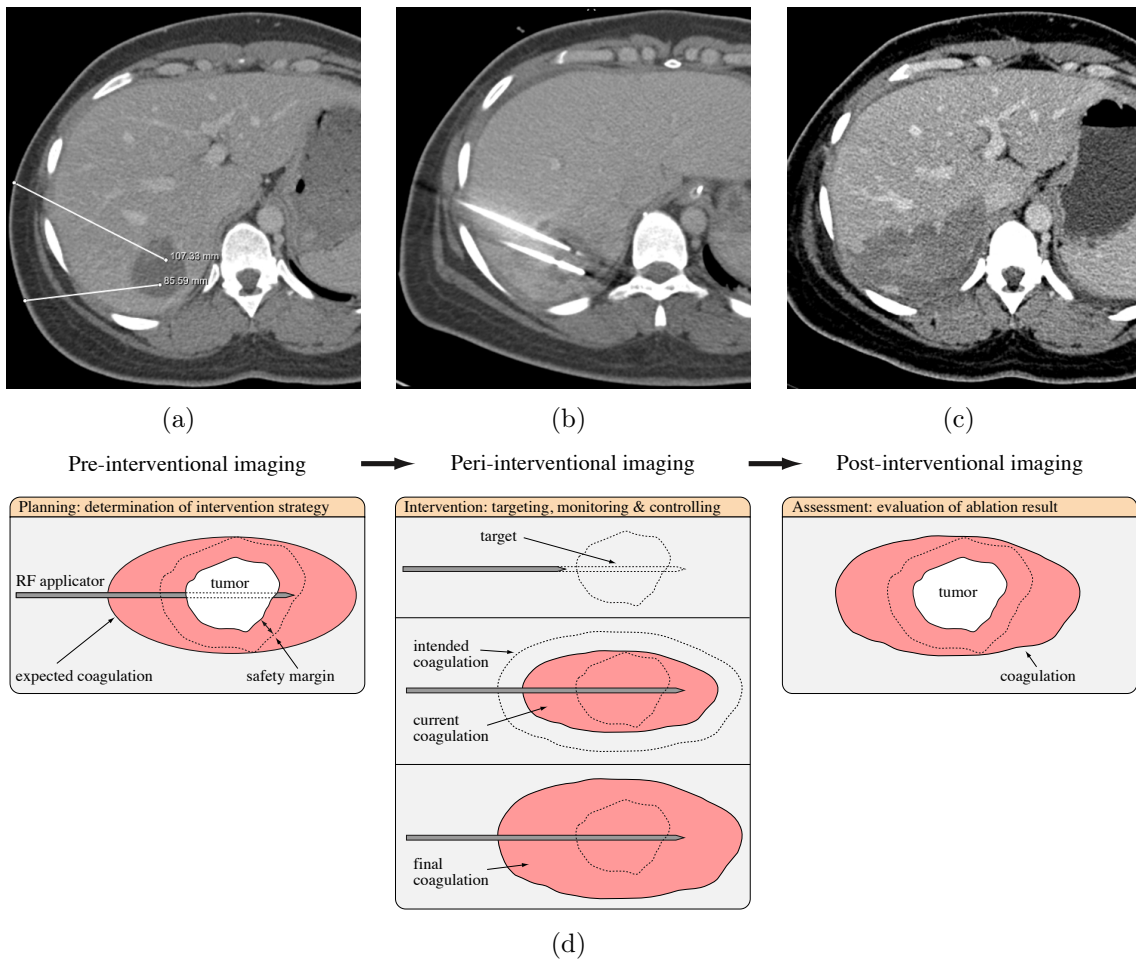


Figure 2.1: Image guidance for thermal ablations consists of pre-interventional (a), peri-interventional (b) and post-interventional (c) imaging (Images are courtesy of the Department of Diagnostic Radiology at RWTH Aachen University). (d) Illustration of the image guidance: In the planning stage, the intervention strategy is determined based on pre-interventional imaging (a). During the intervention, peri-interventional image data (b) is utilized for applicator placement. Subsequently, the current coagulation state can be monitored and ablation parameters can be controlled to obtain the intended coagulation. In the assessment stage, the ablation result can be evaluated based on post-interventional imaging (c).

thermotherapy (LITT), microwave (MW) ablation, cryoablation and high-intensity focused ultrasound (HIFU) ablation. Particularly percutaneous RF ablation is nowadays a widespread ablation therapy in the clinical field, due to its common technical procedure, low complication rate, and low cost.

2.2.1 Introduction

Image guided RF ablation is predominantly supported by interventional radiologists for primary and metastatic liver tumors [163]. This is related to the fact that the liver is, second only to lymph nodes, the most common site for metastatic disease irrespective of primary hepatic tumors [133]. The treatment of bone tumors such as osteoid steoma is also an established application [145]. Primary and secondary pulmonary malignancies are potentially an indication for RFA in the lungs [51], as well as renal cell carcinoma in the kidney [63].

2.2.2 Principles

The principle of the RFA therapy is to insert RF applicators into the target organ, percutaneously through the skin or during open surgery, and place the applicator's active zone in the lesion. The goal is to destroy all cancer cells of the target lesion by inducing thermal injury. The transformation of electrostatic energy to thermal energy leads to thermal necrosis of the tissue. For that, an alternating electric current, that oscillates in the high-frequency (HF) range (200 - 1.200 kHz), is induced into the tissue via the active zone [142]. The tissue ions become agitated following the direction changes of the oscillating HF current. As a consequence, the ion agitation causes resistive heat in the tissue. The focus of heat is the tissue surrounding the active zone of the applicator. Local resistive heating of the tissue to cytotoxic temperatures (50°- 100°C) in the entire target volume results in coagulation necrosis due to irreversible protein denaturation of the destroyed cells.

2.2.3 Biophysical Effects

2.2.3.1 Cell Function

The thermal effect mainly depends on the tissue temperature and the heating duration. Cell homeostasis¹ can be already observed at a slightly higher body temperature of 40°C. A cell temperature of 42-54° results in a higher susceptibility to vital damage. If the cells are heated with more than 45°C for several hours, irreversible cell damage is caused [142]. Higher temperatures of 50-55°C reduce the necessary heating duration to 4-6 minutes. Immediate thermal damage of the cells can be observed in the range of 60-100°C. Histopathologically, temperatures in this range lead to coagulation necrosis due to irreversible protein denaturation, damage to cytosolic and mitochondrial enzymes, and the destruction of important protein structures of

¹Tendency of cell to maintain a constancy of environment consistent with vitality and well being.

the DNA [68]. Figure 2.2 shows a specimen of pig liver ablated ex-vivo without perfusion. Temperatures higher than 100-110°C cause vaporization and carbonization of the tissue. Carbonization of the liver is clearly visible around the applicator's active zone (dark tissue) in Figure 2.3. As a consequence, the tissue impedance is increased which reduces the amount of inducible energy. Optimal temperatures for RFA are of 60-100°C for several minutes within the entire target volume.

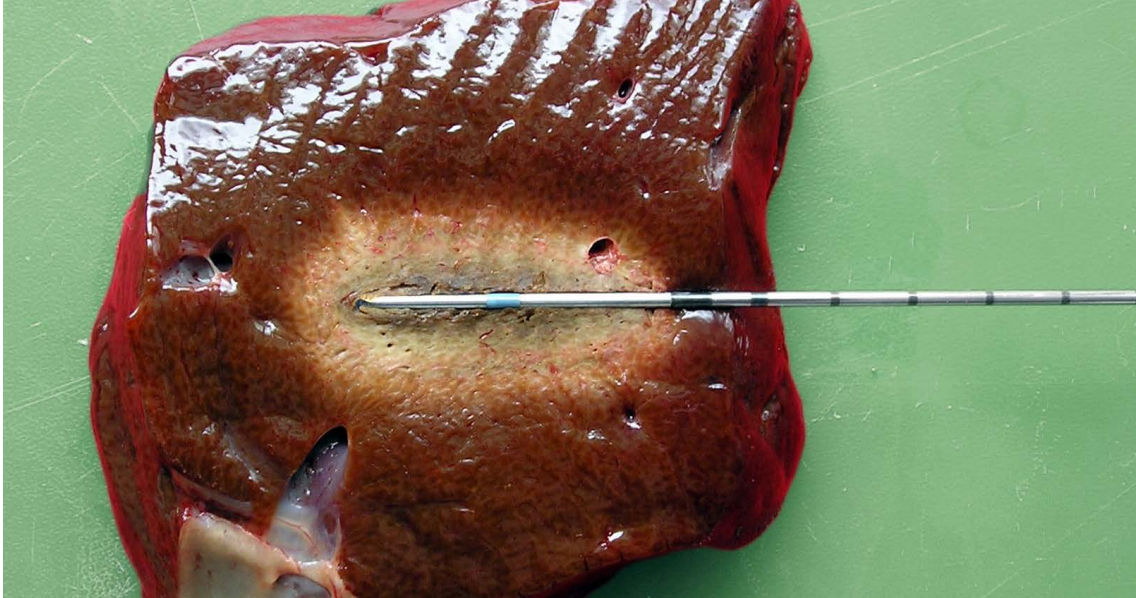


Figure 2.2: Gross specimen of a pig liver after ex-vivo ablation without perfusion. The central zone of high temperatures (greater than 60°C) is created immediately around the applicator's active zone (electrode), and it is surrounded by more peripheral zones of partially vital damage (45°-55°C). Image courtesy of Celon AG, Berlin.

2.2.3.2 Tissue Characteristics

The physical tissue characteristics of the lesion and the surrounding anatomy also have an influence of the effectiveness of the RF ablation therapy. The thermal and electrical conductivity of the tissue influences the electric current and the distribution of heat, respectively. On the one hand, an increased thermal conductivity of the tissue results in a faster diffusion of the heat, and thus, the energy may be increased to achieve larger ablation zones. On the other hand, low thermal conductivity increases the heating in the vicinity of the applicator's active zone [106], particularly if the tumor is surrounded by cirrhotic liver or fat. Also, the electrical conductivity of lesion and background tissue influences the electrical field around the active zone.

2.2.3.3 Blood Flow

In a living organism, the convection by means of blood flow leads to heat removal. The vascularization of tumor and background tissue determines the amount of inducible heat energy. Macroscopic vessels, larger than 1 mm in diameter, lead to the so-called *heat-sink* effect [67]. The heat-sink effect may alternate the shape of the ablation zone in direction of large vessels. Thus, vessels in the vicinity of the target region increase the probability of incomplete tumor ablation due to possible vital tumor cells adjacent to vessels (see Figure 2.3). In addition to the macroscopic vessels, increased microperfusion of the capillary vasculature decreases the size of the ablation zone and increases the duration necessary to achieve thermal ablation [105].

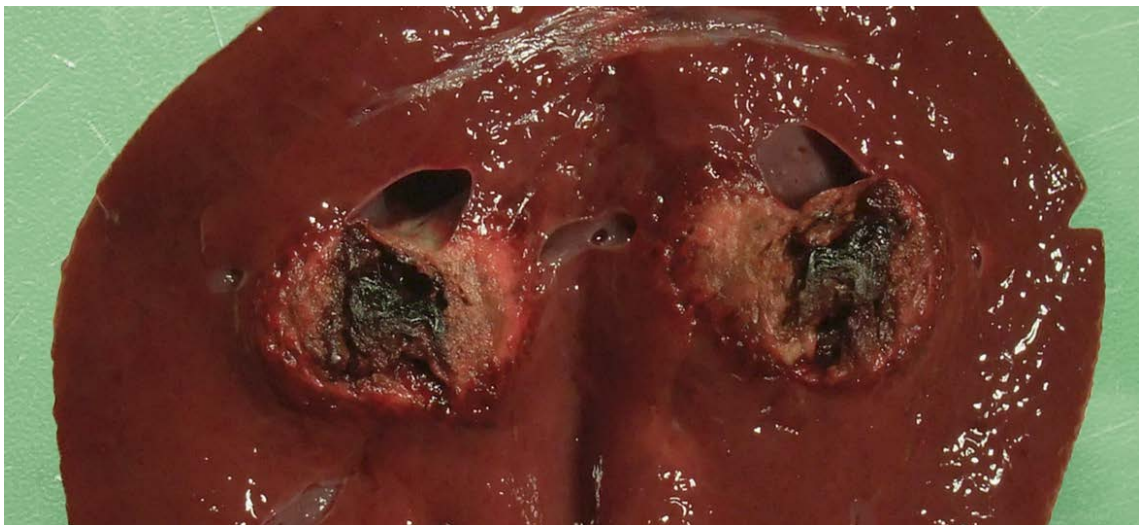


Figure 2.3: Gross specimen of a resected bovine liver after in-vivo ablation. The applicator's active zone is located in the vicinity of a large vessel (\varnothing 5 mm) which causes incomplete coagulation. Image courtesy of Kai Lehmann, Charité University Hospital, Berlin.

2.2.4 RF Systems and Electrodes

Typical RF applicators are needle-shaped and have radii of 0.9 - 1.0 mm and overall lengths between 100 - 250 mm, depending on the type and manufacturer. Commercial systems encompass monopolar and bipolar applicators, different electrode shapes (see Figure 2.6), and are available from 375 - 480 kHz [134].

2.2.4.1 Monopolar RFA

The principle of monopolar RFA is to create a closed-loop circuit consisting of the RF applicator's monopolar electrode, a large dispersive electrode (ground pad) placed on the body, and the patient. The monopolar electrode and the ground pad

are connected via cables to the generator. The RF generator creates the electric current and allows to control the energy deposition by measuring the impedance and temperature at the applicator's active zone. Finally, the alternating electric field is induced through the electrodes, whereby the patient acts as a resistor.

2.2.4.2 Multitined Expandable Electrodes

Multitined expandable electrodes can be found at monopolar RF applicators. It consists of an array of thin electrodes (prongs), which can be expanded from the larger needle cannula. During placement of the electrode, the prongs are folded inside the applicator. Once the electrode is in position, the array is spread to the array shape, and radiofrequency ablation may begin. Typically, after a first ablation cycle, the prongs are folded up, the electrode is pulled back (10-15 mm), and the prongs are expanded for further ablation. Two configurations of the array can be found on commercial systems: the umbrella- and Christmas tree-shaped prongs. Figure 2.4 illustrates an umbrella-shaped monopolar RF applicator.

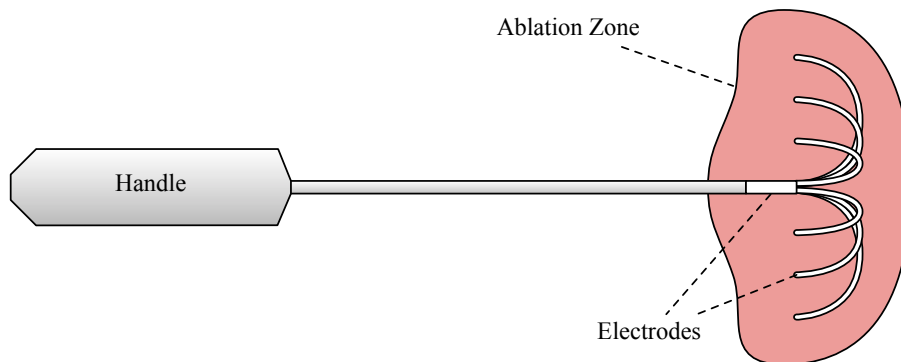


Figure 2.4: Illustration of a monopolar RF applicator with a deployed array of umbrella-shaped electrode prongs and typical ablation zone.

2.2.4.3 Internally Cooled Electrodes

An additional technique to increase the generator output, and thus the size of the ablation zone, is to internally cool the electrodes. Direct heating around the electrode is reduced to prevent the tissue from overheating and charring, which leads to an interruption of the RF circuit. Hence, vaporization and carbonization is prevented.

2.2.4.4 Perfusion Electrodes

The idea of perfusion electrodes is to continuously infuse the tissue with fluid in order to reduce the tissue resistance. Hypertonic saline is used to increase the electrical conductivity and consequently increase the amount of induced energy. The drawback of this method is the potentially unpredictable distribution of fluid

in tissue. Because the direction of infusion can not be regulated, irregularly shaped ablation zones can be observed [134].

2.2.4.5 Multiprobe Arrays

Another technique to increase the ablations zone is the combination of multiple monopolar RF applicators. Due to multiple electrodes, the heat is less dissipated [75]. The energy may be induced into the electrodes in parallel to facilitate an additive heat diffusion [69], or the generator may automatic switch the electrodes based on impedance spikes [99].

2.2.4.6 Bipolar and Multipolar RFA

In contrast to the monopolar applicator, the bipolar applicator consists of two electrodes, separated by an isolator (see Figure 2.5). Because the electric energy is supplied between those two electrodes exclusively, the tissue is heated around both electrodes. Thus, no large dispersive electrode is required for a closed circuit. To increase the ablation zone, up to three bipolar applicators can be placed close to each other and simultaneously connected to a single generator [59]. In such a multipolar setting, the electrical field is induced in a round-robin fashion between all possible combinations, resulting in an extended ablation zone.

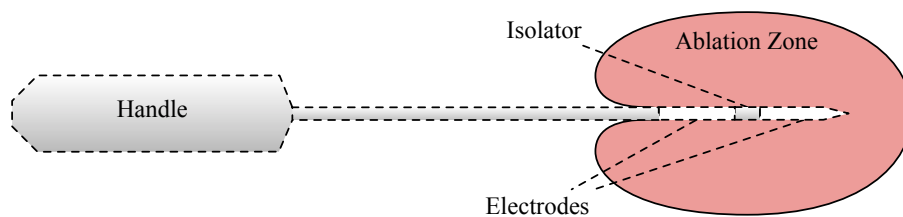


Figure 2.5: Illustration of a bipolar RF applicator with corresponding ablation zone. The two electrodes are separated by an isolator. The applicator shaft is internally cooled resulting in the typical shape of the ablation zone in the direction of the handle.

2.2.5 RFA of Liver Tumors

The human liver is the largest blood filtering organ. Due to the transport of cancer cells in the bloodstream, particularly the liver is frequently affected by metastasis of different tumor entities. RFA of liver tumors is clinically indicated if the tumor is of less than 30 mm in diameter, multiple lesions (1-3 nodules) are scattered in the liver, or a surgical resection is technically or medically contraindicated (10 – 25% of the patients) [133], e.g., due to the general constitution of the patient [122].

However, application of percutaneous thermal therapies are limited by the quality of imaging guidance and, in some cases, by anatomical risk structures as well



Figure 2.6: Photograph of three RF applicators. From left to right: bipolar probe (Pro-Surge[®], Celon AG), Christmas tree shaped probe (StarBurst[®], AngioDynamics), and umbrella shaped probe (LeVein[®], BostonScientific).

as difficult access pathways [19]. The success of the therapy strongly depends on the accurate placement of the RF applicators in order to destroy the complete lesion. Typically, the target volume includes a safety margin of approximately 10 mm around the tumor to handle uncertainties and microscopic clusters of cancer cells around the visible tumor tissue. The local recurrence rates after RFA for tumors with an intentional margin of 0 mm and 10 mm are 14.5% and 6.5%, respectively [121]. Thus, for larger tumors (larger than 30 mm in diameter), a single ablation may not be sufficient to entirely encompass the target volume [19]. In these cases, multiple overlapping ablations (sequential ablation) or simultaneous use of multiple applicators (multipolar ablation) may be required to successfully treat the entire tumor and the surrounding safety margin.

Besides the choice of applicator type, the induced energy and the ablation duration affect the size of the resulting coagulation. Additionally, cooling blood vessels in the vicinity of the RF applicator can lead to the *heat-sink effect*, which locally decreases the size of the coagulation necrosis. A recent study [22] reports that the initial treatment of secondary liver tumors larger than 25 mm has shown a high local recurrence rate because of inaccurately placed applicators or the inability to produce a predictable, large coagulation volume. Although complete destruction of all cancer cells is of primary importance, sparing of healthy liver tissue is also required. Compared with the conventional surgical resection, the advantage of ablation therapies is to destroy only a minimal amount of healthy liver tissue. Also, risk structures such as ribs, vessels or neighboring organs have to be considered for determination of an appropriate applicator trajectory.

2.3 The Graphics Processing Unit

The graphics processing unit (GPU) is a specialized processor for hardware-accelerated 3D graphics. GPUs are highly optimized data-parallel streaming processors which are part of almost every personal computer (PC). GPUs are also used in embedded systems, mobile phones, and game consoles. In contrast to the general-purpose central processing unit (CPU), the GPU is very efficient at manipulation computer graphics. More precisely, their highly parallel structure makes it particularly effective for algorithms, whereas processing of large data blocks is done in parallel.

2.3.1 The Graphics Pipeline

The GPU hardware is designed to accelerate the generation of raster images from a virtual scene description which is represented as polygonal meshes. This process is called *rendering*. All GPUs implement the rendering of polygons as a pipeline consisting of fixed pipeline steps. The input of the rendering pipeline is an ordered stream of vertices. The rendering pipeline converts the vertices of the virtual scene into a raster image consisting of pixels. Figure 2.7 illustrates the rendering pipeline which can be grouped into three basic stages:

Vertex Processing. In the *vertex program* pipeline step, linear transformations of the incoming vertices such as rotation, transformation and scaling are computed in 3D space. Also, the vertices are transformed from model coordinates into screen space (via world and camera space). The processing is done per vertex and independent of the relation to geometric primitives. In the *primitive assembly* step, the vertices are joined into geometric primitives such as points, lines, and triangles. In the last step of the vertex processing stage, primitives which are located outside of the visible volume are removed (*Culling*) and primitives which intersect with the volume borders are subdivided (*Clipping*). Also, x and y coordinates of the vertices are mapped to screen space (*Viewport Mapping*). Finally, the processed primitives are handled over to the fragment processor.

Fragment Processing. The *rasterization* step decomposes each incoming primitive into a set of fragments, depending on the overlap of the underlying screen space pixel. Thus, every fragment corresponds to a single pixel. Vertex attributes such as position, color and texture coordinates are *interpolated* into barycentric coordinates with perspective correction. The *fragment program* computes per fragment the final color from interpolated vertex attributes and texture coordinates.

Compositing. The compositing is the final step of the rendering pipeline. The *frame buffer operations* decide whether the incoming fragment must be displayed on screen or discarded. For instance, the *depth test* operation determines if the current fragment is occluded by a previous fragment at the corresponding raster position using the depth buffer. The *alpha blending* operation decides how the color of the incoming fragment is combined with the stored color from the color buffer. Further operation are the *alpha test* and the *stencil test* in order to discard fragments.

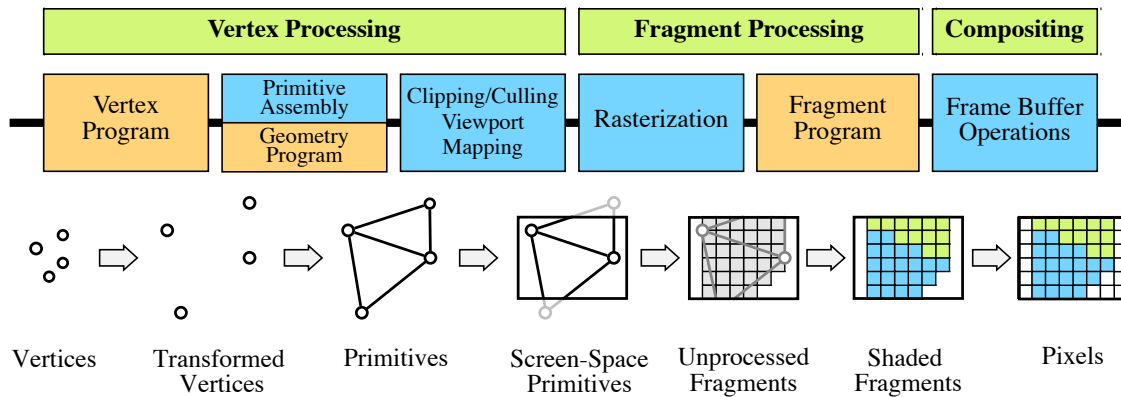


Figure 2.7: Overview of the programmable rendering pipeline. Illustration adapted from [72].

2.3.2 GPU Programming

All stages of the rendering pipeline can be controlled by several parameters. In order to substitute processing parts of the fixed-function pipeline, so called *shader programs*, user written micrograms, can be customized. The following steps can be substituted:

Vertex program. A vertex shader is a main function which is called for each incoming vertex. Only vertex attributes such as position, color, texture coordinate can be alternated. The vertices computed by vertex shaders are typically passed to the primitive assembly step or geometry program.

Geometry program. A geometry shader is a main function which takes a set of vertices as input from the vertex shader's output, then generates geometric primitives such as triangles, lines, or points. Geometry shaders can add and remove vertices in order to procedurally generate geometry.

Fragment program. A fragment shader is a main function which is called for each incoming fragment. Fragment shaders calculate the color and alpha value of

individual pixels after rasterization of the primitives. They are typically used for shading and related effects.

At the beginning of the pipeline, attributes can be attached to every vertex and are copied to input registers. During execution of the shader, the attributes are read from the input registers. Constant parameters in a shader program are typically declared as *uniform variables*. Those parameters are primarily used to adjust the shader program from outside without the need to re-compile the shader code. *Varying variables* are output parameters of the vertex program which are interpolated for every fragment by the rasterization step and subsequently forwarded to the fragment processor. They represent parameters which vary over the primitive. In contrast, *uniform variables* are constant for a primitive and can be read in all programs. Furthermore, all programs can read parameters of the OpenGL state such as light source or material parameters. Figure 2.8 illustrates the input and output parameters of the programmable vertex, geometry and fragment processor.

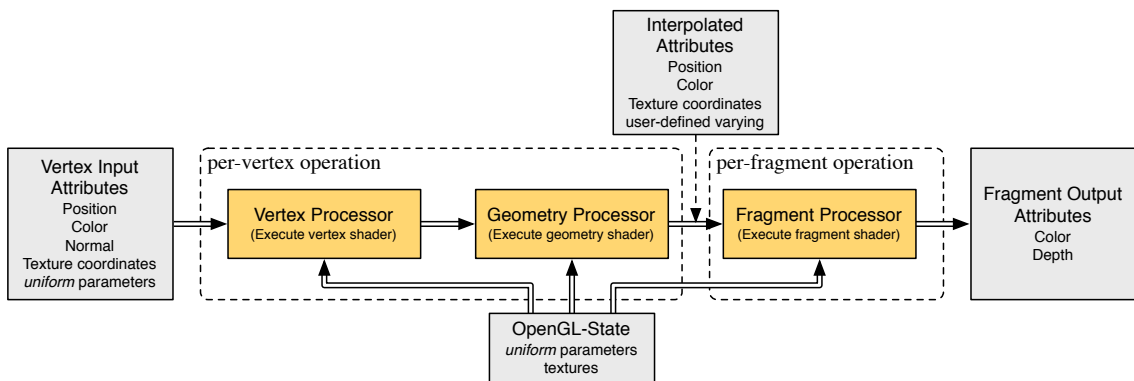


Figure 2.8: Overview of input and output parameters of vertex, geometry and fragment processor.

Typically, shader programs are implemented in specialized high-level programming languages. Various high-level programming languages are associated with different graphics APIs (application programming interfaces), which provide several libraries of data types and operations. Common used languages are the *OpenGL shading language* (GLSL) [148], which is the high level shading language for OpenGL [124], the *High Level Shading Language* (HLSL) for DirectX [30], and *C For Graphics* (Cg [110], runs on NVidia hardware only) for both, OpenGL and DirectX. Since the DirectX is a proprietary API for Microsoft platforms, GLSL is the only operating system and graphics board independent shading language.

2.4 Direct Volume Rendering

Direct volume rendering (DVR) was introduced by Drebin et al. [50] and, in addition to traditional 2D slicing, is now available in almost every medical workstation. It calculates how emitted light is absorbed and scattered along the transport through the volume to the observer. Particularly, GPU-based approaches allow for interactive rendering on consumer graphics hardware [71]. A comprehensive overview including theoretic details on volume rendering can be found in [72].

2.4.1 The Volume-Rendering Pipeline

The calculation of the light transport through the volume can be separated into several steps of a pipeline – the *volume-rendering pipeline* (see Figure 2.9). The following pipeline steps are typically present in common volume-rendering methods:

Sampling. In the first step, sampling positions are chosen along the ray through the volume. For every sample position the corresponding value of the volume is fetched. The samples serve as the basis for the discretization of the continuous light transport through the volume into ray segments.

Interpolation. Since the sampling positions usually differ from the grid points, a continuous 3D field has to be reconstructed in order to obtain the data values for the sample positions. In case of volume rendering, trilinear interpolation is commonly used for fast reconstruction of the uniform grid.

Classification. Scalar volume data represent a volume by density or other attributes at the sample position. Optical properties are commonly not given. Classification maps the values of the volume data to optical properties of the light transport and allows to distinguish different structures or materials in a volume. Typically, classification is based on transfer functions which assign optical properties using color C and opacity α .

Shading. Volume shading can be obtained by illumination of the volume samples from external light sources. The color values of the sample position is alternated according to the chosen illumination model. Local illumination models, such as the Phong reflection model [29], are utilized which calculate the shaded color value using the gradient of the scalar field.

Compositing. The iterative computation of the discretized viewing ray segments is called compositing. The iteration is performed along all samples of the ray through the volume, whereas the current destination color value C_{dst} is

calculated by the previous source color value C_{src} and source opacity value α_{src} . In the case of *Back-to-Front* compositing, it is calculated with:

$$C_{dst} \leftarrow (1 - \alpha_{src})C_{dst} + \alpha_{src}C_{src}. \quad (2.1)$$

In the case of *Front-to-Back* compositing, it is calculated with:

$$\begin{aligned} C_{dst} &\leftarrow C_{dst} + (1 - \alpha_{dst})\alpha_{src}C_{src}, \\ \alpha_{dst} &\leftarrow \alpha_{dst} + (1 - \alpha_{dst})\alpha_{src}. \end{aligned} \quad (2.2)$$

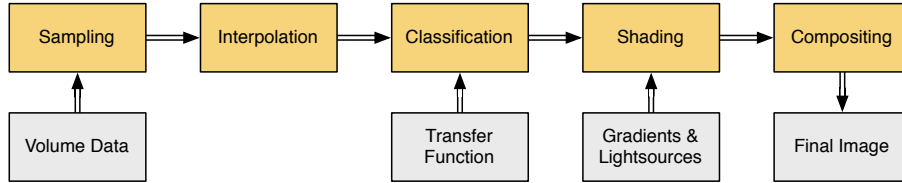


Figure 2.9: Overview of the volume-rendering pipeline.

2.4.2 GPU-Based Volume Rendering

Although modern programmable GPUs are designed to render faces and vertices, they are well-suited for real-time volume rendering. The aim of real-time volume rendering is to allow adjustment of parameters such as view point or transfer function within interactive frame rates. Particularly, two approaches are widespread for rendering of medical volume data:

- *3D texture slicing*, an object-order approach², which decomposes the object into geometric primitives. Typically, a proxy geometry of planar polygons oriented in view direction is used.
- *Ray casting*, an image-order approach³, which directly evaluates the accumulated color and opacity from the ray segments. The proxy geometry is a simple cube representing the border of the volume.

Figure 2.10 illustrates the principle of 3D texture slicing as well as ray casting. The following paragraphs outline the implementation of the above mentioned volume-rendering pipeline utilizing the GPU:

Sampling. 3D texture slicing algorithms create the sample positions by intersection of the planar polygons with the viewing rays through the volume (see Figure 2.10 (a)). The geometry is positioned according to the samples and appropriate texture coordinates are generated in order to sample the 3D texture

²Object order algorithms iterate over the elements in the scene to be rendered

³Image order algorithms iterate over the pixels in the image to be produced

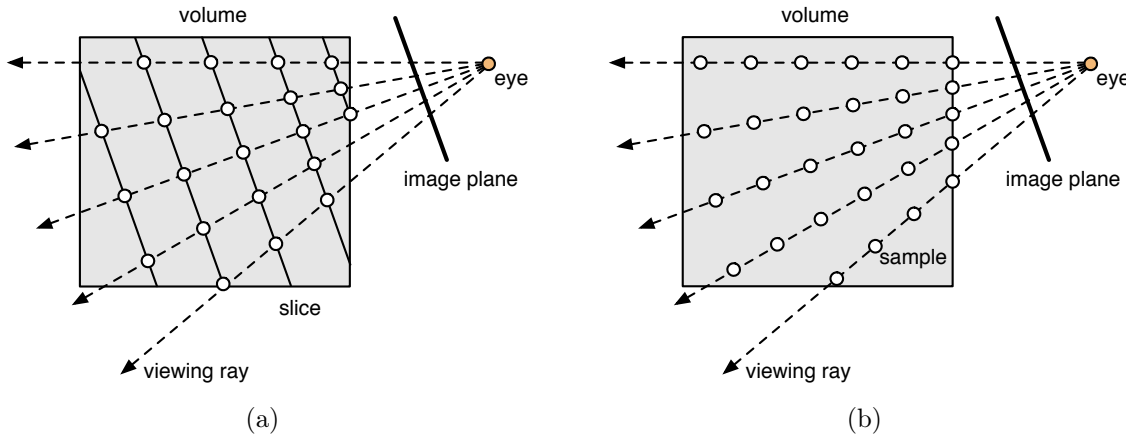


Figure 2.10: Image (a) illustrates the principle of 3D texture slicing. The samples are positioned at the intersections of planar polygons with the viewing rays. Image (b) illustrates the principle of ray casting whereas the samples are positioned along the viewing rays.

in the vertex shader. After rasterization, the interpolated texture coordinates in the fragment shader correspond with the sample positions in the 3D volume. In contrast, ray-casting algorithms set up the viewing rays by generation of entry and exit points using the cube proxy geometry. In the ray-casting loop of the fragment shader, the view rays are traced through the volume and the volume data is resampled to discrete positions along the rays (see Figure 2.10 (b)).

Interpolation. In both methods, the volume data is usually reconstructed with the trilinear interpolation of 3D textures on the GPU. Advanced filtering methods may be implemented in the fragment shader.

Classification. The volume data is classified using transfer functions, which are represented as textures. Typically, color and opacity values are computed by sampling of transfer function textures in the fragment shader.

Shading. Illumination of the volume samples is calculated in the fragment shader by evaluation of the used local shading model. The required normals are obtained with gradients of the scalar volume, either with on-the-fly gradients calculated using central differences, or with a pre-calculated gradient texture.

Compositing. Slicing algorithms utilize the alpha blending operation of the frame buffer. Alpha blending specifies the final pixel color by combination of color and opacity value from the incoming fragment (source) with the stored fragment (destination) from the buffer. In contrast, ray casting updates the previ-

ously accumulated color and opacity values according to Front-to-Back compositing (see Equation 2.2) in the ray-casting loop.

*Very simple ideas lie within the reach
only of complex minds.*

(Remy De Gourmont)

3

Workflow for Interactive Planning of RFA

THE success of a tumor treatment depends considerably on the pre-
ventional planning of the RFA. In this chapter, a workflow allowing for
interactive visualization and image-processing, which is designed to guide
the physician in planning the intervention for clinical practice, is presented. In order to support the physician with spatial information of pathological structures as well as the finding of trajectories, 2D slice and 3D volume visualization techniques for interactive planning of RFA are proposed.

3.1 Introduction

In clinical practice, the RFA therapy is most frequently planned using 2D slices of the planning scan. Because the therapy is performed in 3D space, the identification of a therapy that considers the criteria discussed in Section 2.1.1 can be demanding using 2D slice visualizations alone [85]. Typically, a trajectory is determined using simple ruler or annotation tools, and the expected ablation zone is mentally estimated by the physician. Hence, the process of therapy planning may significantly benefit from computer assistance. Particularly, combined 2D and 3D visualizations allow for a better understanding of the individual patient anatomy. To support the physician in determination of a suitable intervention strategy, additional planning information, such as results of segmentation tasks as well as the integration of virtual applicator models, may also be considered.

Another aspect is to perform the planning within a few minutes. Planning the optimal placement of the applicator immediately before the intervention, while the patient is under anesthesia and the planning scan is acquired, results in the requirement for a fast planning workflow. Thus, a typical application of a radiological workstation with its numerous tools can not be considered due to its complex handling. In contrast, workflow-based software support may guide the physician in performing the necessary and actually required steps for planning the intervention as quickly as possible.

In this PhD thesis, interactive visualization techniques are presented to support the physician in planning of the RFA. The visualization techniques are embedded in a workflow oriented application, designed for the use in clinical practice. Furthermore, three-dimensional applicator models of different manufactures combined with corresponding ablation zones, as specified in homogenous tissue by the manufacturers, are presented to estimate the amount of cell destruction caused by ablation. In order to support the estimation of the ablation zone with respect to the heat-sink effect of the cooling blood flow, a numerical simulation of the heat distribution is also provided. Besides the 2D slice visualization, a volume rendering is integrated to support the physician with spatial information of pathological structures as well as the determination of appropriate trajectories without harming vitally important tissue. A visualization method which automatically defines a transfer function for emphasizing liver vessels without the need of a segmentation mask is integrated. Insufficient visualization results of the displayed vessels caused by low data quality can be improved using local vessel segmentation. Also, an interactive segmentation technique of liver tumors is provided to allow for the volumetric measurement and visualization of pathological tissue combined with anatomical structures.

The outline of this chapter is as follows: In Section 3.2, related work in the field of planning of radiofrequency ablation is discussed. Section 3.3 describes the proposed workflow of the planning software. In Section 3.4, the developed 2D slice visualizations are illustrated. Interactive volume visualizations are presented in Section 3.5. Results are discussed in Section 3.6, and the conclusion of the proposed

methods is provided in Section 3.7.

3.2 Related Work

Treatment planning tools for thermal ablations are an active field of research since several years. The majority of the related works focus on visualization or image processing methods. Particularly 3D surface rendering techniques have been investigated to support the physicians. Because surface reconstructions are based on the classification of object boundaries in image data, segmentation methods have been developed. Only few publications address the issue to integrate all these methods in a suitable planning application designed for clinical practice.

A software tool for preoperative simulation and planning of tumor ablation, including radiofrequency, laser and cryoablation is presented by Butz et al. [38]. In this tool, virtual ablation devices can be visualized within the 3D scene together with surface models of the tumor, main vessels, gallbladder and bones. The visualized ablation devices include a cryo-probe model with an elliptic iceball and radiofrequency clusters, consisting of three needles with a spherical ablation zone. Standard functionalities such as MPR views of 2D slices are also included.

Villard et al. [176] describe a treatment planning tool for RFA of hepatic tumors. In this planning tool, the liver, vessels, pathologies, and surrounding organs are automatically segmented [164] and visualized utilizing surface rendering. Within the 3D scene, virtual applicator models with idealized ellipsoidal regions of coagulation can be placed and manipulated interactively by the user. Nevertheless, 2D slice-based visualization techniques are not considered.

McCreedy et al. [111] present a registration, segmentation, and fusion tool for RFA treatment planning. In this software, the liver, vasculature and lesions can be semi-automatically segmented in 2D slice viewers. Those objects are visualized as surface models within a volume rendering. Also, virtual RF applicator models of various manufacturers, and the corresponding expected regions of coagulation are rendered as surface models. However, visualization of applicators and ablation zones in 2D viewers is not discussed.

Weihusen et al. [179] present a workflow-oriented software platform for image guided RFA. Using this assistant, tumor lesions can be segmented semi-automatically. Furthermore, RF applicators models are visualized in 2D and 3D viewers. The corresponding ablation zone can be numerically simulated incorporating the cooling effects of nearby vessels [96]. The resulting ablation zone is visualized in 2D viewers as an image mask and in a 3D rendering as a surface model.

Zhai et al. [187] present a preoperative surgery planning method for microwave ablation. In their work, the region of coagulation is simulated in an interactive way using GPU-accelerated visualization techniques. The coagulation is visualized together with the probe in 2D slices as image overlay and in 3D as a surface model in combination with anatomical volume rendering. However, risk structures such as hepatic vessels or lungs are not visible in the volume rendering.

Other works focus on automatic access path proposals for RFA [156, 158] and visualization of safe access paths in slice views and volume renderings [155, 87] based on geometric optimization. The *Biopsy Planner* [80] is a system for the visualization, analysis, and validation of biopsy needle pathways. The system uses a multi-level approach for identifying stable needle placements which minimize the risk of hitting blood vessels.

3.3 Workflow-Based Software Support

The basic contribution of this chapter is the identification of requirements to optimize the workflow of a RFA planning software. The following requirements are determined after discussions with medical experts:

- A multi-viewer layout is required in order to display the patient data set with different planar reformations and spatial volume rendering.
- Intuitive handling of virtual objects such as RF applicator models, annotations and measurements has to be facilitated.
- The application has to guide the user in performing the required processing steps.
- Complex and time-consuming processing tasks have to be avoided.

To match with these requirements, the graphical user interface (GUI) is subdivided into three areas, the *viewer area*, the *object navigator*, and the *workflow tab*. The *viewer area* contains four viewers, whereas the large main viewer is typically used for display of the axial slice. The three smaller viewers draw the sagittal and coronal slice and a volume rendering of the target region. The content of the viewers may be switched by drag & drop interaction, e.g. to display the volume rendering in the main view. Also, each viewer can be enlarged to fullscreen mode in order to fully exploit the screen resolution. Beside familiar annotations, a 2D slice viewer contains an additional smaller viewer in the upper left corner, the *Mini-Map*, an overview visualization which is well-known from computer games. It is enabled if the viewer displays only a subset of the current slice (i.e. the view is zoomed in) and shows the complete slice with corresponding subview. Figure 3.1 illustrates the basic concept of the software assistant's GUI.

The *object navigator* allows for intuitive handling of multiple objects such as images, RF applicators, annotations, measurements, segmentation masks, which are represented in a list and persistently stored in a data base. The objects can be selected, hidden and deleted using the navigation tool. To allow the physician a fast exploration of the available objects, the 2D viewers show the corresponding slice of the selected object and a region of interest (ROI) for a preview volume rendering is generated.

The workflow of the software assistant is represented in a vertical tab view, the so called *workflow tab*. Utilizing the tabs, the user is guided through the workflow steps of the application in a top-down manner. Every tab represents a single workflow step, i.e. tumor segmentation, probe placement, vessel segmentation, and numerical simulation. Available parameters are placed in the *parameter box* of each tab. The following sections outline the integrated workflow steps.

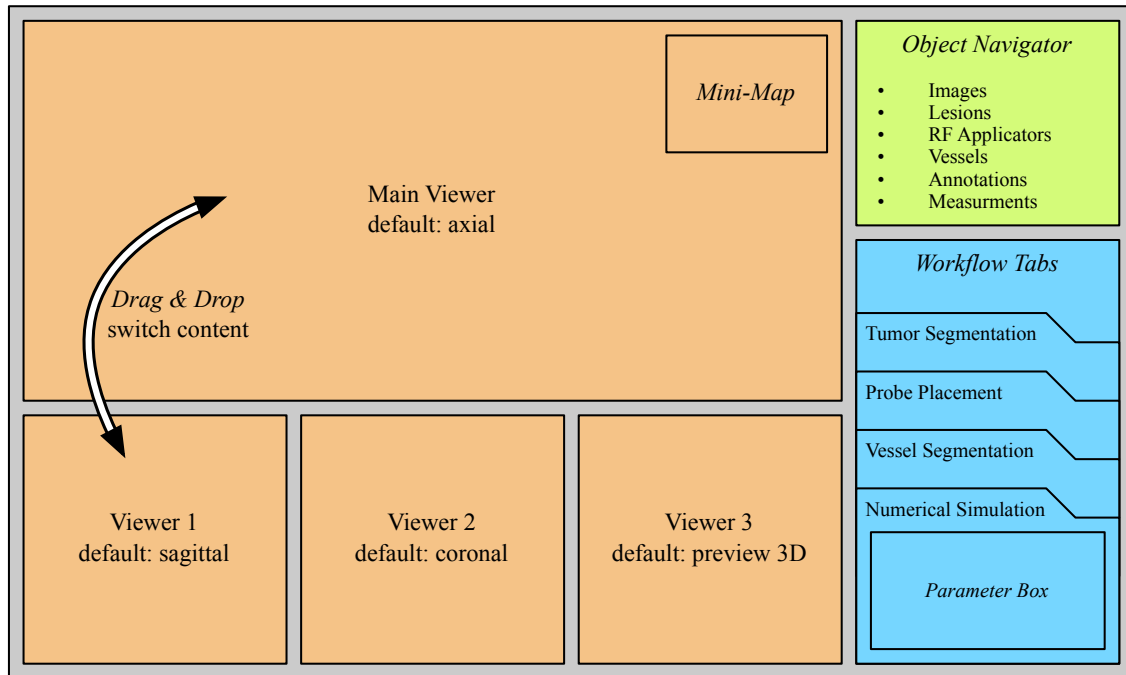


Figure 3.1: Illustrative description of the GUI and workflow concept for the planning software assistant. The GUI is divided into three areas, containing the viewers, the object navigator list view and the workflow tabs.

3.3.1 Tumor Segmentation

To support the physician with quantitative knowledge of the target region, a tumor segmentation is the first step of the planning workflow. The segmentation method employed here is a morphology-based region growing algorithm described by Moltz et al. [120]. This algorithm requires only a stroke across the lesion from the user and has proven to achieve robust segmentation results on different tumor entities and image noise levels within 1-3 seconds. To adjust the shape of the lesion, a manual correction of the segmented mask is provided. The tumor mask can be corrected in order to adjust the regularity of the shape. Also a lesion rim can be added and removed, respectively. After application of a correction, the segmentation mask is immediately updated.

If the physician is not satisfied with the automatic lesion mask, the tumor can be manually contoured in several 2D slices. Subsequently, the contours are interpolated by computing a 3D implicit function that describes a surface [78], and this surface is scanned using a recursive marching-cubes algorithm [109]. The resulting surface is rasterized to a binary image mask. Depending on the lesion's shape, an accurate mask is generated even with few contours.

Segmented lesions are maintained using the object navigator. Every lesion mask is represented as persistent lesion object in the data base. In the navigation view, all lesion objects are listed with name and voxel volume in milliliter. Lesion objects can be selected, hidden, and removed from the data base. Hiding and deleting a lesion object results in hiding and removing the corresponding lesion mask, respectively. If a lesion object is selected, the correlated lesion mask is highlighted and shown in the 2D viewer by selecting the corresponding slice of the image slice stack.

3.3.2 Probe Placement

RF applicator probes of different manufacturers are visualized by corresponding virtual surface models, which can be placed and moved within the scene in 2D as well as in 3D. The location of an applicator model is determined by a pair of spatial coordinates defining the position at the center of the applicator's electrode, and a second position at the applicator's handle. With those two coordinates, position and direction vector of the probe are defined. The coordinates can be separately or collectively positioned by the user to move the applicator within the scene. Also, the RF applicator can be intuitively moved in shaft direction to simulate needle tract ablation (i.e. pulling the electrode back during ablation) known from clinical practice.

In addition to the applicator, the corresponding ablation zone, which is centered at the applicator's electrode, is also visualized in 2D as well as in 3D. The ablation zone is represented as an ellipsoid showing the region of complete cell destruction in homogeneous tissue, which is specified by the RF applicator vendors. It allows a visual estimation whether the expected coagulation zone of the RF applicator is large enough for complete tumor ablation.

Every RF applicator with corresponding ablation zone is represented in the above mentioned object data base, whereas an ablation zone object is a child of the corresponding probe object. Furthermore, RF applicator and ablation zone objects may be hidden, removed or selected in the object navigator, whereas the current applicator type is listed. If an applicator is selected by the user in the 2D slice view, the corresponding object is also selected in the list view. By this, the physician is able to optimize the placement of multiple applicators in an intuitive manner.

3.3.3 Vessel Segmentation

The vessel segmentation is an optional step which is not required for placing or visualizing probes with corresponding ablation zones. It is mainly required for extracting vascular structures which have to be considered in the numerical simulation. The vessel segmentation is a semi-automatic algorithm, which works in a local region of interest, specified by the user by mouse-clicking into one vessel. The algorithm is based on a Bayesian vessel extraction [188] and typically runs less than two seconds to extract a vessel located in a ROI of 64^3 voxels. Segmentation parameters such as the background threshold may be manually adjusted by the physician. Complex vessel trees can be manually composed by multiple clicking into different vessel branches. Utilizing the representation of vessel objects in the object navigator, vessel segments may be hidden or deleted by the user.

3.3.4 Numerical Simulation

Due to the patients' individual anatomy, where tumors can be located in the vicinity of vessels, the cooling of the blood flow should be considered in RFA planning [121]. As a consequence, an ellipsoidal ablation zone of constant diameter can not be expected in clinical practice [108]. Because the manufacturers description of the ablation zone does not incorporate the heat-sink effects, a numerical simulation is also integrated into the workflow. The computation of the heat distribution is based on a FEM-Method [96] and incorporates the characteristics of the chosen RF applicator type as well as the neighboring vascular structures. Also, the heat distribution is handled in the object navigator data base allowing to control visibility and persistence. Thus, different electrode configurations may be simulated and compared with each other by the user.

For consideration of cooling effects, the vessel segmentation has to be performed in the previous workflow step. Due to the high effort to solve the complex mathematical equations, the calculation typically takes around 5-10 minutes on a computation domain resolution of 65^3 nodes and an ablation duration of 5-10 minutes. Only needle-shaped RF applicators are considered because the calculation effort for multitined expandable electrodes is too high for clinical practice due to the necessary higher resolution of the computation domain to sample the small expandable electrodes. Nevertheless, multipolar RFA of up to three bipolar electrodes is supported by the simulation system. In such a setup, the electric current is simulated between all possible electrode configurations as described by the generator vendor. A detailed description of the mathematical background on numerical simulation of the ablation zone is given in the following chapter.

3.4 Interactive Slice Visualization

For planning of RFA, 2D slice representations of three-dimensional data set are commonly used in clinical practice. Thus, visualization methods to overlay the objects onto the anatomical image data are presented. Supplementary to the familiar representation with its axial, sagittal and coronal views, two orthogonal multi-planar reformatted (MPR) views are also integrated in order to allow fast exploration of tissue in the vicinity of the applicator electrode. The first MPR view is oriented along the applicator axis and can be rotated 360 degrees around the applicator. The second MPR view shows the image data perpendicular to the applicator axis and can be sliced from shaft to target. The advantage of the MPR views is that risk structures in the vicinity of the electrode can be intuitively explored, even if the applicator is not placed in plane (double angulated placement).

3.4.1 Contour Rendering of Segmentation Masks

The segmentation masks for lesions and vessels are represented as volumetric overlays on top of the anatomical image. To further emphasize the shape of the segmentation mask, contours are also drawn at the mask's boundary (see Figure 3.4). The contours are displayed with the same color as the overlay, but with higher opacity. Technically, the contour is calculated by detecting the edge from a 4-neighborhood of the image mask utilizing a dilation operation [118].

In the case of the tumor mask, an additional contour can be drawn to visually represent the safety margin of the target region, which is typically taken into account for placing the RF applicator. For that, a Euclidean distance transform (DTF) from the lesion mask is calculated. The contour is calculated by evaluating the distance threshold of the safety margin.

3.4.2 Visualization of Ellipsoidal Ablation Zones

To visually estimate the amount of cell destruction caused by ablation, an interactive rendering of ablation zones is integrated in the 2D slice visualization. The coloring of lesions located in the ablation zone is changed in order to emphasize the area of destruction.

Technically, for each voxel it is computed if the voxel's position \mathbf{x} is inside or outside of the ellipsoid (see Figure 3.2). For that, an implicit function of the ellipsoid is utilized. The result of implicit equation is negative if \mathbf{x} is inside the ellipsoid and positive outside:

$$f(\mathbf{x}) = |\mathbf{x} - \mathbf{x}_0 + \frac{r_{min} - r_{max}}{r_{max}} \hat{\mathbf{v}}(\hat{\mathbf{v}} \cdot (\mathbf{x} - \mathbf{x}_0))|^2 - r_{min}^2 \quad (3.1)$$

where \mathbf{x}_0 denotes the middle point, r_{min} is the minimal radius of the ellipsoid and r_{max} is the maximal radius along orientation \mathbf{v} . The calculation is performed in a shader program on the GPU. A detailed technical description of the used shader

framework and implementation of ablation zone rendering can be found in Chapter 7 of this PhD thesis.

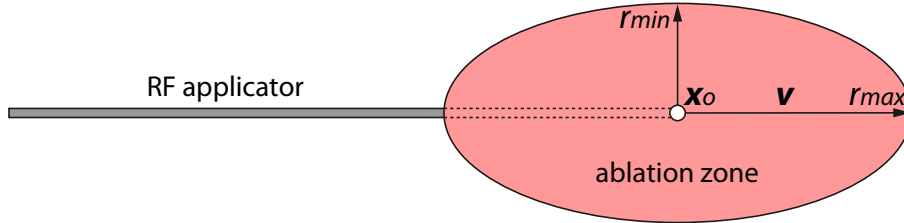


Figure 3.2: An illustrative description of an RF applicator and corresponding ablation zone where \mathbf{x}_0 denotes the middle point, r_{min} is the minimal radius of the ellipsoid and r_{max} is the maximal radius along orientation \mathbf{v} .

In order to treat lesions larger 3 cm in diameter, positioning of multiple RF applicators around the lesion is an alternative ablation procedure in clinical practice [59]. To support multiple ablation zones, the union of all visible ellipsoids is computed, which means that every voxel location has to be tested whether it is inside of the ellipsoids. For that purpose, applicators as well as ablation zones can be interactively created, removed or manipulated by the user. Figure 3.3 shows a slice visualization of a placed RF applicator, segmented lesion and surrounding vessels. The lesion's color is modified for voxels inside of the ablation zone.

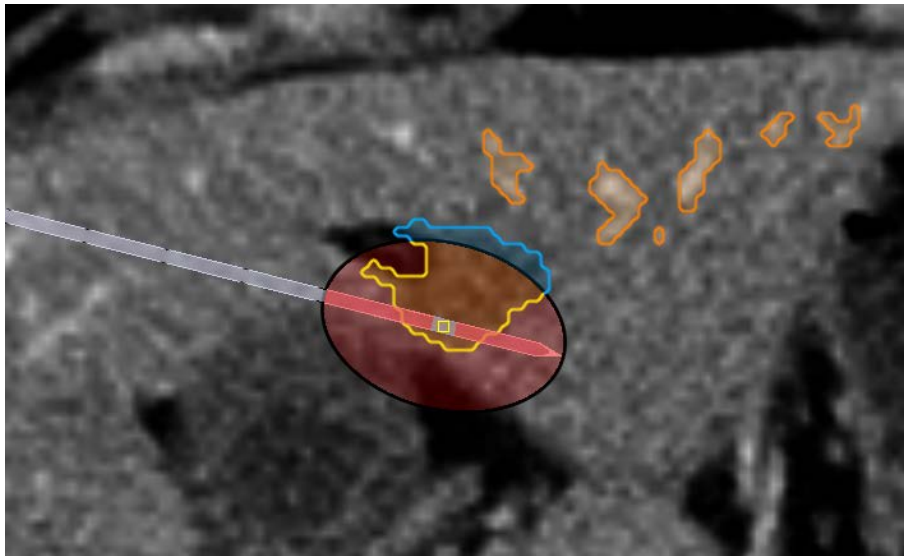


Figure 3.3: Superimposed visualization of the ablation zone of a RF applicator (Olympus ProSurgeTM150-T30). Tumor voxel inside of the ablation zone are colored in yellow, outside in blue.

3.4.3 Contour Rendering of the Coagulation Necrosis

The output of the numerical simulation is a three-dimensional heat distribution around the applicator's electrode. In 2D, the simulated thermal necrosis image is represented as a color-coded temperature map. The goal of the temperature visualization is that the physician is able to verify whether the necessary heat for complete tumor ablation can be reached with the current electrode placement or not. According to the color scheme described by Ahmed et al. [19], tissue which is located in the zone of immediate irreversible cell destruction is colored in red, i.e. temperatures of more than 60°C . Coagulation zones of incomplete destruction are colored in orange and in yellow. The orange contour denotes tissue which will be coagulated after 4-6 minutes (50°C). The yellow contour represents tissue which takes more than several hours at 43° for complete cell destruction. To emphasize the temperature boundaries, contours are calculated similarly to the above mentioned description and superimposed onto the anatomical image. The calculation of the necrosis image is interactively updated for every calculated time step, but the complete simulation has to be re-computed if any geometric parameter, such as electrode position or vessel mask, is changed. Figure 3.4 shows the simulated necrosis image of two bipolar RF applicators.

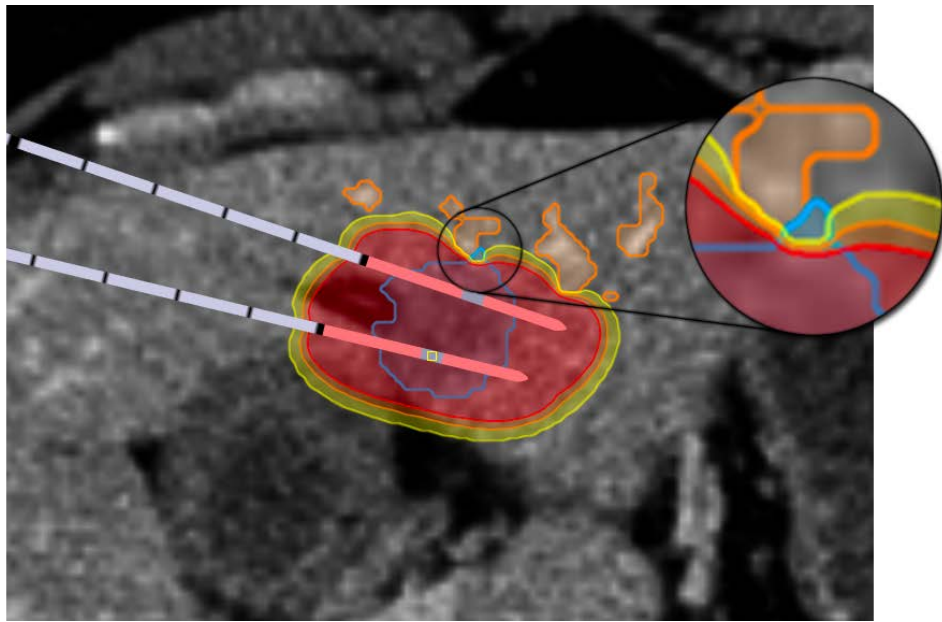


Figure 3.4: Superimposed visualization of the simulated thermal necrosis image from two bipolar RF applicators (Olympus ProSurgeTM150-T30). The critical area of incomplete tumor coverage is caused by the nearby vessel's heat-sink effect.

3.5 Interactive Volume Visualization

Besides the 2D representations as described in Section 3.4, an additional three-dimensional volume rendering is integrated for a spatial view of the scene and all computational results, which helps physicians like surgeons or gastroenterologists planning an RFA procedure more intuitive than only by slicing in 2D.

3.5.1 Anatomical Volume Rendering

The anatomy is visualized as three-dimensional direct volume rendering (DVR) using the possibilities of modern graphics hardware [182]. The goal of the anatomical visualization is to allow a fast recognition of potential risk structures such as liver vessels. Also, landmarks such as skin or ribs can be determined for optimal placement of RF applicators. Due to the clinical requirements, accurate but time consuming segmentation procedures and subsequent 3D reconstructions to surface meshes are not taken into account. To avoid segmentation of the complete vascular tree and other anatomical structures for visualization, the patient's anatomy is directly represented in a volume rendering and classified utilizing a transfer function. Nevertheless, the difficulty in displaying anatomical structures such as vessels and lungs together by volume rendering is to set up an appropriate transfer function. A common trial and error procedure is to define it in a transfer function widget [135]. This method is not suited due to the difficult and time consuming manipulation process to set up the transfer function. Another interaction method is *windowing*, known from medical workstations. Using windowing, the width and center of a ramp transfer function is manipulated using mouse movement along x and y coordinates in the viewer. The drawback of windowing is that the related ramp transfer function limits visual separation of multiple structures with different intensities. For instance, vessels and lungs can not be visually separated (see Figure 3.5 (a)).

To overcome this issue and to allow a fast exploration of the data set, an appropriate transfer function is automatically calculated. The basic idea, which is originally published by Schwier et al. [157], is to set up a 1D transfer function according to the intensity distributions in the liver parenchyma. The input image for this method is a contrast-enhanced venous phase CT image of the liver. Due to its robustness to noise and varying intensity distributions, the fuzzy c-means (FCM) clustering [27] is utilized to determine adequate grey value thresholds in the image. The thresholds are used to set up the 1D transfer function for the volume rendering that emphasizes liver vessel structures. In this work, this method is advanced with the possibility to pre-define an arbitrary transfer function with several control points. Thus, liver vasculature as well as soft tissue such as lungs can be classified with a single 1D transfer function (see Figure 3.5 (b)). The automatic method adjusts only control points which contribute to the intensity range of the liver vasculature. A windowing functionality allows to independently change the transparency of the liver vessels and lungs. To save computation time, the clustering is applied in a local region of

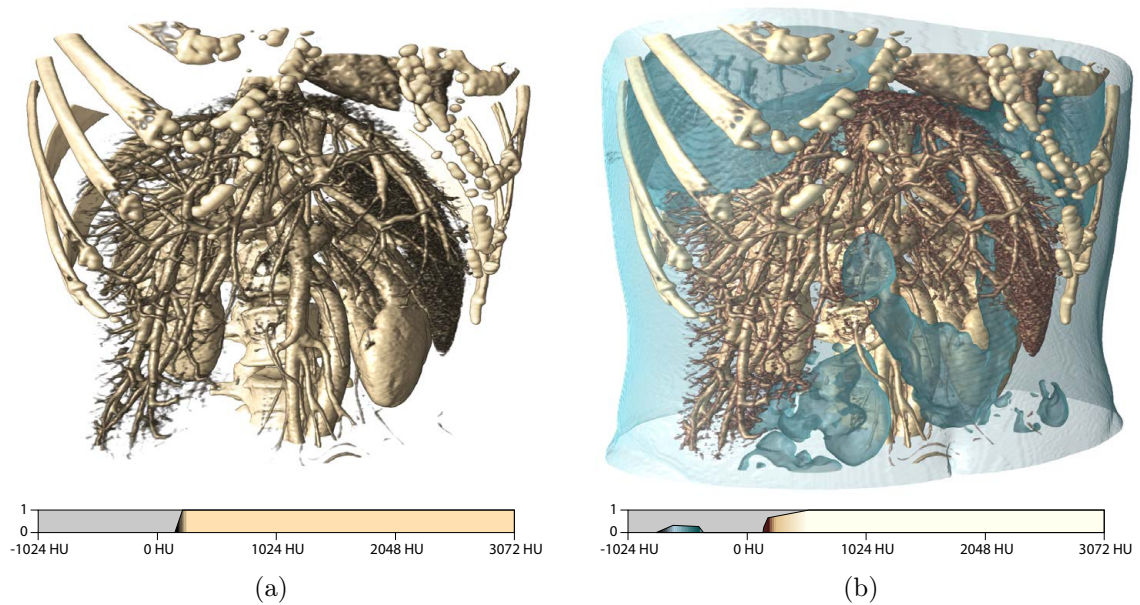


Figure 3.5: In (a) the contrast and alpha window of the volume rendering is manually set by the user; (b) shows the rendering with automatically determined transfer function. Pulmonary structures and other soft tissue organs such as skin and intestine are visible, too.

interest (ROI) around the selected tumor. The clusters are only calculated in the ROI but the final transfer function is used for the volume rendering of the whole data set.

3.5.2 Probe Target View

The general drawback of a three-dimensional view is the determination of a good view point by mouse interactions of the user. To explore possible intersections of the applicator's trajectory with risk structures, the view may be rotated several times due to occlusion of anatomical structures. A solution for that issue is presented with the *target view*. Inspired by the well-known dart board, the *target view* displays the trajectory from incision point at the patient's skin to the target region, i.e. the tumor. Technically, the two spatial coordinates of the current RF applicator are used to define an orthographic projection of the vessel enhanced volume rendering including the lesion mask. If the applicator is moved, the target view is updated interactively. In contrast to the single slice of the MPR view, all anatomical structures along the trajectory are visible. To ease the interpretation of the target view, circled labels are drawn within 10 mm distance on top of the rendering. The red dot at the center illustrates the target, just like the Bullseye of the dart board. Figure 3.6 shows a volume rendering of the target view. It is clearly visible that the current trajectory is placed in the vicinity of liver vessels. Hence, this applicator's placement would be

risky to harm vascular structures.

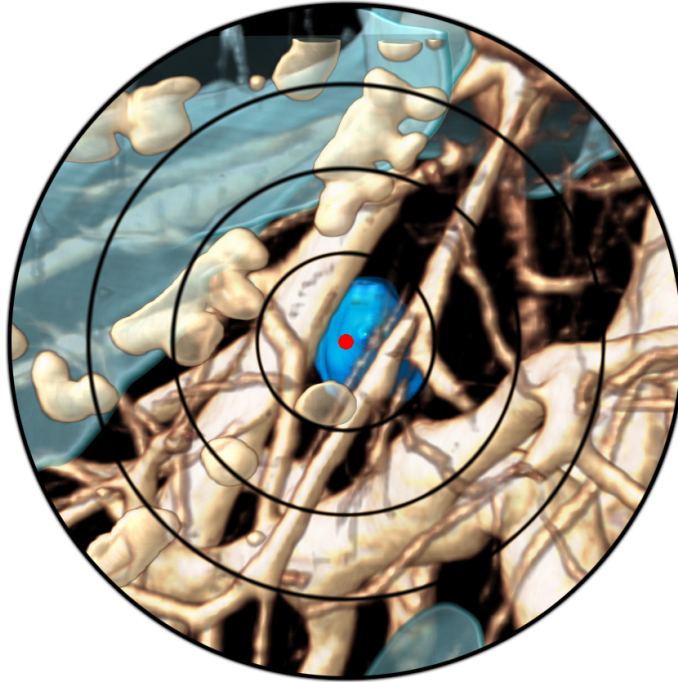


Figure 3.6: A volume rendering of the *target view*. The chosen trajectory passes between several liver vessels with small distance (less than 3 mm).

3.5.3 Visualization of Tumors and Ablation Zones

To allow for exploration of the spatial relations around lesions, the segmented tumors are also integrated into the three-dimensional volume rendering [73]. In contrast to representing the tumors as surface meshes, they are loaded into the renderer as additional volumes, facilitating the tumors' color to be changed depending on the coverage with the ablation zone. For a good perception of shapes and spatial relations, the tumors should look natural. Natural appearance of anatomical structures refers to the smoothness of the surface [Moench:2011fk]. Also, sharp feature edges, as visible in direct visualization of binary masks, attract the observers attention and could disturb the perception. For natural visualization, each binary tumor mask is smoothed using a Gaussian diffusion filter with a noise level of $\sigma = 0.75$. The smoothed data set of the tumor is loaded into the volume rendering and is classified using a sigmoid transfer function

$$s(x) = \frac{1}{1 + e^{\frac{x-c}{w}}} \quad (3.2)$$

where w denotes the width and is set to $w = \frac{range}{32}$, *range* denotes the data range of the transfer function and c denotes the center and is set to $c = w * 0.5$. To

further enhance the spatial shape of the tumors, volume shading is enabled. For that, gradients, which are needed for volume shading, have to be computed using a *Sobel* filter as a pre-processing step. Figure 3.7 shows the visualization of un-shaded, un-smoothed, and smoothed-shaded segmentation mask. Due to the application of the sigmoid transfer function on the smoothed tumor, the maximum tumor diameter as well as the volume may slightly change. Since the visualization is not used for quantification, the error is neglectable.

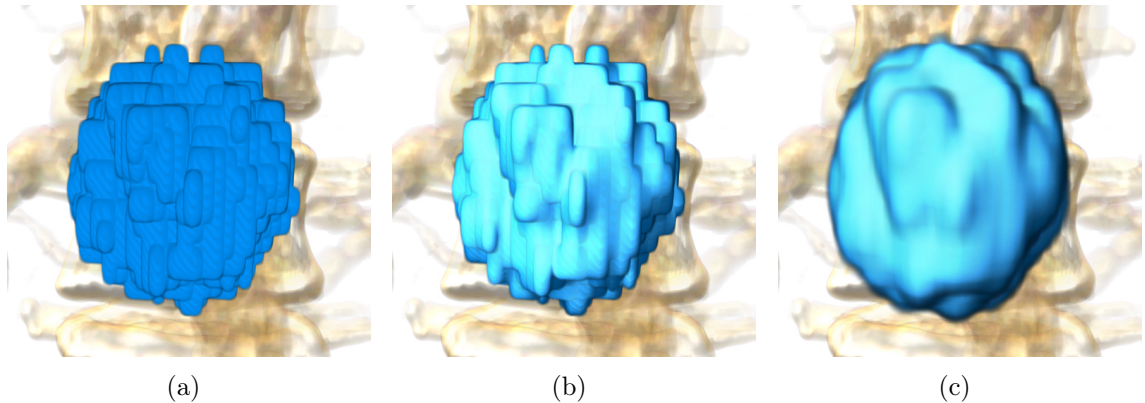


Figure 3.7: In (a) the tumor is rendered as a simple mask. In (b) the tumor is visualized using volume shading. Image (c) shows the shaded volume rendering of the smoothed segmentation mask.

Because the tumors are part of the volume rendering, the same calculation as illustrated in Section 3.4.2 is used for the visualization of the ablation zones. Also, the color of lesion masks inside of the ablation zone is changed. To further emphasize tumor voxel outside of the ablation zone, a silhouette is drawn at the boundary of the ellipsoid. In contrast to the 2D slice rendering, the ablation zones are transparently represented to allow for exploration of embedded lesion structures (see Figure 3.8). Since the shape of ellipsoids is well-known, the loss of depth perception introduced by the use of transparency can be neglected.

3.5.4 Iso-Hull Visualization of the Coagulation Necrosis

In 3D, the numerically computed necrosis image is visualized utilizing three-dimensional iso-hulls, which are integrated into the anatomical volume rendering. According to the two-dimensional visualization, three transparent hulls are rendered utilizing Gaussian distributions in the transfer function for classification of the iso values. Due to the high slope of the Gaussian peaks and the low resolution of the heat image data, the transfer function is sampled using a pre-integrated lookup table [53] allowing for smooth rendering of the shaded hulls (see Figure 3.9). The red hull represents the lower threshold of temperatures higher than 60°C , orange higher than 50°C , and yellow higher than 45°C . Thus, the physician is able to interpret

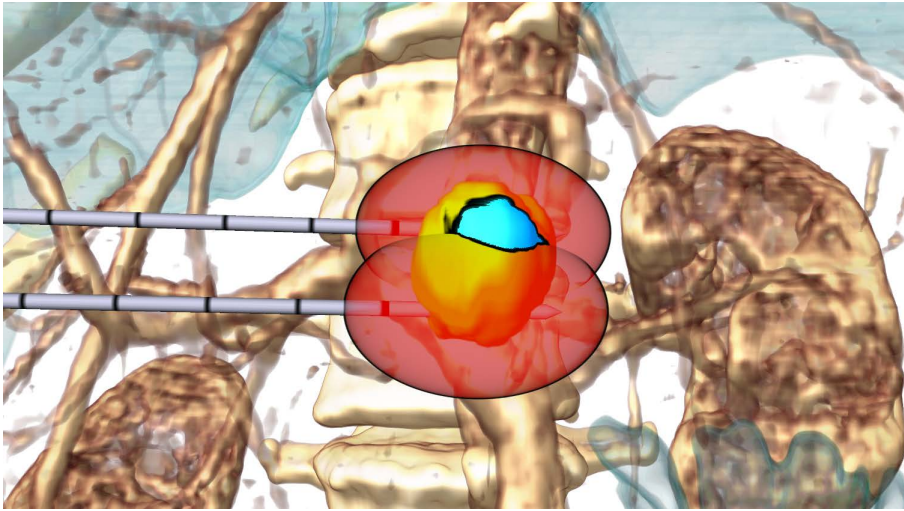


Figure 3.8: Two RF applicators are positioned into a tumor. The color of the tumor is yellow if it is located inside the ablation zone and blue outside. Silhouettes are drawn at the tumor’s boundary to emphasize regions, which will potentially not be ablated.

the simulation result with respect to the spatial relations in 3D. Particularly the heat-sink effects and the corresponding blood vessels, which influence the thermal necrosis, are intuitively explorable.

3.6 Results and Discussion

Clinical partners use the software assistant with integrated methods for scientific projects and clinical evaluations. Informal feedback was collected after discussions with the medical experts. They regard the methods as helpful for planning of complicated interventions, particularly if multiple RF applicators are used or in-plane placement is not possible. Furthermore, most of the respondents judge that the proposed technique for the ablation zone visualization provides faster recognition of potentially untreated tumor tissue compared with slice visualizations alone. According to the 3D visualization, a required adaption of the access path as well as the rapid detection of risk structures along the trajectory is reported as intuitively achievable.

The volume rendering method with automatically determined transfer function enables a 3D visualization of anatomical structures such as bones, vessels, and lungs, without segmentation and thus facilitates an immediate spatial view of the planning situation. Also, pulmonary structures can be distinguished, which is important to prevent harming these structures during electrode placement. To assess the value of the technique, the visual quality of several volume rendered vessel systems with corresponding convolution surface visualizations of manually segmented vasculature

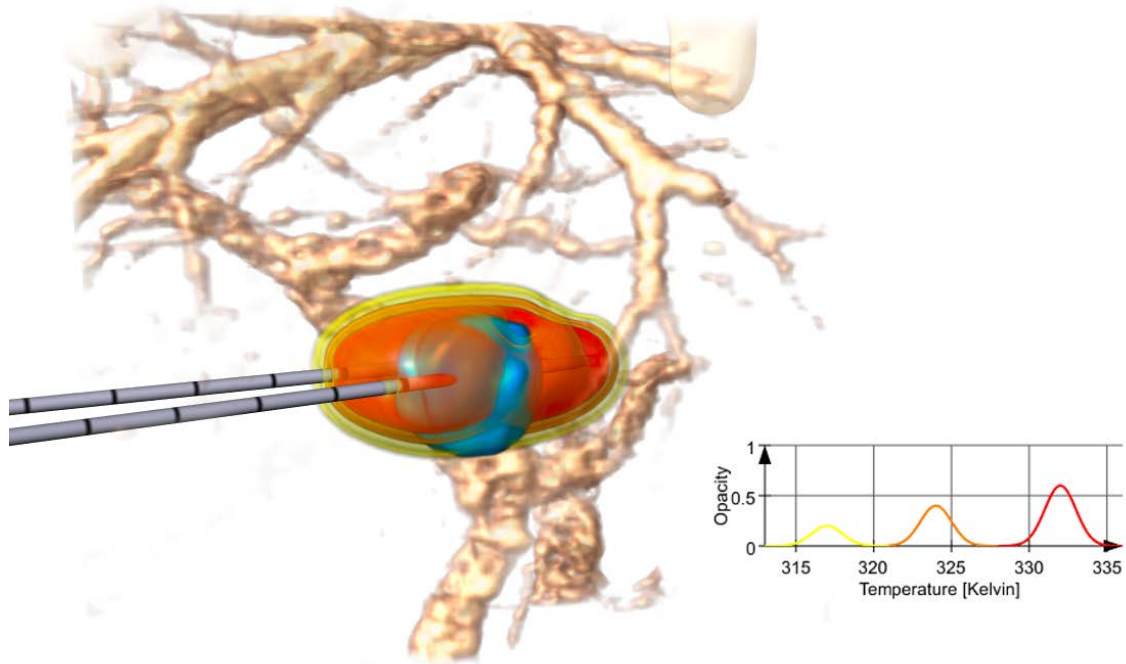


Figure 3.9: Iso-Hull visualization of the simulated thermal necrosis image from two bipolar RF applicators (Olympus ProSurgeTM150-T30) and the used Gaussian transfer function. The corresponding 2D slice visualization can be found in Figure 3.4.

were compared. A good visual quality is defined as a visualization of all vessels with a diameter of more than two millimeter. Vessels smaller than two millimeters are no substantial risk structures for radiofrequency ablation [22]. The manual segmentation [153], which is part of an extensive vasculature analysis for oncological surgery planning, was done by medical technical assistants with high amount of expertise and is thus considered as the ground-truth here. The time effort for the manual segmentation process ranges from 10 minutes for image data with good image contrast to 40 minutes for image data with bad image contrast or strong anatomical deformations. Depending on the CT image quality such as noise, contrast and resolution, it is possible to achieve a visual quality which is close to the convolution surfaces visualization for segmented vasculature (see Figure 3.10). Moreover, if accurate segmentation masks of vessels are not available, even vessels with minor visual quality may support the physician with important anatomical information for radiofrequency planning.

The robustness of the automatic transfer function calculation depends mainly on two parameters: the *contrast* between vessel structures and the liver parenchyma as well as the *noise* in the CT image, i.e. the concept of *Contrast-to-Noise Ratio* (CNR). On the one hand, if the contrast is very high, a good visualization is achievable with high noise in the image. At the other hand, if the noise in the image

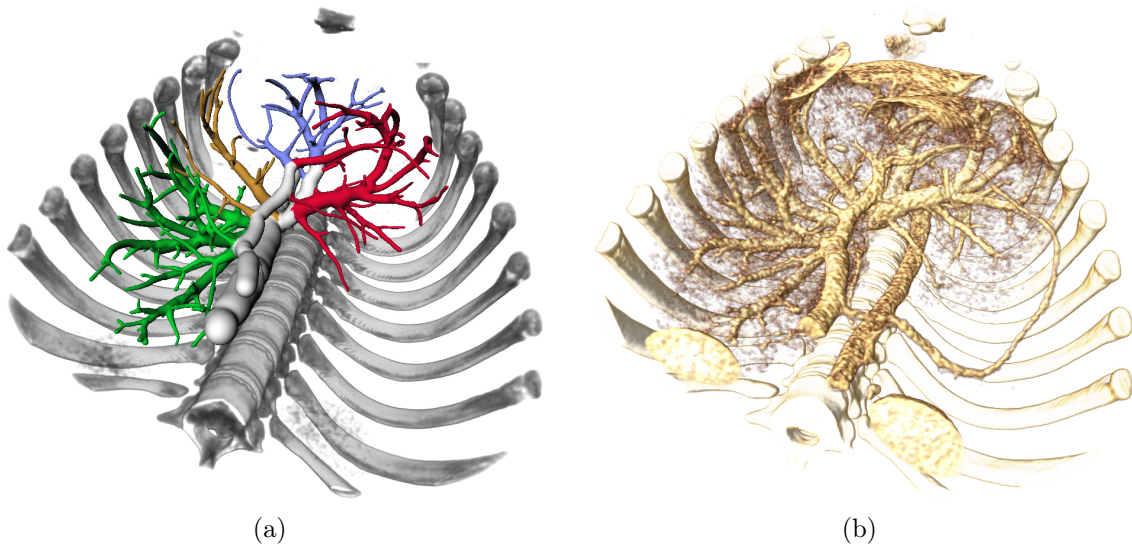


Figure 3.10: Image (a) shows the combined visualization of bone structures using volume rendering and of vessels using convolution surfaces. In (b) the same data set is visualized with our automatic rendering technique.

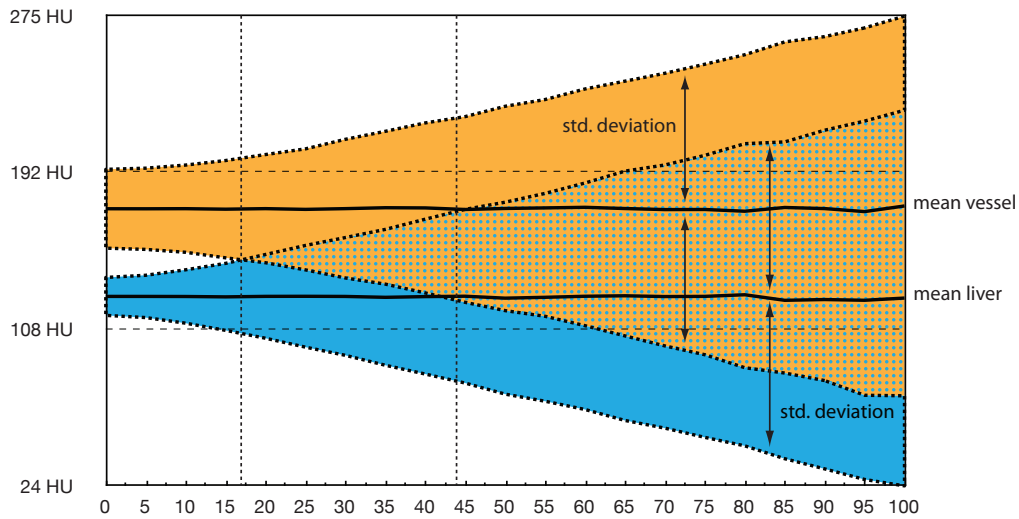


Figure 3.11: The mean and standard deviation of liver parenchyma as well as vessel structures subject to the standard deviation σ of the added Gaussian noise. At a noise level of $\sigma = 17$ the standard deviation of liver parenchyma and vessel structures begin to overlap (see Figure 3.12 (b)) and at $\sigma = 44$ the standard deviations cross the mean values (see Figure 3.12 (c)).

is low, a good visual quality is also possible with low contrast. This is caused by the effect of small intensity differences between liver parenchyma and vessel structures with respect to the image noise level results in intensity clustering of voxels without reasonable object classification. If the contrast between liver and vessels is high, i.e. substantial difference of the mean intensities, a good visual quality is possible in defiance of strong noise, i.e. a huge standard deviation. Figure 3.11 shows the mean and standard deviation values for liver and vessels taken in a ROI image (see Figure 3.12 (a)) where Gaussian noise was added. The vertical axes shows the Hounsfield Units (HU), the horizontal axes the σ values of the Gaussian noise (with mean value = 0). At a Gaussian noise level of $\sigma = 17$ the standard deviation of liver parenchyma and vessel structures begin to overlap. At a noise level of $\sigma = 44$ the standard deviations cross the mean values leading to a significantly lower visual quality due to artifacts, which are mainly undesired liver parenchyma instead of vessels (see Figure 3.12). In contrast to suitable higher dimensional transfer functions, the presented approach is more robust to image noise compared with gradient-based transfer functions [92] and does not requires time consuming preprocessing steps (such as size- and boundary-based transfer functions [47, 160]). A general drawback of the proposed method is that contrast agent inhomogeneities may hamper emphasizing of blood vessels because the transfer function is only globally shifted and thus not optimal for every spatial position. In a recent work, a method is proposed to locally shifted the preset transfer function to automatically emphasize blood vessels [101].

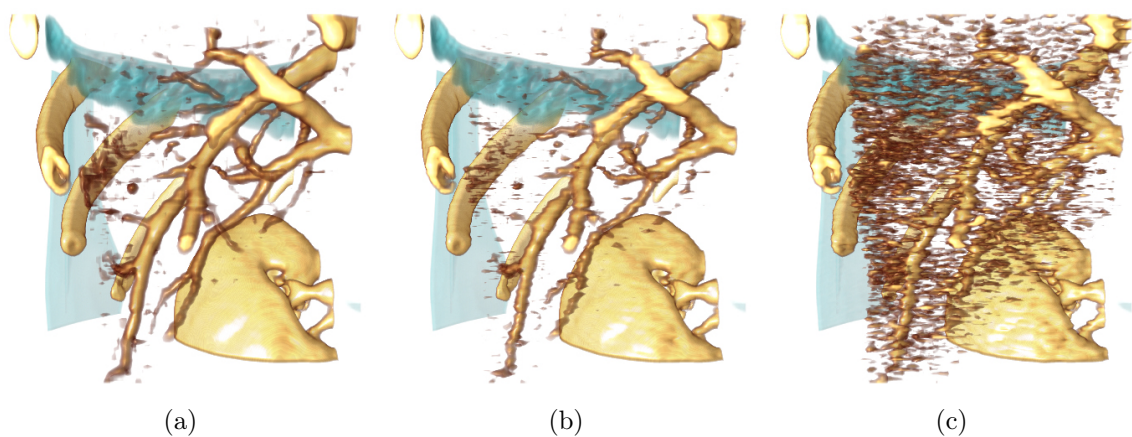


Figure 3.12: Image (a) shows a ROI with automatically determined transfer function. In (b) a Gaussian noise ($mean = 0, \sigma = 17$) was applied onto the image and some artifacts appear. Image (c) shows the resulting rendering with Gaussian noise of $mean = 0$ and $\sigma = 44$ where the calculated transfer function overlaps vessel structures as well as liver parenchyma which results in strong artifacts.

3.7 Conclusions

In this chapter, a workflow to assist physicians in pre-interventional planning of the RFA is presented. The workflow is integrated in a software assistant (see Figure 3.13) and is grouped into four steps in order to guide the user in performing the needed processing:

- **Tumor Segmentation:** An interactive segmentation algorithm for tumors is embedded to allow extraction of quantitative knowledge such as the lesion volume or diameter.
- **Probe Placement:** To support interactive determination of appropriate probe and feasible trajectory, different RF applicators with corresponding ellipsoidal ablation zone, as specified by the vendors, are available as geometric models.
- **Vessel Segmentation:** An interactive vessel segmentation is utilized in order to extract blood vessels which are required for the numerical simulation.
- **Numerical Simulation:** To take the patient-specific anatomy into account, a numerical simulation is also integrated. It allows to calculate the ablation zone incorporating the heat-sink effects and display the heat distribution in the viewers.

Visibility and persistency of segmentation masks, probes or annotations can be managed by the *object navigator* list view.

For visualization of the planning data, several 2D and 3D viewers are integrated in a multi-viewer layout. In the 2D viewers, the planning results are superimposed on top of the anatomical image. Among the cross sectional view, MPR views can also be activated that are aligned to the current RF applicator. Hence, exploration of oblique-angled trajectories regarding the image plane is possible without the need to slice through the image stack.

Besides the 2D viewers, a 3D volume rendering provides an intuitive placement of RF applicators to ensure complete destruction of tumor cells as well as preserving risk structures considering the patients anatomy. Particularly the spatial view of the volume rendering may help physicians like surgeons or gastroenterologists to plan RFA because they are less familiar with image slice representations as radiologists. To overcome the time consuming adjustment of an appropriate transfer function for optimal display of anatomical structures such as vessels or lungs, an automatic method based on fuzzy clustering is utilized. The proposed method allows the physician to explore liver vasculature in a visual quality, which is close to state-of-the-art visualization techniques for segmented vasculature by means of convolution surfaces [129]. In most cases, the visual quality of the automatic method is considered as good as or better as the manual windowed rendering – particularly with regard to the visual separation of different structures – without the need of time-consuming interaction. Another 3D viewer is the probe *target view* which shows anatomical

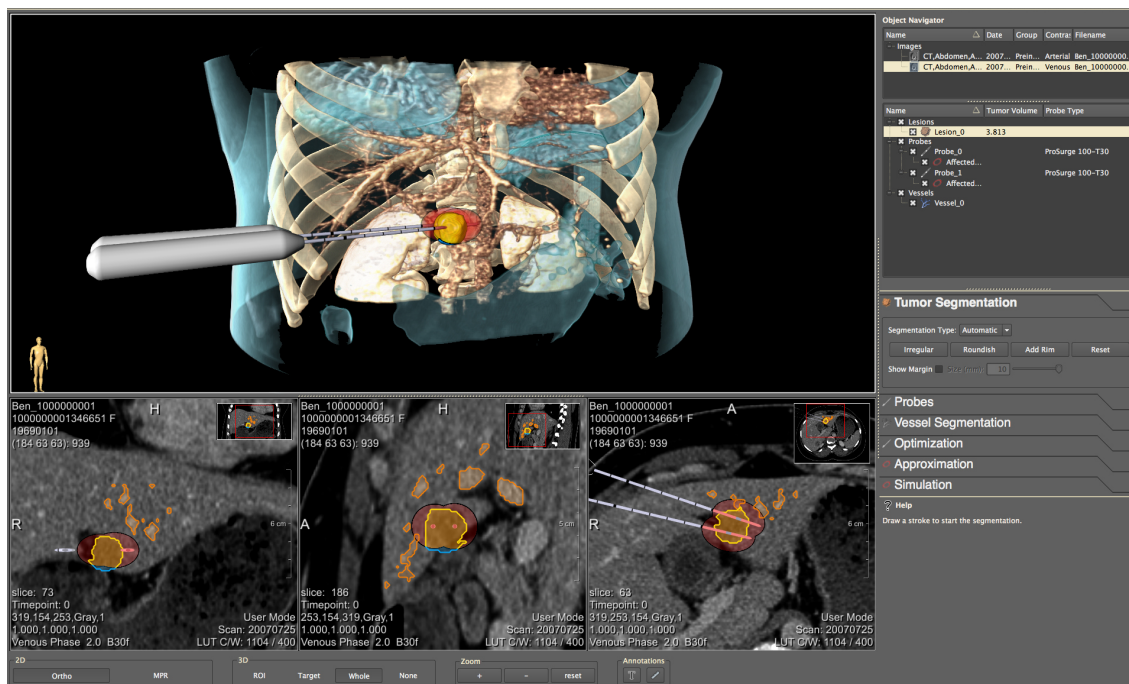


Figure 3.13: The screen shot shows the GUI of the RFA planning software with enabled volume rendering. The RF applicators are positioned close to the selected lesion. With this positioning, the lesion is not completely surrounded by the ellipsoidal ablation zones.

risk-structures along the orthographic projected pathway of an applicator without the need to add segmentation masks or adjust the transfer function.

Although the workflow is developed for planning of RF ablations, it is not restricted to RFA only. Other needle probes such as microwave and cryo-applicators or biopsy needles can be easily integrated in the software assistant if the geometric properties are known. Also, the corresponding ablation zones for homogeneous tissue may be visualized. More adaptations have to be done if other thermal ablations have to be considered in the numerical simulation.

This chapter is in part based on the following publication:

- C. Rieder, M. Schwier, A. Weihusen, S. Zidowitz and H.-O. Peitgen. Visualization of Risk Structures for Interactive Planning of Image Guided Radiofrequency Ablation of Liver Tumors. In: *Proceedings of SPIE Medical Imaging: Visualization, Image-Guided Procedures, and Modeling*, 7261, pp. 726134-1-726134-9, 2009

*There is no original truth, only
original error.*

(Gaston Bachelard)

4

Interactive Approximation of the Ablation Zone

TAKING the patient-specific anatomy into account is essential to successfully achieve complete ablation of the tumor. In the case of RFA, particularly the cooling blood vessels determine the maximum size of the ablation zone. In this chapter, two approaches to rapidly approximate the ablation zone incorporating the heat-sink effects are presented. The first method is based on a geometric reconstruction of pre-computed numerical simulations, which are stored in a lookup table. The second approach utilizes weighted distance fields to approximate the ablation zone on the GPU in real-time.

4.1 Introduction

The usual shape of the RF ablation zone is oval or round. However, it can be slender or irregular. The most important cause of this variability is the so-called heat-sink effect that is due to the adjacent hepatic blood vessels, an effect caused by perfusion-related heat dissipation [89]. As a consequence, the coagulation size may be decreased and the tumor incompletely ablated [121].

The goal of this PhD thesis is to investigate visualization methods to estimate the ablation zone in order to support the physician with software-assisted planning of RFA. In most planning applications, the ablation zones are described as ellipsoids around the RF applicator electrodes [38, 175, 4], which are specified for homogeneous tissue by the applicator manufacturers. However, this estimation of the ablation zone is questionable if patient-specific planning of the intervention is desired. To overcome this issue, numerical simulations based on FEM have been developed to allow an accurate estimation of the ablation zone to incorporate heat-sink effects [96] and integrated into prototypical software assistants. Although the results of these methods are helpful to understand physical effects, they are not suited for clinical practice because of too long processing times.

In this chapter, novel approaches to approximate the ablation zone (coagulation necrosis) incorporating the heat-sink effects are presented in order to support the physician in interactive planning of radiofrequency ablation. Contributions of this work include:

- An image-based, fast approximation of the ablation zone with respect to the cooling blood flow. For that, patient independent numerical simulations of the ablation zone are pre-computations and stored in a lookup table. Subsequently, the lookup table is used to approximate the patient dependent ablation zone mask.
- Proposal of a novel model, based on weighted distance fields to approximate the ablation zone, incorporating heat-sink effects of the blood vessels. The weighted distance fields are retrieved from complex numerical simulations that take the bio-physical effects into account. To consider the cooling blood vessels, the thermal diffusion of the vasculature is calculated in a preprocessing step. The final ablation zone is the result of a heuristic combination of both fields.
- Integration of the novel approximation model into a clinical software assistant. The graphics hardware is utilized in order to calculate and visualize the approximated ablation zone in real-time in both, 2D and 3D. The underlying dynamic shader framework allows the user to perform interactions such as parameter adjustments or intuitive placement of multiple RF applicators with corresponding ablation zones.
- Assessment of the value of the proposed methods. The results of the methods are quantitatively compared with complex numerical simulations. Further-

more, a discussion of the method with interventional physicians in an informal expert study completes the contribution.

The outline of this chapter is as follows: In Section 4.2, related work in the field of planning RFA and modeling the ablation zone is discussed. Section 4.3 explains the mathematic background to model the bio-physical effects of RF ablation. In Section 4.4, an approximation method based on a geometric reconstruction of pre-computed numerical simulations, which are stored in a lookup table, is outlined. Section 4.5 describes the second approach, which utilizes weighted distance fields to approximate the ablation zone on the GPU. The proposed approximation methods are compared in Section 4.7.

4.2 Related Work

In the literature, several planning applications for needle-based interventions are proposed. Although vessel segmentation algorithms are included in some works [38, 111, 156], the patient independent anatomy is not considered and ablation zones are only modeled utilizing simple geometry. For cryoablation, ellipsoids are used to model the frozen zones at the tip of each cryo-needle, and for radiofrequency, spherical or elliptical models represent the ablation zones. In works which focus on visualization of safe access paths for planning of RFA [155, 87], the ablation zone is also not taken into account. Thus, such visualizations may be helpful to determine safe access paths in terms of risk structures, but do not consider the patient dependent tumor coverage and the resulting restriction of feasible pathways.

A software application for planning RFA treatment is described by Villard et al. [175], who focus on planning support for ablation of hepatic tumors. Liver, blood vessels, pathologies, and surrounding organs are automatically segmented and visualized by means of surface rendering. Also, virtual RF applicator models with idealized ellipsoidal ablation zones are available. To model the heat-sink effect, the ablation zone surface models are deformed in real-time by moving their vertices according to the proximity of large surrounding liver vessels [177]. Technically, a morphological opening operation is applied to the vessel mask to eliminate small vessels ($\varnothing < 2\text{-}3$ mm) as a preprocessing step. Using further dilations, a deformation zone is calculated to define the amount of vertex translation. Besides the limitation of the possible vertex deformation of the ellipsoid, this approach is purely heuristic, so that the relation of the applied deformation to the biophysical heat-sink effect of the blood vessels during RFA is unclear.

Littmann et al. [104] present a software system for in-situ laser-induced thermotherapy (LITT) ablations in oncologic liver surgery. LITT applicators are represented as surface models which are visualized in the familiar 2D slice views and a 3D surface rendering. Also, intrahepatic structures can be segmented to simulate the ablation zone. The heat transport incorporating heat-sink effects of surrounding vessels within the liver tissue is calculated by means of a time-consuming FEM method.

Weihusen et al. [179] describe a workflow-oriented software platform for image-guided RFA. Virtual applicator models of different manufactures can be superimposed onto the 2D slice images. Furthermore, tumor lesions and vascular structures can be segmented using semi-automatic methods. The extracted vessels are utilized for the numerical simulation of the ablation zone incorporating the cooling effects of nearby vessels. The ablation zone resulting from the numerical simulation is visualized in 2D viewers as an overlay and also in a volume rendering as a surface model.

Zhai et al. [187] present a preoperative surgery planning method for percutaneous microwave ablation. The microwave ablation zone is simulated utilizing an iterative GPU calculation. The ablation zone is visualized along with the microwave applicator in the 2D slice views and in 3D as a surface model combined with the anatomical volume rendering. Computation times of less than 2 seconds are reported for the simulation, whereas the typical rendering time reaches 20 FPS using an Nvidia GeForce 8800GTS graphics card.

Kröger et al. [97] present an approximation of the numerical forward simulation. In this approach, the patient-specific ablation zone is parameterized by a large number of reference configurations, which are precomputed and stored in a lookup table. During placement of the applicator electrode, the patient-specific ablation zone is reconstructed from the lookup table under consideration of the Euclidean distance from the electrode to the blood vessels and its radii, allowing for interactive frame rates. The major drawbacks of this method are that the basic shape of the ablation zone consists of the union of spheres along the points of the electrode and the critical assumption of an independent cooling effect per vessel segment. Further, this approach is not integrated into a medical application.

Trovato et al. [173] include an approximation of combined multiple ablation zones into their semi-automatic RFA planning system. Although the visualization method is not described in detail, it can be assumed that some kind of implicit blending is used. However, heat-sink effects are not taken into account.

More references and theoretic details on modeling of RFA have been compiled in an overview article by Berjano [25]. A more comprehensive review of computer-assisted planning of liver tumor ablation is presented in the work of Schumann et al. [7].

4.3 Mathematical Background

The bio-physical effects of RF ablation have been described in the literature [25]. A mathematical model for RF ablation essentially consists of two partial differential equations:

$$-\operatorname{div}(\sigma \nabla \phi) = 0, \quad (4.1)$$

$$\rho c \partial_t T - \operatorname{div}(\lambda \nabla T) + \nu(T - T_{\text{body}}) = q. \quad (4.2)$$

The first equation models the electrical potential ϕ , which can be assumed to be quasi-static. Here, σ denotes the electrical conductivity, div the divergence and ∇ the gradient. The second equation models the distribution of the temperature T , where ρ , c , λ , and ν denote material parameters (that is, the density, the heat capacity, the thermal conductivity, and the relative blood flow rate). Further, T_{body} is the human body temperature (a constant), and q is the heat source induced by the electric current flow. It is given by

$$q(\mathbf{x}) = \alpha p(\mathbf{x}), \quad p(\mathbf{x}) = \sigma |\nabla \phi(\mathbf{x})|^2, \quad \alpha = \alpha(\|p\|_{L^1}), \quad (4.3)$$

where α is a one-parameter, scalar-valued function that models the nonlinear behavior of the electric generator due to changes of the tissue impedance. All material parameters are functions of the temperature T . Since the electrical potential ϕ depends on σ (4.1) and the heat source q (4.2) is implicitly dependent on σ (4.3), Equation (4.1) and (4.2) are a coupled system.

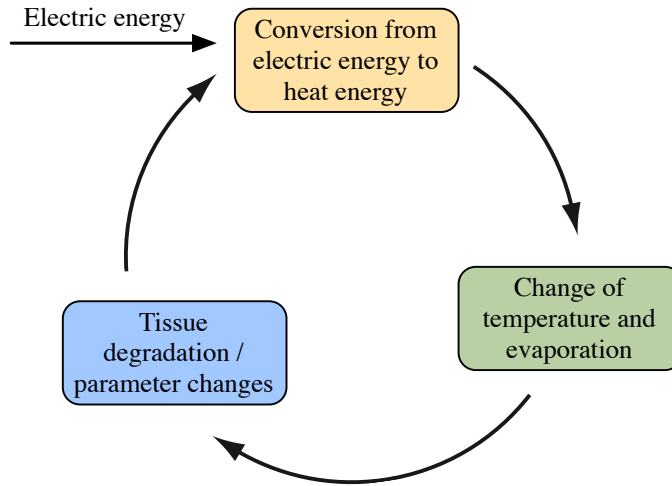


Figure 4.1: Illustration of the iterative circle of the three steps to be solved per time step and domain node.

Equations (4.1), (4.2), and (4.3) compose a generalization of the so-called *thermistor problem*, well-known in the literature. The thermistor problem is recovered for $\alpha = \text{const}$ and $\nu = 0$. The so called *weighted pennes term* $\nu(T - T_{\text{body}})$ models the heat-sink effect due to the small blood vessels (invisible in pre-interventional imaging), by which the tissue is assumed to be pervaded [132]. Equation (4.2) is called the *bio-heat transfer equation* [48].

Both differential equations are considered on a computational domain Ω around the applicator electrodes which is chosen large enough such that effects outside the domain can be safely ignored. The area covered by the applicator is cut out of the domain for (4.1), and also for (4.2) if an internally cooled applicator is considered. The area covered by large blood vessels (visible in pre-interventional imaging) is

cut out of the domain for (4.2). Both equations are supplemented by boundary conditions on the boundary Γ_{out} of the domain as well as on the boundaries of those parts that have been cut out of the domain. The boundary conditions are as follows:

$$\phi(\mathbf{x}) = \pm 1, \quad \mathbf{x} \in \Gamma_{\pm}, \quad (4.4a)$$

$$n(\mathbf{x}) \cdot \nabla \phi(\mathbf{x}) = 0, \quad \mathbf{x} \in \Gamma_{\text{iso}}, \quad (4.4b)$$

$$n(\mathbf{x}) \cdot \nabla \phi(\mathbf{x}) = \frac{n(\mathbf{x}) \cdot (\mathbf{s} - \mathbf{x})}{|\mathbf{s} - \mathbf{x}|^2} \phi(\mathbf{x}), \quad \mathbf{x} \in \Gamma_{\text{out}}, \quad (4.4c)$$

$$T(t, \mathbf{x}) = T_{\text{body}}, \quad \mathbf{x} \in \Gamma_{\pm} \cup \Gamma_{\text{iso}}, \quad (4.4d)$$

$$T(t, \mathbf{x}) = T_{\text{body}}, \quad \mathbf{x} \in \Gamma_{\text{ves}}, \quad (4.4e)$$

$$n(\mathbf{x}) \cdot \nabla T(t, \mathbf{x}) = 0, \quad \mathbf{x} \in \Gamma_{\text{out}}. \quad (4.4f)$$

Here, Γ_{\pm} , Γ_{iso} , and Γ_{ves} denote the boundary of those parts of the domain covered by the electrodes, the electrically isolating parts of the applicator, and the large blood vessels. In Equation (4.4c), \mathbf{s} denotes the centroid of the applicator's active zone. The applicator cooling is modeled in (4.4d) and is removed from the system in case of an uncooled applicator. Equation (4.4e) models the heat-sink effect due to the large blood vessels, which are assumed to not heat up considerably [97]. The equation for the temperature is also supplemented by the initial condition

$$T(t, \mathbf{x}) = T_{\text{body}}, \quad t = 0. \quad (4.5)$$

The coupled system is discretized using finite elements in space and a backward Euler scheme in time. Details can be inferred from a previous publication [96].

In order to determine the area of coagulated tissue, the tissue damage $D = D(t, \mathbf{x})$ is computed using an Arrhenius law [21],

$$D(t, \mathbf{x}) = \int_0^t A \exp\left(\frac{-E}{RT(s, \mathbf{x})}\right) ds,$$

where R is the universal gas constant and A and E are tissue parameters. This law takes a temperature history into account. The area of destroyed tissue (coagulation necrosis mask) is then given by the set

$$I_{\text{sim}} = \{\mathbf{x} \in \Omega : D(t_{\text{max}}, \mathbf{x}) \geq 1\},$$

where t_{max} denotes the total ablation time. Figure 4.1 illustrates the iterative circle which has to be solved per time step and domain node.

Based on the mathematical model described above, an implementation of the numerical simulation for RFA [96] is utilized in this project. The numerical simulation is the underlying model from which both approximation methods are retrieved.

4.4 Lookup Table-Based Approximation of the Ablation Zone

In this section, an image-based, fast approximation of the ablation zone with respect to the cooling blood flow is presented. The method is an advancement of the original surface mesh-based lookup table approach, which has been proposed by Kröger et al. [97]. In the presented method, patient independent numerical pre-computations of the ablation zone are performed and stored in a 4D lookup table. Subsequently, the lookup table is used to approximate the patient dependent ablation zone. In the prototypical software assistant (which is described in Chapter 3), the physician is able to place RF applicator models with corresponding approximated ablation zones, to interactively evaluate the estimated coagulation necrosis caused by ablation.

4.4.1 A Simplified Geometric Model

The basic idea of this method is to pre-calculate the patient independent part of the numerical simulation and subsequently approximate the patient dependent part. For that, the cooling effect of blood vessels, which depends on the vessel radius and its distance to the RF applicator electrode for a given RF applicator and generator type, is calculated. Results of this calculation are stored in a lookup table, which allows for fast estimation of the cooling effect for a given patient dependent applicator placement.

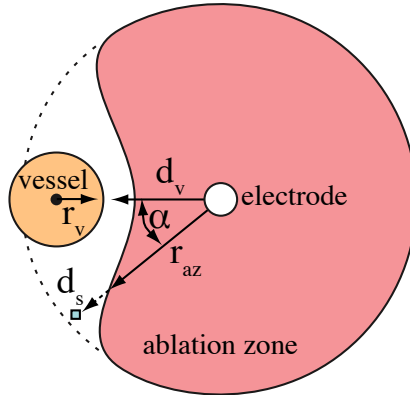


Figure 4.2: Illustrative description of the simplified model: r_v is the vessel radius, r_{az} the radius of the ablation zone, d_v the distance from electrode to vessel and α the angle between d_v and r_{az} .

For the simulation, a simplified setting is assumed, whereas a single blood vessel of infinite length and oriented parallel to the electrode of the RF applicator is considered. Furthermore, it is assumed that the cooling effect of the vessel depends on the radius of the vessel r_v , and the distance d_v from the electrode to this vessel.

The cooling effect is related to the magnitude of the radius of the ablation zone r_{az} , measured from the center of the electrode in all directions orthogonal to the electrode axis (see Figure 4.2). Taking this setting into account, a function of the angle α between the direction under consideration and the direction in which the vessel center is located, the vessel radius r_v and the distance d_v from the electrode to the vessel is defined:

$$(r_v, d_v, \alpha) \rightarrow r_{az}. \quad (4.6)$$

As stated in the original approach [97], the drawback of this simplified 2D model calculated in a three-dimensional scene is that the electrode is assumed to destroy a ball-shaped tissue-region of uniform size if no blood vessels are present. Thus, the basic shape of the ablation zone of the approximation consists of the union of spheres along the points of the electrode (see Figure 4.3).

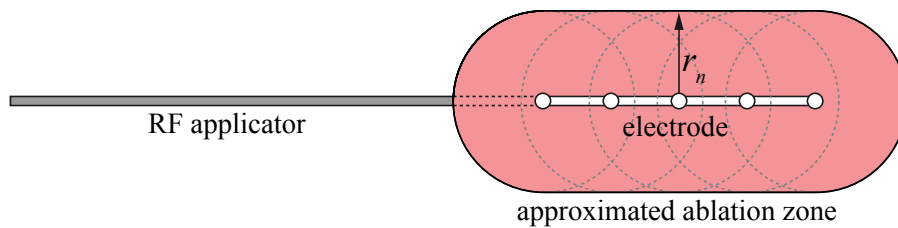


Figure 4.3: According to [97], the basic shape of the ablation zone of the approximation consists of the union of spheres along the points of the electrode.

To overcome this issue, the 2D model is extended to 3D. By exploiting the rotation symmetry of the applicator and the corresponding ablation zone, the electrode is sampled along the electrode's axis. Hence, the function also depends on the distance d_t from current sample to the tip of the electrode:

$$(r_v, d_v, \alpha, d_t) \rightarrow r_{az}. \quad (4.7)$$

For a complete vessel tree, the model is simplified by assuming an independent cooling effect. If multiple vessels are in the vicinity of the electrode, a corresponding ablation zone is individually estimated for each vessel, and the intersection is calculated (see Figure 4.5). This setting is assumed as a clinical sufficiently good approximation.

4.4.2 Pre-Calculation of the Patient Independent Ablation Zone

To pre-calculate all possible configurations of the simplified model, a forward simulation is calculated as described in Kröger et al [97]. The well-known electrostatic potential and bio-heat equation (with Dirichlet boundary at the vessel) are numerically solved via a finite element approach. Since the pre-calculation requires a

vast amount of calls of the forward simulation, the calculating time for this pre-calculation is reduced by using a simplified steady state solution of the forward simulation assuming constant material parameters. Moreover, due to the assumption of a parallel arrangement of the RF applicator relative to the vessel, the temperature is calculated in only two dimensions. In this example, the considered values of the vessel radius r_v range from 1.0 to 7.4 mm (vessels with radius below 1 mm are assumed to occlude during the ablation). The applicator-to-vessel distance d_v varies from 2.0 to 14.8 mm distance (at distances above 14.8 mm the vessel's influence of the ablation zone is negligible). Finally, the angle α takes values between 0° and 180° (angles between 180° and 360° are not considered due to symmetry). Depending on the applicator's geometry, the distance d_t varies from 0 to the length of the electrode with a step size of 1 mm. The resulting four-dimensional sparse lookup table consists of 526 nodes (i.e. entries for the radius r_{az} of the ablation zone) in the (r_v, d_v) plane, 65 nodes in the α direction and 30 nodes in electrode direction (for a 30 mm active zone).

4.4.3 Calculation of the Patient Dependent Ablation Zone

In the prototypical application, the physician is able to place multiple RF applicators using two spatial coordinates for each probe, which define the electrode's orientation and position. As a required preprocessing step, blood vessels have to be segmented, for instance using a semiautomatic segmentation procedure [188]. After placing a marker into a vessel in the vicinity of the tumor, the vessels are segmented automatically. Subsequently, the center line is extracted utilizing a topology-preserving skeletonization algorithm [159]. Additionally to the centerline, the vessel radii at each voxel of the skeleton are calculated. From that, a directed, acyclic graph is generated which allows for fast iteration of the graph nodes representing vessel segments. To reconstruct the ablation zone from the lookup table, the following steps have to be calculated for every voxel \mathbf{s} of image I :

In a loop over all blood vessels in the graph, the minimal distance d_v from vessel to the applicator electrode, the corresponding angle α , and the distance from the current voxel d_s to the electrode tip is calculated. Furthermore, the vessel radius r_v , stored in the graph structure is read. Vessels with radius less than 1 mm are not considered, because smaller ones will usually be destroyed by blood clots [22] during ablation.

Subsequently, a lookup into the table with the calculated parameters is performed. The resulting value of the lookup table is compared with the minimal distance from the current voxel to the electrode. If the stored radius r_{az} of the pre-calculated ablation zone in the considered direction is greater than the minimal distance d_s from the current voxel to the electrode, the voxel \mathbf{s} is classified as part of the ablation zone. Otherwise, the voxel cannot be ablated due to the presence of blood vessels. Thus, the ablation zone mask I_{zone} is calculated by

$$I_{\text{zone}} = \{\mathbf{s} \in I : d_s < r_n\}. \quad (4.8)$$

The complete procedure is repeated whenever the RF applicator configuration, e.g. position of the electrode, is changed. To allow for interactive frame rates, the approximation is calculated slice-based and the result is overlaid on top of the anatomical image.

4.4.4 Results and Discussion

The proposed method is integrated in a software assistant for planning of RFA therapies. The ellipsoid, the interactive approximation of the ablation zone as well as the numerical simulation can be calculated for a selected type of RF applicator. Although the ellipsoid as specified by the manufacturers does not estimate the patient individual ablation zone, it is used in medical workstations as a simple and fast visualization tool in 2D as well as in 3D. However, if particular large vessels are present in the vicinity of the applicator, the question whether all cancer cells can be ablated is not as easy to answer. In contrast, using a numerical simulation, the cooling of the blood vessels can be taken into account. Thus, a patient individual ablation zone can be calculated. Moreover, the numerical simulation allows for the visualization of the thermal field. The drawback of this method is that the calculation of the forward simulation is complex, which results in long computation times (10-15 minutes for 15KJ ablation energy with 65^3 computation domain nodes, 1mm node size, see Table 4.1). Furthermore, a repositioning based on the result of the simulation and a subsequent re-simulation is too time consuming for usage in clinical practice. To reduce this computational effort during application runtime, the interactive ablation zone approximation is developed. Therefore, vessels have also to be segmented, and for every applicator and generator type a corresponding lookup table has to be computed in advance. Using the lookup table, a simplified ablation zone is interactively approximated (see Figure 4.4).

In the presented model, a relationship between the radius of a vessel, the distance of the electrode of an RF applicator to the vessel, and the cooling effect due to this vessel is established in the lookup table based approximation. However, additional parameters such as vessel type, tumor tissue or liver parenchyma properties are not taken into account. The dependence of these parameters will be evaluated in future

	2D	3D	Heat-sink	Output
Ellipsoid	Real-time	Real-time	No	Binary Mask
Approximation	Real-time	3 sec.	Yes	Binary Mask
Simulation	10-15 min.	10-15 min.	Yes	Thermal Field

Table 4.1: Comparison of performance and properties of the simple ellipsoid, the approximated ablation zone and the numerical simulation. The ellipsoid representation of the ablation zone does not incorporate the heat-sink effects. The output of the ellipsoid as well as approximation is binary, in contrast, the numerical simulation's output is a heat distribution.

work.

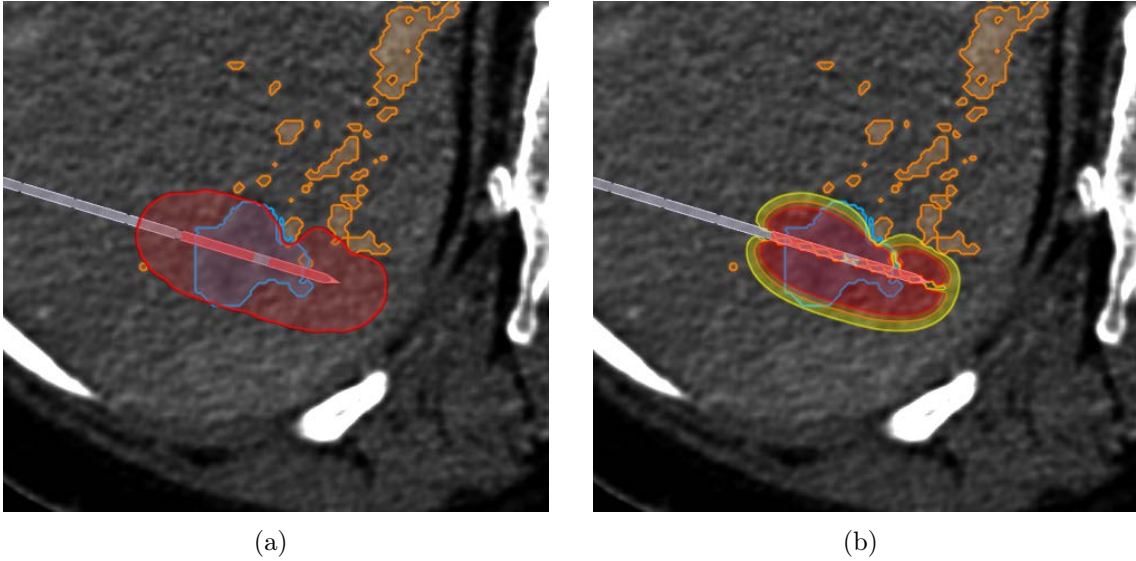


Figure 4.4: (a) The interactive approximated ablation zone in 2D and (c) the resulting heat distribution of the numerical simulation after 15 minutes calculation time in 2D.

Besides the physical electrode and physiologic tissue material parameters, the heat-sink effect particularly depends on the vessel diameter and the distance between vessel surface and applicator electrode. However, preliminary results of the ongoing validation state that the assumption of the independent cooling effect is critical, particularly if vessels are close together. That is, combined cooling effects of two nearby vessels cannot be described by this method. If multiple vessels are located close together, the coagulation zone suffers from spurious sharp edges, see Figure 4.5. The same shortcoming is observed in the work of Villard et al. [177]. Since they utilize a modified Euclidean distance transform of the vessels, whereas the vessel's diameters are taken into account, only the minimal distance from a sample to the nearest vessel is encoded, resulting in comparable sharp edges. Cooling of multiple vessels as it is observed in in-vivo ablations can only be calculated utilizing complex numerical simulations.

Another drawback of this method is the limited performance. Although interactive frame rates are achieved for a single 2D slice, the calculation in 3D takes roughly 3 seconds for a region of interest of 64^3 voxels. After calculation of the ablation zone in 3D, additional processing time may be required for visualization (loading the data into the renderer). The limited performance is related to traversing over all vessel segments, calculating the geometric parameters, and subsequent lookup into the table, which has to be carried out for each voxel in the ROI. If more parameters are taken into account for a more accurate approximation, i.e. the dimensionality of the lookup table is increased, even higher processing times are expected.

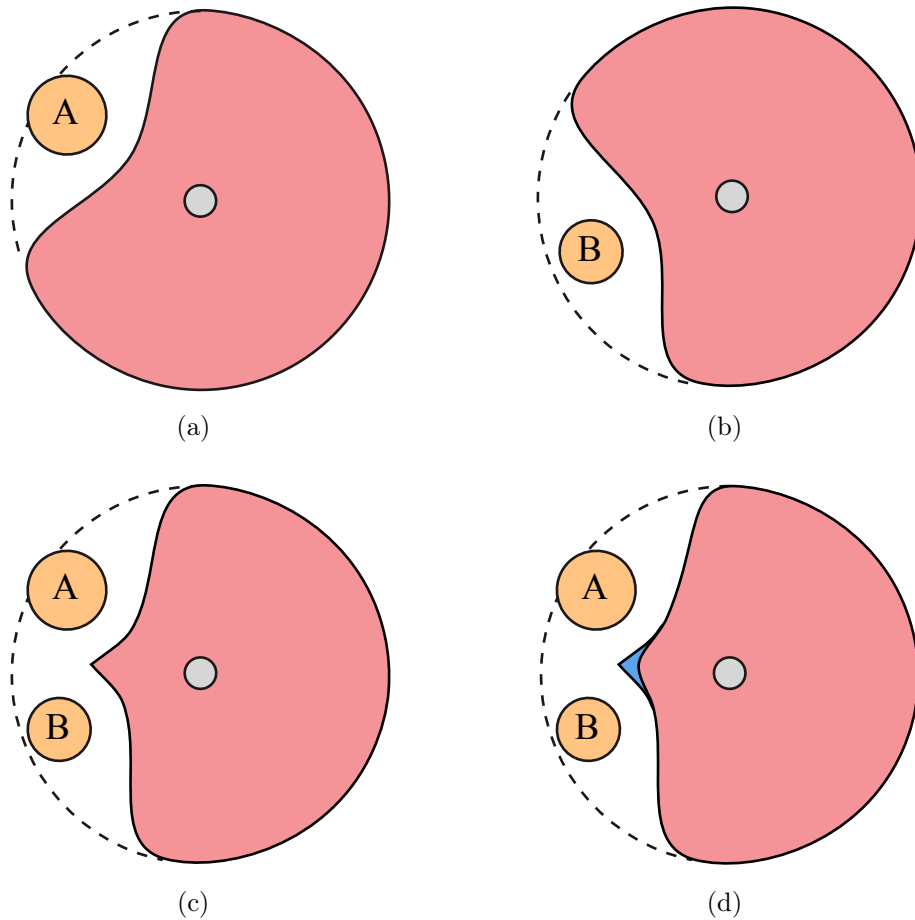


Figure 4.5: In figure (a), the presence of vessel A leads to a deformation of the ablation zone according to the heat-sink effect. A similar situation is illustrated in (b). If an independent cooling effect is assumed, the final ablation zone is achieved by the intersection of both ablation zones (c). In contrast, if both vessels jointly cool the heat field, the heat-sink appears more smoothly (cf. blue peak), similar to the results of numerical simulations (d).

To overcome the performance issue for the 3D case, the ablation zone can be visualized as surface mesh. Instead of calculating the approximation algorithm for each voxel, the algorithm iterates over all vertices of the surface mesh and translate the vertices according the result of the lookup into the table. Another method to speed-up the calculation is to transfer both, the calculation and visualization process, to the GPU. Due to the parallelization paradigm of the GPU, substantial modifications of the proposed method are required, particularly the adaption of the complex graph data structure.

4.5 GPU-Based Approximation of the Ablation Zone

The goal of the second method to be presented in this chapter is to overcome the drawbacks of the lookup-based approximation method presented in Section 4.4. The method allows to approximate the ablation zone in real-time in 3D and supports the interactive planning of optimal probe placement in the tumor with respect to the heat-sink effects of the blood vessels. In contrast to the table-based method, the ablation zone is estimated in real-time on the GPU with weighted distance fields [84] incorporating the electrode geometry. The distance fields are retrieved from results of complex numerical simulations in homogenous tissue, which allow a more realistic representation of the ablation zone than simple ellipsoids or the geometric approximation.

4.5.1 Approximation utilizing a Weighted Distance Field

The key idea of this contribution is the approximation of the coagulation necrosis mask I_{sim} by iso-thresholding a weighted distance transform. Let α be a positive, real parameter. On the computational domain Ω excluding the area covered by the electrodes (that is, on $\Omega \setminus \Omega_{\pm}$ where Ω_{\pm} denotes the area covered by all electrodes), the weighted distance transform is defined

$$f(\mathbf{x}) = \left(\frac{1}{|\Omega_{\pm}|} \int_{\Omega_{\pm}} \frac{1}{|\mathbf{x} - \mathbf{y}|^{\alpha}} d\mathbf{y} \right)^{-1/\alpha}, \quad (4.9)$$

where for any measurable set $A \subset \Omega$, the notation $|A|$ denotes the three-dimensional Lebesgue measure (i.e., the volume) of A . By setting $f(\mathbf{x}) = 0$ on $\overline{\Omega_{\pm}}$, f is defined everywhere on Ω . Using this function and another positive parameter d , the approximation $I_{\text{zone}}(d, \alpha)$ of the coagulation necrosis mask is defined as the d -iso-threshold of f , that is

$$I_{\text{zone}}(d, \alpha) = \{\mathbf{x} \in \Omega : f(\mathbf{x}) \leq d\}.$$

In practice, to evaluate f , a uniform sampling of all electrodes is used and the integral is approximated by an appropriate weighted sum. That is, if there are n electrodes and each electrode is sampled with m points \mathbf{s}_{ij} , $i = 1, \dots, n$, $j = 1, \dots, m$, f is approximated by

$$\tilde{f}(\mathbf{x}) = \left(\sum_{i=1}^n \sum_{j=1}^m \frac{1}{m \cdot |\mathbf{x} - \mathbf{s}_{ij}|^{\alpha}} \right)^{-1/\alpha}. \quad (4.10)$$

Besides the length and shape of the electrodes, the parameters d and α affect the size and shape of the ablation zone $I_{\text{zone}}(d, \alpha)$. Namely, the value of α influences the shape of the mask, and d influences its size. That is, for $\alpha \rightarrow 0$, the limit shape is a ball of diameter d , whereas for $\alpha \rightarrow \infty$, the limit shape is the union of all balls of diameter d around all electrode points (see Figure 4.6).

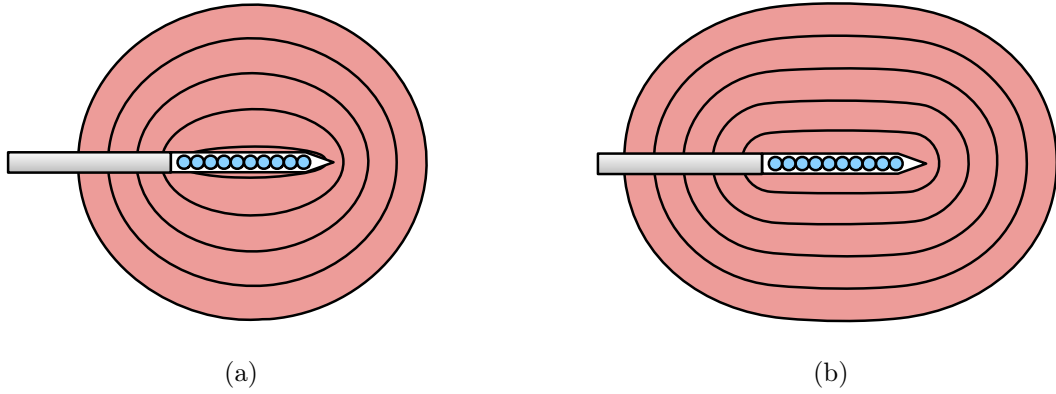


Figure 4.6: Two images of the distance field illustrate the influence of the weight α for fixed-distance iso values. In (a), a low $\alpha = 1$ results in a more spherical shape, i.e., the distance to the electrode's center sample is measured. In (b), a high $\alpha = 25$ results in a shape which is given by a union of balls, i.e., the minimal distance to each sample point is measured.

For any given applicator and given combination of ablation parameters (such as electric power and ablation time), the appropriate parameter values d and α are determined in order to maximize the volumetric overlap between reference and approximated ablation zone. For that, the reference mask I_{sim} is calculated using the simulation described in Section 4.3 and then the optimization problem

$$|(I_{\text{sim}} \setminus I_{\text{zone}}(d, \alpha)) \cup (I_{\text{zone}}(d, \alpha) \setminus I_{\text{sim}})| \xrightarrow{!} \max$$

is solved using the simplex optimization method [125]. To assess the robustness of the parameter fit, different start values for α and d are defined. Figure 4.7 (a) shows the optimization of the ablation zone (Celon ProSurge 150-T30) for following start tuples (α, d) : (2, 2), (3, 3), (4, 4), and (5, 5). All four optimization problems are solved within 60 iterations and lead to the same optimal parameterization: $(\alpha, d) = (3.3, 4.9)$. Figure 4.7 (b) illustrates the progress of the corresponding objective value, i.e. the volumetric overlap. In all four optimization calculations, the volumetric overlap converts to 0.97 within 60 iterations.

The optimal values of d and α are computed for a large variety of ablation configurations, including varying electrode lengths, ablation time, and generator power. The resulting values are stored in a database. This method is also applicable to umbrella-shaped monopolar electrodes by sampling the prong electrodes.

4.5.2 Estimating the Thermal Diffusion of the Vasculature

So far, the presented method allows to estimate the ablation zone in homogenous tissue. However, if the patient individual anatomy is taken into account, the assumption of homogeneous tissue leads to overestimated ablation zones. The major

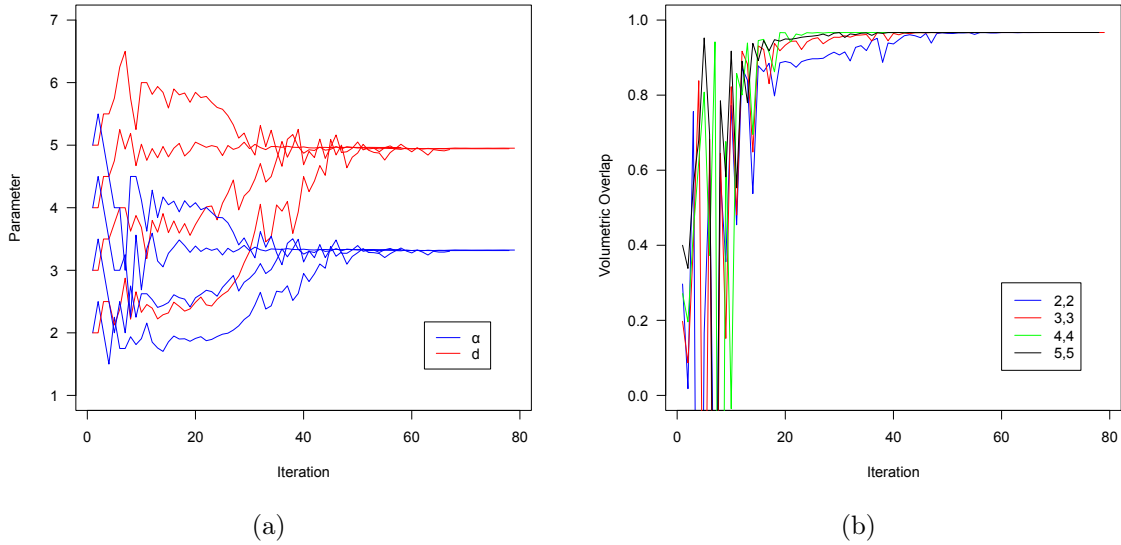


Figure 4.7: Plot (a) shows the optimization of the ablation zone for four start tuples (α, d) : (2, 2), (3, 3), (4, 4), and (5, 5). Plot (b) illustrates the progress of the corresponding objective value.

effect that decreases the size of the ablation zone is the cooling effect of large blood vessels. To take the heat-sink effect into account, an additional distance field from the vessels is calculated. Based on this distance field, the amount of cooling, which affects the thermal heating of the electrodes and thus deforms the shape of the ablation zone, is estimated.

In contrast to the local heat source around the applicator’s electrode, the background is set to a constant heat source and the thermal diffusion of the vasculature, which is caused by the cooling blood flow, is calculated. The resulting diffusion is used to calculate the weighted distance to the vasculature whereas the magnitude of the diffusion gradient is interpreted as the cooling strength. For that, a simplified numerical simulation is used to estimate the space-dependent heat-sink effect independent of the applicator settings. This is done by solving (4.2) (together with the boundary conditions (4.4e) and (4.4f)) where q is now assumed to be a (spatially and temporally) constant heat source. By this, the equation becomes decoupled from (4.1). Also, the material parameters λ and ν are assumed to be constant, which makes the corresponding steady-state equation

$$-\nabla \cdot (\lambda \nabla T) + \nu(T - T_{\text{body}}) = q \quad (4.11)$$

a linear elliptic partial differential equation. The finite element approximation of this PDE can easily be solved in one step. Due to the linearity, the value of the constant heat source q is irrelevant because it simply acts as a scaling parameter.

Technically, the solution of the steady-state equation described above is performed using the full numerical simulation described in Section 4.3, where no applicator is

placed, but rather the value T_{body} is replaced with $T_{\text{warm}} := T_{\text{body}} + q/\nu$ in (4.2) (but not in (4.4e) and (4.5)), and only one very large time step (step size 1000 seconds) is computed. Because the value of q can be chosen arbitrarily, the same holds for T_{warm} . After the solving (4.11), the function g is defined as the normalized steady-state temperature by

$$g(\mathbf{x}) = 1 - \frac{T(\mathbf{x}) - T_{\text{body}}}{T_{\text{warm}} - T_{\text{body}}}. \quad (4.12)$$

In this computation, $T_{\text{warm}} = T_{\text{body}} + 10$ is used, but because T_{warm} only acts as a scaling parameter in (4.11) and this scaling is canceled by (4.12), the function g is independent of the value of T_{warm} . Further, for all \mathbf{x} it is $0 \leq g(\mathbf{x}) \leq 1$, where $g(\mathbf{x}) = 1$ if \mathbf{x} is located inside a vessel, and $g(\mathbf{x}) = 0$ for all \mathbf{x} if there are no vessels present. In particular, large values of g correspond to strong cooling and $g = 0$ corresponds to no cooling. Figure 4.8 (a) shows a single slice of a three-dimensional diffusion field with normalized and inverted values. Contours are drawn with the following thresholds: 1.0 (the vessel), 0.7, 0.6, and 0.3. Figure (b) shows the same slice but with contours based on a scaled Euclidean distance transform. The major difference can be observed in the smoothness of areas containing multiple vessels. This is accordingly illustrated in the scatter plot of the slice by combining the values from the thermal diffusion field with the values from the Euclidean distance transform (see Figure 4.8 (c)). The width in the scatter plot results from the weighted distance which depends on the proximity of multiple vessels. The shape of the plot illustrates the non-linear property of the thermal diffusion field.

4.5.3 Deformation of the Ablation Zone

To estimate the heat-sink effect of the cooling vessels, the function g defined in the previous section is utilized and combined with the weighted distance field of the ablation zone. Formally, the two functions f and g are combined using appropriate transition functions t_1 and t_2 . Because the cooling only decreases the ablation zone size (rather than increasing it), it suffices to perform the additional computation on I_{zone} (where the parameters d and α in the notation are now skipped). By definition, $0 \leq f(\mathbf{x}) \leq d$ on I_{zone} , it is convenient to divide $f(\mathbf{x})$ by d before applying the transition function, because both transition functions then act on the same interval $[0, 1]$. Hence, the modified ablation zone is defined by

$$I_{\text{cool}} = \{\mathbf{x} \in I_{\text{zone}} : t_1(\frac{1}{d}f(\mathbf{x})) + t_2(g(\mathbf{x})) \leq t_1(1) + t_2(0)\}.$$

Note that the threshold has been chosen such that in the case of no vessels ($g(\mathbf{x}) = 0$ for all \mathbf{x}), $I_{\text{cool}} = I_{\text{zone}}$ holds. In numerical experiments, the distances from electrode to simulated coagulation necrosis mask and also from a parallel aligned vessel mask to coagulation necrosis mask are measured. After analyzing the distances for different spacing between vessel and electrode, it heuristically turned out that choosing the arcsin function for both t_1 and t_2 leads to good results. Hence, it is

$$I_{\text{cool}} = \{\mathbf{x} \in I_{\text{zone}} : \arcsin(\frac{1}{d}f(\mathbf{x})) + \arcsin(g(\mathbf{x})) \leq \frac{\pi}{2}\}. \quad (4.13)$$

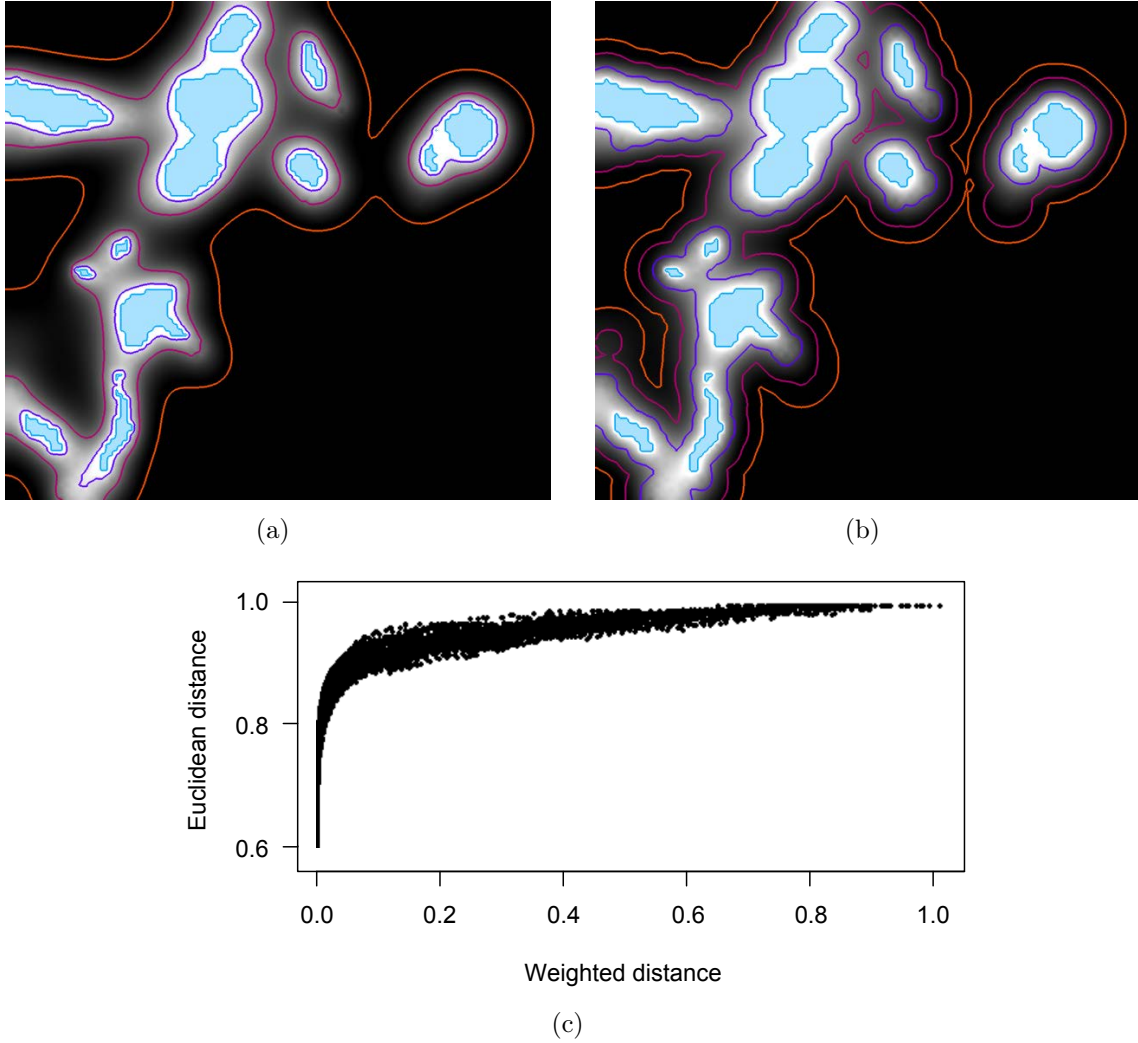


Figure 4.8: Image (a) shows the normalized (and inverted) thermal diffusion of the vasculature with iso contours, and image (b) with contours from a scaled Euclidean distance transform. Image (c) illustrates the scatter plot of the Euclidean and weighted distance (thermal diffusion) field histograms.

In this section, it is described how the approximation of the ablation zone is modeled. By sampling the applicator’s electrodes and calculation of a weighted distance field, the ablation zone can be fitted to the resulting coagulation necrosis mask of a complex numerical simulation. Heat-sink effects are estimated by solving the thermal diffusion of the vasculature and the combination with the weighted distance field.

If, in addition, the applicator is internally cooled, this cooling can be taken into account in the same way as the vessel cooling. However, computation and usage of the combined function g for vessels and cooled applicator is not possible, because

for varying applicator placements, the combined cooling mask would change. Real-time processing could no longer be achieved, because the computation of g involves the solution of a partial differential equation. However, a cooling field g_a for the cooled applicator can be *independently* computed from the cooling field g_v for the vessels in the same manner as described above (see Section 4.5.2). When the applicator is moved, the according affine transformations are performed to g_a , and the approximative ablation zone is then given by

$$I = \left\{ \mathbf{x} \in I_{\text{zone}} : \arcsin\left(\frac{1}{d}f(\mathbf{x})\right) + \arcsin(g_v(\mathbf{x})) + \arcsin(g_a(\mathbf{x})) \leq \frac{\pi}{2} \right\}.$$

Due to the rotational symmetry of the shaft, the function g_a is stored in a one-dimensional lookup table perpendicular to the shaft. Figure 4.9 illustrates the complete approximation model for a cooled bipolar applicator and a thermal field of the cooling vasculature.

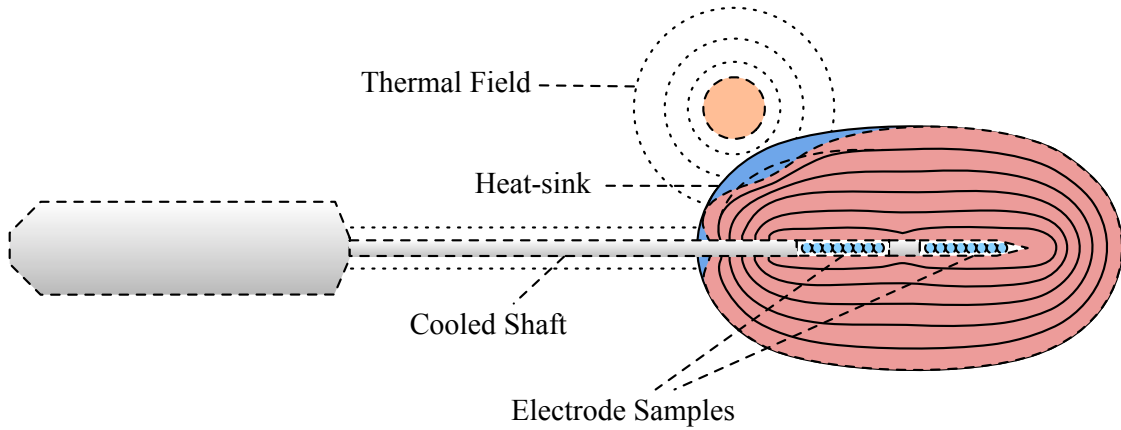


Figure 4.9: Both electrodes of an internally cooled bipolar RF applicator are sampled. The corresponding weighted distance field is illustrated by isoline contours. The thermal fields of the blood vessels and the cooled applicator shaft decrease the ablation zone (blue areas).

4.5.4 Application

In comparable applications, the typical workflow is to load the patient data set, perform segmentation algorithms to classify structures of interest, and place virtual RF applicator models. Patient-independent ablation zones, such as ellipsoids, are available with the corresponding applicators, otherwise patient-specific numerical simulations have to be performed for a determined probe position. For the patient-dependent real-time visualization of approximated ablation zones, the same preprocessing steps are required.

4.5.4.1 Preprocessing

In order to approximate the ablation zone in corporation with the heat-sink effects, local vessels in the target region have to be segmented. This can be done within the workflow as discussed in the previous chapter. Segmentation of the tumor is not necessary for the approximation method, but helpful for visualization. After processing of the vessel segmentation, the thermal diffusion of the vasculature is estimated using the vessel mask as image input as described in Section 4.5.2. Even though a complex PDE has to be solved, the numerical simulation calculates the thermal field in less than 5 seconds (for a ROI of the same size). Once the described preprocessing steps are performed, virtual applicator models can be added to the scene and corresponding ablation zones are visualized.

4.5.4.2 Calculation of the Ablation Zone

To calculate the ablation zone in real-time, the high performance of the graphics hardware is exploited. Technically, a modular shader framework, which is presented in Chapter 7 of this PhD thesis, is used for both, 2D slice and volume rendering. For every RF applicator, the corresponding electrode is represented as a finite number of electrode samples. A rendering shader calculates whether each fragment's spatial position in world space is inside or outside of the ablation zone, by sampling the applicator's electrode. For that, Equation (4.9) (or rather its approximation (4.10)) is evaluated taking the corresponding predefined distance d and weight α into account. Further parameters include the spatial position and the orientation of the RF applicator as well as parameters describing the electrode's geometry. Algorithm 1 illustrates the calculation of the weighted distance field per fragment. The final value is stored in a global data structure of the shader. To facilitate combined ablation zones from multi-applicator settings, the weighted distance field is calculated by sampling all active electrodes.

After calculating the weighted distance field, the cooling effect of the blood vessels is estimated. For all fragments classified as ablation zone, the cooling weight is fetched from the thermal field, represented as scalar volume, and the cooled ablation zone mask is calculated by evaluating Equation (4.13). Subsequently, fragments which belong to the ablation zone, but are cooled under the temperature threshold are tagged as cooled ablation zone and cached in the data structure for later visualization.

4.5.5 2D Slice Visualization

For planning of RFA, 2D slice renderings of volumetric data are commonly used in clinical practice. Thus, visualization methods to overlay the ablation zone onto the anatomical image data such as a pre-interventional CT image are presented. Although displaying of orthogonal projections is the clinical method of choice, few authors in the field of RFA planning focus on comprehensive 2D visualization [171]

```

input : electrode parameters, thermo field
output: ablation zone mask per fragment
1 distance  $\leftarrow$  0;
2 for electrode :  $e \in$  electrodes do
3   | distancee  $\leftarrow$  0;
4   | samplee  $\leftarrow$  (0, 0, 0);
5   | for  $s \leftarrow 0$  to electrode samples do
6   |   | samples  $\leftarrow$  calcSample(s, paramse);
7   |   | dists  $\leftarrow$  distance(samplef, samples);
8   |   | distancee  $\leftarrow$  distancee +  $\frac{1}{\text{maxpow}(\text{dist}_s, \alpha)}$ ;
9   | end
10  | distance  $\leftarrow$  distance + distancee;
11 end
12 distance  $\leftarrow$  pow(distance-1,  $\alpha^{-1}$ );
13 ablationZone  $\leftarrow$  step(distance, d);
14 ablationZone  $\leftarrow$  calcCooling(distance, d, thermofield);

```

Algorithm 1: Calculation of the approximated ablation zone mask per fragment utilizing the weighted distance field and the thermal field of the blood vessels.

in contrast to 3D surface [152] or volume renderings [170]. To display the ablation zone, the following visualization methods are presented:

Volumetric overlay. The most common representation of image masks are volumetric overlays on top of anatomical images. Similarly, the approximated ablation zone is visualized as an overlay combined with the virtual applicator model (see Figure 4.10 (a)). For every fragment classified as ablation zone, a specified color and alpha value is blended with the underlying anatomical image. Different color and alpha values may be assigned to fragments which are under-ablated due to the heat-sink effect, that is, fragments that belong to $I_{\text{zone}} \setminus I_{\text{cool}}$. Additionally, to emphasize tumor voxels which are not covered by the ablation zone, these voxels can be highlighted with a special color (see Figure 4.10 (b)). Technically, the cached values in the global data structure are directly mapped to fragment colors and alpha values, respectively.

Distance contours. Another visualization method to represent the ablation zone is the display of contours [118]. They are utilized to draw isolines with uniform contour interval in order to emphasize the topography of the weighted distance field, particularly if the ablation zone is deformed due to the presence of blood vessels. The advantage of this method is that the visualized topography leads to an intuitive understanding of the involved heat-sink effects. For that, the weighted

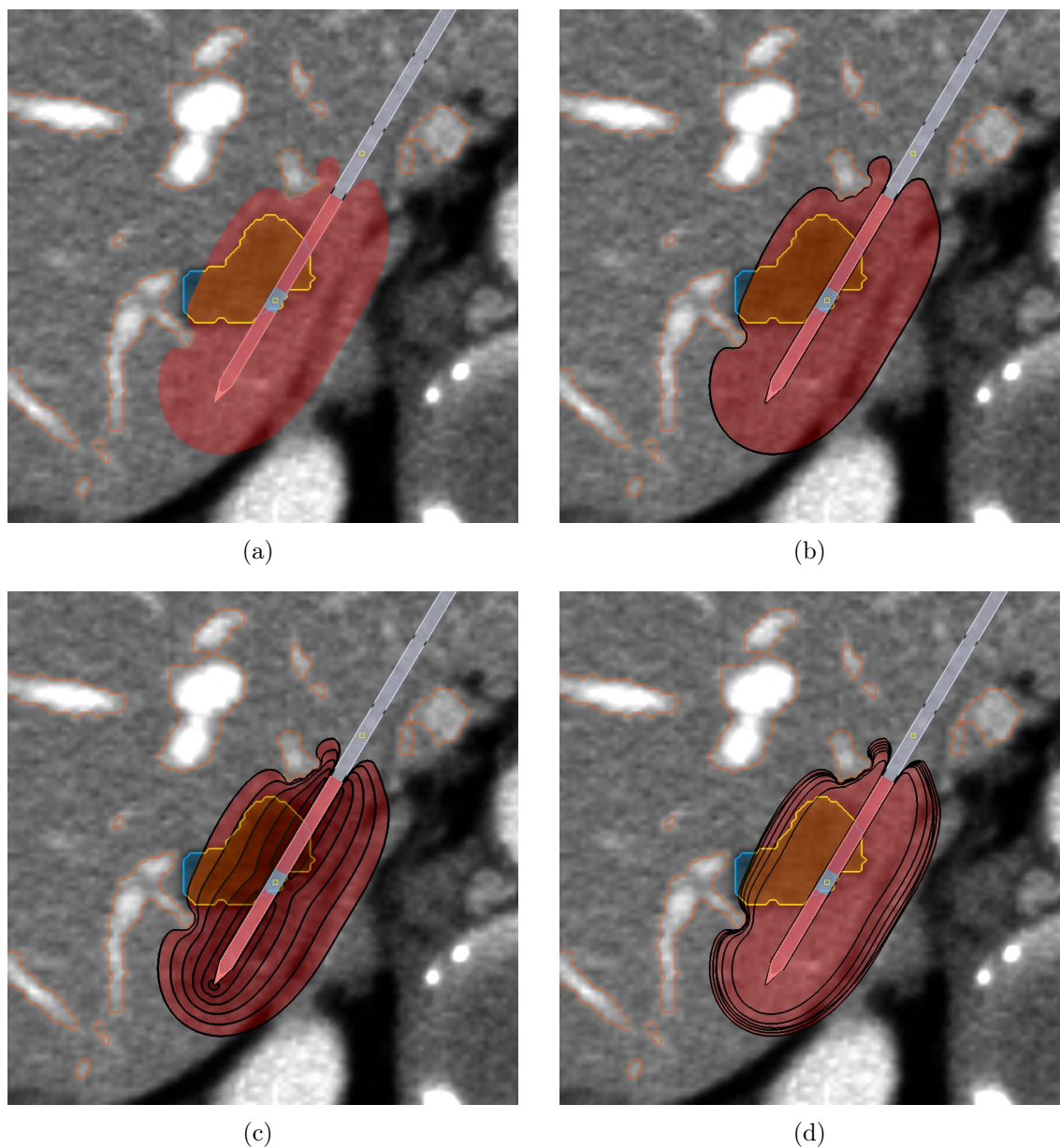


Figure 4.10: Four projected slice visualizations of a bipolar RF applicator with corresponding approximated ablation zone (20 electrode samples, 30 watt generator power). In (a), the ablation zone is displayed as volumetric overlay and in (b) with an additional contour. Uniform isolines represent the topography of the weighted distance field (c). The multi-parameter isoline visualization shows the progress of 1, 2, 4, 8, and 16 minutes of ablation duration (d).

distance field is calculated in the 4-neighborhood of the current fragment. The contour for a specific distance value is extracted by detecting the edge from the neighborhood utilizing a dilatation operation. Multiple contours are drawn by taking varying distance values into account. Optionally, the isolines may be combined with the volumetric overlay, or different colors may be used for different isolines. Figure 4.10 (c) shows five uniform isolines of the distance field combined with the proposed overlay visualization.

Multi-parameter contours. Inspired by the uncertainty visualization of Praßni et al. [139], a further contour visualization method is proposed to represent multiple parameters at the same time. Instead of drawing the contours at different distances to represent the topography, every contour is calculated from an independent weighted distance field. The parameterization of the multiple distance fields may be chosen according to the temporal progression or varying initial generator power of the numerical simulations. Thus, by drawing multiple contours together, the temporal progression of the coagulation necrosis with fixed generator power can be visualized. Analogously, multiple contours can also be utilized to visualize multiple ablation zones with varying generator power together (for a determined ablation duration). Technically, contours from the weighted distance field have to be calculated multiple times, taking varying parameters for the distance and the weight into account. Figure 4.10 (d) shows a multi-parameter isoline visualization. Five ablation durations of 1, 2, 4, 8, and 16 minutes are displayed together. The advantage of this method is that a simultaneous exploration of multiple ablation settings is possible in order to optimize the electrode placement.

4.5.6 3D Volume Visualization

In addition to the 2D slice visualization, the approximated ablation zone is also combined with a 3D volume rendering of the surrounding anatomy. The following requirements are determined:

- A combined visualization of ablation zone and risk structures is needed in order to explore the cooling effects and their relation to the patient's anatomy.
- The shape of the ablation zone should be emphasized to allow recognition of spatial relations.
- The ablation zone has to be calculated within real-time frame rates to allow smooth interaction with the volume rendering.

The liver parenchyma is visualized in a transparent fashion to allow a clear view of the liver vessels, which are emphasized utilizing the automatically determined transfer function (see Section 3.5.1). The benefit of the anatomical volume visualization is a fast recognition of potential risk structures such as the liver vessels, which have

to be protected from harm, combined with the approximated ablation zone. Because physicians like surgeons or gastroenterologists are not as familiar with slice representations as radiologists, the volume rendering may be particularly helpful for them to intuitively recognize the spatial relations [85].

Technically, the ablation zone is calculated with the same rendering shader used for the 2D slice rendering, although the composition is differently parameterized according to the accumulation of the alpha values for volume rendering. Also, tumor voxels outside the ablation zone are emphasized by alternating colors. In order to represent internal structures such as the colored tumor, the ablation zone may be rendered in a transparent fashion. The drawback of the transparent rendering is that the shape of the ablation zone, and thus the constrictions due to the cooling vessel, can not be recognized due to missing shading information.

To emphasize the shape of the ablation zone, volume shading is utilized. The gradients required for the shading model are calculated on-the-fly using central differences [72] from the weighted distance field. Thus, the distance field has also to be calculated for the 6-neighborhood of every sample. To reduce the additional calculation time, the electrodes are down sampled up to one fifth of the original samples in the neighborhood, resulting in a triple increase of the rendering speed. The resulting loss in shading quality is negligible (see Figure 4.11 (a) and (b)). With full sampling (20 samples along the electrode and $6 * 20$ samples for the neighborhood), 5 fps are

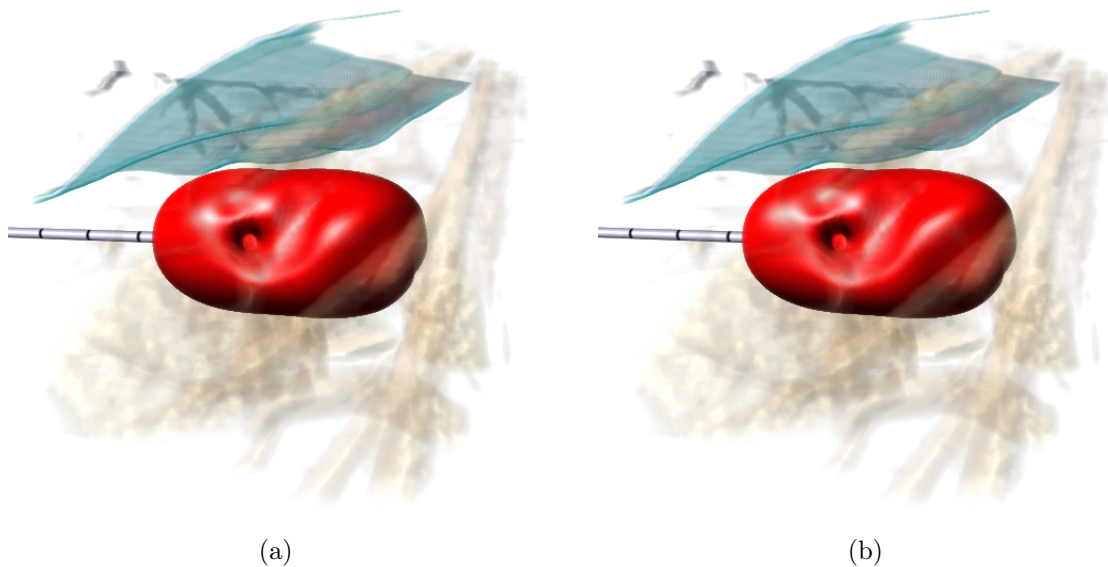


Figure 4.11: Image (a) shows the full sampling (20 samples along the electrode and $6 * 20$ samples for the neighborhood, 5fps) of a 512×512 pixels rendering. Image (b) shows a rendering with reduced neighborhood samples for shading calculation ($6 * 4$ samples for the neighborhood, 15-16 fps). Only negligible differences around the highlights are visible.

measured rendering a region of interest of 110^3 voxels and an image resolution of 512×512 pixels on an ATI Radeon HD 5870. With downsampling the neighborhood to 4 samples per neighbor, 15-16 fps are measured (36 fps without shading, 350 fps without ablation zone calculation).

The advantage of the shaded rendering is the clear representation of the ablation zone's shape. In order to emphasize internal structures of the ablation zone (e.g., the tumor), boundary and silhouette enhancement [141] is utilized. In Figure 4.12 (a-d),

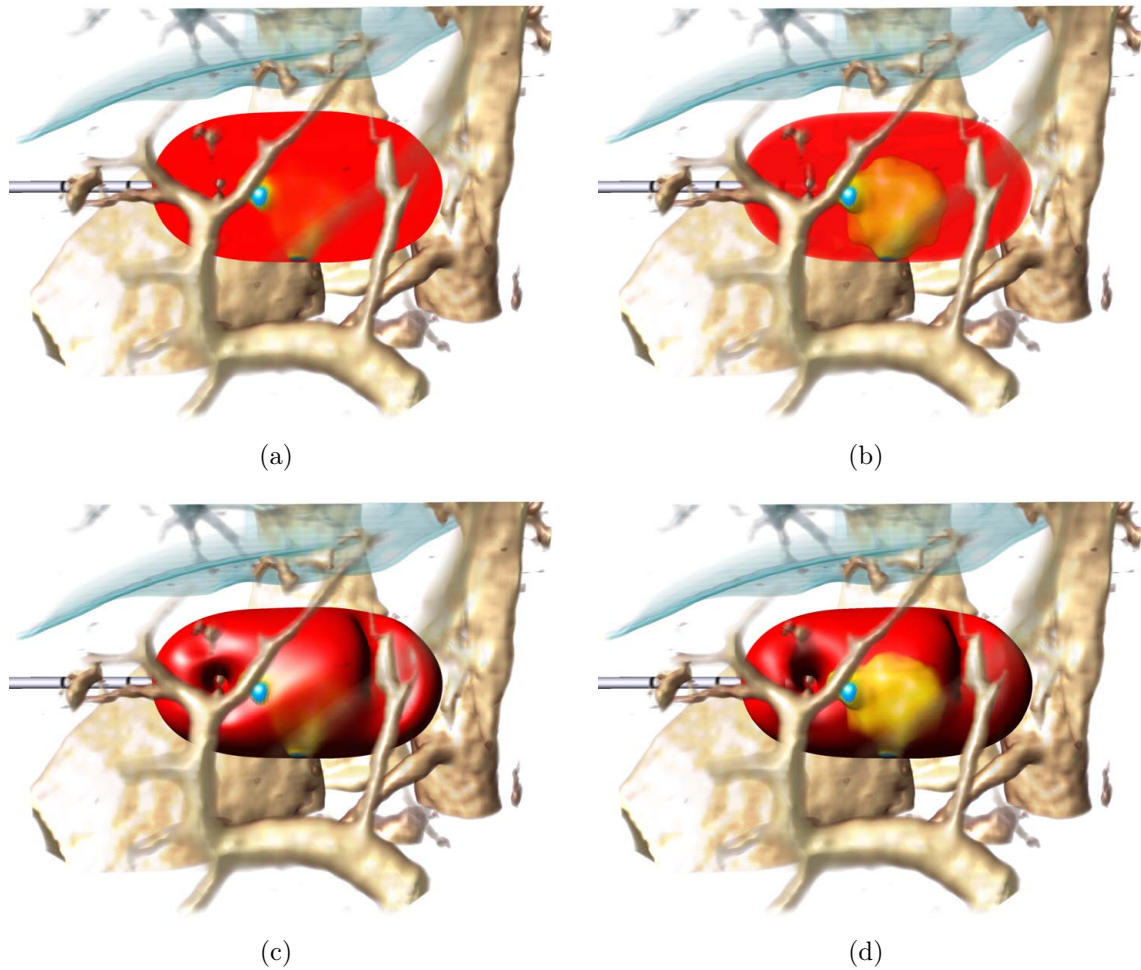


Figure 4.12: Comparison of four volume visualization techniques of the approximated ablation zone. In (a), the ablation zone is rendered without shading, allowing the user to examine the tumor overlap. Image (b) shows a rendering in a transparent fashion in order to additionally display the tumor inside of the ablation zone. In (c) shading is enabled, which results in a clear representation of the the ablation zone's shape. In order to emphasize internal structures, boundary and silhouette enhancement is utilized (d).

the advantage of the enhancement is illustrated. In contrast to the simple rendering, the ablation zone as well as the surrounded lesion can be displayed together without loss of spatial information.

4.6 Results

The goal of the proposed approximation methods is to estimate the ablation zone in real-time as accurate as possible. The accuracy is measured by comparison of both methods with the numerical simulation. Further, feedback from an informal user study with experienced medical experts is presented.

4.6.1 Comparison with the Numerical Simulation

In order to estimate the accuracy of both approximation methods, the ablation zones are compared with the coagulation necrosis masks from numerical simulations in complex vascular situations, extracted from ten interventional data sets. For each case, the simple ellipsoidal ablation zone and both approximation methods are compared with coagulation necrosis mask of a complex numerical simulation. For that, three-dimensional volume masks are reconstructed from slice representations of the ellipsoidal and approximated ablation zones. The same image size as the computation domain of the numerical simulation is chosen. In all cases, bipolar applicators are placed (Celon ProSurge 150-T30TM applicator, active zone length 30 mm, isolator length 3 mm, radius 0.9 mm). The coagulation necrosis masks are simulated for an ablation duration of 16 minutes and a generator power of 30 W. The size of the computation domain is set to $65^3 mm$ (with a typical voxel size of around $0.7 \times 0.7 \times 1.0$ a resolution of approx. $92 \times 92 \times 65$ is defined), and the times for the calculation are between 30 and 50 minutes.

The resulting ablation zone masks are compared utilizing following metrics: volumetric overlap, Dice coefficient [49], and Hausdorff distance [149], i.e., the maximum surface distance of the masks in millimeter. The results are reported in Figure 4.13. In the processed cases, the median Dice coefficient is 0.88 and the median volumetric overlap is 0.83, indicates a good correlation of the GPU-based approximation with the numerical simulation considering a speed up of the calculation time of up to 100,000. Dice coefficient and volumetric overlap after fitting the weighted distance field to the numerical simulation mask without consideration of the vessels are 0.99 and 0.97, respectively. Obviously, the greatest approximation error is introduced by incorporating the heat-sink effect of the blood vessels, which depends on the number of nearby vessels. Besides the promising results, the validation of the numerical simulation is subject of ongoing research [3, 178]. The masks from the lookup table-based approximation and ellipsoidal ablation zone are also compared with the numerical simulation. It is observed that the GPU-based method has higher median Dice coefficient as well as volumetric overlap, and smaller median Hausdorff distance than the other two methods. Interestingly, the accuracy of the lookup table-based

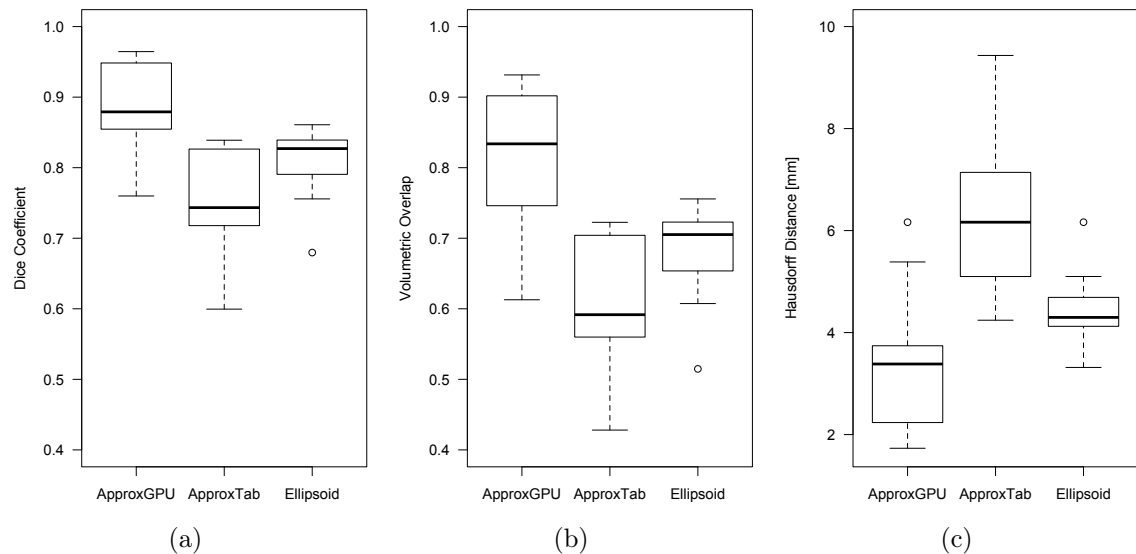


Figure 4.13: Plot (a) represents the averaged Dice coefficients from ten simulation masks with corresponding GPU-based approximation (ApproxGPU), lookup table-based approximation (ApproxTab), and ellipsoid masks, respectively. Plot (b) shows the averaged volumetric overlap and plot (c) the averaged Hausdorff distances in millimeter.

method appears to be smaller than the ellipsoidal ablation zone although the vasculature is considered. One reason is related to the systematic overestimation of the table-based ablation zone toward the tip and the shaft of the applicator and if multiple vessels are present. Second, the ellipsoidal ablation zone clearly underestimates the size of the ablation zone at the tip and toward the shaft, respectively, and overestimates the the maximal extent at the center, independently of the surrounding vessels (see Figure 4.14). This is mirrored in the high minimal Hausdorff distance and the low interquartile variance. Figure 4.14 shows the ablation zone of a bipolar RF applicator represented as simple ellipsoid (a), calculated with the lookup table approximation (b), calculated with the GPU-based distance field approximation (c), and calculated with the numerical simulation (d). To ease visual comparison, all ablation zones are represented with similar contour renderings. Figure 4.15 shows the corresponding volume renderings.

4.6.2 Expert Evaluation

The proposed methods were presented to three experienced interventional physicians. They used the application to retrospectively plan RF ablation of liver tumors on real patient data sets. The clinicians stated on the value of the method for planning RFA, particularly for situations in which large vessels are located in the vicinity of the target lesion or if multiple bipolar electrodes are placed around the le-

sion. In such situations, estimating the ablation zone using alternative methods such as mental suggestion or visualization of simple ellipsoids is challenging. Although mental planning of the RFA treatment by the physician is clinically the method of choice if no planning software is available, a high amount of expertise is required to take the patient-individual anatomy into account. Furthermore, the clinical experts

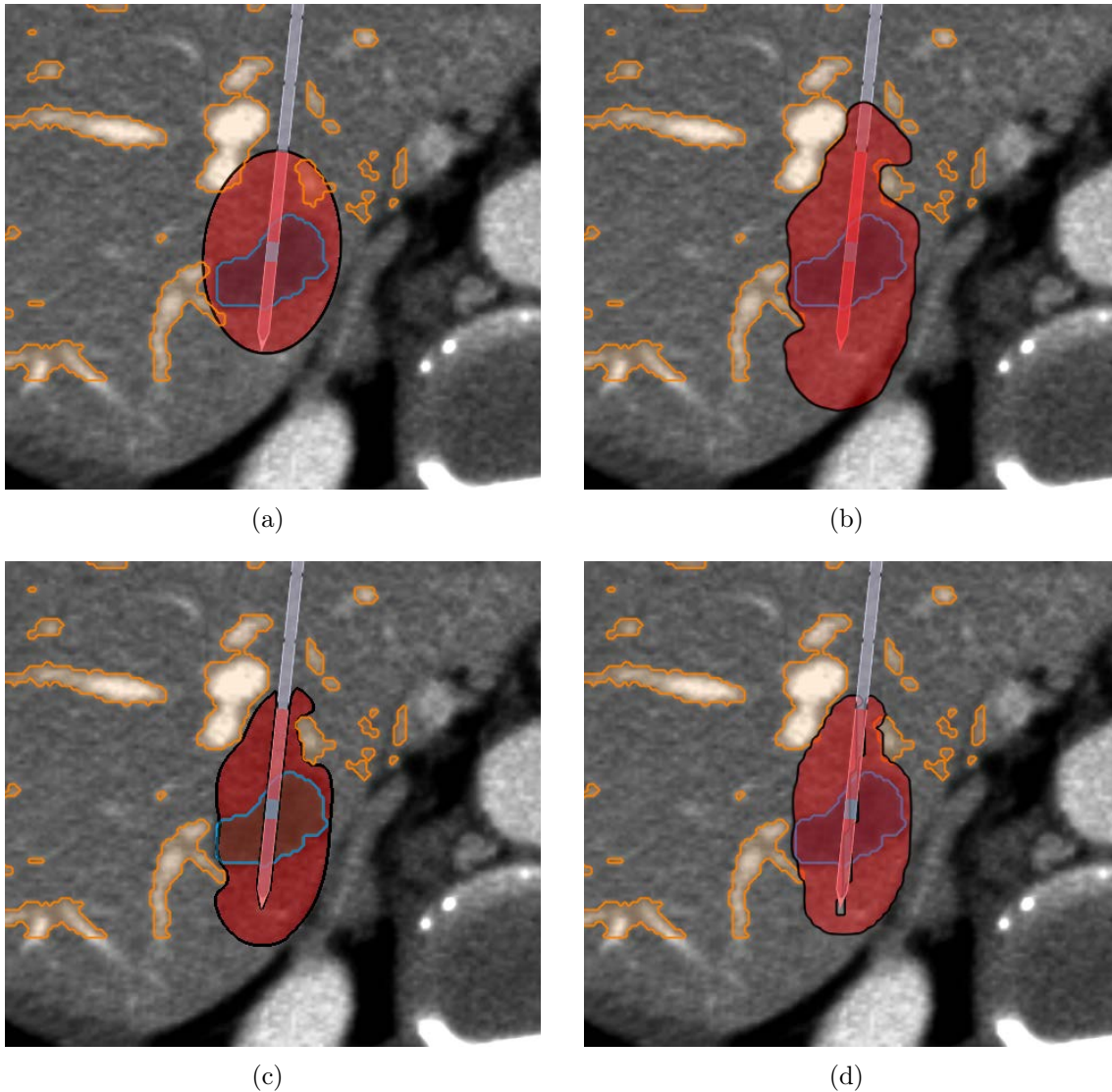


Figure 4.14: Four slice projections with similar visualization parameters of a bipolar RF applicator (Celon ProSurge 150-T30TM, 30 watt, 15 minutes). In (a), the ablation zone is represented as simple ellipsoid. Image (b) shows the approximation method based on the lookup table, and image (c) the approximation method based on weighted distance fields. In (d) the corresponding 60°C thresholded coagulation mask is calculated with the numerical simulation.

explained that the value of the ellipsoid is questionable because heat-sink effects are not considered. In contrast, they stated that the approximated ablation zone looks much more realistic than the ellipsoid and that they would trust the visualization of the ablation zone. Principally, they would prefer the numerical simulation to visu-

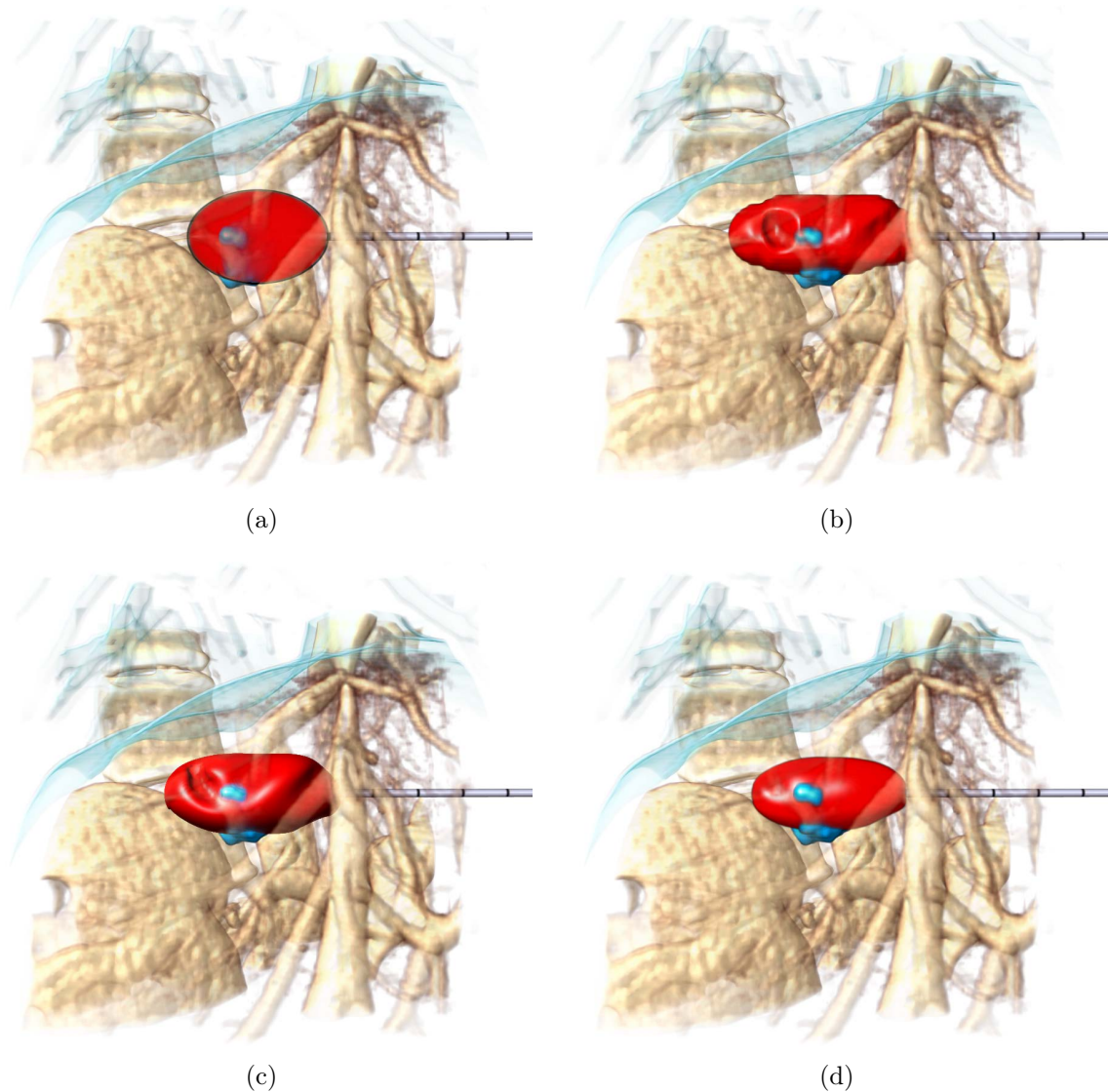


Figure 4.15: Four volume renderings with similar visualization parameters of a bipolar RF applicator (Celon ProSurge 150-T30TM, 30 watt, 15 minutes). In (a), the ablation zone is represented as simple ellipsoid. Image (b) shows the approximation method based on the lookup table, and image (c) the approximation method based on weighted distance fields. In (d) the corresponding 60°C thresholded coagulation mask is calculated with the numerical simulation.

alize the expected ablation zone incorporating the cooling blood vessels. However, due to the high computational effort, which is too time-consuming for clinical use, the approximation was judged as a highly useful method for planning RFA. Also, the medical experts explained that the proposed method is valuable to support inexperienced radiologists in interactively estimating the expected size and shape of the coagulation necrosis and thus find an optimal trajectory to the target volume under consideration of relevant risk structures.

4.7 Discussion and Conclusions

In this chapter, two methods to interactively approximate the ablation zone are presented, which incorporate the heat-sink effect of blood vessels, and assist physicians in pre-interventional RFA planning. The first method is based on a geometric reconstruction of pre-computed numerical simulations, which are stored in a lookup table. The method is based on the originally published work of Kröger et al. [97]. In their approach, the ablation zone is parameterized by a large number of pre-calculated 2D reference configurations, stored in a lookup table. A reference configuration is a simplified two-dimensional setting, whereas a vessel of infinite length is assumed to be parallel to the applicator’s electrode. The approach presented in this work is an advancement of the original surface mesh-based lookup table approach. The lookup table is extended to a 3D setting, taking the length of the active zone into account. In contrast to the original method, the ablation zone is calculated as an image mask instead of representing the cooling effects onto a surface mesh of the tumor. In the case of 2D slice visualization, interactive frame rates are achieved.

To overcome the limited performance and reconstruction issues of the first method, the second approach utilizes weighted distance fields to approximate the ablation zone of different RF applicator models on the GPU. A weighted distance field is utilized, which is fitted to the coagulation necrosis mask retrieved from a numerical simulation in homogeneous tissue under consideration of the biophysical heat transport. The approximated ablation zone is combined with a thermal diffusion field, describing the heat transport of the vasculature in order to estimate the heat-sink effects of nearby blood vessels. Because the parameters describing the ablation zone are determined for homogeneous material parameters (i.e., patient independent) and the thermal field is calculated from the segmented vessel mask in a pre-processing step, the approximation of the resulting coagulation necrosis can be processed in real-time utilizing the GPU.

In contrast to similar work, the ablation zone is not represented as a deformed ellipsoid. Instead, it is approximated utilizing a weighted distance field, retrieved from a numerical simulation. In other work, the heat-sink effect is modeled by translating the vertices of the ellipsoid based on the proximity of large liver vessels. In this approach, the thermal diffusion of the vasculature is calculated and the ablation zone modified by combining the distance field and the thermal field based on heuristics.

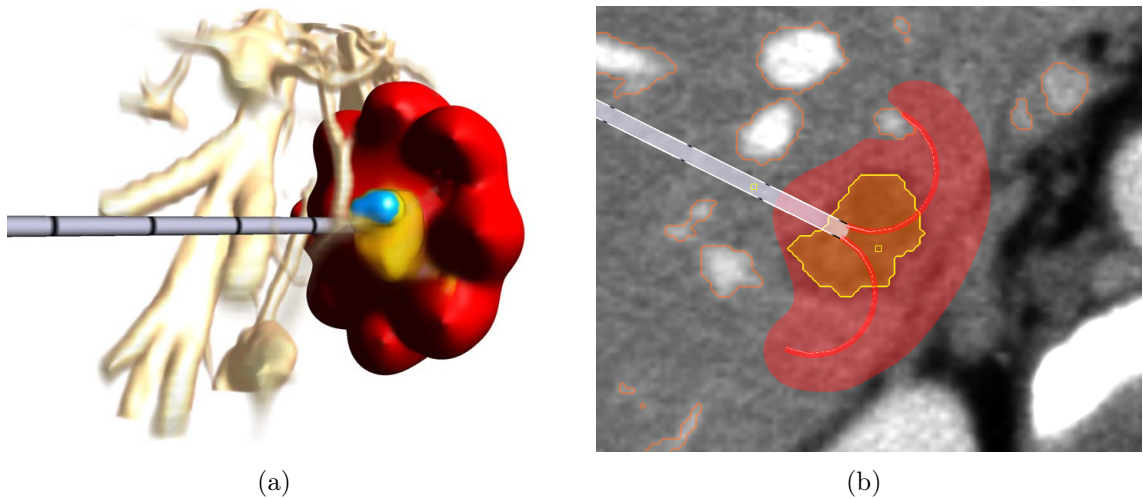


Figure 4.16: Volume rendering of an umbrella-shaped monopolar RF applicator (a), and corresponding visualization of a single slice in plane with the applicator's shaft.

In the lookup table-based approach of Kröger et al. [97] and also in the above mentioned first method, the vascular cooling is calculated under consideration of the Euclidean distance from the electrode to the blood vessels, the vessel radii, and the angle between the direction under consideration and the direction in which the vessel center is located. Thus, the ablation zone is individually calculated for every vessel segment, resulting in an independent cooling effect (see Figure 4.5).

In contrast to related approaches, the combined ablation zone of multiple RF applicators as well as the estimation of different electrode types, such as the umbrella-shaped applicator, is provided by sampling the related electrode geometry and pre-calculation of appropriate weighting parameters (see Figure 4.16). Furthermore, advanced visualization techniques such as multi-parameter contour drawing or shaded volume rendering in 2D and 3D on interactive frame rates is presented.

In the comparison of the approximation with the numerical simulation, it is shown that similar ablation zone masks can be calculated, even in complex vascular situations, for both monopolar and bipolar electrodes and for multiple RF applicator configurations. Several limitations result from the substantial simplifications of the proposed method. The most important limitation is that the approximation is only indirectly related to the biophysical principles. In situations where cooling vessels interrupt the thermal transport of the electrodes, the estimated shape of the ablation zone may be incorrect (cf. Hausdorff distances). However, the major benefit of the approach results from the real-time performance in both 2D and 3D, and the independence from the duration of the estimated ablation procedure. Visualizing a coagulation necrosis by solving numerical simulations results in high computation times ranging from a few minutes to several hours depending on the resolution of the

computational domain (particularly the required high-resolution domain for representing umbrella-shaped electrodes), the ablation duration (5-30 minutes), and the chosen calculation precision. Furthermore, utilizing contour visualization, multiple parameters such as varying ablation duration can be represented together.

For future work, a retrospective user study with medical experts should be conducted to evaluate the clinical value of the method using real patient data. To estimate the benefit, RF applicators will be placed in pre-interventional images and the ablation zones will be compared with the outcome after ablation. A further research direction is the integration of the approximation model into an automatic path proposal method for RF applicator placement. Besides other optimization constraints (e.g., the distance to risk structures), the performance of the proposed method will facilitate a fast estimation of the tumor overlap in order to determine optimal needle placements, automatically. First results are reported at the European Congress of Radiology [15].

This chapter is in part based on the following publications:

- **C. Rieder**, I. Altrogge, T. Kröger, S. Zidowitz and T. Preusser. Interactive Approximation of the Ablation Zone incorporating Heatsink Effects for Radiofrequency Ablation. In: *Proceedings of CURAC*, pp. 9-12, 2010
- **C. Rieder**, T. Kröger, C. Schumann and H. K. Hahn. GPU-Based Real-Time Approximation of the Ablation Zone for Radiofrequency Ablation. In: *IEEE Transactions on Visualization and Computer Graphics (Proceedings Visualization 2011)*, 17, 12, pp. 1812-1821, 2011.

*Medicine is a science of uncertainty
and an art of probability.*

(Sir William Osler)

5

Workflow for Automatic Alignment of Interventional Images

TO verify the treatment success of the RFA therapy, reliable alignment of the pre- and post-interventional images is required. In this chapter, a workflow for automatic alignment of interventional CT images is presented. Based on segmentation masks of tumor and coagulation, the workflow enables an automatic rigid registration algorithm to perform at least as accurately as experienced medical experts, but with significantly less time.

5.1 Introduction

To evaluate the success of the RFA therapy, pre- and post-interventional images are typically acquired to visually compare tumor and coagulation. Due to the varying acquisition times and accordingly different coordinate systems of the pre- and post-interventional images, a registration is required to allow a fused visualization and a quantification of possible local tumor recurrence. Because of the soft-tissue property of the liver, global organ deformations can only be completely compensated with a (nonrigid) deformable registration. However, the use of a nonrigid registration is critical because nonrigid transformations alter the image data. This could lead to volume changes, which make a robust quantification impossible. Only rigid transformations leave the images as acquired, which is necessary for clinically acceptable quantification and verification. Another drawback of a deformable registration is the application of manual correction by the physician, because the resulting transformation after registration is difficult to understand. Heizmann et al. [79] describe in their study that a rigid alignment of the preoperative data can give satisfactory accuracy in a region of interest (ROI) in spite of inevitable deformation of the liver parenchyma. Thus, a rigid registration in a local ROI around the tumor (with diameter less than 30 mm [122]) is considered sufficient for aligning pre- and post-interventional CT images.

A further challenge is the difficulty to align data sets with different disjunctive structures. Regarding typical data obtained for RFA, lesion and coagulation may differ from each other in size, shape and position. The subsequent step after alignment is the comparison of the lesions's geometrical properties. To prevent an automatic registration algorithm from matching of tumor and coagulation, it has to be ensured that both, the tumor as well as the coagulation, are not considered for similarity calculation. Instead, only anatomical structures around the lesions, such as vessels and liver parenchyma, are taken into account.

In this PhD thesis, a workflow for automatic alignment of pre- and post-interventional images based on segmentation masks of tumor and coagulation is proposed. The presented workflow is embedded in a clinical software assistant, which guides the physician in performing the necessary processing steps for comparison of the image data. Based on the aligned lesion masks, advanced visualization and robust quantification techniques can be utilized to facilitate reliable assessment of the therapy success.

The outline of this chapter is as follows: In Section 5.2, related works in the field of registration of soft-tissue images, particularly interventional images, and are discussed. Section 5.3 explains the proposed workflow steps including lesion segmentation, automatic registration, manual registration and result visualization. In Section 5.4, the evaluation method for assessing the accuracy of the proposed method is outlined. The results of the conducted evaluation of 41 RFA cases are presented in Section 5.5, and the conclusion with a discussion of the proposed methods are illustrated in Section 5.6.

5.2 Related Work

Manual rigid registration of medical image data has been proposed for different modalities. An early work presents an interactive technique for registration of three-dimensional images [136]. Using simple mouse interactions for translation and rotation, the physician is able to align the data sets. The method is validated for PET, SPECT, MRI and CT brain studies.

For soft-tissue software assistance, Carillo et al. [41] utilize a manual and semiautomatic rigid registration method to align MR liver images acquired before and after RFA therapy. To assess the accuracy of the proposed methods, distances between iso-contours in selected regions of interests are measured in 2D, and a registration error is estimated in 3D. The authors report a registration accuracy of approximately 3 mm, which is the typical voxel size of their data, for both a manual and a mutual information-based method.

Weihusen et al. [179] describe a software tool which supports visual comparison of pre- and post-interventional RFA data sets. For the comparison, the data sets have to be aligned by the physician utilizing a manual rigid registration procedure [183]. To ease the comparison, a color coding scheme within a 3D surface rendering is utilized. However, the authors do not provide a clinical evaluation of the method.

A feasibility study for evaluation of RFA using registration of pre- and post-operative CT images is presented by Fujioka et al. [60]. An automatic rigid registration method is used to align pre- and postoperative CT images. Additional landmarks may be segmented in both data sets in order to improve the registration result. They conclude that the registration of CT images is a feasible method for evaluation of RFA therapy of primary liver tumors. In a subsequent study, the presented registration method is successfully used to quantify the minimal ablative margin for RFA of Hepatocellular Carcinoma lesions between 2 and 5 mm in diameter to prevent local tumor progression [90]. The authors state that the registration method is valuable for quantitative assessment of the ablation therapy.

Giesel et al. [64] evaluate the feasibility of a rigid registration of pre- and post-RFA images to facilitate early detection of residual disease. Compared with conventional interpretation using mental registration, they state that computer processing may have a more objective and exact view. Several major problems are also outlined. The problem of respiratory motion, whereas organs can significantly alter their shape and location, caused mis-registration and hampered image fusion. Also, organ shift and shrinkage were encountered, as thermal lesions tend to shrink after RFA.

To compensate global deformations of the liver, Charnoz et al. [43] register the segmented vascular tree of the liver for the follow-up of tumor evolution. However, registering the vascular system alone does not take any information regarding deformation of the liver surface into account. Niculescu et al. [128] present a liver surface-based non-rigid method for tracking the tumor across pre- and post-interventional CT images for the assessment of the tumor response after RFA. The volumetric deformations are modeled utilizing a linearly elastic finite element method. However,

surface matching is in most cases not accurate enough when dealing with lesions in the center of the liver.

In a recent work, Kim et al. [88] evaluate a method for nonrigid registration of pre- and post-interventional CT data sets. 31 cases are evaluated to determine the effect on the safety margin assessment after RFA of the liver. The registration accuracy is validated by setting pairs of corresponding landmarks on the pre-interventional data sets and registered post-interventional data sets, and calculating the average distances. The authors report a mean difference of 1.3 mm and conclude that the registration method is an accurate and useful technique for assessing the safety margin after RFA. Because smoothness and volume preservation of the deformation is not reported, assessing the quality of the resulting transformation is not possible.

For further reading, the survey of Viergever et al. [174] may be a starting point. A survey of medical image registration on graphics hardware is presented by Fluck et al. [56].

5.3 Registration Workflow

To allow reliable and effective assessment of the RFA therapy, a registration workflow is presented. In the initial workflow step, segmentation masks from both, the pre-interventional tumor and the post-interventional coagulation are interactively created by the physician (see Figure 5.1). In the next step, the data sets are automatically aligned in a region of interest around the lesion masks to compensate spatial and temporal organ deformations. To post-adjust and quantify the resulting transformation, a manual registration method is also included. In the final step, the lesions are visually and quantitatively compared using image-fusion of the registered data sets.

5.3.1 Lesion Segmentation

The initial preprocessing step is the segmentation of the tumor and coagulation areas in CT data. A semi-automatic, morphologically based region-growing algorithm [120] is used that has proven to be robust and of good performance. For that, the user has to draw a stroke across the lesion, which is utilized for histogram analysis. Based on the drawn stroke, the calculation of the segmentation mask is performed automatically. Because multiple segmentation masks can be created, corresponding lesions are connected by the user to unique tumor-coagulation pairs, which are assessed consecutively.

Subsequently, a region of interest (ROI) is defined from the segmentation masks' centers of gravity (see Figure 5.2). The registration process is initialized by automatic position matching of the centers of gravity of both lesions. The resulting transformation is only applied in the ROI of both lesions to fulfill local rigidity constraints.

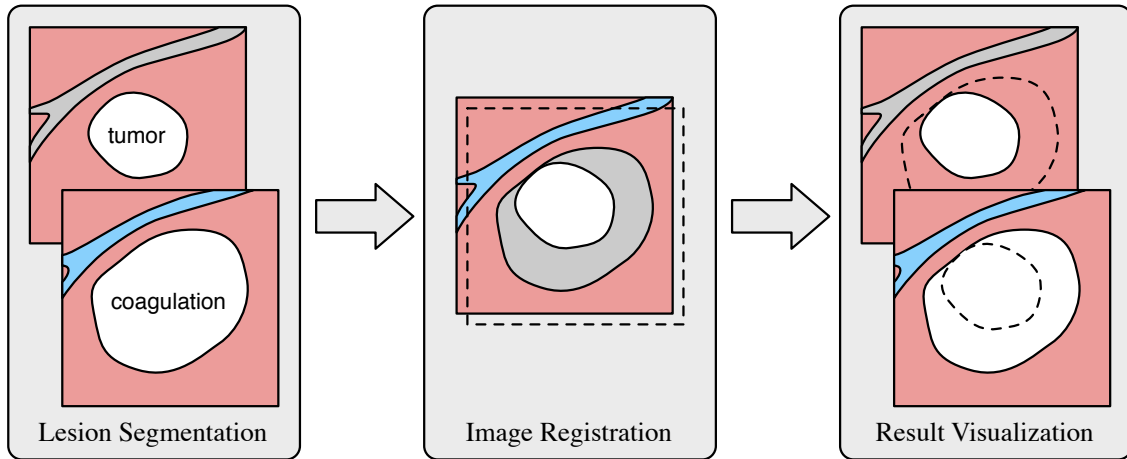


Figure 5.1: Illustration of the assessment workflow. The first step is the segmentation of the pre-interventional lesion and the larger post-interventional coagulation. In the second step the data sets are registered in order to match the anatomical relations. The last step is the visualization of the fused data sets to allow visual comparison of the lesions.

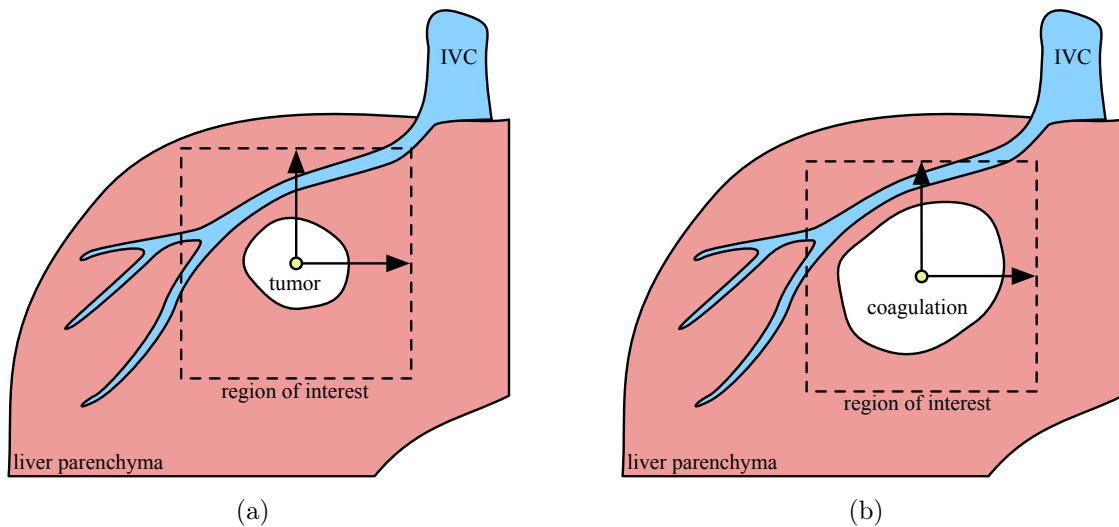


Figure 5.2: Image (a) illustrates a pre-interventional tumor located in the vicinity of the inferior vena cava (IVC). A region of interest with uniform distance to the segmented tumor's center of gravity is automatically defined. Analogously, in (b) the post-interventional coagulation is segmented and the corresponding region of interest calculated.

5.3.2 Automatic Rigid Registration

The preprocessing steps presented in Section 5.3.1 serve as input of the automatic registration method. To prevent the registration algorithm from matching both lesion shapes instead of the surrounding anatomy, a registration mask is specified. For that, the pre-interventional lesion mask is dilated utilizing a morphological operation and subsequently inverted. Thus, the registration algorithm uses only a subset of the pre-interventional image ROI for similarity calculation.

For further exclusion of anatomical structures such as ribs or neighboring organs from the similarity calculation, a rough liver segmentation is computed automatically. With no need to delineate exact liver boundaries, this coarse segmentation is based on the observation that liver tissue mainly contributes to the upper parts of the image's histogram (see Figure 5.3). Voxel with gray values between the last peak in the histogram (v_1) and the 95%-quantile (v_2) are enhanced by multiplication with a Gaussian function with expectation value $\mu = \frac{(v_1+v_2)}{2}$ and standard deviation $\sigma = \frac{v_1-v_2}{2}$. By subsequent thresholding by 0.5 and selective morphological opening (of 15 mm), a mask can be obtained that excludes bones and other abdominal organs. The selective opening is a morphological dilation of an erosion, whereas the largest component of the image is selected by a connected component analysis after morphological erosion. Using this kind of masking, the registration is significantly faster and more robust.

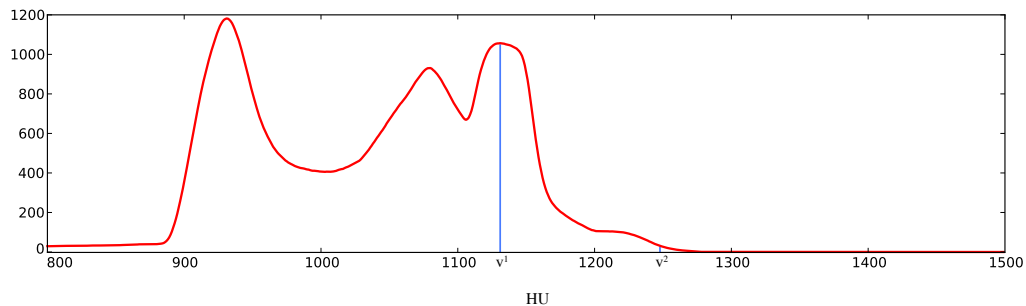


Figure 5.3: The smoothed histogram of a CT data set from which the last peak (v_1) and the 95%-quantile (v_2) are determined.

To compute the complete transformation, an automatic registration algorithm based on the Newton-type optimization scheme [119] using the Local Cross Correlation (LCC) similarity measure [126] is utilized. For a complete overview of the used registration framework, the reader is referred to Böhler et al. [31]. Figure 5.4 illustrates the complete registration workflow.

5.3.3 Manual Rigid Registration

For post-adjustment of the transformation, a manual registration method, which can be used without extensive training, is provided. The manual alignment of the

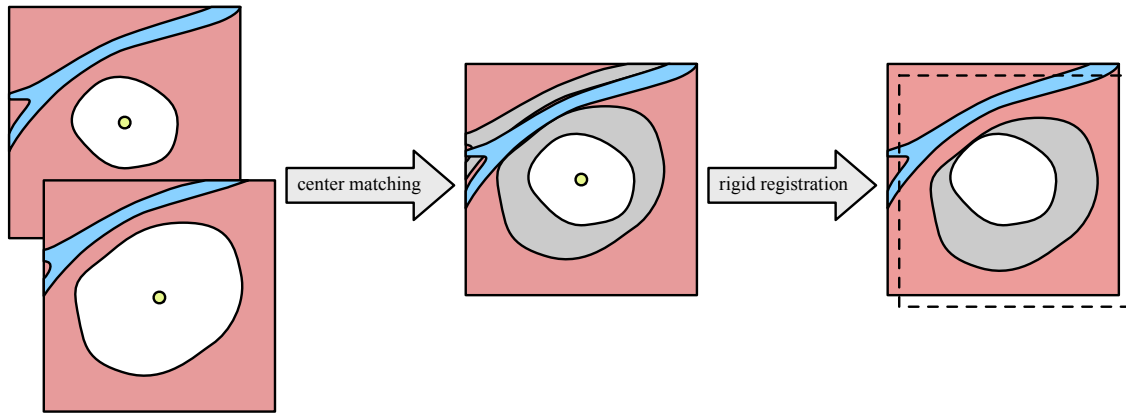


Figure 5.4: As a pre-registration step, the regions of interests of both lesions are overlaid by matching the positions of the corresponding center of gravities. Subsequently, a rigid registration is performed to match anatomical features such as vessels around the lesions. For the automatic registration algorithm, both lesions are masked out of the anatomical images.

data sets is performed in the orthogonal 2D slice views performing simple mouse interactions. The template image can be grabbed and translated in all three main directions. Furthermore, an image menu which is superimposed onto the image data is presented. It allows to translate the data set in a step-by-step manner using buttons for translation, and also for image rotation. The image menu can be displayed at the current mouse pointer and defines the rotation center of the template data set. Figure 5.5 shows the image menu. The four outer arrow buttons allows the physician to translate the template image step by step. The plus and minus buttons realize translation in and inverse direction of the image stack, respectively. The two curved arrows allow to rotate the template image around the menu's center. If the medical expert is not satisfied with the registration result, the software assistant provides an undo button to reset the transformation to the initial matching of the centers of gravity.

The challenge in manual registration is to visually assess if the anatomical structures of the template image and the corresponding anatomical structures in the reference image are properly matched. For that, both images have to be displayed in a combined visualization. Because radiologists are trained to mentally fuse data sets, combined visualization with checkerboard-like overlays [76] or iso-contours are not considered. Because of the goal to match anatomical landmarks, particularly liver vessels, instead of the lesions' boundary, the display of the previously segmented lesion masks is not provided. The data sets are combined using image fusion [168]. Three fusion modes are available:

- An additive color scheme is used to allow a visual separation of the data sets. The reference image is colored in light blue and the template image in the

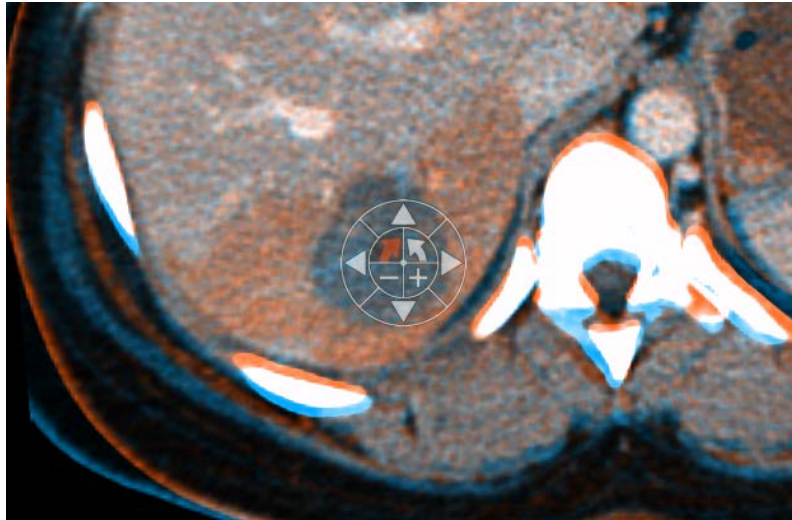


Figure 5.5: Image menu as overlay on top of the anatomical image. The buttons of the menu allow for translation and rotation of the template data set. Also, the rotation center is defined by the image menu.

complementary color, i.e. orange (see Figure 5.6 (a)). Those colors are chosen for the reason that areas of different intensities stay colored and areas with similar intensities become grey. The advantage of the additive color scheme is that no further parameters are required to fuse the data sets, particularly if both data sets represent equal intensities. On the other hand, the drawback is that the data sets have to be represented with similar window and level justification to allow for correct fusion.

- To overcome this problem, both colors can also be merged by linear interpolation of the color values (see Figure 5.6 (c,d)). For that, a slider control allows the user to linearly blend between pre-interventional reference image and post-interventional template image. Thus, the user may independently window both data sets and linearly blend the images from reference only to template only.
- In the last mode, both data sets are merged by linear interpolation, but instead of utilizing colored transfer functions, the original image intensities are displayed (see Figure 5.6 (b)). The user may use the slider control to quickly switch between both data sets allowing for mental fusion of the data sets (morphing).

In addition to the 2D slice views, a three-dimensional multi-volume rendering of both ROIs is integrated. In the volume rendering, the liver vessels of both data sets are emphasized utilizing the automatically determined transfer function (see Section 3.5.1). Also, the color schemes described above are used for the fused volume

rendering of both data sets. If the template image is interactively transformed by the user, the corresponding data set in the volume rendering is also immediately transformed, allowing for a fast exploration of the anatomical correlation of vascular structures. The advantage of the 3D volume rendering is that all vascular structures in the ROI are visible in a single visualization allowing the user to verify the accuracy of the alignment without slicing through the complete image stack (see Figure 5.11).

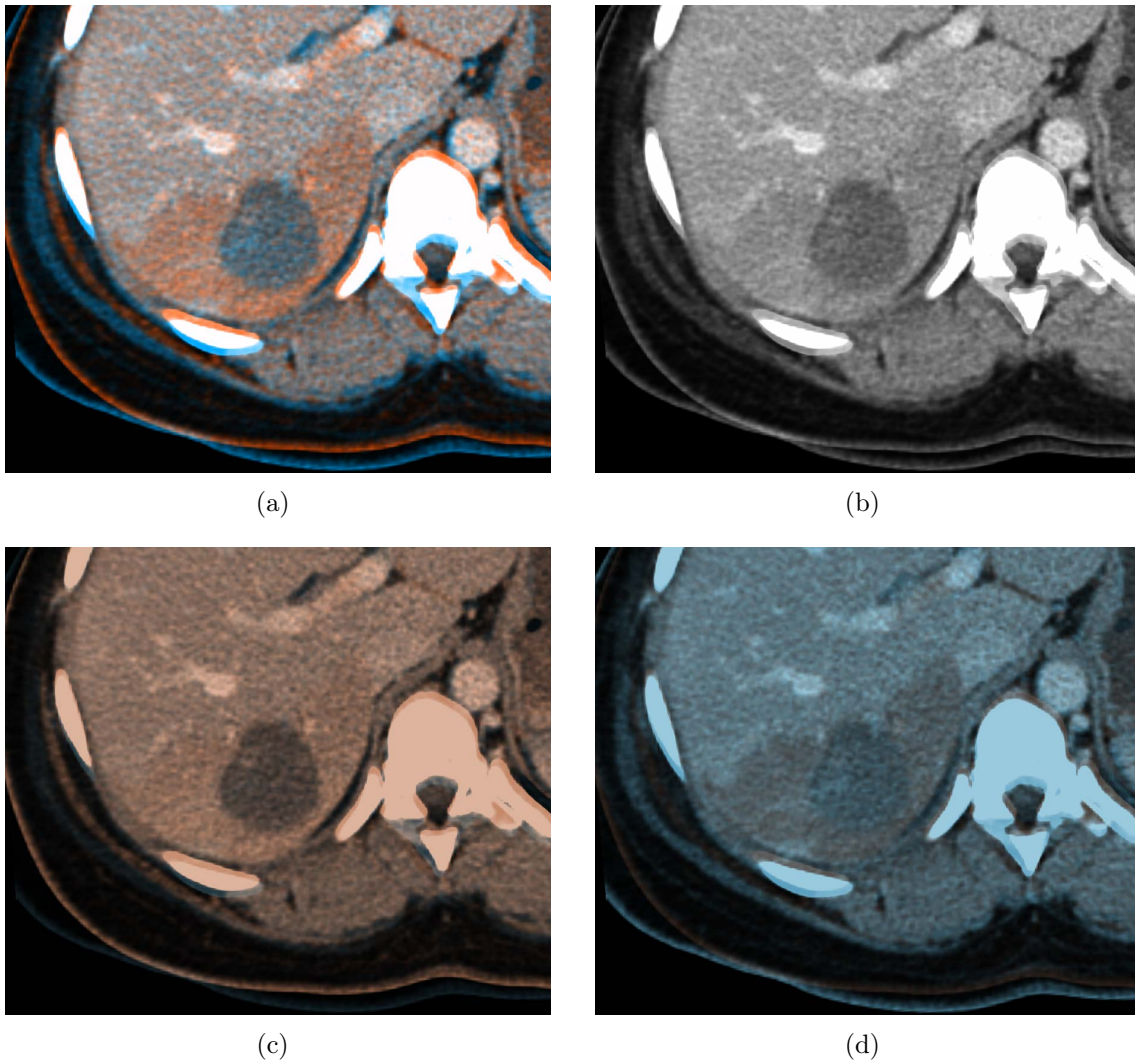


Figure 5.6: Image (a) shows a fused image with the additive color scheme. The pre-interventional image is colored red, the post-interventional image in blue. In (b) the original windowed grey values are linearly merged (blending = 0.5). Image (c) and (d) show the linearly merged colors with blending = 0.25 and blending = 0.75, respectively.

5.3.4 Result Visualization

In the last workflow step, the result of the registration is visually represented. In order to verify if the tumor is completely enclosed by the coagulation, both lesions are visualized together. Both segmentation masks are jointly superimposed onto the anatomical images allowing the physician to visually verify the ablation result. For that, the post-interventional coagulation mask is transformed to the image coordinate system of the pre-interventional tumor mask with the registration matrix and vice versa. Because the segmentation information is now used, the data sets are not visualized according to the fusion schemes presented in Section 5.3.3. Figure 5.7 shows tumor (orange) and corresponding registered coagulation (blue) mask superimposed onto the pre-interventional data set by utilizing the transformation matrix, and also onto the post-interventional data set by utilization of the inverse transformation. Furthermore, quantitative measures such as lesion volumes, maximal diameter or surface distance are calculated. A comprehensive discussion of quantification methods and also proposal of advanced visualizations is presented in the following chapter.

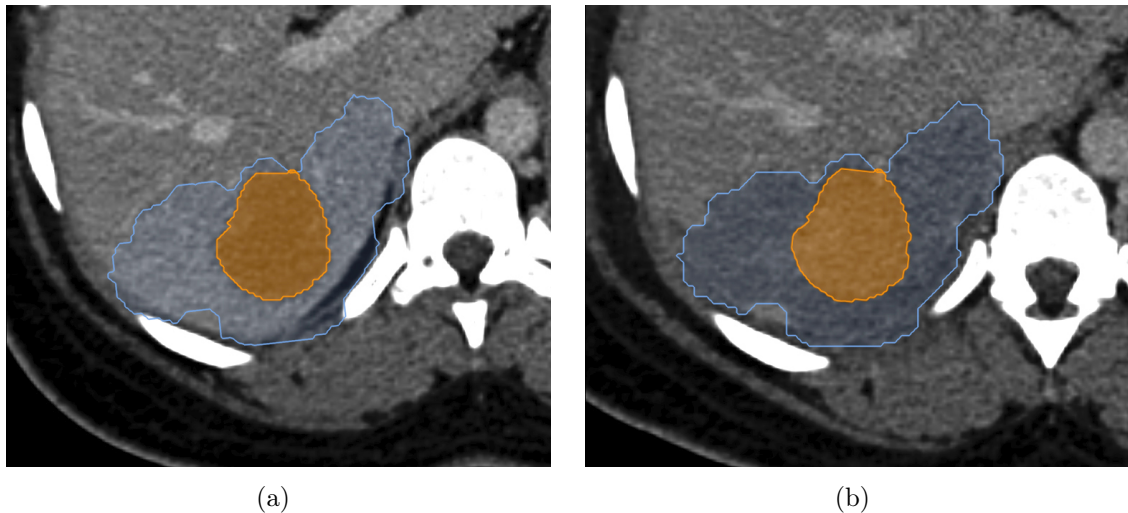


Figure 5.7: Image (a) shows a slice visualization of a tumor (orange) and registered coagulation (blue) superimposed onto the pre-interventional data set. Analogously, in (b) the post-interventional image with coagulation and registered tumor is presented.

5.4 Evaluation

To evaluate the proposed automatic registration method, 41 pre-interventional lesions with corresponding post-interventional coagulations are automatically aligned with the proposed method (see Section 5.3.2). The data sets have been recorded

before and after the RFA therapy, respectively. For statistical analysis, the elapsed processing time as well as the transformation matrix are stored for each case. To assess the processing time and the accuracy of the resulting transformation, the optimal registration is calculated, and all data sets are registered by four medical experts, manually.

5.4.1 Specification of Robust Landmarks

To evaluate the accuracy of the rigid registration, robust ground truth landmarks are specified. For that, a physician defines at least three landmarks around the lesion in the reference data set by clicking into the 2D slice viewer. Subsequently, the corresponding landmarks in the template image are also determined. Because manual determination of landmarks is inaccurate, further landmarks are specified by additional medical experts. For that, the reference landmarks are shown, and each medical expert specifies the corresponding landmarks in the post-interventional template data set.

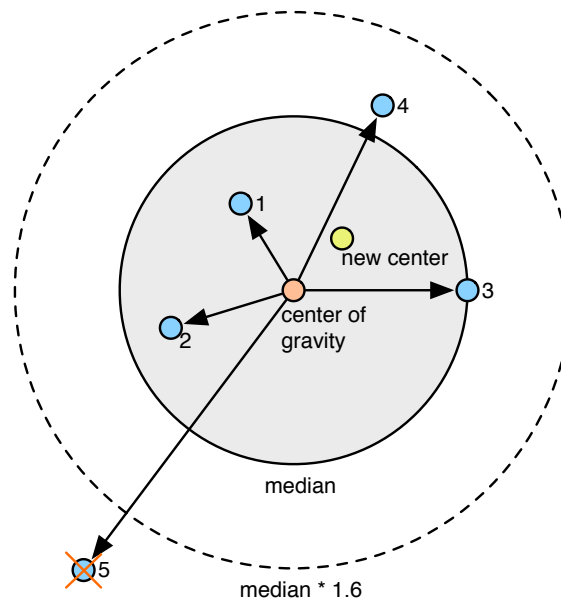


Figure 5.8: Filtering of outlier landmarks from a landmark set. Landmark 5 will be discarded because its distance is larger than 1.6 times of the median distance of all landmarks to the center of gravity. The average landmark is the new center of gravity of the remaining landmarks.

Consequently, for each pre-interventional landmark, multiple corresponding post-interventional landmarks are defined. To increase the robustness of the landmarks, outliers are eliminated and the average landmark is calculated from the remaining landmarks. For that, the center of gravity of all landmarks, matched to a single anatomical feature is calculated. Further, the median distance of all landmarks to

the center is computed. A landmark is specified as an outlier if its distance to the center of gravity is larger than 1.6 times the median distance. Subsequently, all outliers are eliminated, and a new center of gravity is calculated from the remaining landmarks. Thus, the new center of gravity is the stable, robust template landmark of a pre-interventional reference landmark set. Figure 5.8 illustrates the elimination of an outlier and the calculation of the resulting average landmark. Figure 5.10 shows 3D renderings of the tumor and surrounding vessels. Multiple landmarks are placed by five experts onto features of the vessels, whereas each expert is represented by different colored spheres. The black dashed spheres represent the averaged landmarks after elimination of the outliers. Image (a) and (c) presents cases, whereby landmark outlier are clearly visible. The position of the averaged landmark set is now the center of gravity of the remaining landmarks.

5.4.2 Estimation of the Ground Truth Transformation

To estimate the optimal ground truth transformation for all 41 data sets, five experienced medical experts specified 4-5 landmark pairs, from which robust landmarks are calculated, as described in Section 5.4.1. The average distance to the center of gravity after elimination of the outliers is measured per landmark set. The median of all averaged distances is 2.71 mm, the minimum 0.73 mm, and the maximum 33.57 mm (see Figure 5.9). The medium distance emphasizes that the specification of anatomical landmarks in the three-dimensional space is a difficult task for humans.

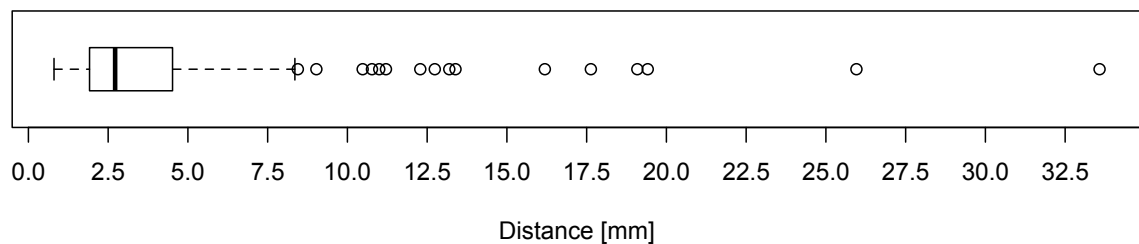


Figure 5.9: The box plot illustrates the average distance to the center of gravity per landmark set after elimination of landmark outliers (182 landmark sets from 41 cases).

Based on the averaged landmarks, the optimal landmark registration is calculated. For that, the Iterative Closest Point (ICP) algorithm [151] is utilized which leads to a mean Euclidean distance of 2.29 mm and a median Euclidean distance of 2.16 mm. The resulting distance after ICP landmark matching is denoted as the *system error* of the rigid registration, which is related to the general variation of landmark positioning by humans and the remaining non-linear transformation fraction of the deformation. The small value of the system error supports the validity of the proposed approach for rigid alignment of interventional image data.

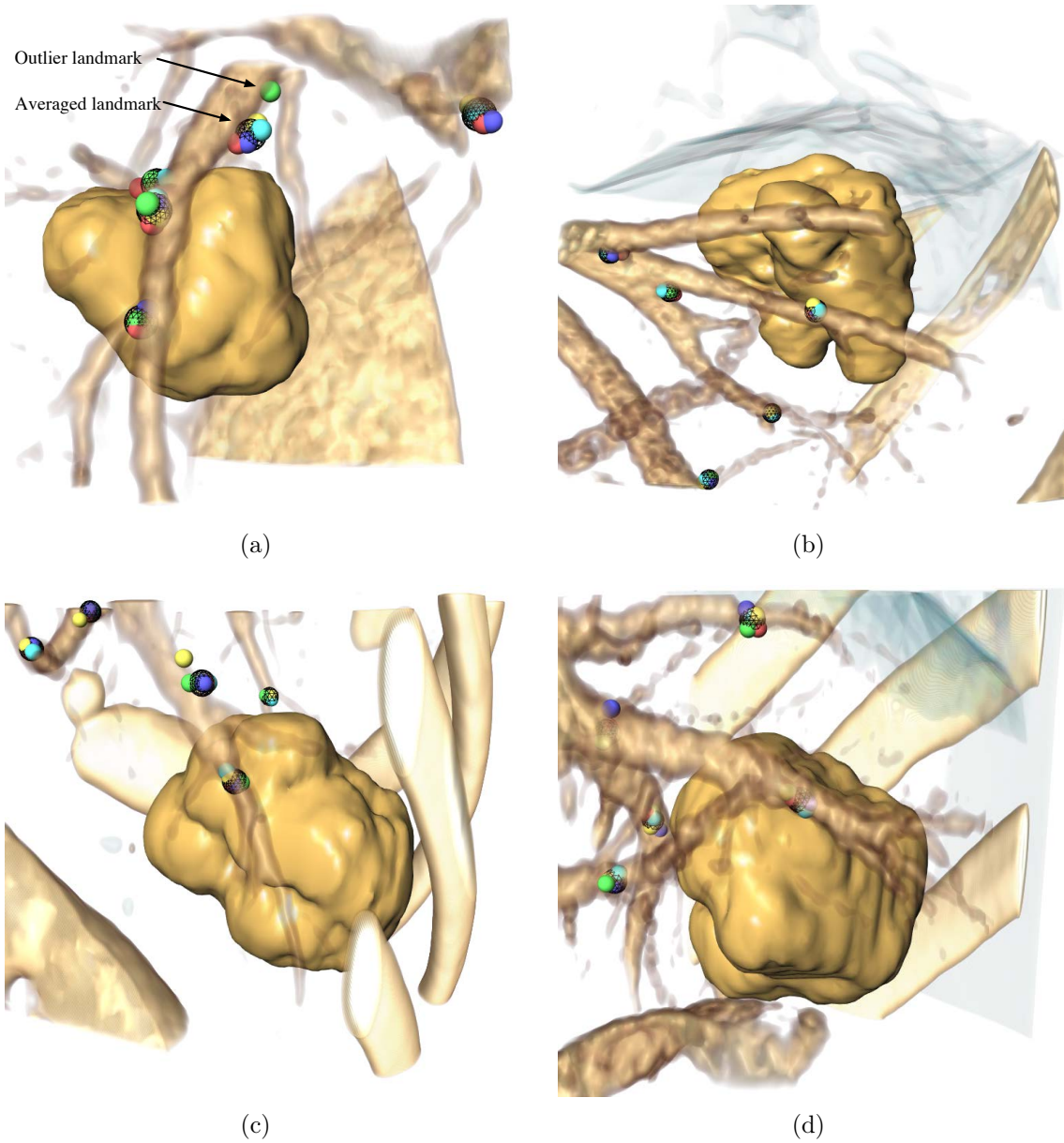


Figure 5.10: Rendering of a pre-interventional lesions and the surrounding vessels as well as ribs (image (a)-(d), case 6, 36, 29 and 17, respectively). In every image, a set of five anatomical landmarks is displayed, whereas each landmark is represented by differently colored spheres from five medical experts. The black dashed spheres represent the averaged landmarks after elimination of the outliers.

5.4.3 Landmark Transformation

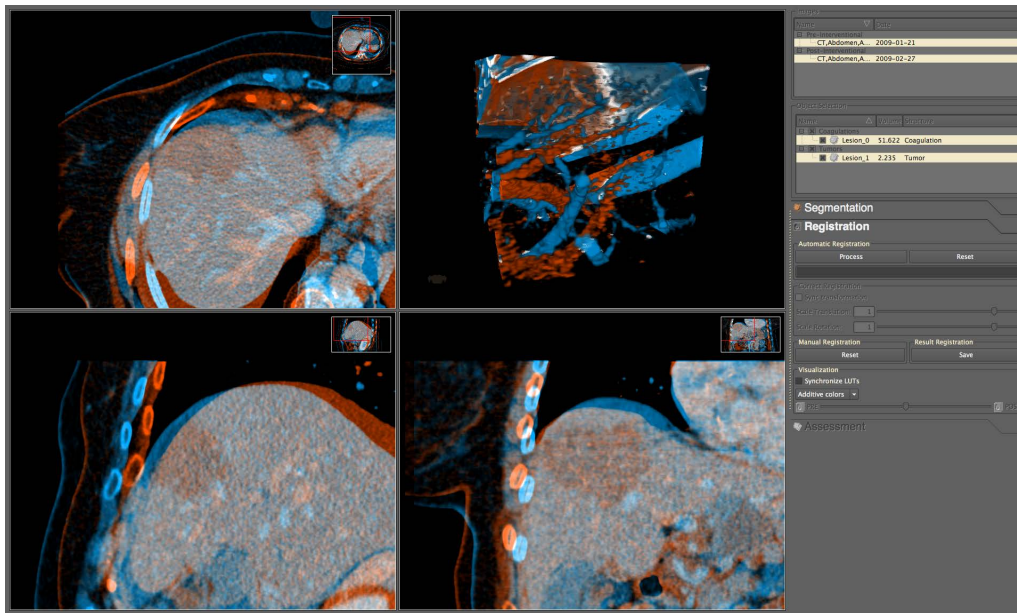
The 41 data sets are registered manually by four medical experts, independently, and also by the automatic method. The processed time and the transformation matrix are stored for every data set. To compare the results of the automatic registration method with the optimal rigid registration and the manual registration, the averaged template landmarks are transformed with the stored registration matrices. After the transformation, the average Euclidean distance from the transformed template landmark set to the reference landmark set is measured for every case.

5.5 Results and Discussion

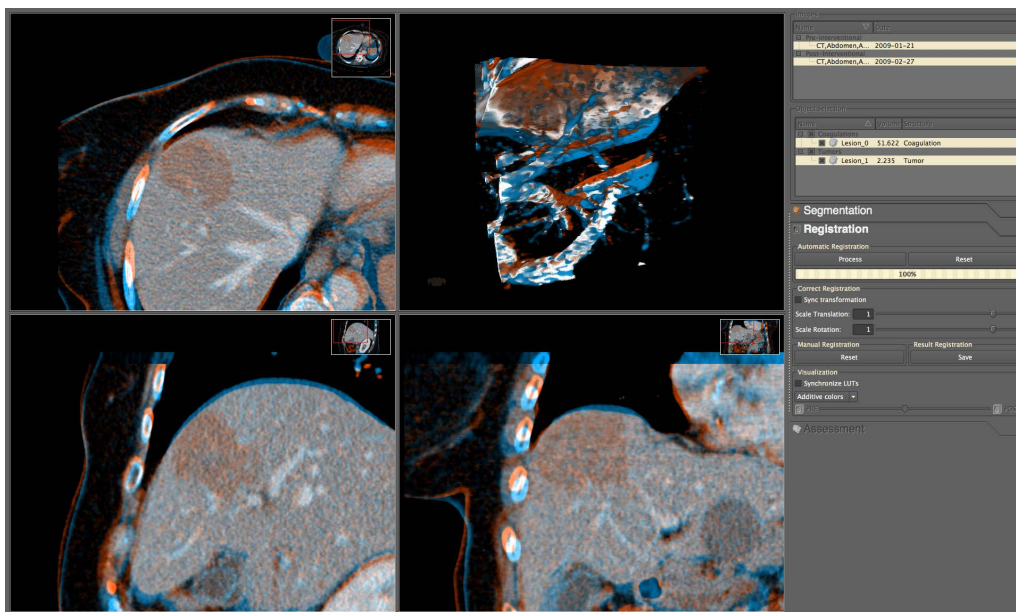
For all medical experts, a mean distance of 5.46 mm and a median distance of 4.60 mm is measured. The mean distance after automatic registration is 6.24 mm and the median distance is 3.95 mm. The mean distance of the automatic method is higher than the averaged distance of all experts, but slightly smaller than the worst medical expert's mean accuracy. The median distance of the method is lower than the median of all medical experts, but roughly 2 mm less accurate than the optimal landmark registration. However, the measured distances indicate that the automatic method is at least accurate as the registration of the medical experts. Regarding the minimal distance of the optimal landmark registration, the automatic registration is 28% less accurate than the system error, and the averaged group of medical experts almost 50% less accurate. In 27% of the cases, the automatic method is more accurate than the manual registration performed by the best medical expert, in 24% the automatic method is less accurate as the experts, and in 49% the method is in the distribution of the medical experts accuracy (in 29% the distance is lower than the median, in 20% higher). Figure 5.12 illustrates the average distance of all registered data sets.

Furthermore, the time consumption of the presented registration methods is compared. The mean processing time of all medical experts for all cases is 333 seconds and the median time is 283 seconds. Also, the computation time for the automatic algorithm, including the calculation of the proposed registration mask is measured. The processing time for data loading and the preprocessing steps (lesion segmentation and ROI calculation) is not included in the measurement of both methods. Figure 5.12 (b) shows the average time per medical expert as well as for the automatic method. Although the even alignment accuracy of all medical experts, the elapsed time significantly differs. For instance, variance and median of the measured time to align the data sets strongly differs of medical expert #1 and #2. Medical expert #2 seems to be more experienced and more efficient (i.e., time-accuracy ratio). The two other experts' time consumptions are in the same range.

The mean calculation time of the automatic registration algorithm is 38 seconds and the median is 32 seconds. Thus, the automatic registration method is significantly faster than the medical experts, resulting in a mean $8.7 \times$ speedup and a



(a)



(b)

Figure 5.11: Screenshot (a) of the software assistant shows case 27 after matching of the centers of gravity. Both lesions are aligned but the surrounding vasculature is mismatched (11 mm). After automatic registration in the region of interest around the lesions (b), the vasculature is matched resulting in a pre-post landmark distance of 3 mm.

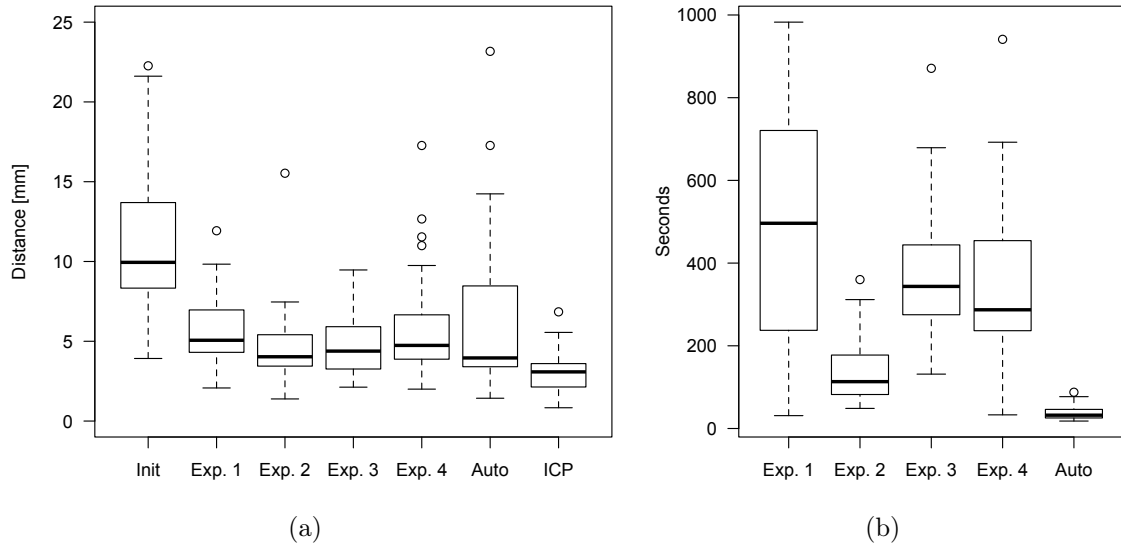


Figure 5.12: Box plots (a) illustrates the average distance of all registered data sets. From left to right, the distance from the initial position matching, medical expert 1 - 4, the automatic method, and the optimal registration after ICP matching of the landmarks. Box plots (b) show the average processing time of the medical experts and the automatic method.

median $8.8 \times$ speedup, respectively. The processing time to segment both lesions is not included in the mean calculation time. Because its mean processing time is 1-2 seconds, the segmentation process does not significantly change the scale of the observed speedup. Figure 5.12 (b) clearly reveals that the median of the automatic method is in the range of the minimal time consumption all medical experts required for manual alignment. With increasing computing performance of the hardware and constant processing time of the medical experts, an even higher speedup can be expected in the future.

Additional observations are, that without the presented masking method, the landmark distance after automatic alignment is significantly greater (mean 8.79, median 6.7 mm). Furthermore, the outliers of the automatic alignment method (cases: 9,15,16,17,19,20,22,33,35,39; see Figure 5.13) all have lesions that are peripherally located (close to the liver's capsule). The inaccurate registration matches are related to inadequate registration masks, which lead the algorithm to also calculate the similarity of extra-hepatic neighboring organs and try to align them.

5.6 Conclusions

In this chapter, an automatic workflow for masking liver tissue, enabling a rigid registration algorithm to perform at least as accurately as experienced medical experts

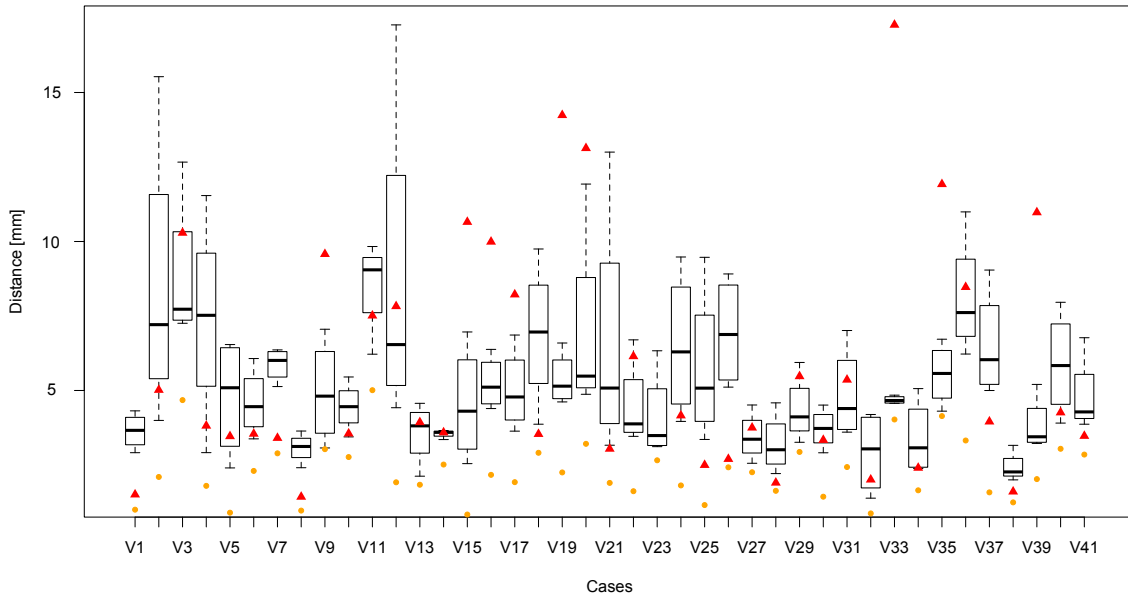


Figure 5.13: Box plot of all 41 cases. The boxes illustrate the landmark distances of the manually registered data sets. The dots show the distance per case after ICP matching of the landmarks and the triangles the distance of the automatic registration method.

is presented. To minimize the effect of global liver deformations, the registration is computed in a local region of interest around the pre-interventional lesion and post-interventional coagulation necrosis. A registration mask excluding lesions and neighboring organs is calculated to prevent the registration algorithm from matching both lesion shapes instead of the surrounding liver anatomy. As an initial registration step, the centers of gravity from both lesions are aligned, automatically. The subsequent rigid registration method is based on the Local Cross Correlation (LCC) similarity measure and Newton-type optimization.

To assess the accuracy of the proposed method, 41 RFA cases are registered and compared with manually aligned cases from four medical experts. Furthermore, the registration results are compared with ground truth transformations based on averaged anatomical landmark pairs. The proposed automatic method reaches an accuracy in the range of the medical experts' registration transformation in significantly less time. Although the variance of the resulting distance after automatic registration is higher than the measured distance from the medical experts, it is shown that the median distance is slightly smaller. Thus, the automatic rigid registration is a useful tool to fuse pre- and post-interventional data sets in a local region of interest to allow assessment of the RFA therapy success. A combination of both automatic and manual approaches is integrated in the software assistant, where the physician is able to manually post-adjust the transformation after automatic registration to achieve the optimal result.

Although the presented alignment workflow is described for comparison of images acquired for planning and assessment of the RFA therapy, it is generally independent of the type of needle intervention. Thus, pre- and post-interventional images from other therapies such as microwave or cryoablation can also be aligned. The method may be generalized for other alignment procedures with comparable requirements such as local rigidity and segmentation masks.

For future work, it will be investigated how the mask calculation can be improved to reach a higher robustness, even for peripheral lesions without significant increase of the processing time. Nevertheless, medical users may be able to detect those failed registration results and may correct the alignment manually using the presented interaction methods.

This chapter is in part based on the following publication:

- **C. Rieder**, S. Wirtz, J. Strehlow, S. Zidowitz, P. Bruners, P. Isfort, A. H. Mahnken and H.-O. Peitgen. Automatic Alignment of Pre- and Post-Interventional Liver CT Images for Assessment of Radiofrequency Ablation. In: *Proceedings of SPIE Medical Imaging: Image-Guided Procedures, Robotic Interventions, and Modeling*. 8316, pp. 83163E-1-83163E-8, 2012.

*What we see depends mainly on what
we look for.*

(Sir John Lubbock)

6

Visual Support for Interactive Assessment of RFA

THE comparison of pre- and post-interventional images for assessment of the treatment result is a challenging task and is prone to human error. In this chapter, a novel visualization as well as a navigation tool, the so-called *tumor map*, is presented to ease the comparison. The tumor map is a pseudo-cylindrical mapping of the tumor surface onto a 2D image. It is used for a combined visualization of the tumor and its surface distance to the coagulation necrosis in order to support reliable therapy assessment. Additionally, the tumor map serves as an interactive tool for intuitive navigation within the 3D volume rendering of the tumor vicinity as well as with familiar 2D viewers.

6.1 Introduction

Visual comparison of shape, size, and position of tumor and coagulation is typically performed to verify the treatment success of the RFA therapy. Generally, a maximal distance between the tumor surface and coagulation surface is required to avoid local tumor recurrence. In clinical practice, the images are often displayed in two separate viewers or even on two different monitors. Subsequently, both images are synchronously viewed in a slice-by-slice manner in order to compare the geometrical properties of tumor and coagulation.

The major challenge using this method is to correlate any spatial position in both images over all slices, which is in particular difficult if the soft-tissue is deformed or the shapes of tumor and coagulation significantly differ. Also, high interaction effort is required to fully examine both data sets because slicing has to be performed in parallel. A further challenge is the difficulty to evaluate the size of the ablative margin exactly as well as quantify the ablation volume in the three-dimensional space. Typically, both lesions are only mentally fused by the physician, which is a time-consuming and inadequate task for robust qualification. In conclusion, the interpretation of the visual context and the respective treatment result is a challenging task and is prone to human error. Thus, comparative and robust quantification of the therapy success is difficult to achieve.

To ease this evaluation, the *tumor map* is presented as an interactive visualization technique for a reliable therapy assessment. Based on robust segmentations of the tumor and coagulation areas and a suitable registration of pre- and post-interventional data, a traffic light color-coding scheme is used for a fast and accurate visualization of the ablation state. Additionally, the tumor map serves as an interactive tool for intuitive navigation within the 3D volume rendering of the tumor vicinity as well as with familiar 2D viewers.

Technical contributions of this work are:

- Utilizing a traffic light color scheme, the minimal distance between tumor and coagulations surface is accurately visualized in 2D slice views as an addition to the visual comparison procedure of pre- and post-interventional CT images.
- In the 3D volume rendering, the traffic light color-coding scheme is mapped onto the tumor's surface, and the coagulation is visualized in a transparent fashion to avoid occlusions. To supply the physician with spatial hints, the surrounding anatomy, including vessels, lungs and bones, is also visualized.
- The tumor map with the applied color scheme is introduced, which allows for immediate visualization of the complete tumor's surface. Thus, residual tumor tissue can be detected as fast as possible by the physician without the need for any interaction.
- Furthermore, the tumor map is used as a novel navigation tool to manipulate the view of the 3D volume rendering as well as the slice in the 2D viewers.

- Finally, the tumor map is also used as an interactive, bidirectional synchronization tool of the 2D viewers (selection of current surface point) with the 3D volume rendering (determination of view to current surface point).

The outline of this chapter is as follows: In Section 6.2, related work focusing on the assessment of radiofrequency ablation is described. Also, works in the fields of direct volume rendering and map projections are discussed. Section 6.3 explains the pre-processing required for the proposed visualization methods. In Section 6.4, the ablation color scheme and the corresponding visualization implemented in 2D and 3D are illustrated. In Section 6.5, the tumor map is presented and the technical realization explained. In this section, different mapping layouts as well as interaction methods are also discussed. Results are presented in Section 6.6, and the conclusion in Section 6.7.

6.2 Related Work

The size and shape of post-interventional RFA lesions have been examined by several research groups with different intentions. Bangard et al. [23] compare a 3D volume of a RFA coagulation in CT data with the largest 3D sphere that fits into this volume to examine the discrepancy between the expected and the achieved coagulation sizes. Stippel et al. [167] use volumetric reconstructions of RFA coagulations to perform a correlation between the recurrency rate and the initial tumor diameter. Both papers seek better knowledge about the achievable ablation area for intervention planning purposes.

Lazebnik et al. [102] describe a geometric 3D-deformable lesion model for segmentation and visualization of RFA lesions in post-interventional MRI data. The methodology is oriented to a treatment assessment based on volumetry. A comparison to pre-interventional data is not performed. Bricault et al. [35] describe a computer-aided diagnosis tool that provides an early detection of local recurrences based on a comparison of the 3D shapes of RFA coagulations in consecutive follow up CT scans. The outcome of the procedure has been evaluated in a clinical study [36]. The methodology aims at the early detection of local recurrences during the clinical follow-up care. The concept of immediate post-interventional therapy assessment, based on the comparison of the tumor- and coagulation areas, is not mentioned.

Samset et al. [152] present a software tool, developed to calculate and visualize 3D temperature distributions during hepatic cryoablation combined with a 3D intra-operative navigation system. Based on segmentations of the tumor and the frozen region, the -40°C isotherm-surface can be shown in relation to the tumor, whereas the tumor is colored according to the current ablation temperature in a surface rendering. The presented visualization of the temperature distribution in the target region is used as guidance for accurate probe replacement.

Weihusen et al. [179] describe a visual support for comparison of pre- and post-interventional RFA data as part of a software assistant. For the comparison, a traffic

light color coding scheme within a 3D surface rendering is used. The colors red, yellow and green are mapped onto the transparently rendered coagulation surface in order to emphasize the minimal distance to the tumor regarding the ablative margin. The drawback of this visualization is the difficulty to relate the tumor's surface to the intended ablative margin. Also, the color scheme is not provided in the slice rendering and no further interaction elements are described.

In addition to traditional 2D slicing, surface rendering (indirect volume rendering) and particularly direct volume rendering (DVR) is now available in almost every medical workstation. The value of DVR has been stated by Zuiderveld et al. [189]. They describe a clinical evaluation of interactive volume rendering and present the medical value in three examples of clinical findings. Antoch et al. [20] comment on the value of volume imaging for optimal placement of radiofrequency ablation probes in liver lesions. For evaluation of RFA, Fujioka et al. [60] comment on the advantage of DVR to multidirectional observe the relationship between tumor and ablation zone.

However, DVR is seldom used in clinical practice due to its complicated and time consuming-adjustment of parameters to achieve meaningful visualizations [85]. Automatic view point selection for volumetric data is addressed in several works [32, 42]. Another aspect which hampers usage of DVR in clinical practice is the often missing synchronization between 2D slice representation and 3D volume rendering. Kohlmann et al. [93, 94] present a new concept to synchronize 2D slice views and volumetric views of medical data sets. They utilize intuitive picking actions on the slice to provide expressive result images in the DVR. The synchronization from DVR to 2D slice view via volume picking is presented in [95]. They extract contextual meta information from the DICOM images and analyze the ray profile for structures which are similar to predefined ray segments of a knowledge database.

In the context of image-based diagnosis, the spatial distribution of function and morphology is of major interest. Due to the complexity of organs such as the brain and blood vessels, flattening approaches have been presented to reduce the exploration space from \mathbb{R}^3 to \mathbb{R}^2 . In the field of neuroanatomical visualization, the folds and fissures of the brain prohibit the combined display of such complex geometry. To overcome this issue, Hurdal et al. [82] present cortical maps to facilitate a view of the entire surface of the human brain. Interaction between 3D surface and map is required to understand the map distortions, to mark regions of interest, and to be able to compare differences between individuals. Neugebauer et al. [127] present an approach for the intuitive and interactive overview visualization of flow data that is mapped onto the surface of a 3D model of a cerebral aneurysm. They utilize a cube-map-based approach to project the surface data of the aneurysm onto an overview visualization. Both works map the surface points of a pre-computed geometric model from three-dimensional space into two-dimensional image space. In the field of virtual colonoscopy, Bartoli et al. [24] introduce virtual colon mapping and Hong et al. [81] present a colon-flattening algorithm to allow rapid searching the whole colon wall for polyps. Therefore, the three-dimensional colon surface is extracted from a CT data set. Subsequently, the surface is conformal mapped to a

two-dimensional rectangle. In the area of vascular visualization, traditional volume visualization techniques are insufficient to provide complete morphological information. Kanitsar et al. [86] present a new technique to visualize the interior of a vessel in a single image based on the automatic estimation of the vessel centerline. A linked multi-view system is presented by Ropinski et al. [144] to allow for interactive exploration of PET/CT scans of mouse aortas. Therefore, a specialized multi-path curved planar reformation, a multimodal vessel flattening technique as well as a 3D view are integrated, and linked in the visualization system. Another system which combines projected views together with a 3D view is presented by Lampe et al. [100].

In cartography, many different projections exist, such as the Mercator projection [162], which preserves distances on the parallels of latitude. Klein et al. [91] use a Mollweide projection of the prostate surface to visualize the spatial distribution of segmentation errors. For evaluation, they compute Euclidean distances between the manual and automatic segmentation boundaries and project the values onto the Mollweide map.

6.3 Preprocessing

In the context of this work, the ablation assessment is based on a comparison of the pre-interventional tumor area with the post-interventional coagulation area. Two pre-processing steps are required for the proposed methods:

- Both areas have to be segmented within the corresponding image data to facilitate quantitative analysis of the therapy success.
- Due to the varying acquisition times and accordingly different coordinate systems of the pre- and post-interventional images, a registration is required to allow a fused visualization.

The initial preprocessing step is the segmentation of the tumor and coagulation masks (see Section 5.3.1). Since multiple segmentation masks can be created, corresponding lesions are connected to unique tumor-coagulation pairs, which are assessed consecutively.

The subsequent preprocessing step is the registration of the pre- and post-interventional data sets to match the spatial positions of tumor and coagulation for the final assessment step. The registration method has to be carefully set up because the goal is to align different structures (lesion and larger coagulation) and subsequently compare the geometrical properties. Thus, it has to be ensured that the structures to be compared are not considered for similarity calculation. A workflow for automatic alignment of pre- and post-interventional images for assessment of RFA is presented in Chapter 5.

6.4 Ablation Color Scheme

During the intervention, RF applicators are placed in the tumor so that all cancer cells as well as a safety margin of approximately 1 cm around the tumor is ablated. The purpose of this margin is to handle uncertainties and microscopic clusters of cancer cells around the visible tumor tissue. The local recurrence rates after RFA for tumors with an intentional margin of 0 cm and 1 cm are 14.5% and 6.5%, respectively [121].

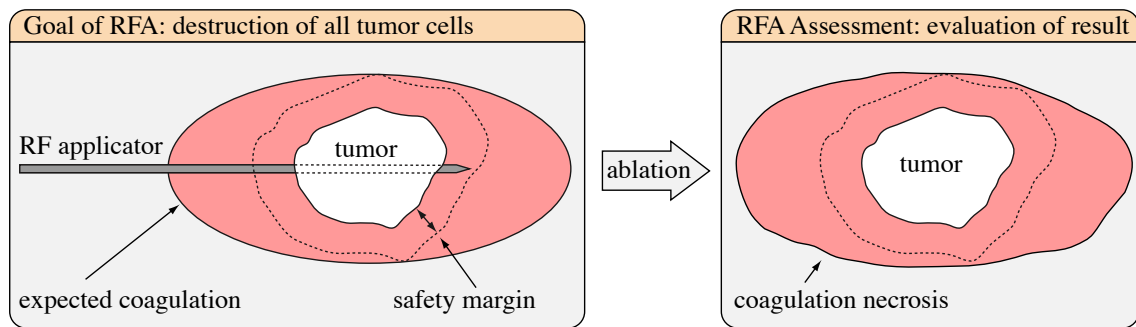


Figure 6.1: The goal of radiofrequency ablation is the destruction of all tumor cells. To handle uncertainties and microscopic clusters of cancer cells around the visible tumor tissue, a safety margin around the tumor is taken into account. In the assessment stage, it is verified if the tumor including the safety margin is completely destroyed.

The goal of post-interventional assessment is to evaluate the therapy result, i.e., to verify whether the aspired region is successfully ablated (see Figure 6.1). Also, it has to be verified if the tumor is completely located inside of the intended safety margin in order to assess the risk of local recurrences and resulting therapy options such as re-ablation.

6.4.1 Color Scheme of Coagulation Zones

The tumor, its surrounding safety margin, as well as the coagulation can be interpreted as three sets. Thus, according to the set theory, the coagulation C is subdivided by tumor T and its safety margin S , with $T \subseteq S$, into three subsets:

1. The intersection of tumor and coagulation, $T \cap C$.
2. The intersection of safety margin and coagulation, $S \cap C$.
3. The relative complement of tumor and margin in coagulation, $C \setminus S$.

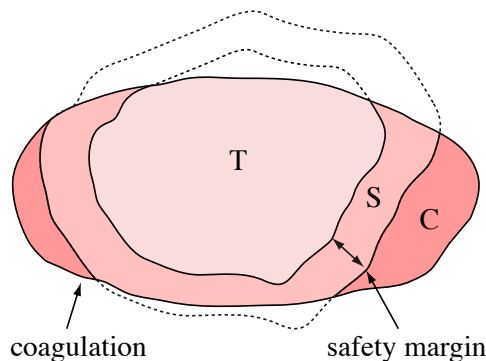


Figure 6.2: The coagulation is subdivided into three zones by the tumor and the tumor's safety margin. Tumor voxel outside of the coagulation mask are not considered.

However, the drawback of the subdivision of the coagulation is that the three zones are only indirectly related to the tumor. Also, the subset $T \setminus C$ which corresponds to tumor area which is outside of the coagulation mask is not considered (see Figure 6.2). Particularly this subset should be visually emphasized because it denotes the zone of tumor cells which could not be ablated. As a consequence, the tumor is subdivided instead of the coagulation in order to allow quantitative and qualitative assessment of the therapy success. For that, the new set N , with $N \subseteq C$, is defined by the negative margin with respect to the coagulation surface (see Figure 6.3). The coagulation C is subdivided by N and T into three zones, which are emphasized by a traffic light color scheme:

1. The *zone of failed tumor ablation* ($T \setminus C$) is the worst case and marked with red, an established signal color in medical applications. In this zone, the ablation strategy has failed and a re-ablation of the tumor is probably necessary.
2. The *zone of incomplete tumor ablation* is marked with yellow ($T \cap (C \setminus N)$). This zone is critical because the distance of the tumor voxel and coagulation surface is less than the intended safety margin, which could lead to potential cancer recurrence.
3. The *zone of complete tumor ablation* is marked with green ($T \cap N$). This zone is the optimal ablation result whereas the distance of all tumor voxels to the coagulation surface is larger than the intended safety margin.

Only the zone of failed tumor ablation is absolutely defined (red). The yellow and the green zone are defined relative to the intended safety margin. If the safety margin is changed, the proportion of both zones also changes.

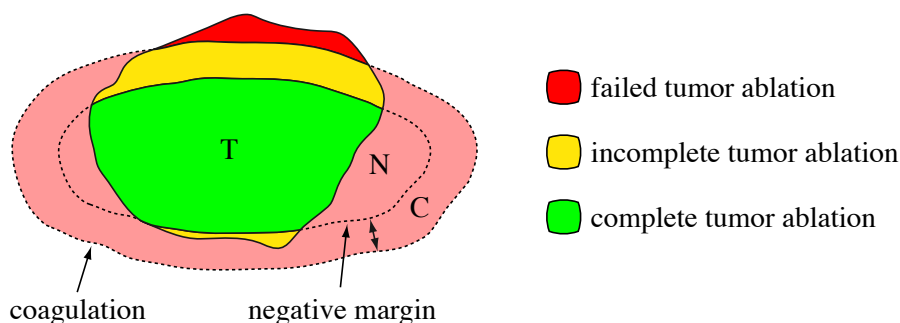


Figure 6.3: The traffic light color scheme of the coagulation zones in the tumor's extent. Red: failed tumor ablation. Yellow: incomplete tumor ablation whereas the distance between tumor and coagulation surface is less than the safety margin. Green: complete tumor ablation (distance between tumor and coagulation surface is larger than the safety margin).

6.4.2 Visualization in 2D

In the 2D viewers, the segmentation masks of tumor and coagulation are visualized together with the original CT-image data using a GPU-based slice renderer. The coagulation is displayed as a blue silhouette and the tumor mask is displayed using the color scheme which is described in the above section.

For that, the color scheme is applied to a two-dimensional rendering of the tumor segmentation mask. The respective zones are computed by means of an inverse Euclidean distance transform of the coagulation mask. The result of the distance transform is a volumetric image for which the Euclidean distance to the coagulation surface is saved as an intensity value for each voxel inside of the coagulation mask. This distance volume is also loaded into the rendering. Subsequently, the renderer applies the color red to every voxel of the tumor mask located outside of the distance volume, i.e., the value zero in the distance volume. The green and yellow zones are calculated using the safety margin threshold defined by the physician. If the distance value of a current tumor voxel is below the distance threshold, the color yellow is applied, above the threshold, the color green. To emphasize the boundaries of the three zones, silhouettes are also drawn (see Figure 6.4).

6.4.3 Visualization in 3D

In addition to the two-dimensional slice rendering, a volume rendering is used to supply the physician with a spatial representation of the ablation result including anatomical structures such as vessels and bones. The rendered volume is a region of interest (ROI) around the selected tumor with a fixed margin. A margin size of 5 cm lead to a good trade off between surrounding anatomical and centered tumor. The

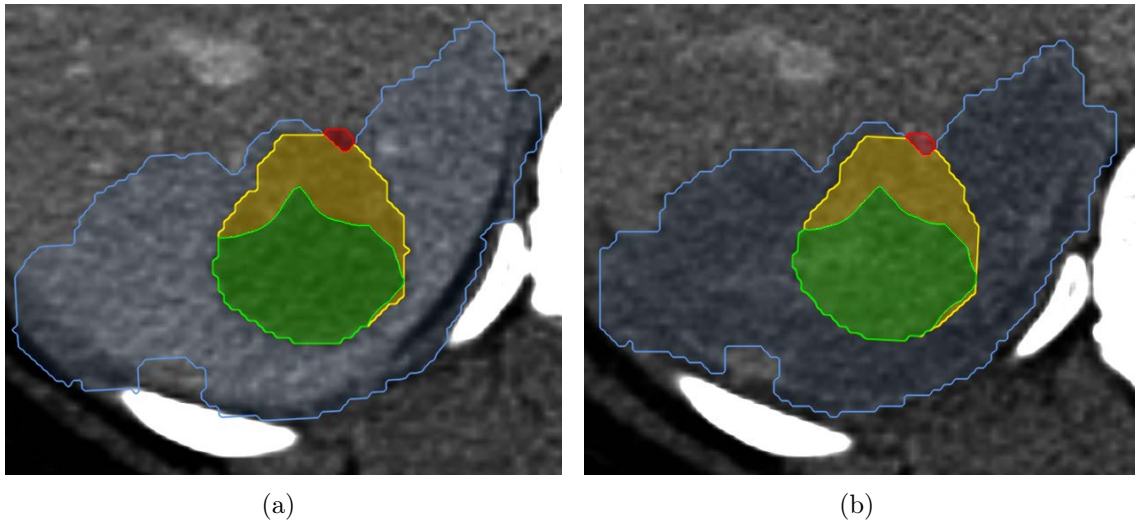


Figure 6.4: Visualization of the ablation zones in 2D, (a) with the pre-interventional image and (b) the registered post-interventional image.

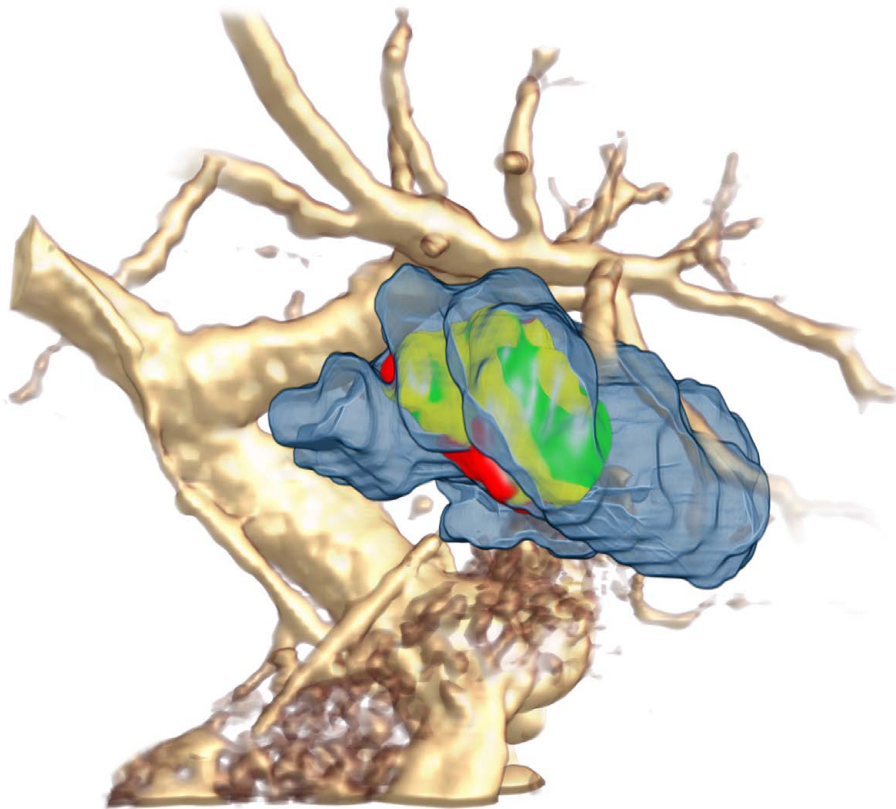


Figure 6.5: Shaded volume rendering of the tumor with applied color scheme, the blue coagulation surface, and surrounding vascular structures.

tumor is visualized in an opaque fashion, whereas the coagulation is visualized in a transparent fashion. To allow high-quality visualizations, a shaded volume rendering is used with pre-integrated [53] transfer functions for both objects. Furthermore, the distance volume is also loaded into the volume renderer to map the color scheme at the tumor's surface. The color scheme is calculated in the same way as in the 2D rendering. Local anatomical structures, such as liver vessels, pulmonary structures, and bones, are emphasized using the automatically determined transfer function utilizing the fuzzy *c*-means algorithm (see Section 3.5.1). To preserve an occlusion of the tumor by anatomical structures, a distance-based clipping plane [180] is applied, which is smoothed to avoid hard clipping edges (see Figure 6.5).

6.5 Tumor Map

The major drawback of the 2D slice and 3D volume rendering is that the complete surface of the tumor is not visible without interaction, i.e. slicing or rotation. To reduce the high amount of interaction needed to observe the complete surface of the tumor, the 3D surface of the tumor can be represented in a 2D map. The following medical requirements for such a mapping are:

- *Properties:* The mapping has to enable the comparative overview visualization of different features. For instance, the area of a local zone of incomplete ablation has to be of equal area as any other zone in the map in order to allow the physician to estimate its surface extension.
- *Interaction:* The 2D map has also to serve as a navigation tool. Marking an interesting point in the map will interactively result in highlighting of the corresponding position in the 2D slice view as well as the volume rendering.
- *Performance:* The generation of the map has to be facilitated without time-consuming processing steps in less than a second.

This mapping can be done using a spherical parameterization of the surface [161] and subsequently flattening into a 2D map. However, the drawback of this method is the high computational effort for solving the required linear systems. To take the above mentioned requirements into account, a simple but fast flattening technique is utilized. Because liver tumors selected for RFA have typically a spherical shape on a macroscopic level, it is assumed that the set of all surface points of the tumor is a star-convex set. Therefore, a cylindrical mapping that transforms the surface points of the tumor into a two-dimensional texture is introduced, the *tumor map*. This map allows the physician to recognize the complete color-coded surface of the tumor in a single view without the need for any interaction. Consequently, critical areas such as the zone of failed tumor ablation, can be recognized immediately.

6.5.1 Map Projection of the Tumor Surface

The well-known *Mercator* projection [162] is a cylindrical map projection proposed by the geographer and cartographer Gerardus Mercator in 1569. The projection is the standard map projection for nautical navigation because lines of constant course (rhumb lines or loxodromes) are straight lines in this map. This is a result of the property that angles are preserved (conformal), i.e. all straight lines in the map are lines of constant azimuth.

Generally, a map projection is a method to represent the surface of a shape on a plane. Projections can be classified according to properties of the model they preserve, e.g.:

- *Conformal* map projections preserve angles locally,
- *Equal-area* map projections preserve area,
- *Equidistant* map projections preserve distance from some standard point or line.

Because the shape of tumors are not developable surfaces, it is impossible to construct a map projection that is both equal-area and conformal.

From a medical point of view, the *Mercator* projection with its major advantage for nautical navigation is not suited because it is not equal-area with distortions strongly decreasing toward the poles. Thus, the goal is to efficiently approximate a equal-area map to fit the above mentioned medical requirements. For that, a two-step approach is used. First, a rectangular map is rendered by means of cylindrical mapping (see Section 6.5.2). Since this mapping is neither conformal nor equal-area but equidistant only with respect to the latitude, a second step is applied. The rectangular map is deformed to representations that are commonly known from cartography that fulfill the equal-area criteria (see Section 6.5.3).

6.5.2 Cylindrical Mapping of the Tumor Surface

For the generation of the initial map, a longitude–latitude mapping, which is an (equi-)rectangular projection, is used. The longitude–latitude mapping is a cylindrical mapping that considers longitude and latitude as a simple rectangular coordinate system:

$$x = \lambda - \lambda_0 \tag{6.1}$$

$$y = \phi \tag{6.2}$$

where ϕ is the latitude, λ is the longitude, and λ_0 is the central meridian (see Figure 6.6). This projection is neither conformal nor equal-area. Scale, distance, area, and shape are all distorted with the distortion increasing toward the poles. The longitude values are denoted in the x axis of the map, the latitude values in the y axis.

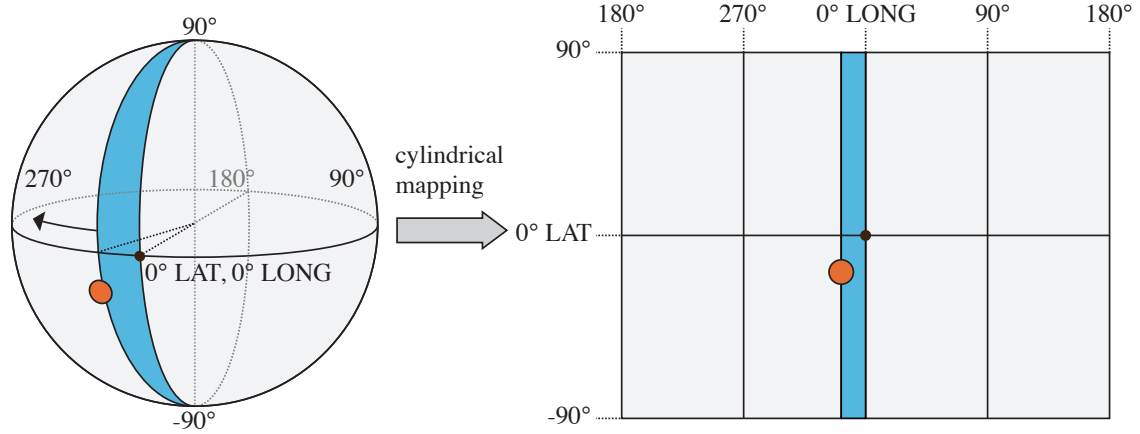


Figure 6.6: The used longitude–latitude mapping is a cylindrical mapping that considers longitude and latitude as a simple rectangular coordinate system.

Technically, the cylindrical map is created in the following steps:

1. Rendering arbitrary number of horizontal tiles of the tumor surface
 2. Compositing of tiles into 2D texture
 3. Vertical deskewing
 4. Application of color scheme
- 1.** The first step is to render an arbitrary number of horizontal tiles of the tumor surface. To do so, a volume rendering with the tumor mask and the distance volume including the Euclidean distance transform from coagulation surface to center of gravity is set up. The view point is set to the tumor center and 60 horizontal tiles are rendered using a perspective camera (with a horizontal field of view of 6 degree and a vertical field of view of 179 degree), which is rotated stepwise by 6 degrees per tile (see Figure 6.7). In the volume rendering, rays are cast until they hit the tumor’s surface. The current value of the distance transformation $d_{coagulation}$ as well as the current distance from center to surface voxel d_{center} are stored in the target image.
 - 2.** In the second step, the rendered tiles are composed into a 2D texture of size 512×256 , which has to be mirrored in the horizontal direction due to the rendering order from inside to outside. Thus, every pixel in the texture map represents an area of the tumor surface with saved distance to the coagulation as well as distance to the tumor’s center of gravity.

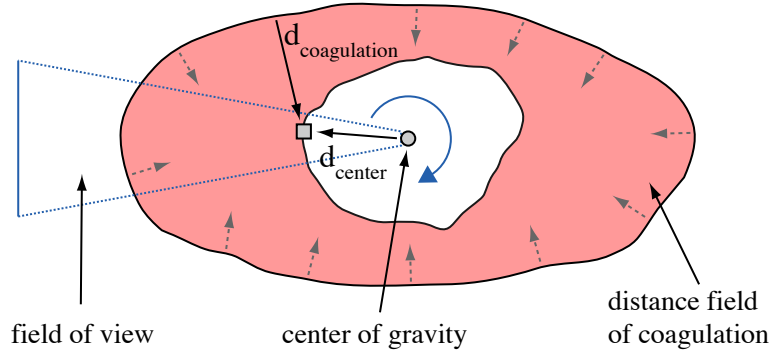


Figure 6.7: Illustration of the rendering of the rectangular map. The values $d_{coagulation}$ and d_{center} are stored in the map.

3. The resulting rectangular map contains vertical distortions (see Figure 6.8), which are a result of the perspective rendering of the tiles. To compensate the distortion, a vertical deskew is applied on the map:

$$y_{out} = 0.5 + \frac{\tan((y_{[0..1]} - 0.5)FOV_{[0..\pi]})}{2 \tan(FOV_{[0..\pi]}0.5)} \quad (6.3)$$

where $y_{[0..1]}$ is the vertical input position, y_{out} the new vertical position, and $FOV_{0..\pi}$ the vertical field of view. The horizontal distortion can be neglected for large numbers of horizontal tiles, because in this case, one tile only covers a few degrees. This projected texture is denoted as the *distance map*.

4. Finally, the color scheme is applied to the distance values of the coagulation surface stored in the distance map using a transfer function according to the safety margin defined by the user. The distance values from the center of gravity to the tumor surface are not visualized in the tumor map (see Section 6.5.4).

6.5.3 Tumor Map Layout

To further reduce the distortions of the longitude–latitude mapping, additional map projections are applied. One major disadvantage is the strong distortion of the area increasing toward the poles. Because regions at the poles are stretched in the x-dimension, the areas of different regions can not be compared. Thus, the simplest equal-area map, the sinusoidal projection is included. The sinusoidal projection is a pseudo-cylindrical equal-area map projection, for which the length of each parallel is proportional to the cosine of the latitude:

$$x = (\lambda - \lambda_0) \cos \phi \quad (6.4)$$

$$y = \phi \quad (6.5)$$

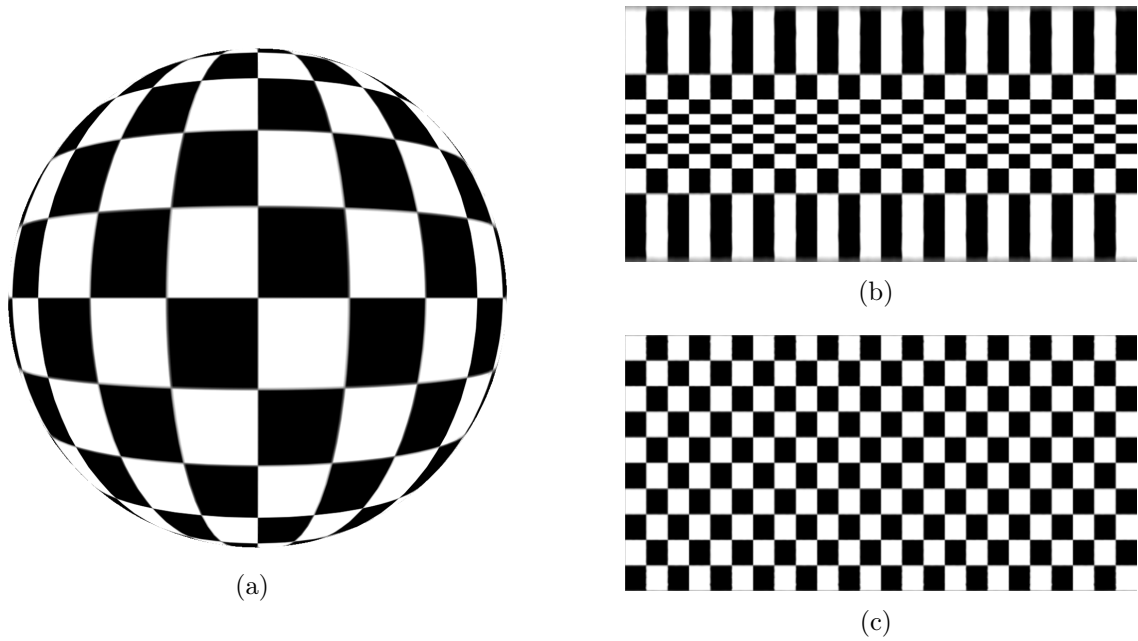


Figure 6.8: Projection of a checkerboard sphere (a) into a rectangular map (b). The vertical distortion in the map increases in vertical direction. After compensation for the distortions, the checker board is regularly scattered (c).

Another more complex map projection which is quite often used to map the surface of the earth in geographic atlases is the Mollweide projection, which was first published by mathematician and astronomer Karl B. Mollweide in 1805. It is also a pseudo-cylindrical, equal-area map projection:

$$x = \frac{2\sqrt{2}}{\pi} \lambda \cos \theta \quad (6.6)$$

$$y = \sqrt{2} \sin \theta \quad (6.7)$$

where θ is defined by:

$$2\theta + \sin 2\theta = \pi \sin \phi \quad (6.8)$$

Technically, texture coordinate maps of both, the sinusoidal, and the Mollweide projection layout, are calculated by discretization of the above mentioned equations into a 1024×512 image (see Figure 6.9). The texture coordinates are used to compose the deformed rectangular projection with stored distance values according to the custom projection layout. Moreover, using predefined texture coordinate maps, any map projection known in cartography may be used as a tumor map.

To support the interpretation of the tumor map, labels are added to the corresponding mapping layout. The labels show bold isolines of $\lambda = -90, 0$, and 90 degree as well as $\phi = 0$ degree. Thin isolines are drawn between the bold lines. The letters



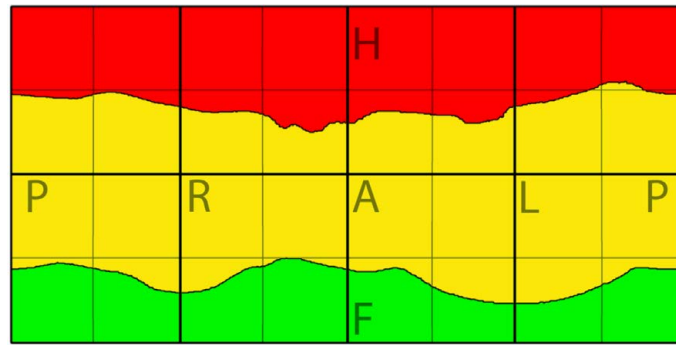
Figure 6.9: The sinusoidal projection (a) and the Mollweide projection (b) with color-coded texture coordinates (x = red channel, y = green channel).

A , L , P , R , H , and F (anterior, left, posterior, right, head, and foot respectively) are also included, which are common orientation directions in medical workstations. Figure 6.10 shows the three tumor map layouts with traffic light color scheme and labels. To allow correct interpretation of the tumor map, it is essential to distinguish the three traffic light colors and to relate the colors with the assigned ablation states. For people with some sort of color vision deficiency, particularly with red-green color deficit (Deutan and Protan defect), differentiation of the colors from a traffic light color scheme is a difficult task. To overcome this issue, the used colors can be adjusted according to the Color Universal Design (CUD) [83]. The set of colors in the CUD is unambiguous both to colorblinds (deuteranopes, protanopes) and non-colorblinds (trichromats). Figure 6.11 (a) shows the original tumor map color scheme (pure RGB colors: $(1,0,0)$, $(1,1,0)$, and $(0,1,0)$). Image (c) is the corresponding Deuteranope simulation [34] and (e) the Protanope color simulation. In both simulated images, two areas are difficult to distinguish. Figure 6.11 (b) shows the traffic light colors, selected from the set of CUD colors. Image (d) and (f) demonstrate that all areas are unambiguous to colorblinds and non-colorblinds.

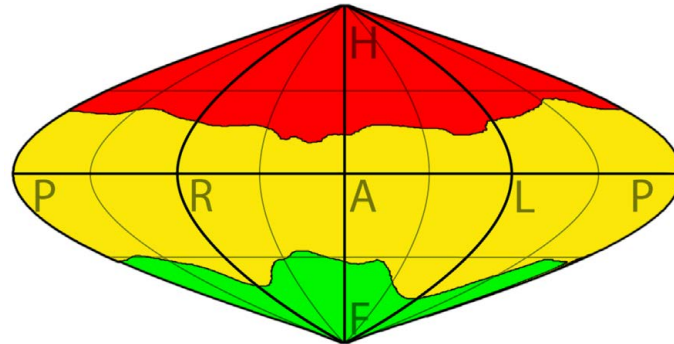
6.5.4 Interaction with the Tumor Map

In the introduced tumor map, surface voxels of the tumor mask are represented in a color-coded 2D image. Hence, all critical areas can immediately be recognized without requiring any interaction. However, assessing the ablation result itself can not be performed accurately using the tumor map alone due to the missing contextual information. On the one hand, the location of an specific area (e.g., a red coagulation zone) can be perceived on the map, but on the other hand, the anatomical context remains unclear. Hence, for every pixel in the tumor map, a visualization of the corresponding position in the volume rendering as well as in the 2D slice view is needed.

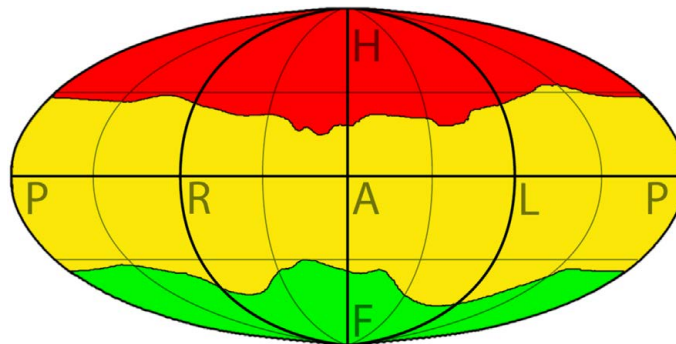
To synchronize the different viewers used for assessment with the tumor map, the mapping from \mathbb{R}^2 to \mathbb{R}^3 has to be calculated. If the user marks a point on the tumor



(a)



(b)



(c)

Figure 6.10: The images show the three tumor map layouts with traffic light color scheme: The equirectangular longitude–latitude mapping layout with high horizontal distortions at the poles (a), the tumor map with sinusoidal mapping layout (b), and the Mollweide projection (c).

map using the mouse, a lookup into the rectangular map is performed using the texture coordinate map of the layout projection. Subsequently, the corresponding distance value d (distance from tumor surface to center of gravity) stored in the rectangular map is fetched. Using this distance value and the position of the center of gravity \mathbf{p}_{tumor} , the corresponding world position can be calculated immediately.

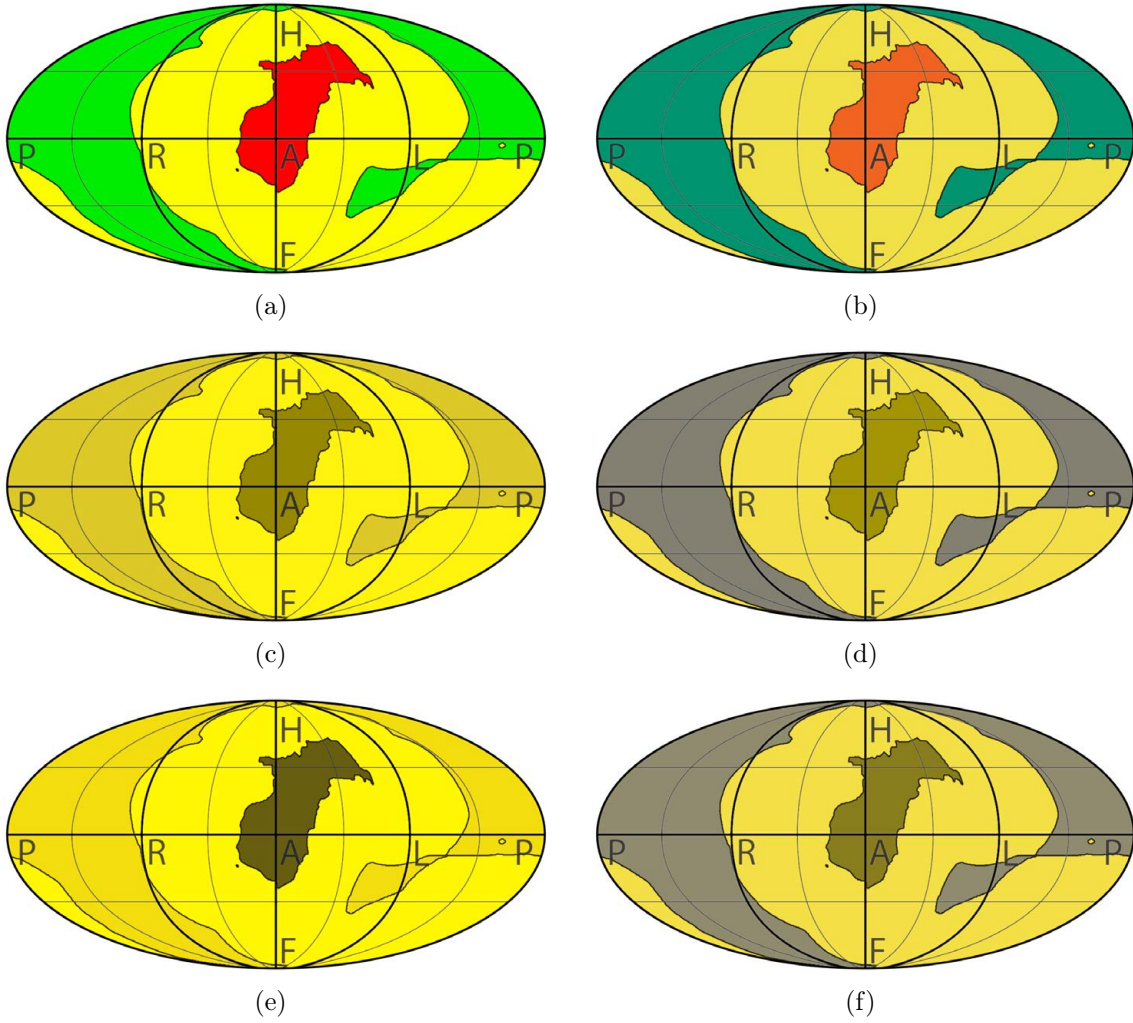


Figure 6.11: The images show a tumor map with traffic light color scheme (a) and the Color Universal Design color scheme (b) as it would be perceived by normal trichromats, deuteranopes (c,d), and protanopes (e,f). With the CUD colors, all areas are unambiguous, to colorblinds and non-colorblinds (d,f).

The longitude λ , defined from 0 to 2π , and the latitude ϕ , defined from 0 to π , can be calculated:

$$\lambda_{[0..2\pi]} = 2\pi \frac{p_x}{s_x} \quad (6.9)$$

$$\phi_{[0..\pi]} = \pi \frac{p_y}{s_y} \quad (6.10)$$

where $p_{x,y}$ is the position in the map texture and $s_{x,y}$ is the size of the map. The following equation calculates the corresponding world position \mathbf{p}_{world} for the given

geographic coordinates λ and ϕ :

$$\mathbf{p}_{world} = (\sin \lambda \sin \phi, \cos \lambda \sin \phi, -\cos \phi)d + \mathbf{p}_{tumor} \quad (6.11)$$

where \mathbf{p}_{tumor} is the center of gravity of the tumor.

The resulting world position is used to draw a cursor at the voxel position in the pre-interventional viewer as well as to automatically adjust the current slice stack. The post-interventional viewer is also adjusted using the registration matrix. If the user drags the mouse along a longitudinal direction from left to right, an interactive, counterclockwise movement of the cursor at the tumor's outline can be observed in the axial view. Analogously, a top-to-bottom mouse movement along the latitudinal direction causes the cursor to follow the tumor's outline in pole direction and causes the slice stack to change.

In the 3D volume rendering, an interactive adaptation of the view position is calculated to allow for observation of the point of interest marked in the tumor map. Using the longitude λ and latitude ϕ from Equations (6.9) and (6.10), the rotation vector $\mathbf{R}(\mathbf{v}, \alpha)$ is composed from rotation \mathbf{R}_λ and \mathbf{R}_ϕ :

$$\mathbf{R}(\mathbf{v}, \alpha) = \mathbf{R}_\lambda((0, 0, 1), \lambda)\mathbf{R}_\phi((- \cos \lambda, \sin \lambda, 0), \phi) \quad (6.12)$$

The rotation matrix \mathbf{M}_R is then composed from the rotation $\mathbf{R}(\mathbf{v}, \alpha)$ and the center point \mathbf{p}_{tumor} . Finally, the rotation matrix is applied to the volume rendering. Upon mouse movement in the longitudinal direction, the volume rendering rotates around the z axis; for latitudinal direction, the volume rendering rotates around the x and y axes. Consequently, the view point is always oriented to the currently selected surface point of the tumor. Moreover, using the equations given above, the inverse mapping from world position, marked by the user in the 2D viewer, onto the tumor map can be calculated. In fact, this mapping is only defined for surface voxels of the tumor mask. However, the visualization of the corresponding tumor map position is less interesting than the calculation of the rotation of the volume rendering. Therefore, for every world position \mathbf{p}_{world} , the normalized vector $\hat{\mathbf{v}} = \mathbf{p}_{world} - \mathbf{p}_{position}$ to the center point of the tumor \mathbf{p}_{tumor} with distance $d = 1$ is calculated:

$$\hat{\mathbf{v}} = (\sin \lambda \sin \phi, \cos \lambda \sin \phi, -\cos \phi) \quad (6.13)$$

Longitude λ and latitude ϕ can be evaluated resolving Equation (6.11). Finally, the necessary rotation matrix can be calculated with Equation (6.12).

6.6 Results

The proposed traffic light color scheme is an intuitive method to enhance the visualization of critical ablation areas for assessment of RFA. The color scheme is used in the familiar 2D slice visualizations as well as in the 3D volume rendering of a region of interest around the tumor. The volume rendering enables the immediate recognition of the spatial relation of the lesion within anatomical structures such as

vessels. However, the traffic color scheme is not suitable for people with color vision deficiencies such as color blindness. Thus, alternative traffic light color schemes under consideration of the CUD may be utilized.

The tumor map is developed as a novel visualization and interaction tool. It allows for a visualization of the color-coded ablation result using a cylindrical mapping of the tumor surface into a 2D texture map. Critical zones, such as the zone of incomplete cell destruction, can be recognized immediately. Moreover, the tumor map is an intuitive navigation tool. The user is able to navigate in the map using mouse interaction. Subsequently, the mapped world position is highlighted in the 2D viewer, and the slice stack is adjusted automatically so that the corresponding slice is visible. Additionally, the volume rendering view is adapted in such a way that the point of interest is always visible. Distance-based clipping prevents occlusion of the lesions by anatomical structures.

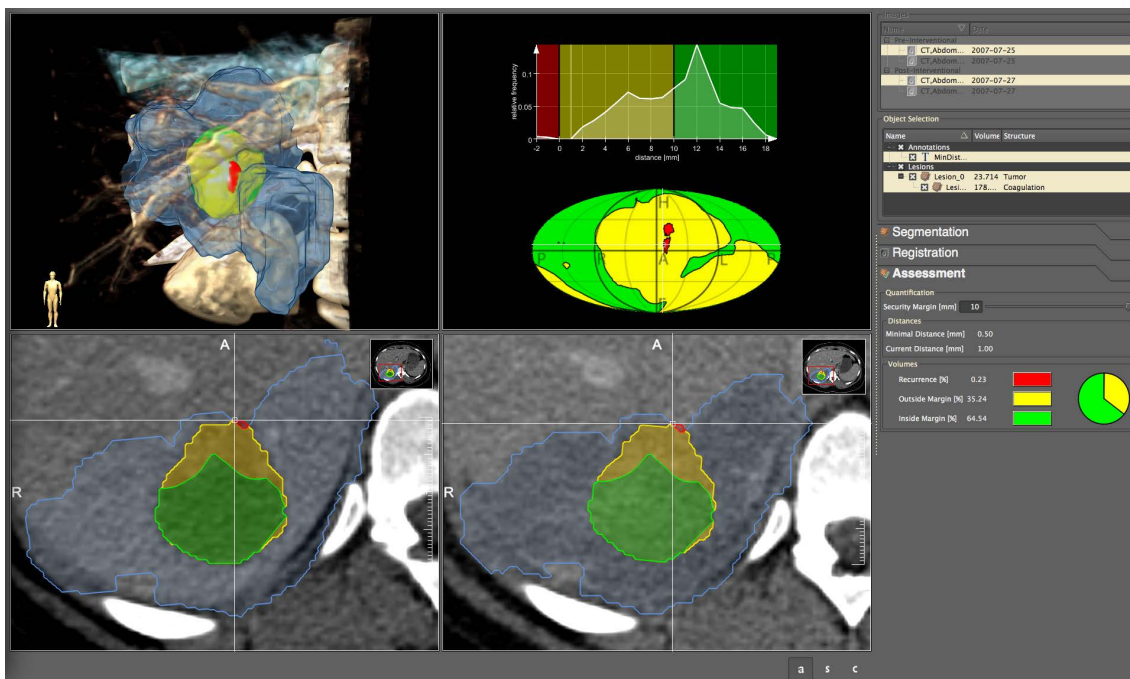


Figure 6.12: Integrated tumor map and visualization of tumor and coagulation with color scheme in the clinical software assistant. The plot above the tumor map displays relative distances from tumor to coagulation surface.

6.6.1 Implementation

The rapid prototyping software *MeVisLab* is used to develop C++ algorithms and GLSL shaders. The proposed methods are integrated in a software assistant (see Figure 6.12), designed for assessment of needle-based interventions. The preprocess-

ing, as discussed in Section 6.3, is integrated in the software assistant as an essential part of the assessment workflow.

6.6.2 Performance

The compositing of the tumor map takes approximately one second (2x2.66 GHz Xeon, ATI RadeonX 1900) and has to be performed once after applying the registration result. It is a minor performance bottleneck compared with reformation of the registered data set. After generation of the tumor map, the security margin can be changed interactively, because a fast texture lookup using the computed distance map is performed. Also, the visualization of the color scheme in 2D and 3D changes interactively, since only the distance threshold is changed for comparison with the fetched value of the loaded distance volume. Finally, the calculation of the corresponding world position from the current tumor map position is performed on the fly. Hence, using the tumor map, the user is able to navigate interactively through the data set.

6.6.3 Evaluation

The advantage of the tumor map is that the entire surface of the ablated tumor can be immediately explored without the need for any interaction. An evaluation of this obvious fact is not necessary. Thus, the evaluation is focused on whether interaction with the tumor map (under consideration of the Mollweide and equirectangular projections) is faster and more accurate than the rotation of a 3D scene with the widely used virtual trackball metaphor.

To answer these questions, a user study is set up with 13 subjects (4 female, 9 male, mean age 30.4), including natural scientists (3), computer scientists (6), and

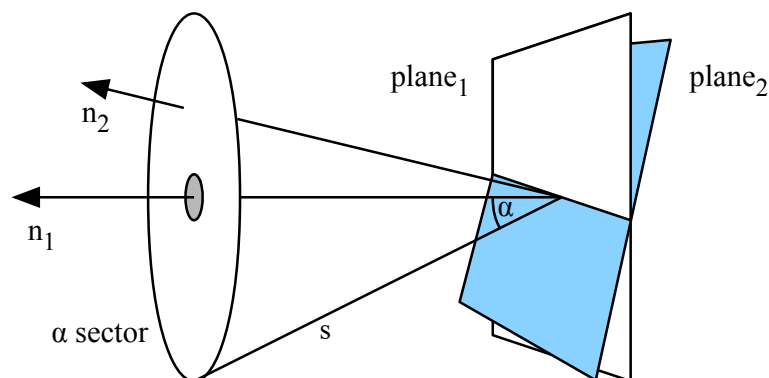


Figure 6.13: The α sector is defined by the angle α between orientation axis n_1 (the normal of $plane_1$) and the vector s . The orientation axis n_2 of the rotated $plane_2$ intersects the α sector (i.e., $\angle n_1, n_2 < \alpha$).

medical experts (4). 20 data sets, each with real lesion and artificial coagulation, are combined. Each subject has to rotate the tumor object to a given orientation (presented in a separate viewer) in random order. The subjects have to repeat the procedure using the tumor map with Mollweide and equirectangular layouts, respectively. Three circular cone sectors with 5, 10, and 15 degree opening angles from the reference orientation vector are defined (see Figure 6.13). If the user's orientation vector hits one sector (and does not leave it afterwards), the required time in milliseconds is measured. Additionally, the elapsed time until the user accepts his orientation as well as the accuracy in degree is measured.

Initially, the viewers show a black screen for every test case. To start the time measurement, the user has to start the current evaluation case manually by clicking onto the start button and the viewers display the color-coded lesion and the tumor map, respectively. The upper left viewer shows the reference orientation of the colored lesion and the upper right the template lesion to be rotated by the user. In the case of the tumor map, the cursor is used to rotate the template lesion to the reference orientation. In the case of the virtual trackball metaphor, the user directly rotates the template tumor in the viewer. Finally, if the user is satisfied, the rotation is accepted by typing the space key, the time is stopped and the angle measured. This procedure is repeated for every test case. Figure 6.14 shows the evaluation application with tumor map setting (a) and virtual trackball setting (b).

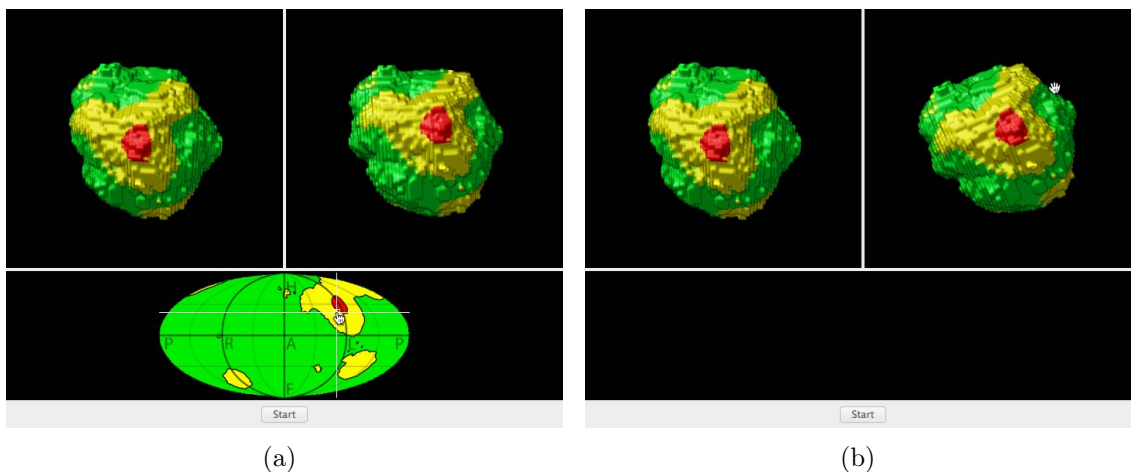


Figure 6.14: Screenshots of the evaluation application. Image (a) shows the setting for tumor map interaction, image (b) the virtual trackball metaphor. The upper left viewer displays the lesion with reference orientation and the upper right viewer the lesion to be rotated.

The stored times of the study are analyzed with an analysis of variance (ANOVA). Statistically significant ($p < 0.05$) changes in the mean of the needed time to enter the 15 degree sector are observed. The measured times with the equirectangular layout are the smallest ($\bar{x} = 7,25$ sec), followed by the Mollweide map ($\bar{x} = 8,70$ sec)

and the virtual trackball metaphor ($\bar{x} = 9,97$ sec)). Despite the high distortions of the simple longitude–latitude mapping, the subjects can better navigate, because longitudes and latitudes are mapped onto a rectangular grid. In contrast, for a vertical rotation in the Mollweide map, the subjects have to follow the curved longitudinal lines, which is not easy to achieve. The mean times of other two sectors (10 and 5 degree) show generally the same trend, but are not significantly different for all three modalities. Figure 6.15 shows the elapsed seconds per sector and mapping modality. Also, a low variance of the equirectangular mapping compared with the other mappings can be observed for all three sectors.

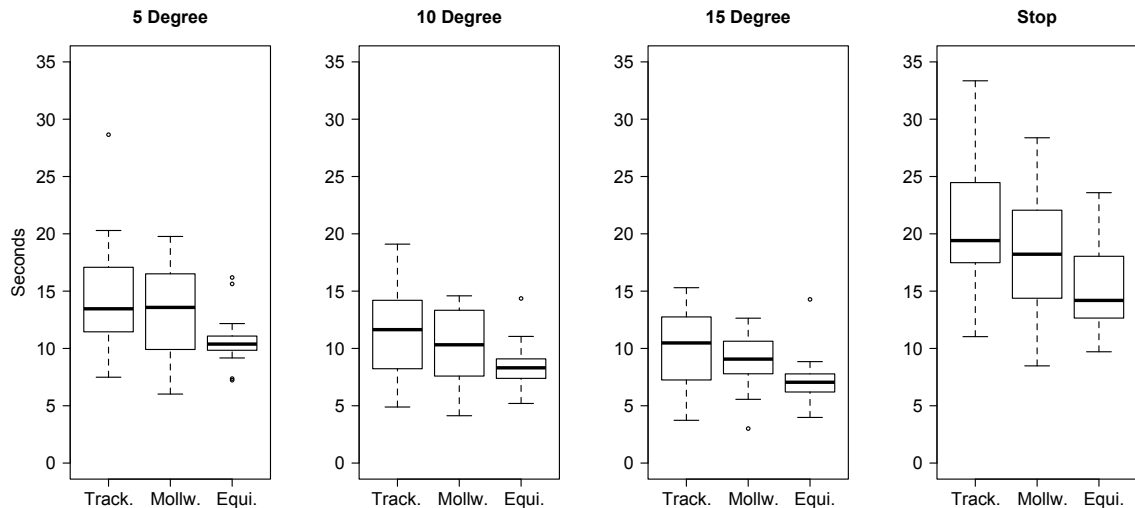


Figure 6.15: The box plots show the elapsed seconds for every mapping modality for all three sectors and the final orientation accepted by the subjects.

Table 6.1 shows the mean time to hit the sectors, the mean times the subjects defined as the optimal orientation match and the resulting mean angles. Because the subjects did not hit all sectors, those sectors are ignored in this evaluation. Table 6.2 shows the mean hit rate for all three sectors. For all modalities, equal hit rates per sector are measured. Thus, the small difference of the hit rates supports the validity to compare the measured sector times for all modalities. Another aspect of this user study is that differences in the influence of the chosen cases can be observed. Navigation with the tumor map is particularly faster if expressive color or shape features are visible on the tumor (see Figure 6.14). Without features, no significant changes are measured.

Supplementary results of the study are that there is no statistically significant differences in the achieved orientations with all three modalities (Trackball: $\alpha = 4,33^\circ$, equirectangular: $\alpha = 4,30^\circ$, Mollweide: $\alpha = 4,02^\circ$). Furthermore, a significant deviation in the elapsed time is not measured. All subjects tried to achieve maximum accuracy and required on average an equal amount of time with all methods. In

	5° (sec)	10° (sec)	15° (sec)	stop (sec)	angle (°)
Trackball	15,15 ± 5,6	11,92 ± 4,3	9,97 ± 3,6	21,94 ± 8,5	4,33 ± 1,3
Mollweide	13,45 ± 4,4	9,87 ± 3,4	8,70 ± 2,8	18,67 ± 6,3	4,02 ± 1,4
Equirect.	10,83 ± 2,6	8,15 ± 2,3	7,25 ± 2,5	15,71 ± 4,5	4,30 ± 1,4

Table 6.1: The table shows the mean time to hit the sectors (5, 10 and 15 degree), the mean time the subjects stopped the interaction and the mean angle.

	5° hit rate (%)	10° hit rate (%)	15° hit rate (%)
Trackball	70,4 ± 12,2	95,5 ± 6,4	99,2 ± 2,4
Mollweide	76,9 ± 13,2	94,3 ± 6,7	98,0 ± 3,5
Equirect.	71,7 ± 13,1	94,3 ± 5,0	99,2 ± 2,4

Table 6.2: The table shows the mean rate to hit the sectors (5, 10 and 15 degree) for trackball metaphor, the Mollweide projection and the equirectangular projection.

conclusion, using the tumor map (with the equirectangular layout), the subjects are able to navigate significantly faster close to the target orientation. Figure 6.16 gives a detailed overview of the measured times per subjects for all modalities. Note that the rate to hit the sectors influences the averaged times in the plots.

6.6.4 Clinical Study

In order to compare the clinical value of the presented interactive visualization method with the traditional visual comparison of pre- and post-interventional images, a retrospective clinical study is conducted. Comparing the software assistance with the conventional method, the following hypotheses are evaluated:

- **H1:** Local tumor recurrence can be more accurately predicted.
- **H2:** Local tumor recurrence can be more rapidly predicted.

For that, four radiologists with different levels of experience (5, 3, 4, and 7 years clinical practice, referred as R1-4) assess the treatment success in 39 cases (tumor-coagulation pairs), retrospectively. The 39 cases to be evaluated are extracted from 31 patients, whereas 29 cases are without post-interventional findings and 10 cases with local tumor recurrence. The medical experts use the proposed software assistant (referred as software-assisted method) and a simple synchronized viewer (referred as conventional method) for comparison of the CT images. In the evaluation software, tumors and corresponding coagulations are already segmented using interactive segmentation tools. The segmented image masks are verified by an experienced physician. Also, the registration of the data sets is calculated beforehand.

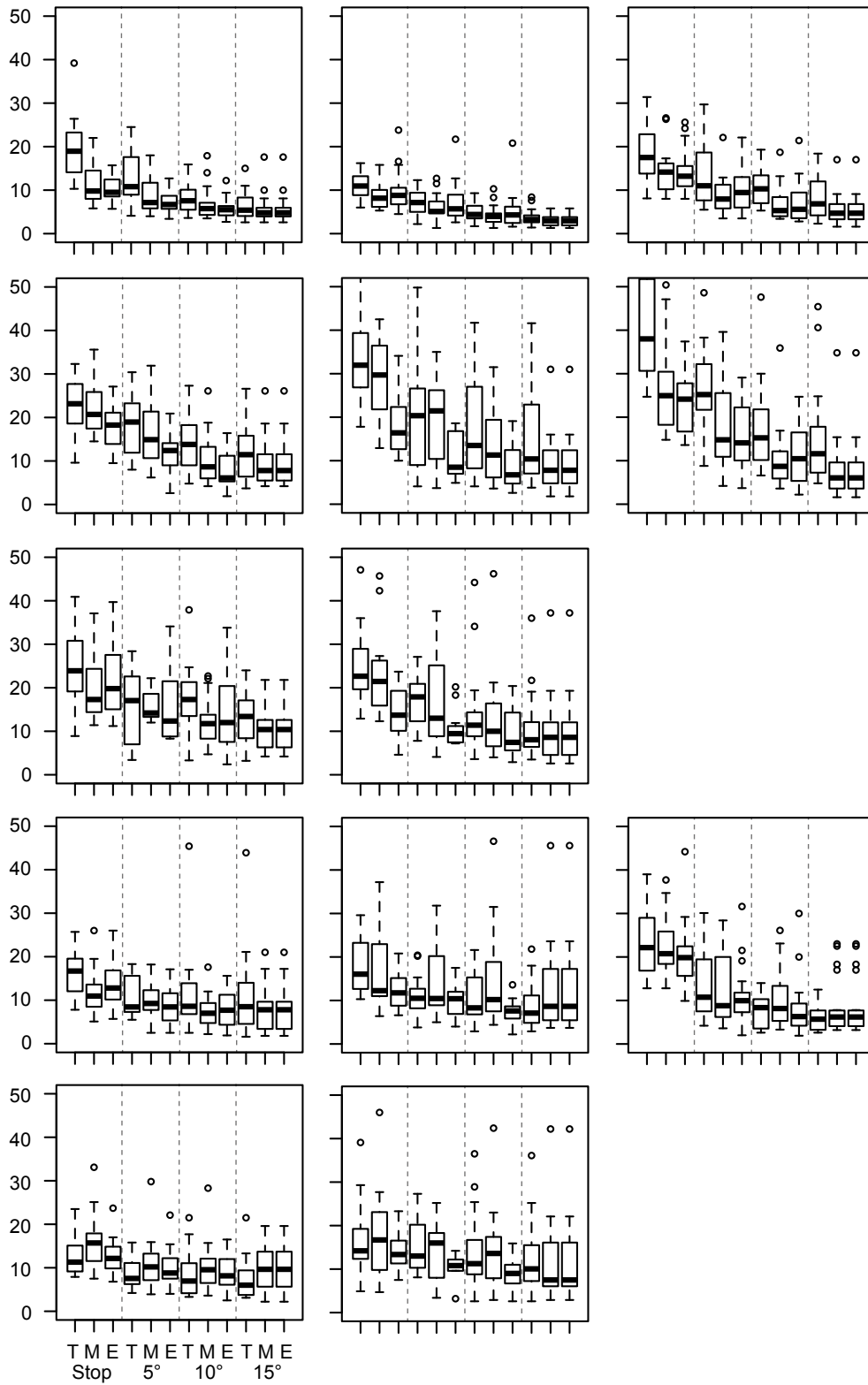


Figure 6.16: The plots shows the elapsed time per subject for the 5, 10, 15 degree sector and the stopped interaction, respectively (T=Trackball, M=Mollweide, and E=Equirectangular).

Since the data sets from the previously discussed registration study are used, the optimal registration result after landmark matching is applied for image comparison (see Section 5.4.2).

To avoid any recall bias, the cases are randomized and are evaluated in two sessions within a 4-week interval. The cases are alternately analyzed with the two methods. Thus, per session each case is only once analyzed with the software-assisted and the conventional method, respectively. Further, the study is blinded for the readers, i.e. the final patient outcome (ground truth) is not known.

In the conventional evaluation application, both data sets are presented in two parallel viewers. The data sets can be reformatted to axial, sagittal and coronal images. The slices as well as the windowing of both viewers can be synchronized by the reader. No additional tools are available. In the novel software assistant, the registered pre- and post-interventional data sets are simultaneously displayed in two slice viewers. Using the registration information, the viewers are synchronized and both, the tumor mask as well as the coagulation mask, are superimposed onto the CT images. The presented traffic light color scheme is applied on the tumor mask as discussed in Section 6.4. Further, a volume rendering of the ROI around the tumor as well as the *tumor map* are displayed. In both software applications, each reader starts and ends the reading process by clicking a start and next button, respectively. The elapsed time is measured during this reading process excluding case loading time. To finalize a case, the reader has to determine if he expects local tumor recurrence. Also, the estimated minimal safety margin on a 4-point scale (< 0 , < 2.5 , < 5 , ≥ 5 mm) and the self-confidence on a six-point scale (min confidence: 1, max confidence: 6) are specified in the GUI of the software by the reader. Optionally, comments may be written.

	unfiltered		$d < 4$ mm		$d < 3$ mm	
	conv.	assist.	conv.	assist.	conv.	assist.
Sensitivity	0.35	0.60	0.41	0.72	0.45	0.90
Specificity	0.89	0.83	0.92	0.86	0.92	0.90
PPV	0.52	0.55	0.65	0.64	0.69	0.78
NPV	0.80	0.86	0.82	0.90	0.80	0.96

Table 6.3: The averaged sensitivity, specificity, positive predictive value (PPV), and negative predictive value (NPV) to predict tumor recurrence with conventional (conv.) and software-assisted (assist.) method, respectively. The results are grouped into the 39 unfiltered cases, cases with landmark registration distance of $d < 4$ mm and of $d < 3$ mm.

After conduction of the complete reading process, the measured parameters are analyzed. To verify **H1**, the performance to predict local tumor recurrence with the conventional (abbreviated as conv.) and the software-assisted (abbreviated as assist.) method is compared. Using the ground truth, the prediction performance is

measured with sensitivity, specificity, positive predictive value (PPV), and negative predictive value (NPV). The averaged sensitivity of all readers, i.e. the percentage of correctly identified tumor recurrences, using the software-assisted method is higher for all readers (0.6 vs. 0.35). The averaged specificity of all readers, i.e. the percentage of correctly identified successful ablations, is slightly lower with the software-assisted method (0.83 vs. 0.89). The values reflect the ability of the software-assisted method to correctly detect a higher percentage of tumor recurrences, but also a higher percentage of incorrectly detected successful ablations. Table 6.3 shows the averaged performance of the readers to predict local tumor recurrence out of all unfiltered 39 cases with the conventional and the software-assisted method. Table 6.4 gives an overview of the reader’s individual performance analyzing all cases.

	Reader 1		Reader 2		Reader 3		Reader 4	
	conv.	assist.	conv.	assist.	conv.	assist.	conv.	assist.
Sensitivity	0.30	0.60	0.40	0.50	0.40	0.70	0.30	0.60
Specificity	0.89	0.82	0.93	0.86	0.79	0.72	0.93	0.90
PPV	0.50	0.55	0.67	0.56	0.40	0.47	0.60	0.67
NPV	0.79	0.86	0.81	0.83	0.79	0.87	0.79	0.87

Table 6.4: The individual sensitivity, specificity, positive predictive value (PPV), and negative predictive value (NPV) for each reader to predict tumor recurrence with conventional (conv.) and software-assisted (assist.) method, respectively.

Since the accuracy of the optimal registration result after landmark matching is known (see Section 5.4.2), the cases are filtered by a landmark distance of $d < 4$ mm and of $d < 3$ mm, respectively. After filtering with $d < 4$ mm, 23 normal cases and 8 recurrence cases are left over, with $d < 3$ mm, 12 normal cases and 5 recurrence cases. The averaged performance is calculated for both filtered populations. It turns out that all statistical measures using the software-assisted method increase, particularly the sensitivity (0.72 and 0.9, respectively), whereas the measures using the conventional method only slightly differ. The increasing performance indicates the strong dependency of the software-assisted method on the registration accuracy.

Because the presented performance does not take the individual confidence of the reader into account, a receiver operating characteristic (ROC) is calculated. For that, the binary decision *recurrence or not* is weighted with the self-confidence specified by the reader. Thus, the ROC curve illustrates the performance of the binary classifier system as its discrimination threshold (self-confidence) is varied. The red ROC curve in Figure 6.17 shows the performance using the conventional method, the blue ROC curve the performance with the software assistance. The filled point in each curve illustrate the unweighted sensitivity and specificity of the two methods as reported in Table 6.4. It is observed that the averaged performance using the software-assisted method is slightly better than the conventional method. If the

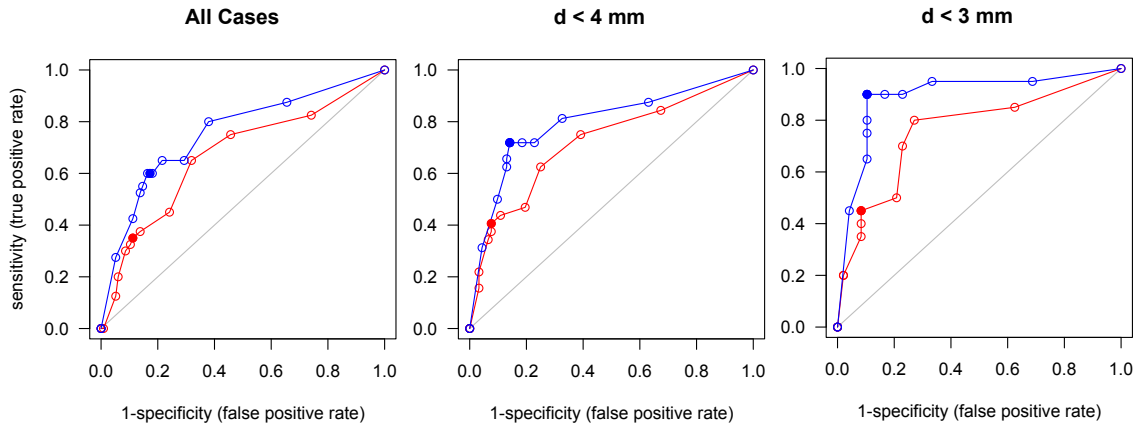


Figure 6.17: Receiver operating characteristic (ROC) for all readers. The red ROC curve shows the performance with the conventional method, the blue ROC curve the software-assisted method. The ROC plots are divided into the 39 unfiltered cases, cases with landmark registration distance of $d < 4$ mm and of $d < 3$ mm.

cases are again filtered by $d < 4$ mm and $d < 3$ mm, respectively, it is clearly visible that the software-assisted curve is significantly improved. Thus, if the registration accuracy is higher, more local tumor recurrences can be correctly identified whereas the percentage of incorrectly identified successful ablations decreases.

Figure 6.18 shows the ROC curves for each reader comparing both methods using all cases. The software-assisted curves (blue) of R3 and R4 show a higher classification performance compared with the conventional method (red). Thus, their prediction accuracy significantly improves from the additional software-assisted methods. In contrast, R2 does not benefit, and R1 only partially benefits from software assistance. Further, the conventional curve (red) of R2 noticeably differs from all other curves. Three observations could be responsible for the difference: first, R2 needed more time for conventional assessment than all other readers, second, he used sagittal and coronal reformations more often (particularly for peripherally located lesions), and third, he weighted his findings with a higher self-confidence variability. Generally, the varying ROC curves show the different prediction performance of the four readers concerning sensitivity and specificity.

To verify **H2**, the elapsed times the readers need for both, conventional and software-assisted method, are analyzed (see Figure 6.19). It is observed that only R2 is significantly slower with the conventional method (mean increase of 43 seconds). R2 and R3 are slightly slower and R4 slightly faster with the software-assisted method. The minor differences result from the similarity of the performed analyses. The readers use the software-assisted method in the same way as the conventional method. The tumor map, the volume rendering, and the color overlay are used as additional features for slice-by-slice analysis. Particularly the color overlay is used

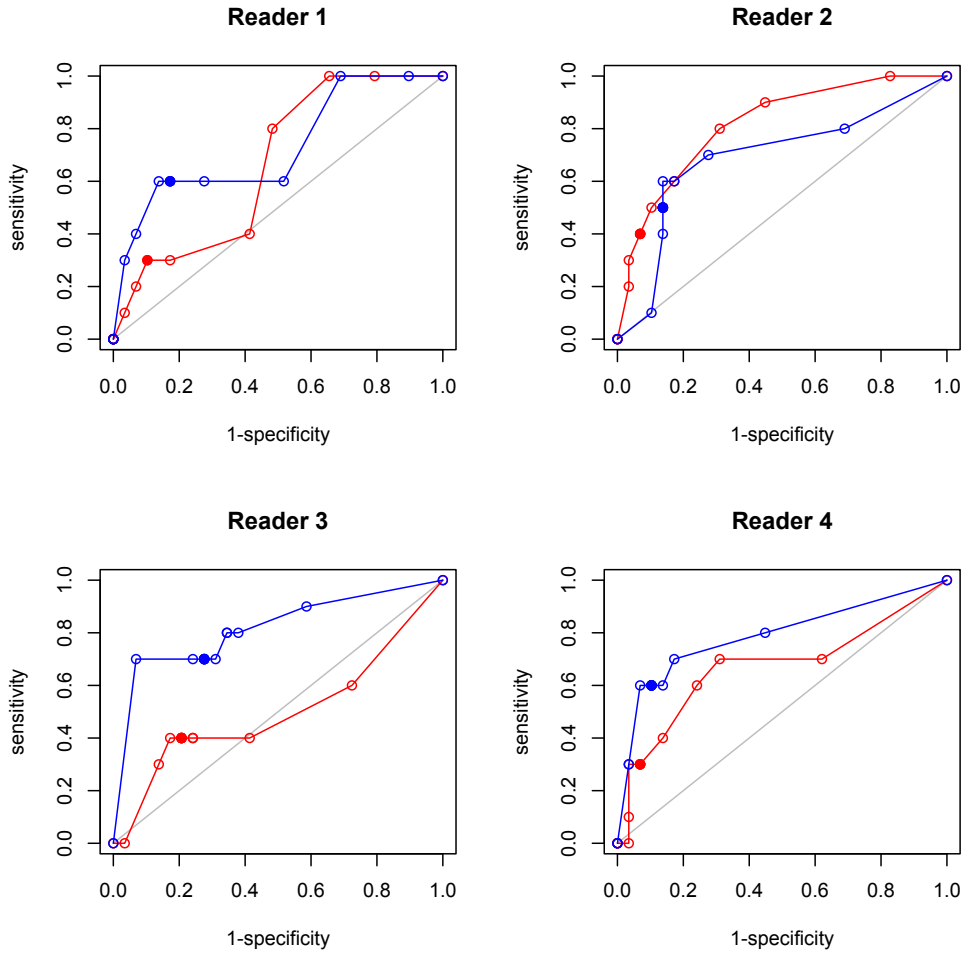


Figure 6.18: Receiver operating characteristic (ROC) for each reader. The red ROC curve shows the performance with the conventional method, the blue ROC curve the software-assisted method.

to verify the tumor's shape and location regarding the coagulation necrosis. The tumor map as well as the volume rendering are mainly used to rapidly get an overview of the complete tumor's surface. The detailed assessment of the treatment result is done by examination of the anatomical image slices.

6.6.5 Outlook: Tumor Map for Intervention Planning

The tumor map is a general method to display distances (or thresholded distances, i.e. ablation states) in a map projection. Thus it is not restricted to the assessment of RFA. Another useful application is the interactive visualization of the traffic light color scheme in a tumor map for planning of the optimal electrode position. The tumor map is based on the projection of the ablation zone onto the target lesion's surface. Two additional requirements can be determined for interactive visualization:

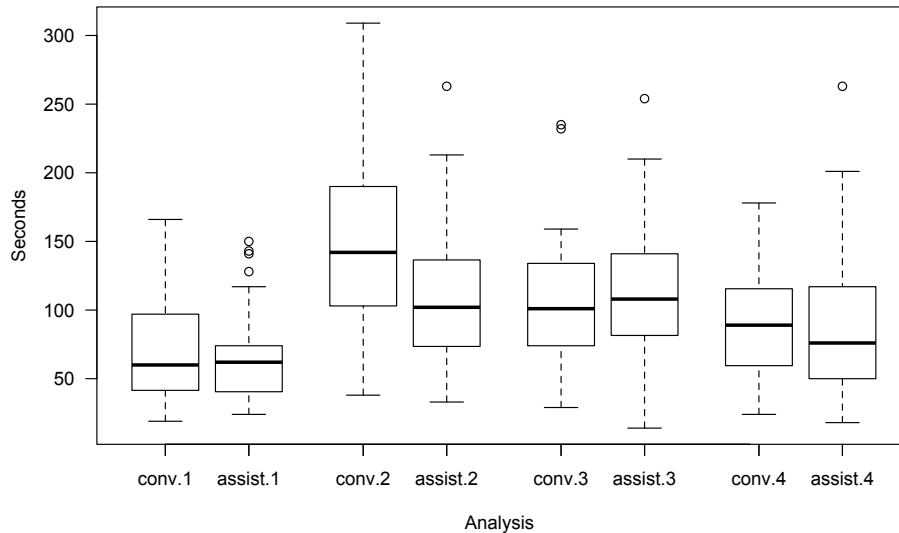


Figure 6.19: The elapsed time for the reading process with conventional and software-assisted method for each reader.

- Fast calculation of the Euclidean distance transform.
- Fast compositing of the tumor map projection.

Since the applicator with corresponding ablation zone can be moved by the user, the goal is to update the *tumor map* interactively. Thus, the inverse Euclidean distance transform of the estimated ablation zone has to be calculated in real-time in order to allow interactive visualization of the ablation state. For that, a fast GPU-based implementation of a distance transform may be utilized [154].

Rendering of arbitrary number of horizontal tiles of the tumor surface is too time consuming for interactive updating of the *tumor map*. As an alternative method, the cube map approach [70] may be utilized to render the complete surface of the tumor into a single texture (see Figure 6.20). For that, 6 perpendicular views using perspective cameras are set up and render in parallel into frame buffer objects [127]. The cube map is composed from the 6 frame buffer objects. Subsequently, the cube map has to be transformed into a rectangular map by means of trigonometry. Because the resulting rectangular map does not contain vertical distortions, the deskew filter has not to be applied. The last step is the application of the color scheme as described in Section 6.5.2. Figure 6.21 shows a proof-of-concept of the tumor map for planning of RFA interventions.

6.7 Discussion and Conclusion

In this chapter, novel visualization and interaction techniques for software-assisted assessment of needle-based interventions are presented. Familiar methods of medical

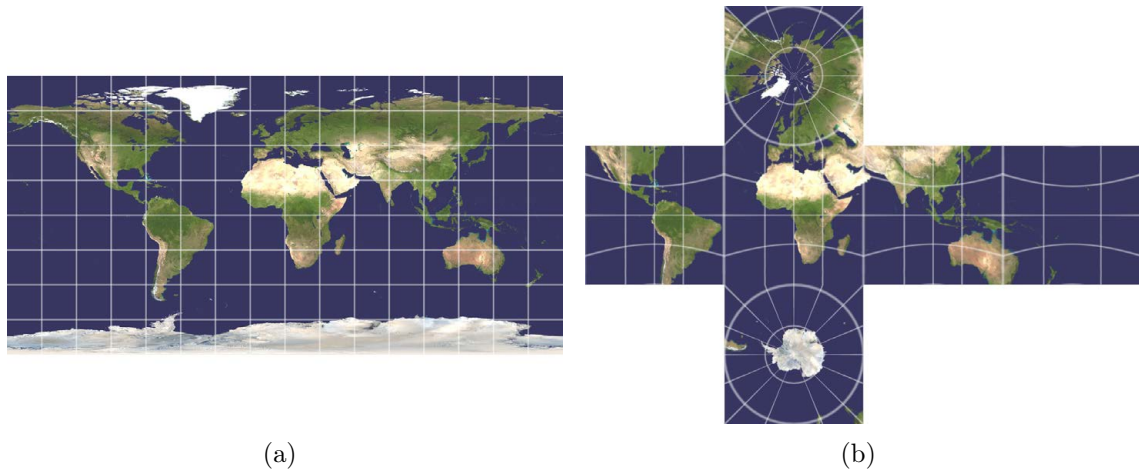


Figure 6.20: Image (a) shows an equirectangular map of the Earth and (b) the corresponding cube map. Note the curved pathways of the rectangular isolines in the cube map.

workstations, such as 2D slicing, and anatomical 3D volume rendering, are combined with new approaches, such as the color-coding scheme and the tumor map. Interactive view selection and automatic determination of transfer function for volume rendering substantially reduce the required interaction time.

The main contribution of this work is the immediate detection of local tumor recurrence in the tumor map by the physician without the need for any interaction. However, a drawback of the chosen cylindrical mapping is that tumors which are concave and not star-convex (a ray from center to surface has multiple exit points) can not be accurately mapped into a 2D image. This issue can be solved by adapting the rendering of the rectangular map. Instead of storing the distance at the first exit point, the distance has to be stored at the last exit point (see Figure 6.22). Although not all surface points are mapped into the resulting map, the missing points are implicitly represented as voxels inside of the tumor. From a medical point of view, this issue can be neglected, because local tumor recurrence is generally expected at the tumor's rim.

An additional advantage of the proposed method is the possibility to mark suspicious regions in the tumor map which are immediately visible in the 2D viewers and in the volume rendering. For this task, the Mollweide map is the preferred layout because of the intuitive, well-known shape and the less distortion. The evaluation shows that rotating the tumor object using the tumor map with the rectangular layout is significantly faster than rotating with the virtual trackball metaphor. Thus, navigation with the equirectangular tumor map is an intuitive alternative to common techniques for interactive exploration of tumors. Hence, in the software assistant, the user is able to switch between the tumor map layouts. Due to the synchronization of the 2D and 3D viewers, the tumor map may be used as navigation tool which

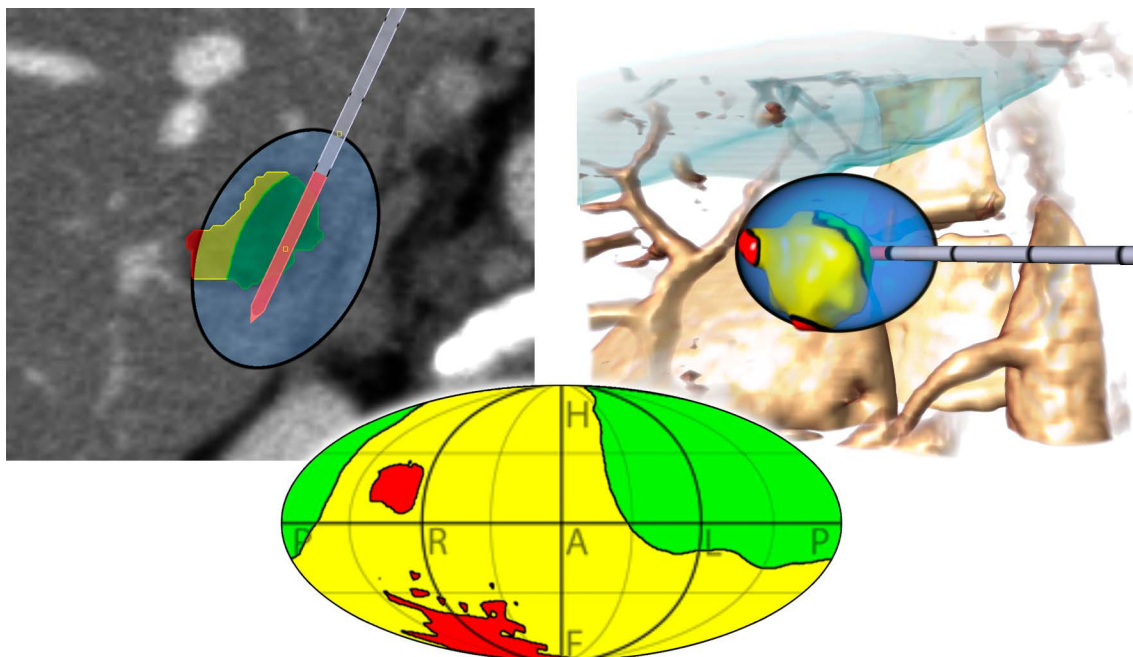


Figure 6.21: Tumor map for planning of RFA. Similarly to the originally proposed approach, the tumor is colored with the ablation states retrieved from the ellipsoidal ablation zone (originally coagulation). The corresponding tumor map is interactively updated if the ablation zone is changed, e.g. moved by the user.

could lead to a higher acceptance of the volume rendering in a medical workstation.

In the clinical study, 39 cases are retrospectively analyzed by four radiologists with the conventional as well as the software-assisted method. Goal of this study is the verification of two hypotheses, first, if local tumor recurrence can be more accurately predicted, and second, if local tumor recurrence can be rapidly predicted. The results of the study are compared with the medical ground truth. The analysis of the data confirms that the software-assisted method allows the experts to correctly identify local tumor recurrence with a higher percentage (sensitivity: 0.6 vs. 0.35), whereas the percentage of correctly identified successful ablations is slightly reduced (specificity: 0.83 vs. 0.89). It is also shown that the registration accuracy determines the performance to correctly predict local tumor recurrence with the software-assisted method. Furthermore, assessment using the software-assisted method is slightly slower than using the conventional method (average: 104 vs. 94 seconds). This is caused by the fact that the readers use the software-assisted method in the same way as the conventional method, i.e. mainly slice-by-slice analysis (with registered traffic light color overlay). Thus, they do not exploit the full potential of the proposed software-assisted method.

A further observation of the study is the difficulty to handle peripheral lesions,

In conclusion, the presented methods support the physician in interactive achieving a reliable therapy assessment. However, the accuracy of the ablation verification depends heavily on the robustness of the segmentation and the precision of the registration of pre- and post-interventional image data. Moreover, the results generally depend on the resolution of the image data. Suitable interactive segmentation as well as automatic registration algorithms are subjects of ongoing research.

The methods proposed in this chapter are presented to support interactive assessment of the RFA. However, they are basically independent from any type of intervention or image data. Since the requirements of the interactive visualization methods are segmentation masks of the areas to be compared and the corresponding registration, they can be also applied for other interventions such as MWA or cryoablation.

This chapter is in part based on the following publication:

- **C. Rieder**, A. Weihusen, C. Schumann, S. Zidowitz and H.-O. Peitgen. Visual Support for Interactive Post-Interventional Assessment of Radiofrequency Ablation Therapy. In: *Computer Graphics Forum (Special Issue on Eurographics Symposium on Visualization)* 29, 3, pp. 1093-1102, 2010.

The word user is the word used by the computer professional when they mean idiot.

(Dave Barry)

7

A Shader Framework for Rapid Prototyping

IN medical visualization, specific visualization algorithms are commonly developed to create meaningful images for diagnosis, treatment planning, or intra-operative image guidance. However, rapid customization of such algorithms is a challenging task. In this chapter, a rapid prototyping framework for GPU-based volume rendering is presented. Therefore, a dynamic shader pipeline based on the *SuperShader* concept is proposed and the design decisions are illustrated. Also, important requirements for the development of such a system are presented.

7.1 Introduction

Direct volume rendering (DVR) is used to create meaningful images from 3D data sets [50]. It calculates how emitted light is absorbed and scattered along the transport through the volume to the observer. GPU-based approaches that allow for interactive rendering on consumer graphics hardware have been proposed [71]. Interactive GPU-based DVR is used in many fields, particularly in medical visualization. However, the creation of meaningful visualizations for medical diagnosis is challenging, due to the particular needs of the medical users [115]. In the literature, effective visualization algorithms have been proposed, which often focus on specific image acquisition strategies and medical questions [26]. A key problem of common rendering frameworks is the high amount of effort which is required to develop appropriate visualizations and to customize the algorithms rapidly.

As part of this PhD thesis, a rapid prototyping framework for GPU-based volume rendering is presented, which supports computer scientists in the development of expressive volume visualizations. The framework extends the volume renderer of *MeVisLab* [143, 116], a freely available development environment for medical image processing and visualization, to allow the developer to interactively append custom shader code. Thus, appropriate solutions for specific visualization problems can be developed rapidly. The main contributions of this chapter are:

- The determination of important requirements for the development of a rapid prototyping framework for volume rendering upon which the design decisions are based.
- The introduction of a dynamic rendering configuration to facilitate a customized extension of the rendering shader. Technically, a flexible and modularized shader pipeline based on the *SuperShader* concept is presented.
- The realization of a rapid prototyping environment, in which custom shader code can be interactively edited and attached to the shader pipeline during run-time.
- The demonstration of the usage and usefulness of the proposed system, which is used to rapidly develop medical visualizations and integrate them in clinical applications.

The outline of this chapter is as follows: In Section 7.2, related works in the fields of dynamic creation of volume rendering shaders and volume rendering frameworks are discussed. Section 7.3 explains the important requirements for DVR-based rapid prototyping. In Section 7.4, design decisions and the basic approach of the proposed dynamic shader pipeline are illustrated. In Section 7.5, the prototyping environment and the technical realization of the custom shader pipeline are explained. Three example application of the presented framework are outlined in Section 7.6. A comparison with related systems is discussed in Section 7.7, and the conclusion with outlook is described in Section 7.8.

7.2 Related Work

Dynamic shader creation has been a research topic even before modern programmable GPUs became available. It is an important topic in many fields of image generation, not only volume rendering. One of the first approaches for the combination of multiple techniques for illumination and texturing are *Shade Trees* [46], which combine basic shading operations using a data flow concept. Abram and Whitted [18] combine that approach with a graphical user interface to enable efficient generation of shader programs and represent the first *Visual Shading Language*. In recent years, similar implementations have been proposed for GPU-based realtime rendering [65, 112, 114]. All these visual programming based approaches are aimed at simplifying the shader definition for the user, e.g., for an artist [66, 169]. However, this does not reflect the needs of application-controlled shader adaption for GPU-based realtime rendering in complex visualization systems or games. Such scenarios require the generation of specific effects at run-time without the requirement to store all possible permutations [57]. Furthermore, a general strategy for providing common and controllable effects while maintaining high performance is needed.

A concept designed for these special needs is the *SuperShader* [113]. The basic idea of this approach is to break down the whole shader into smaller parts [77], in a way that its subdivision is based on components of the underlying rendering pipeline. The *SuperShader* contains all potentially required parts in the form of code snippets and allows for deactivation of undesired parts. Communication between the parts is achieved by means of a global data structure. Trapp et al. [172] extend that approach by adding a *Shader Management System* that concatenates the shader at run-time instead of disabling unused parts.

A simple and flexible volume rendering framework for GPU-based raycasting is presented by Stegmaier et al. [166]. New algorithms are implemented by writing completely new shaders. Bruckner et al. [37] present *VolumeShop*, a prototyping platform for visualization research, and direct volume illustration in particular. Its main aim is to provide maximum flexibility for the developer to create illustrative visualizations such as exploded views or three-dimensional selection painting. Also, several volume rendering frameworks specifically address rendering of multiple intersecting volumes. Brecheisen et al. [33] describe a raycasting-based multi-volume rendering system, which uses a depth-peeling approach to combine geometry and multiple volumes in one rendering. Plate et al. [137], present a multi-volume shader framework that focuses on rendering very large, multi-resolution intersecting volumes. A shader composer which is based on the data flow model allows composing predefined shader nodes to a final rendering shader at run-time.

Voreen [117], based on raycasting, provides a graphical user interface for defining a network of so-called processors which assemble a rendering pipeline. Predefined functions of a shader library can be edited or substituted by the user before they are included into the final shader. Although *Voreen* gives control over the rendering pipeline, it does not allow for dynamically changing parts of the rendering shader

without modifying the remaining shader code. This is possible within the render graph concept introduced by Rössler et al. [147, 146]. Using this approach, modularized shading algorithms can be defined and interactively combined to render multiple volumes. To extend this system with new render nodes, the user has to inherit from existing C++ base classes. Thus, the abstract render nodes can not be edited on the fly, nor can they be automatically created by the application. In contrast to these concepts, the framework proposed in this PhD thesis focuses on the developer- or application-controlled dynamic editing of modularized shader code.

Further systems in the medical imaging community allow to combine visualization and image processing algorithms. Bitter et al. [28] compare four freely available frameworks for image processing and visualization that use ITK¹. A survey of the most successful open-source libraries and prototyping frameworks for medical application development is presented by Canban et al. [39]. Another prototyping environment is the eXtensible Imaging Platform (XIP) [140, 185], which has basically a comparable functionality as *MeVisLab* [143, 116]. However, none of the related prototyping and volume rendering frameworks allow dynamically extending the rendering shader with modularized custom shaders snippets, which can be freely edited by the developer during run-time.

7.3 Rapid Prototyping

The general motivation to use rapid prototyping for volume rendering is the possibility of developing appropriate solutions for a current visualization problem in an interactive way, without recompilation of the C++ program, and to quickly integrate the solution into stand-alone applications. For instance, in medical visualization, specific visualizations have to be created for image-guided surgery planning, diagnosis support for various diseases, or anatomical exploration of the patient data. In many cases, changing high-level rendering parameters of existing features does not solve such complex visualization problems. Hence, the volume renderer has to be extended with new features, which is often not possible in the underlying C++ code level at run-time. Because the recompilation of programs impedes the concept of rapid prototyping, the renderer has to be configured in a level between low-level C++ code programming and high-level parameter adjustment. Thus, the following important requirements for DVR-based rapid prototyping have been determined:

Rendering Extension. The developer has to be able to manipulate the rendering configuration, particularly the shader code. To create new rendering effects, modularized custom shader code should be created and positioned into the existing rendering configuration while ensuring a valid shader.

¹Insight Segmentation and Registration Toolkit: www.itk.org

Dynamic Rendering Configuration. To allow the evaluation of the rendering extension of the prototyping application at run-time, a dynamic rendering configuration is needed. Hence, the shader code of the volume renderer has to be structured in a way that high-level changes of the rendering configuration result in the implicit modification of the underlying shader code.

Function Library. In an efficient prototyping environment, frequently-used shader functionality should be defined in shader functions and stored in a function library. With access to these functions, the user is able to rapidly implement custom shader code.

Suitable User Interface. To facilitate the implementation of the modifications mentioned above, a suitable user interface (UI) has to be available within the prototyping environment. Such an UI allows the user to develop custom shader code, which uses the function library, and to specify the extension of the renderer with the custom shader. Additionally, shader parameters, such as uniform variables and texture samplers, can be attached to the renderer.

7.4 Dynamic Shader Pipeline

The dynamic shader pipeline is the core functionality, which allows for interactive rendering extension and dynamic configuration of the volume rendering. The OpenGL Shading Language (GLSL) is used due to the independence from graphics card vendors and computer platforms.

7.4.1 Design Decisions

The design decisions upon which the proposed system is based relate to three key ideas:

- Breaking down the shader code into sections containing code for different computations.
- Definition of shader code as freely combinable, modularized shader blocks.
- Insertion of custom shader code between blocks without invalidating the final shader.

The *Shade Trees* as well as a *SuperShader*-based concept are identified as possible approaches for the modularized framework. In the *Shade Tree* concept, modularized shading components are arranged as a tree. The shading result of every basic shading block is propagated up the tree until the final result in the root is reached. The root denotes the output, and the leaves denote the input of the shader. Generally, *Shade Trees* allow high flexibility and are well suited for visual representation, but the

usage is laborious because custom shader code has to be inserted in a complex tree structure.

The *SuperShader* concept assumes the existence of a finite number of fragments, ordered in a linear list. Each fragment contains a code snippet that calculates a certain effect. The effect shaders are generated and optimized by a control shader at run-time using static branching.

Originally, the shader pipeline of the prototypical framework is implemented using the *Shade Trees*. Atomic shader blocks can be edited and connected using a visual representation of the graph. The replacement of shader blocks is possible considering the signature of input and output values, whereas the internal shader code can be neglected. After discussions and user evaluations, it is decided to switch to the *SuperShader* concept, because replacing shader code under consideration of the child and parent node's signatures is difficult to handle in practice. The signature has to be well known to replace atomic shader blocks with custom functionality. In contrast, the signatures of all shader fragments in the *SuperShader* approach are identical. Thus, the shader can be combined more freely, and custom shader code may inserted flexibly. Furthermore, the linearly ordered list of the shader blocks are a more intuitive representation of the volume rendering pipeline.

7.4.2 Basic Approach

In the presented *SuperShader*-based approach, the code snippets are directly copied into the shader code instead of using a control shader, allowing the addition of custom shader code dynamically. Two general ideas of the *SuperShader* concept are utilized:

1. The assumption that a shader can be subdivided into a linear order of rendering operations such as sampling or lighting.
2. The code snippets use a global data structure for communication which is passed to the snippets at execution. Input values are read from the data structure and output values are written into the data structure.

7.4.2.1 Shader Pipeline

The rendering shader is subdivided into a linearly ordered shader pipeline. A pipeline step is modeled as a subset of several shader pipeline functions, which contain the GLSL shader code. Figure 7.1 shows a schematic overview of the proposed rendering pipeline.

For introspection, the following parameters have to be explicitly defined for each pipeline function: *shader parameters*, *struct parameters*, and *library functions*. Thus, several shader parameters, such as varying or uniform variables, can be attached to each pipeline function. Furthermore, the global data structure is a globally defined *struct* in the final shader. The struct is passed as input and output parameter to the pipeline functions. Input values are read from the struct and output values

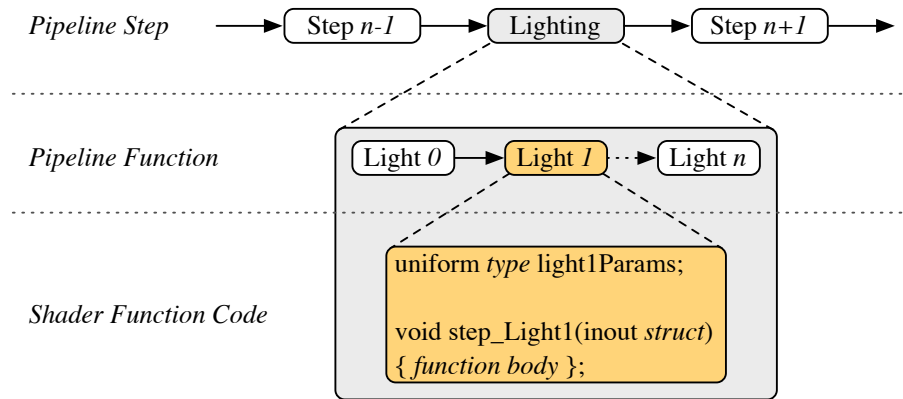


Figure 7.1: Three layers of the rendering pipeline. Pipeline steps are in the top layer, which are subdivided into a subset of pipeline functions. The GLSL code itself is located below, in the shader function code layer.

are written into the struct. The struct can be interpreted as the global state of the pipeline which represents the intermediate and final results of the rendering computation. Thus, all pipeline functions have the same signature, no return value, and can only communicate via the global struct. Figure 7.2 shows the shader code of a pipeline function, which writes shading multipliers into the global struct.

Furthermore, the use of a function library is proposed to allow the reuse of common shader components such as shading or texture fetching. A library function is specified as a code snippet which calculates a specific shader effect or color value per sample. Because library functions are stored in an external library and are generally independent from the pipeline, global shader attributes can not be attached. Thus, library functions have no access to the global struct of the pipeline and have to write the calculated effect as a return value. However, library functions can be called within the pipeline functions themselves. Figure 7.3 shows the shader code of a library function which calculates the diffuse and specular multipliers for a light source.

7.4.2.2 Shader Generation

To generate the final shader, a shader factory algorithm combines the resulting shader from the active pipeline steps. The shader pipeline consists of the *pipeline map*, a data structure to reference pipeline functions. The corresponding shader string is generated using the pipeline map.

Setup of Data Structure. The key of the pipeline map is *pipeline position*, and the value is *pipeline step*. A pipeline step contains an ordered list of pipeline function references. For all pipeline steps of the data structure, the active pipeline functions are added.

```
uniform vec4 lightColor0;  
uniform vec3 lightVector0;  
uniform vec3 halfVector0;  
uniform float specularity;
```

```
void vrStep_directionalLight0(inout globalStruct state) {  
    vec2 result = vrLib_getShadingFromLight(state.gradient,  
                                           lightColor0,  
                                           lightVector0,  
                                           halfVector0,  
                                           specularity);  
  
    state.diffuse0 = result.x;  
    state.specular0 = result.y;  
}
```

Figure 7.2: Pipeline function to obtain shading from a light source using a library function (see Figure 7.3). The function reads the gradients from the global struct and writes both, diffuse and specular multipliers back into the struct.

Generation of Shader String. Subsequently, the pipeline map is used to generate the corresponding shader string. Input is the ordered list of functions, given implicitly in the map. Output is the final shader string. The following steps are processed:

1. The used information (shader pipeline context) for each pipeline function is stored in an additional temporary data structure:
 - Used varyings/uniforms.
 - Used parameter struct entries.
 - Used library functions.
2. The declarations (stored in the temporary data structure) are appended to the shader string:
 - Varying/uniform declarations.
 - Parameter struct declaration.
 - Library function declarations of used functions only.
 - All pipeline function declarations.
3. The main function is appended to the shader string:
 - Struct instantiation of the default values for the struct.
 - Call to pipeline functions in correct order (as defined in the map).

Figure 7.4 (a) gives an illustrative overview of the resulting *SuperShader* pipeline.

```

vec2 vrLib_getShadingFromLight( in vec3 inGradient,
                               in vec4 inLightColor,
                               in vec3 inLightVector,
                               in vec3 inHalfVector,
                               in float inSpecularity) {
    float diff = max(dot(inGradient, inLightVector), 0.0);
    float spec = max(dot(inGradient, inHalfVector), 0.0);
    spec = inLightColor.a * pow(spec, inSpecularity);
    return vec2(diff, spec);
}

```

Figure 7.3: The library function returns diffuse and specular multipliers as a vector with two elements (`vec2`), which are required for volume shading.

7.4.3 Application to Volume Rendering

In the slicing-based volume rendering system [103] of *MeVisLab*, 16 fixed pipeline steps are defined for the available rendering effects (see Figure 7.4 (b)). The pipeline steps are grouped into four main rendering steps according to the general volume rendering pipeline. The first group consists of the *Sampling* pipeline steps, which fetch the sampling value for each active data set. A sampling step may contain a shader pipeline function for trilinear or tricubic filtering [74]. The *Classification* group contains the steps for the application of corresponding transfer functions to the samples. Shading operations such as lighting, boundary enhancement, or tone shading are located in the *Shading* group. The *Compositing* group is the last group in the pipeline and contains the final composition of the samples to calculate the output fragment color.

Due to input–output parameter dependencies of the pipeline functions (e.g., gradients are needed for illumination calculation), the positions of the pipeline steps are arranged in a fixed order. However, the shader code of the pipeline steps may be changed depending on rendering parameters, e.g., on the number of active light sources. Generally, the pipeline steps are activated according to the enabled rendering effects of the volume renderer. For instance, if volume shading is enabled, the rendering system activates the gradient calculation pipeline step, which is positioned before the illumination step. If no gradients are needed, the gradient pipeline step will be deactivated. Because the implementations of shader functions are generally independent from each other, the underlying gradient calculation algorithm may be changed (texture based or on-the-fly [72] gradients) during run-time without affecting other pipeline steps.

7.4.4 Application to Slab Rendering

In addition to 3D renderings, the volume renderer is utilized to enable rendering of orthographic projections, which allows efficient visualization of arbitrary multi-

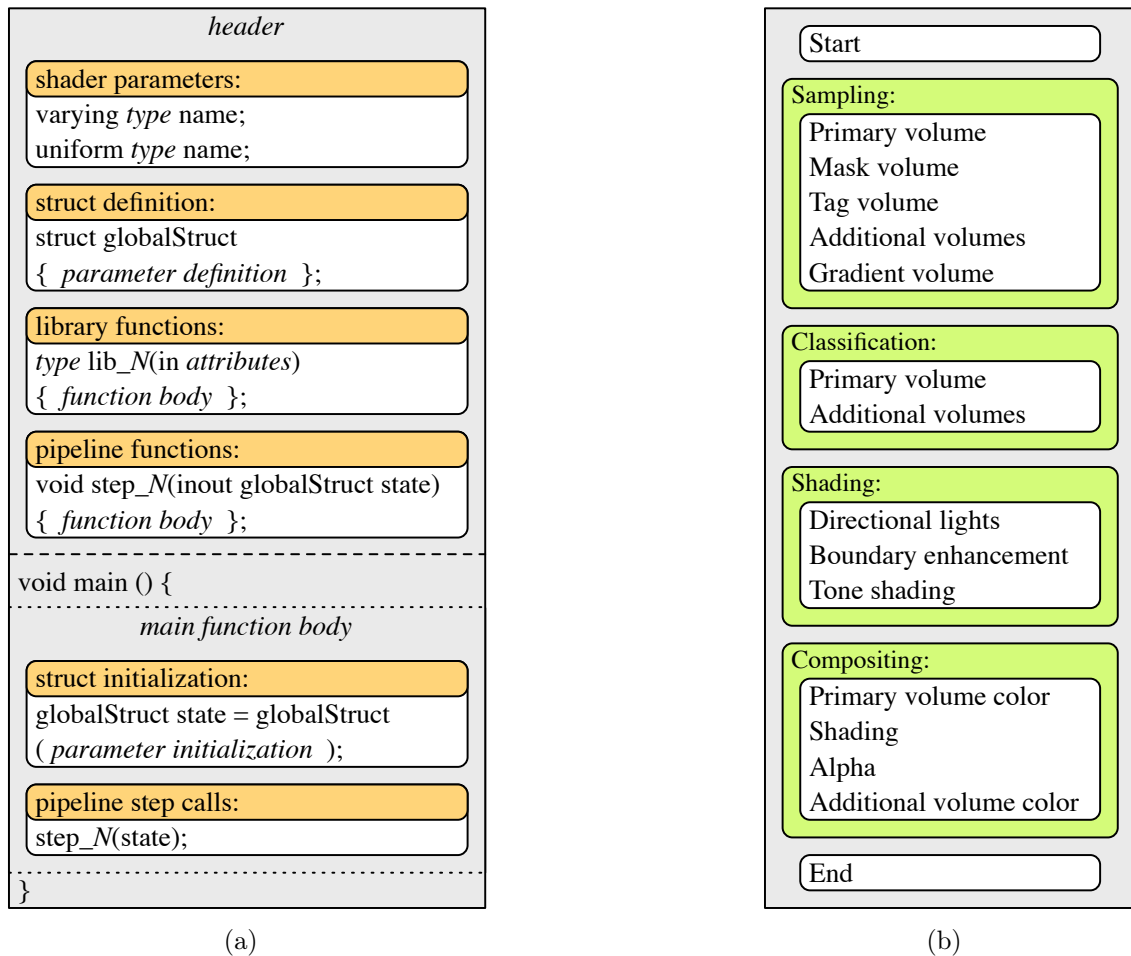


Figure 7.4: Overview of the composed *SuperShader* code of the pipeline with library and pipeline function (a). The 16 pipeline steps are grouped in four main rendering steps (b).

planar reformations. Furthermore, the data sets have to be loaded only once into memory and can be shared by multiple renderers. Hence, the shader pipeline can also be utilized for advanced 2D slice visualizations.

7.5 Prototyping Environment

The developed visual prototyping environment supports a Graphical User Interface (GUI) and scripting functionality to allow customization of the GLSL shader pipeline of the volume renderer. An API to develop C++ code is also supported.

7.5.1 Volume Rendering Scene Graph

The volume rendering system of *MeVisLab* is based on the *OpenInventor* scene graph [165]. The volume renderer itself is a scene graph node. Supplementary nodes are various volume data nodes (e.g., additional volume and mask volume), transfer function nodes, and rendering effect nodes such as shading or boundary enhancement [52]. The scene graph concept allows the utilization of the same volume renderer in different scenes. Thus, the data set has to be loaded only once into memory and can simultaneously be visualized in multiple viewers with varying render configurations.

If the state of a node changes, the scene graph will be traversed at the next frame and all node elements will be collected. Subsequently, the shader factory of the renderer generates the shader string (see Section 7.4.2.2) and compares it with the last compiled shader program. If the shader programs differ from each other, the new shader is compiled. Due to the compilation process of the alternated shaders, a performance overhead can be observed. In order to prevent re-compilation per rendering frame, the compiled shader programs are cached in the GPU memory, allowing for rapid reuse of previously executed shader configurations. The compiled shader is used to check which parameters are bound to the OpenGL context in order to set their values. Finally, the image is rendered with the generated shader. Figure 7.5 illustrates the shader generation process.

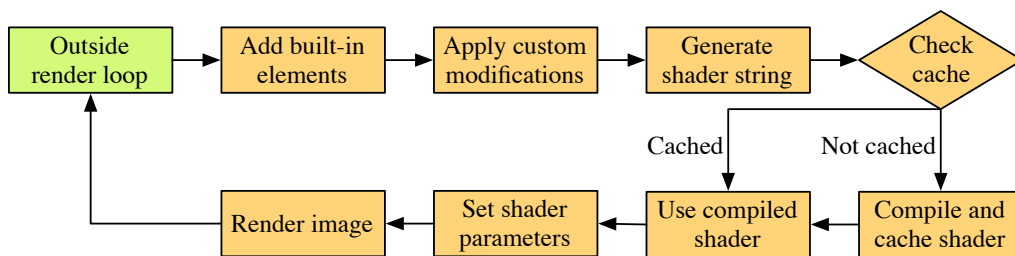


Figure 7.5: Illustration of the shader generation process which has to be repeated for every frame.

Because of the visual representation of the nodes in the prototyping environment, the developer is able to connect the nodes to the scene graph interactively. Thus, the volume rendering can be easily extended at run-time.

7.5.2 Custom Shader Pipeline

The presented fixed pipeline steps with the pipeline functions implement the available rendering effects in the *SuperShader*. To allow the extension of the rendering pipeline with additional rendering effects, custom pipeline functions are introduced. A custom pipeline function is a shader function for which the function body as well as the parameters can be edited by the user. Custom pipeline functions can

be attached to a pipeline step in order to add or replace existing pipeline step implementations (see Figure 7.6). Therefore, the shader function node is presented, which is the core functionality to edit the custom shader function and to control the appending to the pipeline. Two additional nodes allow adding shader parameters and attaching shader code to the header, such as library functions, to the shader pipeline. An inspector node can be used to visualize the current pipeline as well as the composed shader used for rendering.

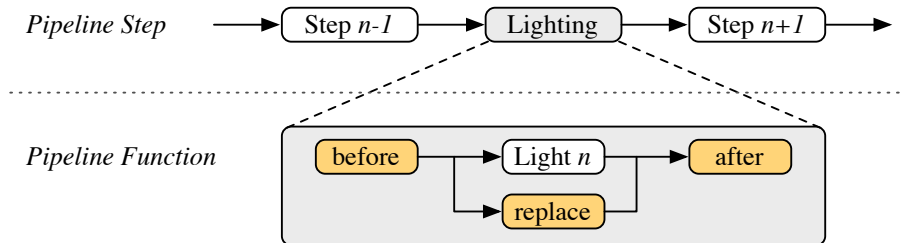


Figure 7.6: Custom pipeline functions (orange) can be attached before or after, or replace the pipeline functions of a selected pipeline step.

7.5.2.1 Shader Function Node

The shader function node is used to implement a custom pipeline function. The GUI has been designed to be as simple as possible to allow fast and intuitive modifications without limiting the ability to create advanced shader effects.

Function Declaration. A text field with GLSL syntax highlighting allows the function body to be implemented and the function name to be defined (see Figure 7.7). Access to the global struct is achieved via the instance name *state*.

Parameter Declaration. The parameters of the global struct have to be defined for communication with the pipeline. For that, the new keyword *state* is introduced to identify variables of the global struct. State parameters have to be defined with a default value, to always ensure a valid definition of the struct constructor in the shader's main function. Moreover, used varying and uniform parameters have to be declared in the parameter section.

Pipeline Modification. One of the available (vertex or fragment) pipeline steps has to be specified for the placement of a custom shader function. If multiple pipeline functions subdivide a pipeline step (compare with Figure 7.1), the placement can be applied to a single pipeline function (substep) or to all pipeline functions (default). Four placement modes are available: *Add Before*, *Add After*, *Replace*, and *Remove*. In the *Add Before* mode, the custom pipeline function will be inserted into the selected step before the specified pipeline function and all functions, respectively.

Analogously, the *Add After* mode will insert the custom function after the pipeline function. In the *Replace* mode, the custom function will replace the selected pipeline function and all functions, respectively. Finally, the *Remove* mode can be used to completely remove all functions in the pipeline step. Additionally, an optional rule can be applied to all placement modes: If the selected pipeline step is not active, the custom shader function will not be inserted into the pipeline.

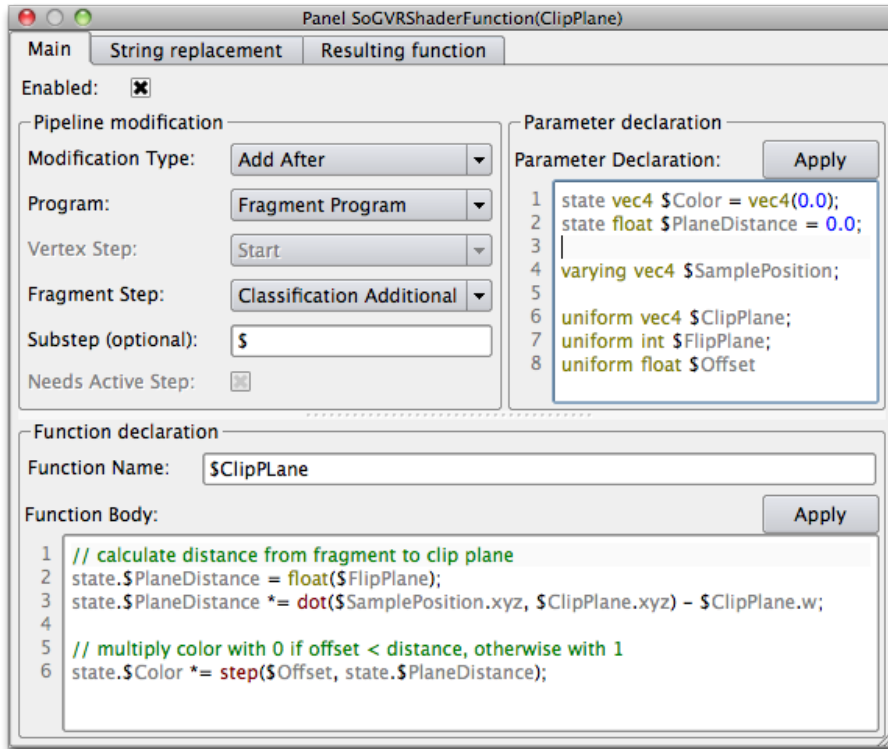


Figure 7.7: The GUI of the custom shader function node. In this example, the function calculates a clip plane and modifies the color of the specified volume. The character $\$$ is a wildcard for the current volume name.

String Replacement. An important requirement for prototyping is to facilitate a dynamic and flexible definition of the custom shader function. For that, a string replacement mechanism is integrated into the shader function node. The string replacement allows for replacing any string in the parameter declaration, substep, function name, and function body text fields before appending the shader function. In Figure 7.7, the character $\$$ is used as a wildcard for the volume texture name. This allows for multiple instances, each with a unique identifier.

7.5.2.2 Shader Parameter Node

If uniform parameters are used in the custom shader, the parameter values have to be bound to the OpenGL context and transferred to the graphics card. For that, shader parameter nodes with a simple GUI can be connected to the scene graph (see Figure 7.8). The following data types are supported: bool, 4×4 matrix, and vector[1..4] of type float and integer, respectively. Additionally, for uploading images, 1D, 2D, and 3D texture samplers as well as frame buffer sampler and cube map sampler nodes are available.



Figure 7.8: The GUIs of three shader parameter nodes. From left to right: three component float vector (vec3), integer, and color (vec3).

7.5.2.3 Shader Include Node

To allow the extension of the function library with custom functions or global parameters, the shader include node is introduced. With the shader include node, custom shader code can be added to the shader header of the rendering pipeline for use in custom shader functions (see Figure 7.9). In contrast to the global function library, the shader include is only valid in the connected scene graph.

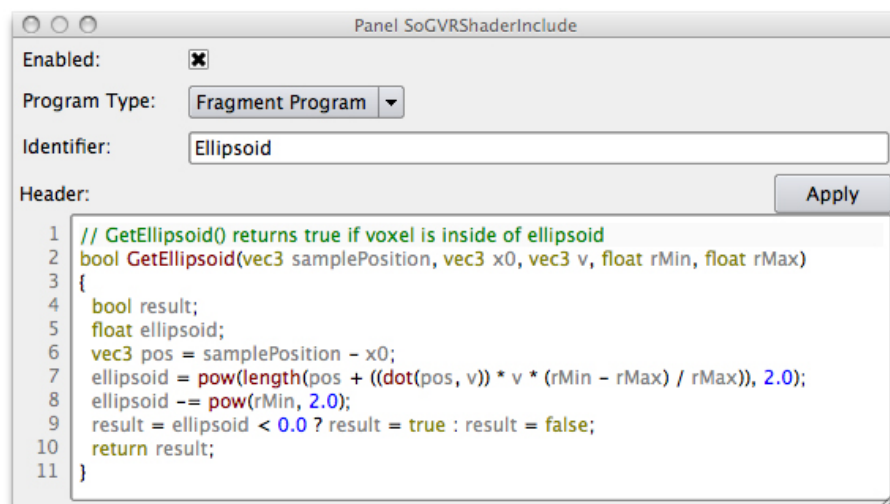


Figure 7.9: The GUI of the shader include node. The function *GetEllipsoid()* is added into the fragment shader header.

7.5.2.4 Shader Diagnosis Node

To ease the implementation of custom shader functions, a shader diagnosis node is included, which allows to inspect the active shader pipeline. The shader diagnosis node supports the representation of all active built-in shader functions of the volume renderer as well as custom shader functions, added by the user. Every function in the list can be selected to show defined states, varying and uniform variables, as well as the function body. In addition, the available uniforms, states, and includes can be inspected. Figure 7.10 shows the GUI of the shader diagnosis node.

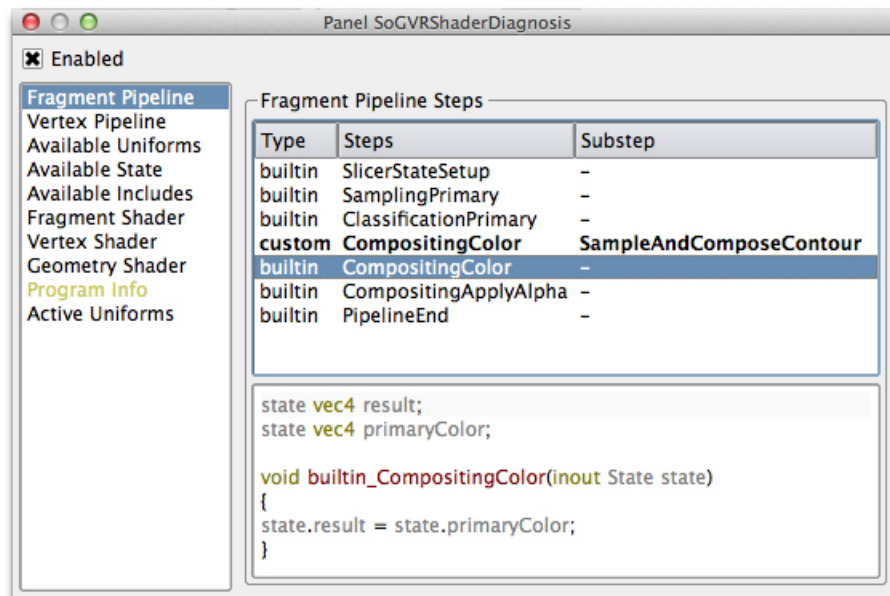


Figure 7.10: The GUI of the shader diagnosis node represents the current fragment pipeline. A custom shader function is placed before the *CompositingColor* pipeline step. The *CompositingColor* function is selected in the list so that used variables as well as the shader function's body is shown.

7.6 Example Applications

In this section, three examples for the usage of the prototyping environment are presented. The first example illustrates how a simple rendering effect can be attached to the rendering pipeline. In the second example, it is demonstrated how the shader pipeline can be used to implement flexible fragment clipping operations for multi-volume rendering. The third example illustrates the implementation of rendering effects for planning of radiofrequency ablation (see Section 3.4.2).

7.6.1 Stochastic Jittering of the Sample Position

Stochastic jittering of the sample position can be used to reduce sampling artifacts such as wood-grain without increasing the sampling rate. The values of a pre-calculated noise texture are used to move the sampling positions along the view ray. Thus, the volume will be constantly sampled with reduced wood-grain artifacts.

For this purpose, the sampling pipeline function is replaced with a custom pipeline function, which implements stochastic jittering. In this example, the jittering shader code proposed in [72] is used. Additionally, a 2D sampler node is used to load the required noise texture with the stochastic jittered values into the volume renderer. Furthermore, a shader parameter node allows for controlling the amount of jittering (see Figure 7.11). Because the jittering pipeline step is generally independent from other pipeline functions, the rendering configuration can be changed dynamically, e.g., with additional effects such as volume shading, boundary enhancement or tone shading. Figure 7.12 shows renderings of a CT data set with different shading effects and stochastic jittering.

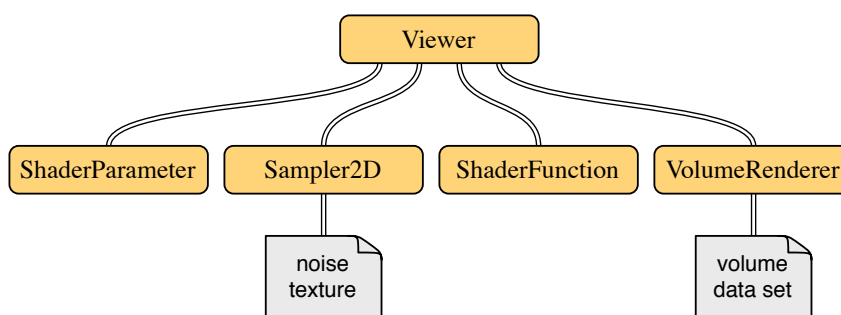


Figure 7.11: An illustration of the scene graph used for stochastic jittering of the sample position. The jittered sampling is implemented in the shader function node. The pre-calculated noise texture is loaded as 2D sampler. The amount of jittering may be adjusted in the shader parameter node.

7.6.2 Fragment Clipping for Multi-Volume Rendering

Multi-volume volume rendering is commonly used in neurosurgical and neuroradiological workstations, for the fusion of data sets from different imaging modalities. The general drawback of multi-volume volume rendering is the occlusion problem. Varying opaque anatomical structures may overlay other important structures. A common solution is to clip the data sets in the rendering. Clipping is commonly implemented by the *glClipPlane* instruction of OpenGL, in which the proxy geometry of the volume rendering is clipped. Visualizing multi-modal volume data typically requires the interactive definition of multiple clip planes per volume data set. Which volume has to be clipped away, and which has to be excluded from

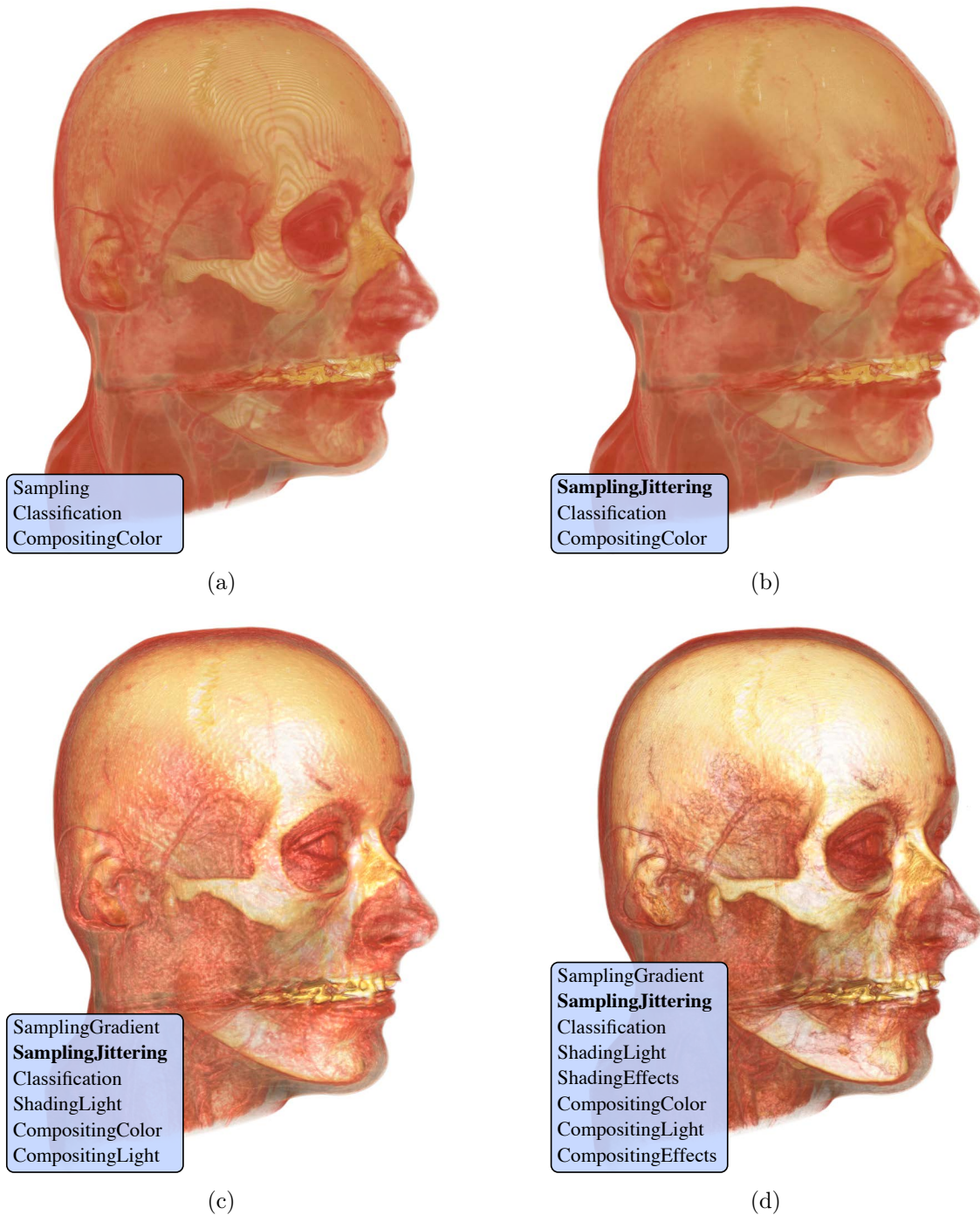


Figure 7.12: Image (a) shows a volume rendering of a CT data set with low sampling rate, which results in wood-grain artifacts. The blue box illustrates the active steps of the fragment shader pipeline. In (b), the sample position is jittered with a custom shader to mitigate the artifacts without increasing the sampling rate. Image (c) shows the jittered rendering with enabled shading. In (d), boundary enhancement and tone shading are additionally enabled. OsiriX sample data set *MANIX*.

clipping must be defined for each clip plane. Because clipping the proxy geometry results in collective clipping of all loaded data sets, OpenGL clip planes are not suitable. A technique allowing this is fragment clipping, which was introduced by Weiskopf et al. [181]. Here, the clipping is calculated in the fragment shader and can be individually specified for each volume. Nevertheless, designing a shader to handle this is challenging, because the exclude rule depends on the data sets which are currently enabled. Also, the shader should be valid if the rendering configuration changes, e.g. if a rendering effect such as shading is enabled. The following medical visualization case demonstrates a solution to integrate clip planes in multi-modal volume rendering.

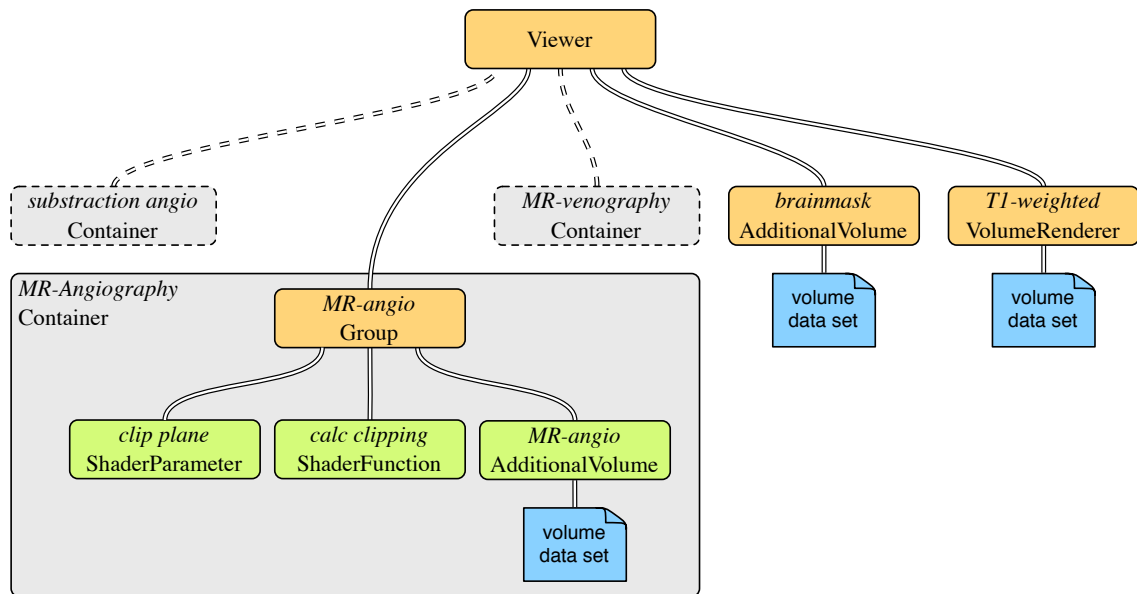


Figure 7.13: Illustrative description of the multi-volume rendering scene graph. Every additional volume container node has corresponding child nodes for clipping calculation, parameter specification, and the data set.

A cerebral arteriovenous malformation (AVM) is an abnormal connection between veins and arteries in the brain. The complex angio-architecture of the AVM as well as the three-dimensional shape of the feeding and draining vessels has to be understood before surgery. For that, various datasets, such as T_1 -weighted main volume, MR subtraction angiography, and time-of-flight (TOF) datasets have to be visualized simultaneously. To support the neurosurgeon in this challenging task, a viewer application is developed [11], which allows the neurosurgeon to intuitively adjust clip planes for all data sets to explore the AVM. In this application, every data set can be appended to the volume rendering during run-time of the application. Corresponding shading parameters, clip planes, and transfer functions are independently defined for each data set and can be controlled by the neurosurgeon in the GUI of the application. Figure 7.14 shows four volume renderings with different param-

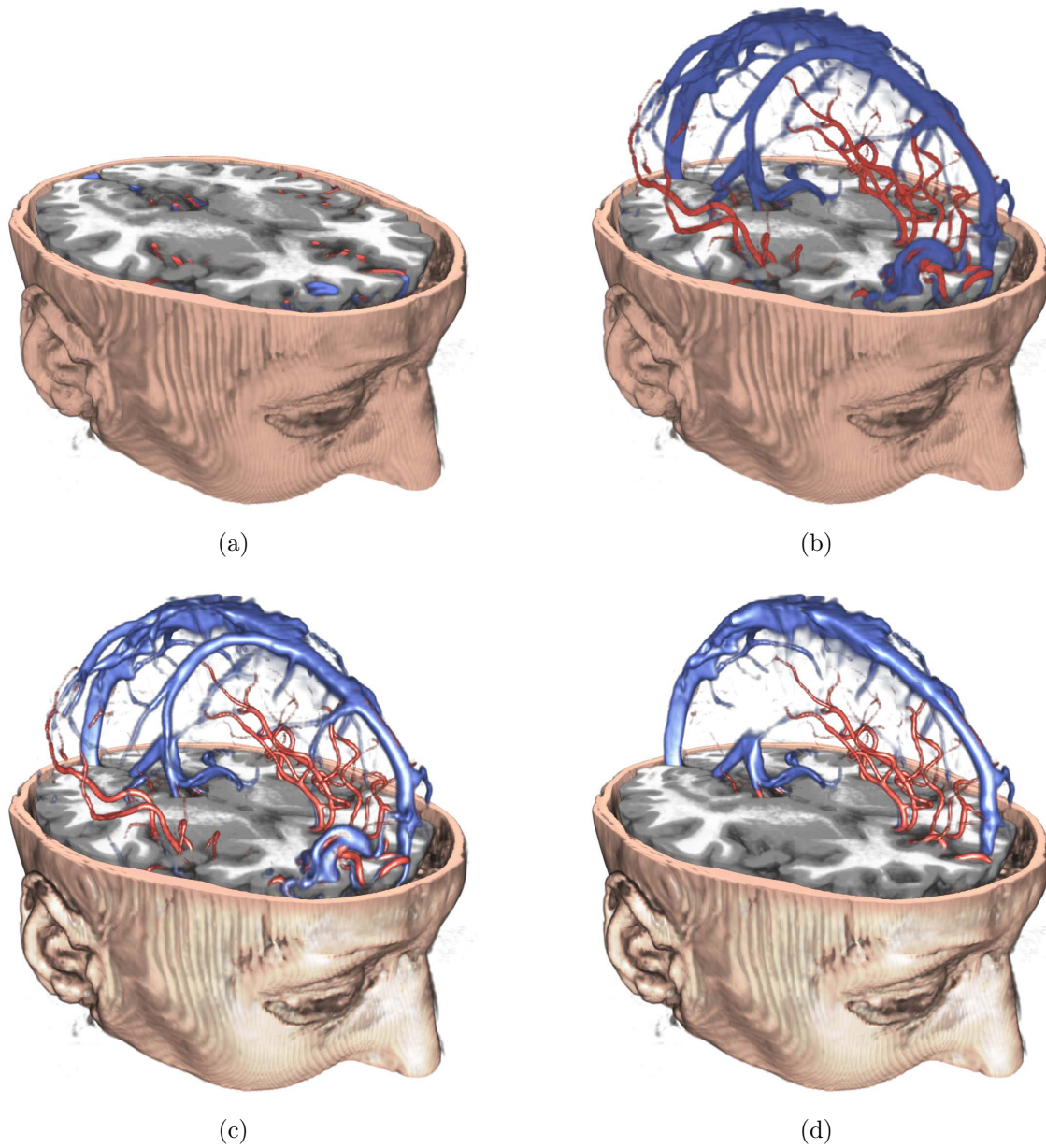


Figure 7.14: Image (a) shows a multi-modal rendering of three MR data sets and a defined clip plane. The vessel data sets (red arteries, Time-of-Flight MRI; blue veins, contrast enhanced T1-weighted MRI) are excluded from clipping (b). Image (c) shows enabled shading of all data sets. In (d), additional clip planes are defined to clip the vessels. Data sets courtesy by Lahey Clinical Center, Burlington.

terized clip planes and shading effects. The additional datasets are loaded into the volume renderer and fused utilizing the *max* operator in the shader [40]. Because of the difficult three-dimensional perception of flat-shaded objects, volume shading is enabled. Thus, for every data set, the corresponding gradients have to be calculated and stored in a volume texture. Additional shading effects such as toon shading or boundary enhancement [141] can be independently enabled per volume.

Utilizing the proposed framework, a container node (subgraph with child nodes) is developed to allow the reuse of the clip plane in the scene graph. The container includes a single custom shader function node with the GLSL implementation of the clip plane and required parameters nodes (e.g., plane vector and a name string of the volume to be clipped). The shader code is simple: the length from sample to plane is calculated, and the volume's color is multiplied with zero if the length is negative, otherwise it is multiplied with one (see Figure 7.7 for the used shader code). The pipeline is modified with the following setting: *Fragment Step* is set to *Classification Additional*, *Substep* is set to the current volume name via the wildcard *\$* and the *Modification Type* is set to *Add After*. Thus, the clip plane function is always inserted after the classification of the specified volume. If the volume's classification is inactive, i.e., the volume is disabled, the clip plane function is not appended. Furthermore, a clip plane function is independent of all other pipeline function. Hence, the rendering configuration can be adjusted (e.g., varying shading modes or disabling of volumes) without invalidating the final rendering shader. Figure 7.13 illustrates the scene graph for multi-volume rendering. For every additional volume, a container node with corresponding visualization parameters is connected to the main volume renderer.

7.6.3 Dynamic Visualization of RF Ablation Zones

For planning of image-guided radiofrequency ablation (RFA), the cell destruction caused by the ablation has to be estimated. An important requirement is that different applicator models with corresponding ablation zones, specified as ellipsoids by the manufacturers, can be visualized in the slice views and the corresponding volume rendering simultaneously. For planning of RFA, multiple applicator models with varying settings may be placed, moved, and toggled on or off in real time to discover the optimal ablation scenario (see Section 3.4.2 and 3.5.3).

For this purpose, a shader include node, which adds a custom library function into the shader pipeline, is inserted into the scene graph of the system. The custom library function evaluates whether a sample is inside or outside of the ablation zone's ellipsoid (see Figure 7.9 for the used shader code). Additionally, an applicator container node is defined, which encapsulates a single shader function node as well as the required applicator and ablation zone shader parameters. The parameter nodes hold the attributes which define the ellipsoids' size, position, and orientation. The custom pipeline function is inserted before the start step of the rendering pipeline. It calls the library ellipsoid function with the ellipsoid attributes and stores in the global state whether the current sample is inside or outside the ablation zone. To

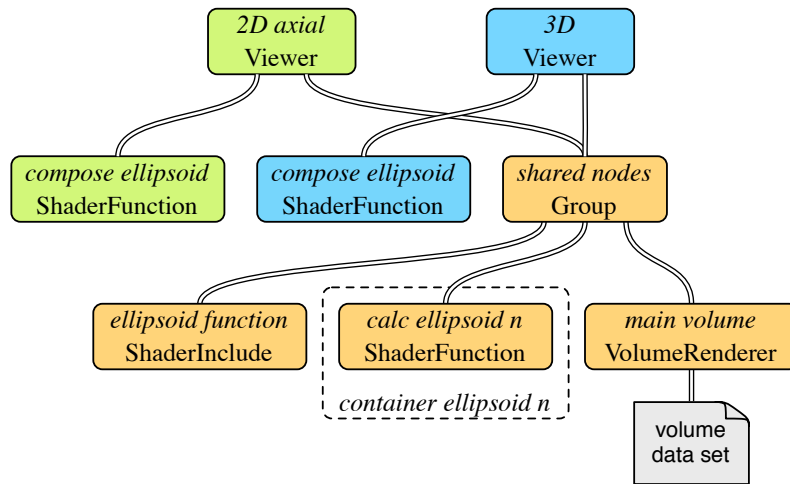


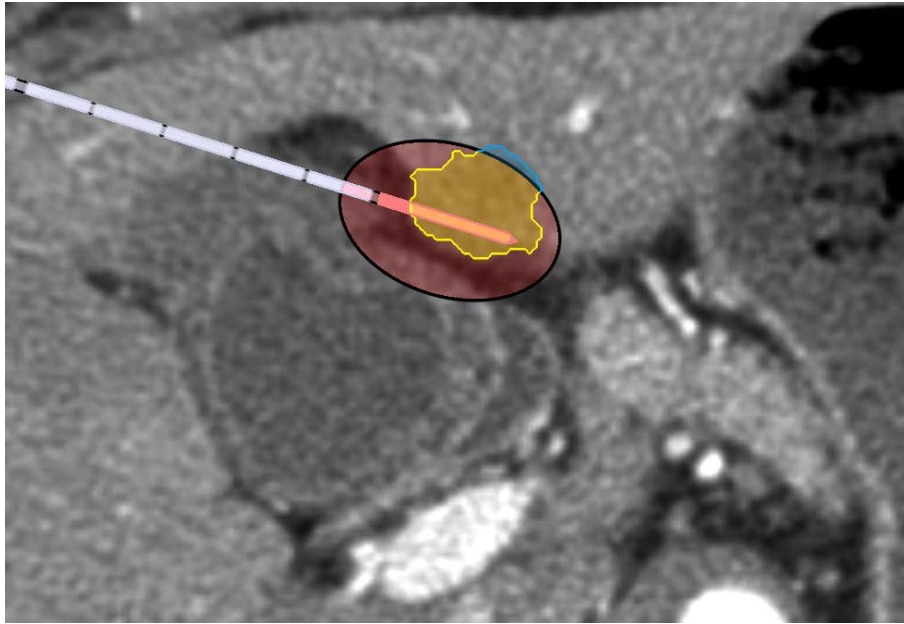
Figure 7.15: An illustration of the scene graph used for the visualization of the ablation zone. Varying shader functions are used for the correct composition of the alpha value of the 2D and 3D viewers, respectively.

visualize the final ablation zone, a single function node outside the container is connected to handle the visual properties (color, alpha, silhouette) of the ellipsoids. The shader function is appended to the pipeline after the compositing step. This design allows for adjustment of the visualization properties for varying viewers, e.g., changing the alpha value of the ablation zone for a 2D visualization. Figure 7.15 illustrates the used scene graph. The volume renderer and the ellipsoid header include as well as all container nodes are shared by both viewers. In contrast, the compositing of the ablation zone is implemented differently in separated shader function nodes.

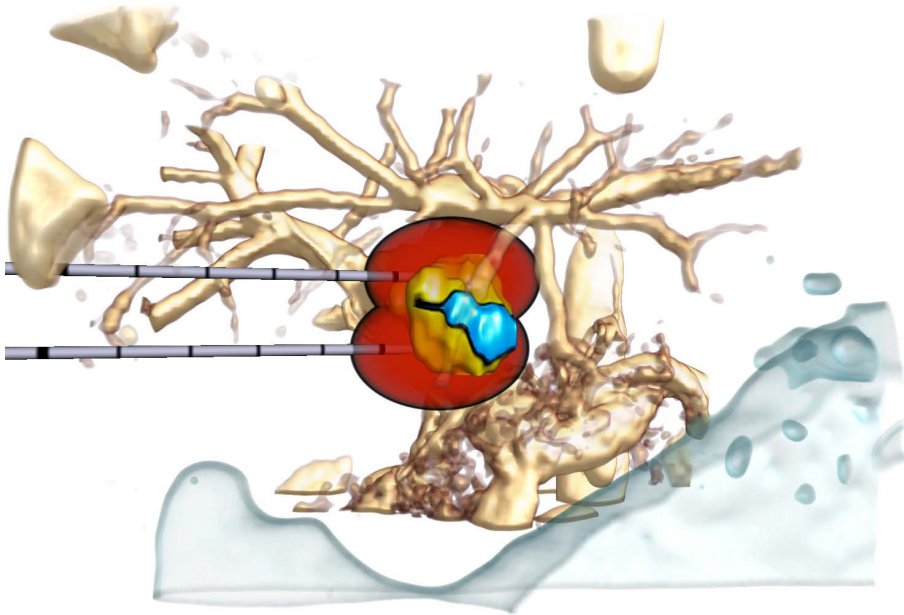
An extended version of this scene graph has been integrated into the presented medical software assistant for planning of RFA (see Chapter 3). If an applicator model is added by the end user from the application’s GUI, the application automatically generates a container node with the required shader parameters and connects it to the scene graph. Thus, multiple RF applicators with corresponding ablation zones can be manipulated interactively and visualized in 2D and 3D simultaneously (see Figure 7.16). Moreover, utilizing a custom function, the color of tumor voxels outside of the ellipsoid is adjusted.

7.7 Results and Discussion

In this PhD thesis, a prototyping framework for DVR is presented, which is integrated in the *MeVisLab* development environment. In contrast to the original *SuperShader* concept, no control shader is used. Instead, the shader snippets are directly copied into the resulting shader string to be able to add custom shader code dynamically. To allow the compilation of the shader pipeline with custom



(a)



(b)

Figure 7.16: Two RF applicators are positioned into a tumor. Image (a) shows a 2D visualization of a single slice, occluding the upper located applicator. Image (b) shows the corresponding 3D volume rendering of the same data set. Using the shader pipeline, for each representation, different visual features are applied (colors, silhouettes, transparency), but the underlying information is equal (ellipsoid properties, image data, tumor mask).

shader code, the shader factory creates the shader string at each rendering frame and caches compiled shaders for reuse. Due to the optimization of the GLSL compiler, no changes in the final rendering performance are measured, although the pipeline shader string is three times longer than the manually optimized shader.

Three examples are presented, from which two are integrated in stand-alone medical applications developed with *MeVisLab*. The first example demonstrates how the rendering shader can be extended with stochastic jittering of the sample position. Utilizing a custom shader function, the jittering rendering effect replaces the built-in linear sampling of the volume texture. It is also shown that the custom effect does not interfere with other built-in effects such as volume shading or boundary enhancement. In the second example, it is demonstrated how a simple rendering effect can be developed and attached to the pipeline several times in order to achieve flexible clipping of multiple volumes. The third example shows how varying rendering effects are developed and subsequently integrated into a medical multi-viewer software assistant. Effects such as the visualization of ellipsoids can be dynamically integrated several times in the volume rendering pipeline without considering the remaining shader. Furthermore, custom shader functions in the scene graph are used to alter the composition of the ellipsoids allowing for simultaneous visualization in different viewers (2D and 3D). In the final software assistant (as described in Chapter 3), the presented effects with varying parameters can be interactively manipulated (e.g. add or move RF applicators with corresponding ablation zones) by the end user, i.e., the physician.

For preliminary feedback, the system is presented to a medical image processing expert, who is not involved in the development of the system. He utilized custom shader functions to implement clip planes attached to specific pipeline steps to define a dependence to the volume to be clipped. Suitable GUIs in the scene graph supported the researcher in intuitively editing custom shader code at run-time. Although the shader pipeline concept is new and the detailed internal structure of the rendering shader is unknown, the developer easily managed to implement the clip planes within a few minutes. Only basic knowledge of shader programming and volume rendering is required.

System aim. The presented framework targets supporting the developer to extend the volume rendering with custom shader algorithms and to integrate the resulting volume visualization into software applications with minimum development overhead. In contrast, the shader composer proposed by Plate et al. [137] aims to support the creation of special purpose shader programs utilizing data flow widgets. The work of Rössler et al. [146] is intended to wrap complex shading algorithms into a graph representation to allow the user to concentrate on the visualization result. *VolumeShop* [37] is a prototyping platform for visualization research that provides maximum flexibility to the developer. *Voreen* [117] facilitates the research of new interactive visualization techniques for volumetric data sets with high flexibility. The system proposed in this PhD thesis is limited to customize shading effects and

adjust the configuration of the render core at run-time. Extending the render core with additional, configurable features needs to be done in C++.

Modular combinability. A dynamic shader pipeline is proposed, which facilitates substituting pipeline steps during run-time while ensuring a valid final shader. In other systems, the final shader is composed using predefined GLSL functions (cf. *Voreen* [117]) or by collecting the shader snippets from predefined nodes (cf. Plate et al. and Rössler et al. [146]). The advantage of the dynamic shader pipeline is that shader effects can be freely combined without modifying the remaining shader code or adding all possible combinations. For instance, arbitrary lights or additional volumes can be enabled, resulting in an automatic insertion of the corresponding shader code.

Extension of the rendering shader. The shader pipeline allows the developer to interactively extend the rendering by appending arbitrary custom shader functions without recompiling the C++ code. Utilizing the global struct for communication, the pipeline steps are independent from each other and can be changed without affecting other pipeline functions (e.g., swap gradient calculation). In contrast, the frameworks of Rössler et al. [146] and Plate et al. [137] do not support editing of the node's shader code without recompiling the C++ project. In *Voreen* [117], functions of a shader library can be interactively edited and are included in the final shader using defines. However, custom shader code has to be inserted in the final shader by hand. Similarly, *XIP* [140, 185] and *VolumeShop* [37] allow for editing and free combination of shader snippets. Because no mechanism for positioning of the snippets is available, the snippets also have to be manually combined to a valid shader. In conclusion, none of the related systems allow for adding and editing of custom shader code during run-time without the need to adjust the remaining shader (cf. arbitrary clip planes), e.g., to add a call to the shader's main function. Thus, inserting multiple custom shader code with varying parameterizations is difficult to achieve with these systems.

Application prototyping. Since the presented system is based on a scene graph, custom shader nodes can be dynamically connected to sub-graphs, resulting in modified rendering pipelines for different viewers (cf. compositing of ellipsoids), whereas the basic rendering shader remains unmodified. To the author's knowledge, this is a unique benefit, particularly for research and development of specialized rendering effects for medical applications. Furthermore, the stability of the shader core eases the generic extension of rendering effects for long-term use in *MeVisLab*.

7.8 Conclusions

The presented rapid prototyping framework for GPU-based volume rendering allows for flexible extension and dynamic alteration of the rendering configuration. The

underlying approach is a dynamic rendering pipeline based on the *SuperShader* concept, to which custom shader functions can be attached at run-time. With the user interface of the prototyping environment, intuitive modification of the custom shader is possible at run-time. The usage and usefulness of the framework is demonstrated in examples, which is successfully embedded into medical applications.

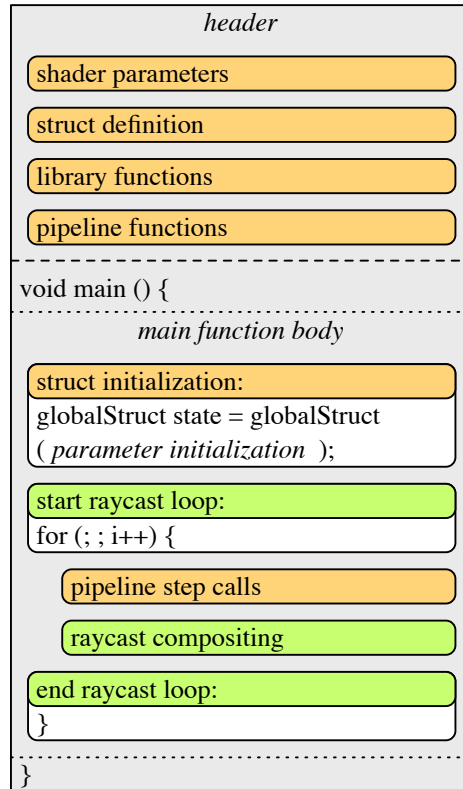


Figure 7.17: Overview of the composed *SuperShader* code for GPU-based volume raycasting. The green boxes indicate raycasting specific pipeline steps.

The system is integrated into the prototyping environment *MeVisLab*. Nevertheless, the approach of the dynamic shader pipeline is generally independent from *MeVisLab*. Also, a slicing-based volume renderer, which is part of *MeVisLab*, is utilized as underlying rendering core of the system. However, the approach is not restricted to slicing-based volume rendering.

For future work, the shader pipeline may also be applied to a raycasting-based volume renderer. The major implementation difference is that the shader function calls of the pipeline have to be embedded into the raycasting loop of the fragment shader's main function. Here, the global struct is initialized before the raycasting loop. Additional pipeline steps for start and end of the raycasting loop implement the loop in the shader code. In contrast to slicing-based volume rendering, whereas the blending is done using the frame buffer, the sample points are composited along the view ray to calculate the final color value. Thus, the blending has to be calculated

in the last step of the raycasting loop in a special pipeline function. Definition of pipeline and library functions as well as the shader parameter definitions remain in the shader's header. Figure 7.17 illustrates a possible *SuperShader* pipeline for GPU-based volume raycasting.

In conclusion, the design of the proposed shader pipeline allows to be integrated into slicing-based as well as raycasting-based volume rendering systems. Also, creating 2D slab renderings utilizing orthographic projections for multi-planar reformations are possible.

This chapter is in part based on the following publications:

- **C. Rieder**, S. Palmer, F. Link and H. K. Hahn. A Shader Framework for Rapid Prototyping of GPU-Based Volume Rendering. In: *Computer Graphics Forum (Special Issue on Eurographics Symposium on Visualization)* 30, 3, pp. 1031-1040, 2011.
- F. Weiler, **C. Rieder**, C. A. David, C. Wald and H. K. Hahn. AVM-Explorer: Multi-Volume Visualization of Vascular Structures for Planning of Cerebral AVM Surgery. In: *3rd Prize of the Eurographics competition Dirk Bartz Prize*, 9-12, 2011

*In the beginning there was nothing,
which exploded.*

(Terry Pratchett)

8

Summary

THE primary goal of thermal tumor ablation utilizing needle-based interventions is to destroy all viable malignant cells within a designated target volume. Further, sparing normal surrounding tissue and accuracy of the therapy are also required. In clinical practice, concurrently achieving all goals is a challenging task. The overall aim of this PhD thesis is to provide interactive visualization methods for software assistance for needle-based interventions to support the physician to accurately and safely conduct the therapy.

Challenges

The clinical value of needle-based interventions depends mainly on pre-interventional planning of the therapy, accurate punctuation during the interventions, and post-interventional assessment of the therapy success. In the planning phase, an appropriate placement of the needle has to be determined in order to achieve complete tumor ablation. In the case of pre-interventional planning of the RFA therapy, the following challenges are addressed in this PhD thesis:

- Identification of safe pathways to the target region under consideration of important risk structures using 2D slice visualizations alone.
- Fast estimation of the patient-dependent ablation zone incorporating the cooling effect of nearby blood vessels.

After therapy, pre- and post-interventional images are used in order to compare shape, size, and position of tumor and coagulation necrosis. The following challenges of the assessment phase of needle-based interventions are addressed:

- Automatic alignment of pre- and post-interventional CT images for reliable therapy assessment.
- Visual comparison and quantification of the geometric properties of the ablated tumor and the coagulation necrosis.

To meet these challengers, various visualization methods have to be developed and customized. Thereby, the following technical challenge is also addressed:

- Rapid development and customization of volume visualization algorithms without recompilation of C++ source code.

Contributions

The goal of this PhD thesis is the investigation of interactive visualization methods to support the physician in planning and assessing needle-based interventions with software assistance. The first contribution of this work is a workflow allowing for interactive visualization and image-processing, which is designed to guide the physician in planning the intervention for use in clinical practice. In order to support the physician with spatial information about pathological structures as well as finding trajectories without harming vitally important tissue, 2D slice and volume visualization techniques for interactive planning of RFA are proposed. The workflow is integrated in a clinical software assistant designed for planning RFA.

A further contribution of this PhD thesis is the fast approximation of the ablation zone, incorporating the heat-sink effects of blood vessels. Two approaches are presented. The first method is based on a geometric reconstruction of pre-computed numerical simulations stored in a lookup table. Due to performance limitations of the first approach, a second approach proposes using weighted distance fields to

approximate the ablation zone on the GPU. The resulting ablation zone masks and computing performance of this method are compared with complex numerical simulations. In the comparison, similar ablation zone masks can be calculated even in complex vascular situations. Several limitations result from the substantial simplifications of the proposed method. However, the major benefit of the approach results from the real-time performance in both 2D and 3D.

A contribution in the field of RFA assessment is a workflow for automatic alignment of interventional CT images which is based on segmentation masks of tumor and coagulation. To assess the accuracy of the proposed method, 41 RFA cases are registered and compared with manually aligned cases from four medical experts. Furthermore, the registration results are compared with ground truth transformations based on averaged anatomical landmark pairs. In significantly less time, the proposed automatic method reaches an accuracy in the range of the medical experts' registration transformation. A combination of both automatic and manual approaches is integrated in the software assistant, with which the physician is able to manually adjust the transformation after automatic registration to achieve the optimal result.

A further contribution is a novel visualization as well as a navigation tool, the so-called tumor map. The goal of this method is the combined visualization of the tumor and its surface distance to the coagulation necrosis in order to support reliable therapy assessment. Additionally, the tumor map serves as an interactive tool for intuitive navigation within the 3D volume rendering of the tumor vicinity as well as with familiar 2D viewers. The evaluation shows that rotating the tumor object using the tumor map with the rectangular layout is significantly faster than rotating with the virtual trackball metaphor. Thus, navigation with the equirectangular tumor map is an intuitive alternative to common techniques for interactive exploration of tumors. Due to the synchronization of the 2D and 3D viewers, the tumor map may be used as navigation tool, which could lead to a higher acceptance of the volume rendering on a medical workstation. In the retrospective clinical study, it is confirmed that the software-assisted method allows physicians to correctly identify local tumor recurrence with a higher percentage than the conventional method (sensitivity: 0.6 vs. 0.35), whereas the percentage of correctly identified successful ablations is slightly reduced (specificity: 0.83 vs. 0.89).

A technical contribution of this PhD thesis is a shader framework for rapid prototyping, which was integrated in the MeVisLab development environment. The presented framework supports flexible extension and dynamic alteration of the rendering configuration of a GPU-based volume rendering. The underlying approach is a dynamic rendering pipeline based on the *SuperShader* concept, to which custom shader functions can be attached at run-time. With the user interface of the prototyping environment, intuitive modification of the custom shader is possible at run-time. The usage and usefulness of the framework is demonstrated in examples, which are successfully embedded into medical applications. The framework is used as basic technology for all interactive visualizations presented in this PhD thesis.

Conclusion

In this PhD thesis, novel methods integrated in a software-assisted planning and assessment application for needle-based interventions are proposed. In the planning stage, interactive visualization techniques are presented and fully integrated in a novel software-assisted workflow which supports the physician in rapidly planning RFA therapies. Integrated in the planning software is a novel GPU-based method to interactively approximate the ablation taking the cooling blood flow into account. The aim of the planning software is to support the physician to evaluate possible ablation strategies before the intervention under consideration of the patient-specific situation to minimize the risk and maximize the outcome of the therapy. As part of the assessment stage, a workflow allowing alignment and subsequent comparison of interventional images is proposed. An automatic registration algorithm is presented which allows the physician to rapidly fuse pre- and post-interventional data sets as accurately as experienced medical experts. Novel visualization methods are proposed that support the physician in sensitive and objective assessment of the treatment success. It is shown that the assessment software has the potential to improve the overall evaluation performance of interventional physicians. The presented visualization methods are developed with a novel shader framework for rapid prototyping of volume rendering. As demonstrated in this PhD thesis, this framework facilitates rapid development and customization of appropriate visualization algorithms. Moreover, the framework itself is part of medical applications which are developed with MeVisLab and allows developers to efficiently transfer research results into the clinical environment.

Outlook

To provide reliable software assistance for needle-based interventions such as RFA, further research directions may be possible. For the planning phase, interactive visualization methods are proposed. One goal for future work is automatizing the determination of safe and feasible needle pathways. Several approaches have been proposed based on projections or mathematic optimization of risk structures. However, no method allows quickly proposing probe placements under consideration of risk structures and heat-sink effects. Furthermore, some methods require segmentation masks of various organs, which are difficult to extract automatically. Integrating the proposed approximation method, that only requires a local vessel mask, could refine such automatic path proposal methods.

In this PhD thesis, methods for software-assisted planning and assessment of needle-based interventions are proposed. Software assistance for the important intra-interventional phase is not addressed. Particularly if software-assisted proposals of needle pathways have to be transferred into the operative room, intra-interventional software assistance is required to provide accurate realization of the planned intervention. For that, optical infrared or electromagnetic tracking systems should be utilized to reconstruct the spatial position of the tracked needle, i.e., the tip of the

probe, in order to guide the physician without needing to acquire new data sets. Visualization methods, such as the enhancement of vascular structures or approximation of ablation zones, may be also helpful during the intervention.

As stated in the conclusions of the methodical chapters, this PhD thesis is focused on RFA, the most common needle-based tumor ablation therapy. However, other interventions found in clinical practice, such as microwave ablation (MWA) or irreversible electroporation (IRE), which is currently under clinical investigation [150], should also supported. Methods such as interactive visual assessment are not related to a single ablation procedure and thus are applicable to all needle-based interventions. But RFA specific methods, such as the approximation of the ablation zone, have to be adjusted according to the properties of the current ablation procedure.

Appendix

List of Abbreviations

ANOVA	Analysis Of Variance
AVM	Arteriovenous Malformation
CT	Computed Tomography
CUD	Color Universal Design
DTF	Distance Transform
DVR	Direct Volume Rendering
FCM	Fuzzy C-Means
FEM	Finite Element Method
GLSL	OpenGL Shading Language
GPU	Graphics Processing Unit
GUI	Graphical User Interface
HF	High Frequency
HIFU	High-Intensity Focused Ultrasound
HU	Hounsfield Units
IRE	Irreversible Electroporation
IVC	Inferior Vena Cava
LCC	Local Cross Correlation
LITT	Laserinduced Thermotherapy
MPR	Multiplanar Reformation
MRI	Magnetic Resonance Imaging
MW(A)	Microwave (Ablation)
RF(A)	Radiofrequency (Ablation)
ROI	Region Of Interest
US	Ultrasound

List of Figures

1.1	A monopolar applicator is percutaneously placed in the liver.	3
2.1	Overview of the clinical steps of image-guided interventions.	11
2.2	Gross specimen of a pig liver after ex-vivo ablation without perfusion.	13
2.3	Gross specimen of a resected bovine liver after in-vivo ablation.	14
2.4	Illustration of a monopolar RF applicator.	15
2.5	Illustration of a bipolar RF applicator with ablation zone.	16
2.6	Photograph of three RF applicators.	17
2.7	The programmable rendering pipeline.	19
2.8	I/O parameters of vertex, geometry and fragment processor.	20
2.9	Overview of the volume-rendering pipeline.	22
2.10	3D texture slicing vs. ray casting.	23
3.1	Illustrative description of the GUI and workflow concept.	29
3.2	Illustrative description of an RF applicator and ablation zone	33
3.3	Superimposed visualization of the ablation zone.	33
3.4	Superimposed visualization of the simulated thermal necrosis image.	34
3.5	Anatomical volume rendering with transfer function.	36
3.6	A volume rendering of the target view.	37
3.7	Volume renderings of the tumor mask.	38
3.8	Volume rendering of ablation zones and tumor.	39
3.9	Iso-Hull visualization of the simulated thermal necrosis image.	40
3.10	Combined visualization of bone structures and vessels.	41
3.11	Mean and standard deviation of liver parenchyma and vessels.	41
3.12	ROIs with automatically determined transfer function.	42
3.13	Screen shot of the RFA planning software.	44
4.1	Illustration of the iterative circle.	49
4.2	Illustrative description of the simplified model.	51
4.3	Union of spheres along the points of the electrode.	52
4.4	Approximated ablation zone and numerical simulation in 2D views.	55
4.5	Deformation of the ablation zone from multiple vessels.	56
4.6	Illustration of the influence of the approximation parameters.	58

4.7	The optimization of the ablation zone for four start tuples.	59
4.8	The normalized thermal diffusion of the vasculature.	61
4.9	Illustration of the approximation model.	62
4.10	Projected slice visualizations of approximated ablation zones.	65
4.11	Rendering with reduced neighborhood samples for shading.	67
4.12	Comparison of volume visualization techniques of the ablation zone. .	68
4.13	Comparing differences of ablation zone models.	70
4.14	Four slice projections with similar visualization parameters.	71
4.15	Four volume renderings with similar visualization parameters.	72
4.16	Rendering of an umbrella-shaped monopolar RF applicator.	74
5.1	Illustration of the assessment workflow.	81
5.2	Illustration of a tumor located in the vicinity of vascular structures. .	81
5.3	The smoothed histogram of a CT data set.	82
5.4	Registration workflow steps.	83
5.5	Image menu as overlay on top of the anatomical image.	84
5.6	Color fusion schemes for slice rendering.	85
5.7	Slice visualization of a tumor and registered coagulation.	86
5.8	Filtering of outlier landmarks from a landmark set.	87
5.9	The average distance to the center of gravity per landmark set	88
5.10	Renderings of pre-interventional lesions and the surrounding anatomy.	89
5.11	Screenshot of the software assistant.	91
5.12	Illustration of the average distance of all registered data sets.	92
5.13	Box plot of all 41 cases.	93
6.1	The goal of radiofrequency ablation.	100
6.2	Subdivided of the coagulation into three zones.	101
6.3	The traffic light color scheme in the tumor's extent.	102
6.4	Visualization of the ablation zones in 2D.	102
6.5	Shaded volume rendering of the tumor with applied color scheme. . .	103
6.6	The used longitude–latitude cylindrical mapping.	107
6.7	Illustration of the rendering of the rectangular map.	108
6.8	The checkerboard shows the vertical distortion in the map.	109
6.9	Texture coordinates of the sinusoidal and the Mollweide projection. .	110
6.10	Three tumor map layouts with traffic light color scheme.	111
6.11	Tumor map with traffic light color scheme and CUD color scheme. . .	112
6.12	Screenshot from the assessment step in the clinical software assistant.	114
6.13	Illustration of the three circular cone sectors.	115
6.14	Screenshots of the evaluation application.	116
6.15	The box plots show the elapsed seconds for every mapping.	117
6.16	The elapsed time per subject all sectors and the stopped interaction.	119
6.17	Receiver operating characteristic (ROC) for all readers.	122
6.18	Receiver operating characteristic (ROC) for each reader.	123
6.19	The elapsed time for the reading process.	124

6.20	Equirectangular map of the Earth and the corresponding cube map.	125
6.21	Tumor map for planning of RFA.	126
6.22	Rendering of the rectangular map in the case of a concave tumor.	127
6.23	Screenshots of the software-assisted evaluation application	127
7.1	Schematic overview of the shader pipeline.	135
7.2	Pipeline function to obtain shading using a library function.	136
7.3	Library function to calculate diffuse and specular multipliers.	137
7.4	Overview of the composed SuperShader code of the pipeline.	138
7.5	Illustration of the shader generation process.	139
7.6	Insertion of custom pipeline functions.	140
7.7	The GUI of the custom shader function node.	141
7.8	The GUIs of three shader parameter nodes.	142
7.9	The GUI of the shader include node.	142
7.10	The GUI of the shader diagnosis node.	143
7.11	The scene graph used for stochastic jittering.	144
7.12	Examples for stochastic jittering.	145
7.13	Illustrative description of the multi-volume rendering scene graph.	146
7.14	Multi-modal rendering of three MR data sets	147
7.15	The scene graph used for the visualization of the ablation zone.	149
7.16	2D and 3D visualization of ellipsoidal ablation zones.	150
7.17	Overview of the SuperShader for GPU-based volume raycasting.	153

List of Tables

4.1	Comparison of performance and properties of ablation zone models. . .	54
6.1	The mean time to hit the sectors.	118
6.2	The mean rate to hit the sectors.	118
6.3	Averaged performance to predict tumor recurrence.	120
6.4	Individual performance to predict tumor recurrence for each reader. .	121

List of Own Publications (chronological)

- [1] Rieder, C., Ritter, F., Raspe, M., and Peitgen, H.-O. “Interactive Visualization of Multimodal Volume Data for Neurosurgical Tumor Treatment.” In: *Computer Graphics Forum (Special Issue on Eurographics Symposium on Visualization)*, 27(3) (2008), pp. 1055–1062.
- [2] Rieder, C., Schwier, M., Hahn, H. K., and Peitgen, H.-O. “High-Quality Multimodal Volume Visualization of Intracerebral Pathological Tissue.” In: *Eurographics Workshop on Visual Computing for Biomedicine* (2008), pp. 167–176.
- [3] Lehmann, K., Ritz, J., Valdeig, S., Knappe, V., Schenk, A., Weihusen, A., Rieder, C., et al. “Ex situ quantification of the cooling effect of liver vessels on radiofrequency ablation.” In: *Langenbeck’s Archives of Surgery*, 394(3) (2009), pp. 475–481 (cited on p. 69).
- [4] Rieder, C., Schwier, M., Weihusen, A., Zidowitz, S., and Peitgen, H.-O. “Visualization of Risk Structures for Interactive Planning of Image Guided Radiofrequency Ablation of Liver Tumors.” In: *Proceedings of SPIE Medical Imaging*, 7261 (2009), pp. 726134.1–726134.9 (cited on p. 46).
- [5] Zidowitz, S., Bourquain, H., Hansen, C., Rieder, C., Weihusen, A., Prause, G., and Peitgen, H.-O. “Software Assistance for Planning of RF-Ablation and Oncological Resection in Liver Surgery.” In: *4th European Conference of the International Federation for Medical and Biological Engineering*. Vol. 22. IFMBE Proceedings. Springer Berlin Heidelberg, 2009, pp. 114–117.
- [6] Hansen, C., Wieferich, J., Ritter, F., Rieder, C., and Peitgen, H.-O. “Illustrative visualization of 3D planning models for augmented reality in liver surgery.” In: *International Journal of Computer Assisted Radiology and Surgery*, 5 (2 2010), pp. 133–141.
- [7] Schumann, C., Rieder, C., Bieberstein, J., Weihusen, A., Zidowitz, S., Moltz, J.-. H., and Preusser, T. “State of the Art in Computer-Assisted Planning, Intervention and Assessment of Liver Tumor Ablation.” In: 38(1) (2010), pp. 31–52 (cited on p. 48).

- [8] Rieder, C., Weihusen, A., Schumann, C., Zidowitz, S., and Peitgen, H.-O. “Visual Support for Interactive Post-Interventional Assessment of Radiofrequency Ablation Therapy.” In: *Computer Graphics Forum (Special Issue on Eurographics Symposium on Visualization)*, 29(3) (2010), pp. 1093–1102.
- [9] Rieder, C., Altrogge, I., Kröger, T., Zidowitz, S., and Preusser, T. “Interactive Approximation of the Ablation Zone incorporating Heatsink Effects for Radiofrequency Ablation.” In: *Proceedings of CURAC* (2010), pp. 9–12.
- [10] Zidowitz, S., Altrogge, I., Hansen, C., Hindennach, M., Kröger, T., Ojdanic, D., Rieder, C., et al. “Computer-Assisted Risk Prevention in Surgical and Interventional Treatment of Liver Tumor.” In: *Zeitschrift für Biomedizinische Technik*, 55 (2010), pp. 74–77.
- [11] Weiler, F., Rieder, C., David, C. A., Wald, C., and Hahn, H. K. “AVM-Explorer: Multi-Volume Visualization of Vascular Structures for Planning of Cerebral AVM Surgery.” In: *EG 2011 - Dirk Bartz Prize* (2011), pp. 9–12 (cited on p. 146).
- [12] Rieder, C., Palmer, S., Link, F., and Hahn, H. K. “A Shader Framework for Rapid Prototyping of GPU-Based Volume Rendering.” In: *Computer Graphics Forum (Special Issue on Eurographics Symposium on Visualization)*, 30(3) (2011), pp. 1031–1040.
- [13] Rieder, C., Kröger, T., Schumann, C., and Hahn, H. K. “GPU-based Real-time Approximation of the Ablation Zone for Radiofrequency Ablation.” In: *IEEE Transactions on Visualization and Computer Graphics (Proceedings Visualization 2011)*, 17(12) (2011), pp. 1812–1821.
- [14] Rieder, C., Wirtz, S., Zidowitz, S., Bruners, P., Isfort, P., Mahnken, A. H., and Peitgen, H.-O. “Automatic Alignment of Pre- and Post-Interventional CT Images for Assessment of Radiofrequency Ablation Therapy.” In: *Proceedings of SPIE Medical Imaging*, 8316 (2012), 83163E.1–83163E.8.
- [15] Haase, S., Rieder, C., Schumann, C., Suess, P., Teichert, K., Küfer, K.-H., and Preusser, T. “Software-Assisted Access Path Planning and Optimization of Image-Guided Radiofrequency Ablation.” In: *Proceedings of European Congress of Radiology (ECR)*. 2012 (cited on p. 75).
- [16] Weiler, F., Rieder, C., David, C. A., Wald, C., and Hahn, H. K. “On the Value of Multi-Volume Visualization for Preoperative Planning of Cerebral AVM Surgery.” In: *Eurographics Workshop on Visual Computing for Biomedicine* (2012), pp. 49–56.
- [17] Rieder, C., Poch, F., Tiesler, H., Lehmann, K., and Preusser, T. “Software Tool for the Analysis of the Coagulation Zone from Multipolar Radiofrequency Ablation.” In: *Proceedings of CURAC* (2012), in press.

Bibliography

- [18] Abram, G. D. and Whitted, T. “Building Block Shaders.” In: *ACM SIGGRAPH Computer Graphics*, 24(4) (1990), pp. 283–288 (cited on p. 131).
- [19] Ahmed, M., Brace, C. L., Lee, F. T., and Goldberg, S. N. “Principles of and Advances in Percutaneous Ablation.” In: *Radiology*, 258(2) (2011), pp. 351–69 (cited on pp. 8, 9, 17, 34).
- [20] Antoch, G., Kuehl, H., Vogt, F. M., Debatin, J. F., and Stattaus, J. “Value of CT volume imaging for optimal placement of radiofrequency ablation probes in liver lesions.” In: *Journal of vascular and interventional radiology : JVIR*, 13(11) (2002), pp. 1155–61 (cited on p. 98).
- [21] Arrhenius, S. “Über die Reaktionsgeschwindigkeit bei der Inversion von Rohrzucker durch Säuren.” In: *Zeitschrift für Physikalische Chemie*, 4 (1889), pp. 226–248 (cited on p. 50).
- [22] Baere, T. de, Denys, A., Wood, B. J., Lassau, N., Kardache, M., Vilgrain, V., Menu, Y., et al. “Radiofrequency liver ablation: experimental comparative study of water-cooled versus expandable systems.” In: *AJR American Journal of Roentgenology*, 176(1) (2001), pp. 187–92 (cited on pp. 2, 17, 40, 53).
- [23] Bangard, C., Wiemker, R., Rösgen, S., Wahba, R., Hellmich, M., Fischer, J., Stippel, D. L., et al. “Optimal visualization and 3D-asphericity quantification for postoperative result assessment of hepatic radiofrequency ablations.” In: *Journal of Computer Assisted Radiology and Surgery*, 4(Supplement 1) (2009), pp. 59–70 (cited on p. 97).
- [24] Bartroli, A. V., Wegenkittl, R., König, A., Gröller, E., and Sorantin, E. “Virtual Colon Flattening.” In: *VisSym '01 Joint Eurographics - IEEE TCVG Symposium on Visualization* (2001), pp. 127–136 (cited on p. 98).
- [25] Berjano, E. “Theoretical modeling for radiofrequency ablation: state-of-the-art and challenges for the future.” In: *BioMedical Engineering OnLine*, 5(1) (2006), p. 24 (cited on p. 48).
- [26] Beyer, J., Hadwiger, M., Wolfsberger, S., and Bühler, K. “High-Quality Multimodal Volume Rendering for Preoperative Planning of Neurosurgical Interventions.” In: *IEEE Transactions on Visualization and Computer Graphics*, 13(6) (2007), pp. 1696–1703 (cited on p. 130).

- [27] Bezdek, J. C. *Pattern Recognition with Fuzzy Objective Function Algorithms*. Norwell, MA, USA: Kluwer Academic Publishers, 1981 (cited on p. 35).
- [28] Bitter, I., Van Uitert, R., Wolf, I., Ibanez, L., and Kuhnigk, J.-M. “Comparison of Four Freely Available Frameworks for Image Processing and Visualization That Use ITK.” In: *IEEE Transactions on Visualization and Computer Graphics*, 13(3) (2007), pp. 483–493 (cited on p. 132).
- [29] Blinn, J. F. “Models of light reflection for computer synthesized pictures.” In: *ACM SIGGRAPH Computer Graphics*, 11(2) (1977), pp. 192–198 (cited on p. 21).
- [30] Blythe, D. “The Direct3D 10 system.” In: *ACM Transactions on Graphics*, 25(3) (2006), pp. 724–734 (cited on p. 20).
- [31] Boehler, T., Straaten, D. van, Wirtz, S., and Peitgen, H. “A robust and extendible framework for medical image registration focused on rapid clinical application deployment.” In: *Computers in Biology and Medicine*, 41(6) (2011), pp. 340–349 (cited on p. 82).
- [32] Bordoloi, U. and Shen, H. “View Selection for Volume Rendering.” In: *Proceedings of IEEE Visualization* (2005), pp. 487–494 (cited on p. 98).
- [33] Brecheisen, R., Bartroli, A. V. i, Platel, B., and Haar Romeny, B. ter. “Flexible GPU-based Multi-Volume Ray-Casting.” In: *Proceedings of Vision, Modeling, and Visualization* (2008), p. 303 (cited on p. 131).
- [34] Brettel, H., Vienot, F., and Mollon, J. “Computerized simulation of color appearance for dichromats.” In: *Journal of the Optical Society of America*, 14(10) (1997), pp. 2647–2655 (cited on p. 110).
- [35] Bricault, I., Kikinis, R., vanSonnenberg, E., Tuncali, K., and Silverman, S. “3D Analysis of Radiofrequency-Ablated Tumors in Liver: A Computer-Aided Diagnosis Tool for Early Detection of Local Recurrences.” In: *Proceedings of MICCAI - Lecture Notes in Computer Science*, 3217 (2004), pp. 1042–1043 (cited on p. 97).
- [36] Bricault, I., Kikinis, R., Morrison, P. R., Vansonnenberg, E., Tuncali, K., and Silverman, S. G. “Liver metastases: 3D shape-based analysis of CT scans for detection of local recurrence after radiofrequency ablation.” In: *Radiology*, 241(1) (2006), pp. 243–50 (cited on p. 97).
- [37] Bruckner, S. and Gröller, M. E. “VolumeShop: An Interactive System for Direct Volume Illustration.” In: *Proceedings of IEEE Visualization*. 2005, pp. 671–678 (cited on pp. 131, 151, 152).
- [38] Butz, T., Warfield, S., Tuncali, K., Silverman, S., Sonnenberg, E. van, Jolesz, F., and Kikinis, R. “Pre- and intra-operative planning and simulation of percutaneous tumor ablation.” In: *Proceedings of MICCAI - Lecture Notes in Computer Science*, 1935 (2000), pp. 317–326 (cited on pp. 27, 46, 47).

-
- [39] Caban, J. J., Joshi, A., and Nagy, P. “Rapid Development of Medical Imaging Tools with Open-Source Libraries.” In: *Journal of Digital Imaging*, 20 Suppl 1 (2007), pp. 83–93 (cited on p. 132).
- [40] Cai, W. and Sakas, G. “Data intermixing and multi-volume rendering.” In: *Computer Graphics Forum*, 18(3) (1999), pp. 359–368 (cited on p. 148).
- [41] Carrillo, A., Duerk, J., Lewin, J., and Wilson, D. “Semiautomatic 3-D image registration as applied to interventional MRI liver cancer treatment.” In: *IEEE Transactions on Medical Imaging*, 19(3) (2000), pp. 175–185 (cited on p. 79).
- [42] Chan, M., Qu, H., Wu, Y., and Zhou, H. “Viewpoint selection for angiographic volume.” In: *Proceedings of International Symposium on Visual Computing*, 4291 (2006), p. 528 (cited on p. 98).
- [43] Charnoz, A., Agnus, V., and Soler, L. “Portal vein registration for the follow-up of hepatic tumours.” In: *Proceedings of MICCAI - Lecture Notes in Computer Science* (2004), pp. 878–886 (cited on p. 79).
- [44] Chen, M.-H., Yang, W., Yan, K., Zou, M.-W., Solbiati, L., Liu, B., and Dai, Y. “Large liver tumors: protocol for radiofrequency ablation and its clinical application in 110 patients—mathematic model, overlapping mode, and electrode placement process.” In: *Radiology*, 232(1) (2004), pp. 260–71 (cited on p. 8).
- [45] Clasen, S. and Pereira, P. L. “Magnetic resonance guidance for radiofrequency ablation of liver tumors.” In: *J Magn Reson Imaging*, 27(2) (2008), pp. 421–33 (cited on p. 10).
- [46] Cook, R. L. “Shade Trees.” In: *ACM SIGGRAPH Computer Graphics*, 18(3) (1984), pp. 223–231 (cited on p. 131).
- [47] Correa, C. and Ma, K.-L. “Size-based transfer functions: A new volume exploration technique.” In: *IEEE Transactions on Visualization and Computer Graphics*, 14(6) (2008), pp. 1380–1387 (cited on p. 42).
- [48] Deuffhard, P. and Hochmuth, R. “Multiscale analysis of thermoregulation in the human microvascular system.” In: *Mathematical Methods in the Applied Sciences*, 27(8) (2004), pp. 971–989 (cited on p. 49).
- [49] Dice, L. R. “Measures of the Amount of Ecologic Association Between Species.” In: *Ecology*, 26(3) (1945), pp. 297–302 (cited on p. 69).
- [50] Drebin, R., Carpenter, L., and Hanrahan, P. “Volume Rendering.” In: *SIGGRAPH ’88: Proceedings of the 15th annual conference on Computer graphics and interactive techniques* (1988) (cited on pp. 21, 130).
- [51] Dupuy, D. E., Zagoria, R. J., Akerley, W., Mayo-Smith, W. W., Kavanagh, P. V., and Safran, H. “Percutaneous radiofrequency ablation of malignancies in the lung.” In: *AJR American Journal of Roentgenology*, 174(1) (2000), pp. 57–9 (cited on p. 12).
-

- [52] Ebert, D. and Rheingans, P. "Volume Illustration: Non-Photorealistic Rendering of Volume Models." In: *Proceedings of IEEE Visualization*. Salt Lake City, Utah, United States, 2000, pp. 195–202 (cited on p. 139).
- [53] Engel, K., Kraus, M., and Ertl, T. "High-Quality Pre-Integrated Volume Rendering Using Hardware-Accelerated Pixel Shading." In: *Proceedings of the ACM SIGGRAPH/EUROGRAPHICS workshop on Graphics hardware* (2001), pp. 9–16 (cited on pp. 38, 104).
- [54] Feliberti, E. C. and Wagman, L. D. "Radiofrequency ablation of liver metastases from colorectal carcinoma." In: *Cancer Control*, 13(1) (2006), pp. 48–51 (cited on p. 2).
- [55] Ferlay, J., Parkin, D., and Steliarova-Foucher, E. "Estimates of cancer incidence and mortality in Europe in 2008." In: *European Journal of Cancer*, 46(4) (2010), pp. 765–781 (cited on p. 2).
- [56] Fluck, O., Vetter, C., Wein, W., Kamen, A., Preim, B., and Westermann, R. "A survey of medical image registration on graphics hardware." In: *Computer Methods and Programs in Biomedicine*, 104(3) (2011), e45–57 (cited on p. 80).
- [57] Folkegård, N. and Wesslén, D. "Dynamic Code Generation for Realtime Shaders." In: *Linköping Electronic Conference Proceedings*. 2004 (cited on p. 131).
- [58] Forner, A., Llovet, J. M., and Bruix, J. "Hepatocellular carcinoma." In: *Lancet*, 379(9822) (2012), pp. 1245–55 (cited on pp. 2, 8).
- [59] Frericks, B. B., Ritz, J. P., Roggan, A., Wolf, K.-J., and Albrecht, T. "Multipolar radiofrequency ablation of hepatic tumors: initial experience." In: *Radiology*, 237(3) (2005), pp. 1056–62 (cited on pp. 10, 16, 33).
- [60] Fujioka, C., Horiguchi, J., Ishifuro, M., Kakizawa, H., Kiguchi, M., Matsuura, N., Hieda, M., et al. "A feasibility study: evaluation of radiofrequency ablation therapy to hepatocellular carcinoma using image registration of preoperative and postoperative CT." In: *Academic Radiology*, 13(8) (2006), pp. 986–94 (cited on pp. 79, 98).
- [61] GANGI, A. "Trajectory optimization for the planning of percutaneous radiofrequency ablation of hepatic tumors." In: *Computer Aided Surgery*, 12(2) (2007), pp. 82–90 (cited on p. 8).
- [62] Garrean, S., Hering, J., Saied, A., Helton, W., and Espat, N. "Radiofrequency ablation of primary and metastatic liver tumors: a critical review of the literature." In: *American Journal of Surgery*, 195 (2008), pp. 508–520 (cited on p. 2).
- [63] Gervais, D. A., McGovern, F. J., Arellano, R. S., McDougal, W. S., and Mueller, P. R. "Renal cell carcinoma: clinical experience and technical success with radio-frequency ablation of 42 tumors." In: *Radiology*, 226(2) (2003), pp. 417–24 (cited on p. 12).

- [64] Giesel, F. L., Mehndiratta, A., Locklin, J., McAuliffe, M. J., White, S., Choyke, P. L., Knopp, M. V., et al. “Image fusion using CT, MRI and PET for treatment planning, navigation and follow up in percutaneous RFA.” In: *Experimental Oncology*, 31(2) (2009), pp. 106–14 (cited on p. 79).
- [65] Goetz, F., Borau, R., and Domik, G. “An XML-based Visual Shading Language for Vertex and Fragment Shaders.” In: *Web3D '04: Proceedings of the ninth international conference on 3D Web technology*. 2004, pp. 87–97 (cited on p. 131).
- [66] Goetz, F. and Domik, G. “Visual shaditor: a seamless way to compose high-level shader programs.” In: *ACM SIGGRAPH 2006 Research posters*. Boston, Massachusetts, 2006 (cited on p. 131).
- [67] Goldberg, S. N., Grassi, C. J., Cardella, J. F., Charboneau, J. W., Dodd, G. D., Dupuy, D. E., Gervais, D., et al. “Image-guided tumor ablation: standardization of terminology and reporting criteria.” In: *Radiology*, 235(3) (2005), pp. 728–39 (cited on pp. 8–10, 14).
- [68] Goldberg, S. N., Gazelle, G. S., Compton, C. C., Mueller, P. R., and Tanabe, K. K. “Treatment of intrahepatic malignancy with radiofrequency ablation: radiologic-pathologic correlation.” In: *Cancer*, 88(11) (2000), pp. 2452–63 (cited on pp. 10, 13).
- [69] Goldberg, S. N., Gazelle, G. S., Dawson, S. L., Rittman, W. J., Mueller, P. R., and Rosenthal, D. I. “Tissue ablation with radiofrequency using multiprobe arrays.” In: *Academic Radiology*, 2(8) (1995), pp. 670–4 (cited on p. 16).
- [70] Greene, N. “Environment mapping and other applications of world projections.” In: *IEEE Computer Graphics and Applications*, 6 (11 1986), pp. 21–29 (cited on p. 124).
- [71] Hadwiger, M., Kniss, J., Engel, K., and Rezk-Salama, C. *High-Quality Volume Graphics on Consumer PC Hardware*. ACM SIGGRAPH Course Notes 42. 2002 (cited on pp. 21, 130).
- [72] Hadwiger, M., Kniss, J. M., Rezk-salama, C., Weiskopf, D., and Engel, K. *Real-Time Volume Graphics*. Natick, MA, USA: A. K. Peters, Ltd., 2006 (cited on pp. 19, 21, 67, 137, 144).
- [73] Hadwiger, M., Berger, C., and Hauser, H. “High-quality two-level volume rendering of segmented data sets on consumer graphics hardware.” In: *Proceedings of IEEE Visualization* (2003), pp. 301–308 (cited on p. 37).
- [74] Hadwiger, M., Theußl, T., Hauser, H., and Gröller, E. “Hardware-accelerated high-quality filtering on PC hardware.” In: *Proceedings of Vision, Modeling, and Visualization* (2001), pp. 105–112 (cited on p. 137).

- [75] Haemmerich, D. and Schutt, D. J. “Sequential activation of multiple grounding pads reduces skin heating during radiofrequency tumor ablation.” In: *International Journal of Hyperthermia*, 23(7) (2007), pp. 555–66 (cited on p. 16).
- [76] Hajnal, J., Hill, D., and Hawkes, D. *Medical Image Registration*. CRC, 2001 (cited on p. 83).
- [77] Hargreaves, S. “Generating Shaders from HLSL Fragments.” In: *ShaderX³: Advanced Rendering with DirectX and OpenGL*. Ed. by Engel, W. 2004. Chap. 7.3, pp. 555–568 (cited on p. 131).
- [78] Heckel, F., Konrad, O., Hahn, H. K., and Peitgen, H.-O. “Interactive 3D Medical Image Segmentation with Energy-Minimizing Implicit Functions.” In: *Computers & Graphics: Special issue on Visual Computing for Biology and Medicine*, 35(2) (2011), pp. 275–287 (cited on p. 30).
- [79] Heizmann, O., Zidowitz, S., Bourquain, H., Potthast, S., Peitgen, H., Oertli, D., and Kettelhack, C. “Assessment of Intraoperative Liver Deformation During Hepatic Resection: Prospective Clinical Study.” In: *World Journal of Surgery*, 34(8) (2010), pp. 1887–1893 (cited on p. 78).
- [80] Herghelegiu, P., Manta, V., Perin, R., Bruckner, S., and Gröller, M. E. “Biopsy Planner - Visual Analysis for Needle Pathway Planning in Deep Seated Brain Tumor Biopsy.” In: *Computer Graphics Forum (Special Issue on EuroVis)*, 31(3) (2012). presented at EuroVis 2012, pp. 1085–1094 (cited on p. 28).
- [81] Hong, W., Gu, X., Qiu, F., Jin, M., and Kaufman, A. “Conformal Virtual Colon Flattening.” In: *Proceedings of the ACM symposium on Solid and physical modeling* (2006), pp. 85–93 (cited on p. 98).
- [82] Hurdal, M., Kurtz, K., and Banks, D. “Case Study: Interacting with Cortical Flat Maps of the Human Brain.” In: *Proceedings of IEEE Visualization* (2001), pp. 469–591 (cited on p. 98).
- [83] Ichihara, Y., Okabe, M., Iga, K., Tanaka, Y., Musha, K., and Ito, K. “Color Universal Design-The Selection of Four Easily Distinguishable Colors for all Color Vision Types.” In: *Proceedings of SPIE*, 6807 (2008), 68070O (cited on p. 110).
- [84] Jones, M., Baerentzen, J., and Sramek, M. “3D Distance Fields: A Survey of Techniques and Applications.” In: *IEEE Transactions on Visualization and Computer Graphics*, 12(4) (2006), pp. 581–599 (cited on p. 57).
- [85] Kainz, B., Portugaller, R., Seider, D., Moche, M., Stiegler, P., and Schmalstieg, D. “Volume visualization in the clinical practice.” In: *Augmented Environments for Computer-Assisted Interventions* (2012), pp. 74–84 (cited on pp. 26, 67, 98).

-
- [86] Kanitsar, A., Wegenkittl, R., Fleischmann, D., and Groller, M. “Advanced Curved Planar Reformation: Flattening of Vascular Structures.” In: *Proceedings of IEEE Visualization* (2003), pp. 43–50 (cited on p. 99).
- [87] Khlebnikov, R., Kainz, B., Muehl, J., and Schmalstieg, D. “Crepuscular rays for tumor accessibility planning.” In: *IEEE Transactions on Visualization and Computer Graphics (Proceedings Visualization 2011)*, 17(12) (2011), pp. 2163–72 (cited on pp. 28, 47).
- [88] Kim, K. W., Lee, J. M., Klotz, E., Kim, S. J., Kim, S. H., Kim, J. Y., Han, J. K., et al. “Safety Margin Assessment After Radiofrequency Ablation of the Liver Using Registration of Preprocedure and Postprocedure CT Images.” In: *American Journal of Roentgenology*, 196(5) (2011), W565–W572 (cited on p. 80).
- [89] Kim, Y.-S., Rhim, H., Lim, H. K., Choi, D., Lee, M. W., and Park, M. J. “Coagulation necrosis induced by radiofrequency ablation in the liver: histopathologic and radiologic review of usual to extremely rare changes.” In: *Radiographics*, 31(2) (2011), pp. 377–90 (cited on pp. 10, 46).
- [90] Kim, Y.-S., Lee, W. J., Rhim, H., Lim, H. K., Choi, D., and Lee, J. Y. “The Minimal Ablative Margin of Radiofrequency Ablation of Hepatocellular Carcinoma (> 2 and < 5 cm) Needed to Prevent Local Tumor Progression: 3D Quantitative Assessment Using CT Image Fusion.” In: *American Journal of Roentgenology*, 195(3) (2010), pp. 758–765 (cited on pp. 10, 79).
- [91] Klein, S., Heide, U. A. V. D., Lips, I. M., Vulpen, M. V., Staring, M., and Pluim, J. P. W. “Automatic segmentation of the prostate in 3D MR images by atlas matching using localized mutual information.” In: *Medical Physics*, 35(4) (2008), p. 1407 (cited on p. 99).
- [92] Kniss, J., Kindlmann, G., and Hansen, C. “Multidimensional Transfer Functions for Interactive Volume Rendering.” In: *IEEE Transactions on Visualization and Computer Graphics*, 8(3) (2002), pp. 270–285 (cited on p. 42).
- [93] Kohlmann, P., Bruckner, S., Groller, M. E., and Kanitsar, A. “LiveSync: Deformed Viewing Spheres for Knowledge-Based Navigation.” In: *IEEE Transactions on Visualization and Computer Graphics*, 13(6) (2007), pp. 1544–1551 (cited on p. 98).
- [94] Kohlmann, P., Bruckner, S., Kanitsar, A., and Gröller, M. “LiveSync++: enhancements of an interaction metaphor.” In: *Proceedings of Graphics Interface 2008* (2008) (cited on p. 98).
- [95] Kohlmann, P., Bruckner, S., Kanitsar, A., and Groller, M. “Contextual Picking of Volumetric Structures.” In: *Proceedings of IEEE Pacific Visualization Symposium* (2009), pp. 185–192 (cited on p. 98).

- [96] Kröger, T., Altrogge, I., Preusser, T., Pereira, P., Schmidt, D., Weihusen, A., and Peitgen, H. “Numerical simulation of radio frequency ablation with state dependent material parameters in three space dimensions.” In: *Proceedings of MICCAI - Lecture Notes in Computer Science*, 4191 (2006), pp. 380–388 (cited on pp. 27, 31, 46, 50).
- [97] Kröger, T., Pätz, T., Altrogge, I., Schenk, A., Lehmann, K. S., Frericks, B. B., Ritz, J., et al. “Fast Estimation of the Vascular Cooling in RFA Based on Numerical Simulation.” In: *The Open Biomedical Engineering Journal* (2009), pp. 1–11 (cited on pp. 48, 50–52, 73).
- [98] Kuvshinoff, B. W. and Ota, D. M. “Radiofrequency ablation of liver tumors: influence of technique and tumor size.” In: *Surgery*, 132(4) (2002), (cited on p. 8).
- [99] Laeseke, P. F., Sampson, L. A., Haemmerich, D., Brace, C. L., Fine, J. P., Frey, T. M., Winter, T. C., et al. “Multiple-electrode radiofrequency ablation: simultaneous production of separate zones of coagulation in an in vivo porcine liver model.” In: *Journal of vascular and interventional radiology : JVIR*, 16(12) (2005), pp. 1727–35 (cited on p. 16).
- [100] Lampe, D., Correa, C., Ma, K., and Hauser, H. “Curve-Centric Volume Reformation for Comparative Visualization.” In: *IEEE Transactions on Visualization and Computer Graphics*, 15(6) (2009), pp. 1235–1242 (cited on p. 99).
- [101] Lathen, G., Lindholm, S., Lenz, R., Persson, A., and Borga, M. “Automatic Tuning of Spatially Varying Transfer Functions for Blood Vessel Visualization.” In: *IEEE Transactions on Visualization and Computer Graphics*, 18(12) (2012), pp. 2345–2354 (cited on p. 42).
- [102] Lazebnik, R., Breen, M., Lewin, J., and Wilson, D. “Automatic Model-Based Evaluation of Magnetic Resonance-Guided Radio Frequency Ablation Lesions with Histological Correlation.” In: *Journal of Magnetic Resonance Imaging*, 19(2) (2004), pp. 245–254 (cited on p. 97).
- [103] Link, F., Koenig, M., and Peitgen, H.-O. “Multi-Resolution Volume Rendering with per Object Shading.” In: *Proceedings of Vision, Modeling, and Visualization*. 2006, pp. 185–191 (cited on p. 137).
- [104] Littmann, A., Schenk, A., Preim, B., Prause, G., Lehmann, K., Roggan, A., and Peitgen, H.-O. “Planning of anatomical resections and in situ ablations in oncologic liver surgery.” In: *International Congress Series (Proceedings of Computer Assisted Radiology and Surgery)* (2003) (cited on p. 47).
- [105] Liu, Z., Ahmed, M., Sabir, A., Humphries, S., and Goldberg, S. N. “Computer modeling of the effect of perfusion on heating patterns in radiofrequency tumor ablation.” In: *International Journal of Hyperthermia*, 23(1) (2007), pp. 49–58 (cited on p. 14).

-
- [106] Liu, Z., Ahmed, M., Weinstein, Y., Yi, M., Mahajan, R. L., and Goldberg, S. N. “Characterization of the RF ablation-induced ‘oven effect’: the importance of background tissue thermal conductivity on tissue heating.” In: *International Journal of Hyperthermia*, 22(4) (2006), pp. 327–42 (cited on p. 13).
- [107] Livraghi, T., Goldberg, S. N., Lazzaroni, S., Meloni, F., Ierace, T., Solbiati, L., and Gazelle, G. S. “Hepatocellular carcinoma: radio-frequency ablation of medium and large lesions.” In: *Radiology*, 214(3) (2000), pp. 761–8 (cited on p. 9).
- [108] Lobik, L., Leveillee, R. J., and Hoey, M. F. “Geometry and temperature distribution during radiofrequency tissue ablation: an experimental ex vivo model.” In: *Journal of Endourology*, 19(2) (2005), pp. 242–7 (cited on p. 31).
- [109] Lorensen, W. E. and Cline, H. E. “Marching cubes: A high resolution 3D surface construction algorithm.” In: *ACM SIGGRAPH Computer Graphics*, 21 (4 1987), pp. 163–169 (cited on p. 30).
- [110] Mark, W. R., Glanville, R. S., Akeley, K., and Kilgard, M. J. “Cg: a system for programming graphics hardware in a C-like language.” In: *ACM Transactions on Graphics*, 22(3) (2003), pp. 896–907 (cited on p. 20).
- [111] McCreedy, E. S., Cheng, R., Hemler, P. F., Viswanathan, A., Wood, B. J., and McAuliffe, M. J. “Radio Frequency Ablation Registration, Segmentation, and Fusion Tool.” In: *IEEE Transactions on Information Technology in Biomedicine*, 10(3) (2006), pp. 490–496 (cited on pp. 27, 47).
- [112] McDonnell, B. and Elmqvist, N. “Towards Utilizing GPUs in Information Visualization: A Model and Implementation of Image-Space Operations.” In: *IEEE Transactions on Visualization and Computer Graphics*, 15(6) (2009), pp. 1105–1112 (cited on p. 131).
- [113] McGuire, M. “The SuperShader.” In: *ShaderX⁴: Advanced Rendering Techniques*. Ed. by Engel, W. 2005. Chap. 8.1, pp. 485–498 (cited on p. 131).
- [114] McGuire, M., Stathis, G., Pfister, H., and Krishnamurthi, S. “Abstract Shade Trees (preprint).” In: *Symposium on Interactive 3D Graphics and Games*. Redwood City, CA, 2006 (cited on p. 131).
- [115] Meissner, M., Lorensen, B., Zuiderveld, K., Simha, V., and Wegenkittl, R. “Volume rendering in medical applications: we’ve got pretty images, what’s left to do?” In: *Proceedings of IEEE Visualization* (2002), pp. 575–578 (cited on p. 130).
- [116] MeVis Medical Solutions AG. *MeVisLab, medical image processing and visualization*. <http://www.mevislab.de>. 2011 (cited on pp. 130, 132).

- [117] Meyer-Spradow, J., Ropinski, T., Mensmann, J., and Hinrichs, K. H. “Voreen: A Rapid-Prototyping Environment for Ray-Casting-Based Volume Visualizations.” In: *IEEE Computer Graphics and Applications*, 29(6) (2009), pp. 6–13 (cited on pp. 131, 151, 152).
- [118] Mitchell, J. L., Brennan, C., and Card, D. “Real-time image-space outlining for non-photorealistic rendering.” In: *ACM SIGGRAPH conference abstracts and applications*. 2002, pp. 239–239 (cited on pp. 32, 64).
- [119] Modersitzki, J. *Numerical methods for image registration*. Oxford University Press, USA, 2004 (cited on p. 82).
- [120] Moltz, J., Bornemann, L., Kuhnigk, J.-M., Dicken, V., Peitgen, E., Meier, S., Bolte, H., et al. “Advanced Segmentation Techniques for Lung Nodules, Liver Metastases, and Enlarged Lymph Nodes in CT Scans.” In: *IEEE Journal of Selected Topics in Signal Processing*, 3(1) (2009), pp. 122–134 (cited on pp. 29, 80).
- [121] Mulier, S., Ni, Y., Frich, L., Burdio, F., Denys, A. L., Wispelaere, J.-F. D., Dupas, B., et al. “Experimental and clinical radiofrequency ablation: proposal for standardized description of coagulation size and geometry.” In: *Annals of Surgical Oncology*, 14(4) (2007), pp. 1381–96 (cited on pp. 2, 4, 17, 31, 46, 100).
- [122] Mulier, S., Ni, Y., Jamart, J., Michel, L., Marchal, G., and Ruers, T. “Radiofrequency Ablation Versus Resection for Resectable Colorectal Liver Metastases: Time for a Randomized Trial?” In: *Annals of Surgical Oncology*, 15(1) (2008), pp. 144–57 (cited on pp. 2, 16, 78).
- [123] Mundeleer, L., Wikler, D., Leloup, T., and Warzee, N. “Development of a computer assisted system aimed at RFA liver surgery.” In: *Comput Med Imag Grap*, 32(7) (2008), pp. 611–621 (cited on p. 10).
- [124] Neider, J. and Davis, T. *OpenGL Programming Guide: The Official Guide to Learning OpenGL*. Addison-Wesley Longman Publishing Co., 1993 (cited on p. 20).
- [125] Nelder, J. A. and Mead, R. “A Simplex Method for Function Minimization.” In: *The Computer Journal*, 7(4) (1, 1965), pp. 308–313 (cited on p. 58).
- [126] Netsch, T., Rösch, P., Muiswinkel, A. van, and Weese, J. “Towards Real-Time Multi-Modality 3-D Medical Image Registration.” In: *Proceedings of IEEE Computer Vision*, 1 (2001), p. 718 (cited on p. 82).
- [127] Neugebauer, M., Gasteiger, R., Beuing, O., Diehl, V., Skalej, M., and Preim, B. “Map Displays for the Analysis of Scalar Data on Cerebral Aneurysm Surfaces.” In: *Eurographics/IEEE-VGTC Symposium on Visualization*, 28(3) (2009), pp. 895–902 (cited on pp. 98, 124).

-
- [128] Niculescu, G., Forand, D., and Nosher, J. “Non-rigid Registration of the Liver in Consecutive CT Studies for Assessment of Tumor Response to Radiofrequency Ablation.” In: *Proceedings of IEEE Engineering in Medicine and Biology Society* (2007), pp. 856–859 (cited on p. 79).
- [129] Oeltze, S. and Preim, B. “Visualization of Anatomic Tree Structures with Convolution Surfaces.” In: *in Proc. Joint IEEE/EG Symposium on Visualization. Eurographics Association* (2004), pp. 311–320 (cited on p. 43).
- [130] Padma, S., Martinie, J. B., and Iannitti, D. A. “Liver tumor ablation: percutaneous and open approaches.” In: *J Surg Oncol*, 100(8) (2009), pp. 619–34 (cited on p. 9).
- [131] Park, M.-h., Rhim, H., Kim, Y.-s., Choi, D., Lim, H. K., and Lee, W. J. “Spectrum of CT findings after radiofrequency ablation of hepatic tumors.” In: *Radiographics*, 28(2) (2008), (cited on p. 10).
- [132] Pennes, H. H. “Analysis of tissue and arterial blood temperatures in a resting forearm.” In: *Journal of Applied Physiology*, 1 (1948), pp. 93–122 (cited on p. 49).
- [133] Pereira, P. L. “Actual role of radiofrequency ablation of liver metastases.” In: *European Radiology*, 17(8) (2007), pp. 2062–70 (cited on pp. 2, 9, 10, 12, 16).
- [134] Pereira, P. L., Trübenbach, J., Schenk, M., Subke, J., Kroeber, S., Schaefer, I., Remy, C. T., et al. “Radiofrequency ablation: in vivo comparison of four commercially available devices in pig livers.” In: *Radiology*, 232(2) (2004), pp. 482–90 (cited on pp. 14, 16).
- [135] Pfister, H., Lorensen, B., Bajaj, C., Kindlmann, G., Schroeder, W., Avila, L., Raghu, K., et al. “The transfer function bake-off.” In: *IEEE Computer Graphics and Applications*, 21(3) (2001), pp. 16–22 (cited on p. 35).
- [136] Pietrzyk, U., Herholz, K., Fink, G., Jacobs, A., Mielke, R., Slansky, I., Würker, M., et al. “An interactive technique for three-dimensional image registration: validation for PET, SPECT, MRI and CT brain studies.” In: *Journal of nuclear medicine: official publication, Society of Nuclear Medicine*, 35(12) (1994), p. 2011 (cited on p. 79).
- [137] Plate, J., Holtkaemper, T., and Froehlich, B. “A Flexible Multi-Volume Shader Framework for Arbitrarily Intersecting Multi-Resolution Datasets.” In: *IEEE Transactions on Visualization and Computer Graphics*, 13(6) (2007), pp. 1584–1591 (cited on pp. 131, 151, 152).
- [138] Poon, R. T., Ng, K. K., Lam, C. M., Ai, V., Yuen, J., Fan, S. T., and Wong, J. “Learning curve for radiofrequency ablation of liver tumors: prospective analysis of initial 100 patients in a tertiary institution.” In: *Annals of surgery*, 239(4) (2004), pp. 441–9 (cited on p. 8).
-

- [139] Praßni, J., Ropinski, T., and Hinrichs, K. H. “Uncertainty-Aware Guided Volume Segmentation.” In: *IEEE Transactions on Visualization and Computer Graphics (TVCG) (Vis Conference Issue)*, 16(6) (2010), pp. 1358–1365 (cited on p. 66).
- [140] Prior, F. W., Erickson, B. J., and Tarbox, L. “Open Source Software Projects of the caBIG™ In Vivo Imaging Workspace Software Special Interest Group.” In: *Journal of Digital Imaging*, 20(S1) (2007), pp. 94–100 (cited on pp. 132, 152).
- [141] Rheingans, P. and Ebert, D. “Volume Illustration: Nonphotorealistic Rendering of Volume Models.” In: *IEEE Transactions on Visualization and Computer Graphics*, 7(3) (2001), pp. 253–264 (cited on pp. 68, 148).
- [142] Rhim, H., Goldberg, S. N., Dodd, G. D., Solbiati, L., Lim, H. K., Tonolini, M., and Cho, O. K. “Essential techniques for successful radio-frequency thermal ablation of malignant hepatic tumors.” In: *Radiographics*, 21 Spec No (2001), (cited on pp. 8, 12).
- [143] Ritter, F., Boskamp, T., Homeyer, A., Laue, H., Schwier, M., Link, F., and Peitgen, H.-O. “Medical Image Analysis.” In: *IEEE Pulse*, 2(6) (2011), pp. 60–70 (cited on pp. 130, 132).
- [144] Ropinski, T., Hermann, S., Reich, R., Schafers, M., and Hinrichs, K. “Multi-modal Vessel Visualization of Mouse Aorta PET/CT Scans.” In: *IEEE Transactions on Visualization And Computer Graphics*, 15(6) (2009), pp. 1515–1522 (cited on p. 99).
- [145] Rosenthal, D. I., Hornicek, F. J., Torriani, M., Gebhardt, M. C., and Mankin, H. J. “Osteoid osteoma: percutaneous treatment with radiofrequency energy.” In: *Radiology*, 229(1) (2003), pp. 171–5 (cited on p. 12).
- [146] Rößler, F., Botchen, R. P., and Ertl, T. “Dynamic Shader Generation for GPU-based Multi-Volume Raycasting.” In: *IEEE Computer Graphics and Applications*, 28(5) (2008), pp. 66–77 (cited on pp. 132, 151, 152).
- [147] Rößler, F., Botchen, R., and Ertl, T. “Dynamic Shader Generation for Flexible Multi-Volume Visualization.” In: *Proceedings of IEEE Pacific Visualization Symposium* (2008), pp. 17–24 (cited on p. 132).
- [148] Rost, R. J., Licea-Kane, B. M., Ginsburg, D., Kessenich, J. M., Lichtenbelt, B., Malan, H., and Weiblen, M. *OpenGL Shading Language (3rd Edition)*. Addison-Wesley Professional, 2009 (cited on p. 20).
- [149] Rote, G. “Computing the minimum Hausdorff distance between two point sets on a line under translation.” In: *Information Processing Letters*, 38 (3 1991), pp. 123–127 (cited on p. 69).
- [150] Rubinsky, B., Onik, G., and Mikus, P. “Irreversible electroporation: a new ablation modality—clinical implications.” In: *Technology in Cancer Research and Treatment*, 6(1) (2007), pp. 37–48 (cited on p. 159).

-
- [151] Rusinkiewicz, S. and Levoy, M. “Efficient variants of the ICP algorithm.” In: *Proceedings of 3-D Digital Imaging and Modeling* (2001), pp. 145–152 (cited on p. 88).
- [152] Samset, E., Mala, T., Aurdal, L., and Balasingham, I. “Intra-operative visualisation of 3D temperature maps and 3D navigation during tissue cryoablation.” In: *Computerized Medical Imaging and Graphics*, 29(6) (2005), pp. 499–505 (cited on pp. 64, 97).
- [153] Schenk, A., Prause, G. P. M., and Peitgen, H.-O. “Efficient Semiautomatic Segmentation of 3D Objects in Medical Images.” In: *Proceedings of MICCAI - Lecture Notes in Computer Science*. London, UK: Springer-Verlag, 2000, pp. 186–195 (cited on p. 40).
- [154] Schneider, J., Kraus, M., and Westermann, R. “GPU-Based Real-Time Discrete Euclidean Distance Transforms With Precise Error Bounds.” In: *Proceedings of Computer Vision Theory and Applications*. 2009, pp. 435–442 (cited on p. 124).
- [155] Schumann, C., Bieberstein, J., Braunewell, S., Niethammer, M., and Peitgen, H.-O. “Visualization support for the planning of hepatic needle placement.” In: *International Journal of Computer Assisted Radiology and Surgery* (2011) (cited on pp. 28, 47).
- [156] Schumann, C., Bieberstein, J., Trumm, C., Schmidt, D., Bruners, P., Niethammer, M., Hoffmann, R. T., et al. “Fast Automatic Path Proposal Computation for Hepatic Needle Placement.” In: *Proceedings of SPIE Medical Imaging*, 7625 (2010), (cited on pp. 28, 47).
- [157] Schwier, M., Dicken, V., and Peitgen, H.-O. “3D Visualization of Vascular Structures around Liver Tumors using Fuzzy Clustering.” In: *Proceedings of CARS*, 3 (2008), pp. 403–404 (cited on p. 35).
- [158] Seitel, A., Engel, M., Sommer, C., Radeleff, B., Essert-Villard, C., Baegert, C., Fangerau, M., et al. “Computer-assisted trajectory planning for percutaneous needle insertions.” In: *Med. Phys.* 38 (2011), p. 3246 (cited on p. 28).
- [159] Selle, D., Preim, B., Schenk, A., and Peitgen, H.-O. “Analysis of vasculature for liver surgical planning.” In: *IEEE Transactions on Medical Imaging*, 21(11) (2002), pp. 1344–57 (cited on p. 53).
- [160] Sereda, P., Bartroli, A., Serlie, I., and Gerritsen, F. “Visualization of boundaries in volumetric data sets using LH histograms.” In: *IEEE Transactions on Visualization and Computer Graphics*, 12(2) (2006), pp. 208–218 (cited on p. 42).
- [161] Shen, L. and Makedon, F. “Spherical Parameterization for 3D Surface Analysis in Volumetric Images.” In: *ITCC '04: Proceedings of the International Conference on Information Technology: Coding and Computing*, 2 (2004), p. 643 (cited on p. 104).
-

- [162] Snyder, J. P. *Map Projections - A Working Manual*. 1987 (cited on pp. 99, 105).
- [163] Solbiati, L., Livraghi, T., Goldberg, S. N., Ierace, T., Meloni, F., Dellanoce, M., Cova, L., et al. "Percutaneous radio-frequency ablation of hepatic metastases from colorectal cancer: long-term results in 117 patients." In: *Radiology*, 221(1) (2001), pp. 159–66 (cited on p. 12).
- [164] Soler, L., Delingette, H., Malandain, G., Montagnat, J., Ayache, N., Koehl, C., Dourthe, O., et al. "Fully automatic anatomical, pathological, and functional segmentation from CT scans for hepatic surgery." In: *Computer Aided Surgery*, 6(3) (2001), pp. 131–42 (cited on p. 27).
- [165] Sommer, O., Dietz, A., Westermann, R., and Ertl, T. "An interactive visualization and navigation tool for medical volume data." In: *Computers & Graphics*, 23(2) (1999), pp. 233–244 (cited on p. 139).
- [166] Stegmaier, S., Strengert, M., Klein, T., and Ertl, T. "A Simple and Flexible Volume Rendering Framework for Graphics-Hardware-based Raycasting." In: *Proceedings of Volume Graphics* (2005), pp. 187–241 (cited on p. 131).
- [167] Stippel, D. L., Brochhagen, H. G., Arenja, M., Hunkemöller, J., Hölscher, A. H., and Beckurts, K. T. E. "Variability of Size and Shape of Necrosis Induced by Radiofrequency Ablation in Human Livers: A Volumetric Evaluation." In: *Annals of Surgical Oncology*, 11(4) (2004), pp. 420–5 (cited on p. 97).
- [168] Stokking, R., Zubal, I., and Viergever, M. "Display of fused images: Methods, interpretation, and diagnostic improvements." In: *Seminars in Nuclear Medicine*, 33(3) (2003), pp. 219–227 (cited on p. 83).
- [169] Tatarchuk, N. "RenderMonkey: an effective environment for shader prototyping and development." In: *ACM SIGGRAPH Sketches*. 2004, pp. 91– (cited on p. 131).
- [170] Tiede, U., Schiemann, T., and Hohne, K. "High quality rendering of attributed volume data." In: *Proceedings of IEEE Visualization* (1998), pp. 255–262 (cited on p. 64).
- [171] Tietjen, C., Meyer, B., Schlechtweg, S., Preim, B., Hertel, I., and Strauß, G. "Enhancing slice-based visualizations of medical volume data." In: *IEEE/Eurographics Symposium on Visualization (EuroVis)* (2006), pp. 123–130 (cited on p. 63).
- [172] Trapp, M. and Döllner, J. "Automated Combination of Real-Time Shader Programs." In: *Proceedings of Eurographics*. 2007, pp. 53–56 (cited on p. 131).
- [173] Trovato, K., Dalal, S., Krücker, J., Venkatesan, A., and Wood, B. J. "Automated RFA planning for complete coverage of large tumors." In: *Proceedings of SPIE Medical Imaging*. Vol. 7261. 2009, pp. 72610D.1–72610D.7 (cited on p. 48).

-
- [174] Viergever, J. and Maintz, J. “A survey of medical image registration.” In: *Medical Image Analysis*, 2(1-36) (1998), p. 476 (cited on p. 80).
- [175] Villard, C., Soler, L., and Gangi, A. “Radiofrequency ablation of hepatic tumors: simulation, planning, and contribution of virtual reality and haptics.” In: *Computer Methods in Biomechanics and Biomedical Engineering*, 8(4) (2005), pp. 215–227 (cited on pp. 46, 47).
- [176] Villard, C., Soler, L., Papier, N., Agnus, V., Gangi, A., Mutter, D., and Marescaux, J. “RF-Sim: a treatment planning tool for radiofrequency ablation of hepatic tumors.” In: *Proceedings of Information Visualization* (2003), pp. 561–566 (cited on p. 27).
- [177] Villard, C., Soler, L., Papier, N., Agnus, V., They, S., Gangi, A., Mutter, D., et al. *Virtual radiofrequency ablation of liver tumors*. 2003 (cited on pp. 47, 55).
- [178] Weihusen, A., Hinrichsen, L., Carus, T., Dammer, R., Rascher-Friesenhausen, R., Kröger, T., Peitgen, H., et al. “Towards a verified simulation model for radiofrequency ablations.” In: *Information Processing in Computer-Assisted Interventions* (2010), pp. 179–189 (cited on p. 69).
- [179] Weihusen, A., Ritter, F., Kröger, T., and Preusser, T. “Workflow oriented software support for image guided radiofrequency ablation of focal liver malignancies.” In: *Proceedings of SPIE Medical Imaging*, 6509(650919) (2007), p. 650919 (cited on pp. 27, 48, 79, 97).
- [180] Weiskopf, D., Engel, K., and Ertl, T. “Interactive Clipping Techniques for Texture-Based Volume Visualization and Volume Shading.” In: *IEEE Transactions on Visualization and Computer Graphics*, 9(3) (2003), pp. 298–312 (cited on p. 104).
- [181] Weiskopf, D., Engel, K., and Ertl, T. “Volume Clipping via Per-Fragment Operations in Texture-Based Volume Visualization.” In: *Proceedings of IEEE Visualization* (2002), pp. 93–100 (cited on p. 146).
- [182] Westermann, R. and Ertl, T. “Efficiently Using Graphics Hardware in Volume Rendering Applications.” In: *Proceedings of SIGGRAPH*, 98 (1998), pp. 169–178 (cited on p. 35).
- [183] Wilson, D., Carrillo, A., Zheng, L., Genc, A., Duerk, J., and Lewin, J. “Evaluation of 3D image registration as applied to MR-guided thermal treatment of liver cancer.” In: *Journal of Magnetic Resonance Imaging*, 8(1) (1998), pp. 77–84 (cited on p. 79).
- [184] Wood, T., Rose, D., Chung, M., Allegra, D., Foshag, L., and Bilchik, A. “Radiofrequency ablation of 231 unresectable hepatic tumors: Indications, limitations, and complications.” In: *Annals of Surgical Oncology*, 7(8) (2000), pp. 593–600 (cited on p. 8).
-

- [185] XIP. *The Open eXtensible Imaging Platform Project*. <http://www.openxip.org>. 2011 (cited on pp. 132, 152).
- [186] Yaniv, Z., Cheng, P., Wilson, E., Popa, T., Lindisch, D., Campos-Nanez, E., Abeledo, H., et al. “Needle-Based Interventions With the Image-Guided Surgery Toolkit (IGSTK): From Phantoms to Clinical Trials.” In: *Biomedical Engineering, IEEE Transactions on*, 57(4) (2010), pp. 922–933 (cited on p. 10).
- [187] Zhai, W., Xu, J., Zhao, Y., Song, Y., Sheng, L., and Jia, P. “Preoperative Surgery Planning for Percutaneous Hepatic Microwave Ablation.” In: *Proceedings of MICCAI - Lecture Notes in Computer Science* (2008), pp. 569–577 (cited on pp. 27, 48).
- [188] Zidowitz, S., Drexl, H., Kröger, T., Preusser, T., Ritter, F., Weihusen, A., and Peitgen, H.-O. “Baysian Vessel Extraction for Planning of RF-Ablation.” In: *Bildverarbeitung für die Medizin* (2007), pp. 187–191 (cited on pp. 31, 53).
- [189] Zuiderveld, K., Ooijen, P. van, and Chin-A-Woeng, J. “Clinical Evaluation of Interactive Volume Visualization.” In: *Proceedings of IEEE Visualization* (1996), pp. 267–370 (cited on p. 98).